

IEEE ROBOTICS & AUTOMATION MAGAZINE

Vol. 21, No. 3 September 2014

ISSN 1070-9932

<http://www.ieee-ras.org/publications/ram>

Autonomous Micro Helicopters

Navigation in GPS-Denied Environments



IEEE

RA[®]

Meet the **new** State of the Art in Intelligent Research Platforms

**The Pioneer LX is everything you
need to get your research rolling.**

For over 15 years Adept MobileRobots has served the academic community with intelligent, rugged, research robots. We are proud to offer our newest robot, the Pioneer LX. Based on the Adept Lynx platform, the Pioneer LX combines the reliable operation of a professional industrial platform with the development tools and support of a Pioneer research robot.

Developers can easily access and program the robot's on-board computer. Software libraries are provided to speed the development of custom applications, and accessible I/O and power supplies make hardware integration easy. With included laser guidance and autonomous navigation software, the Pioneer LX can be tasked with up to **13 hours** of autonomous navigation, carrying up to **60 Kg** of sensors, effectors, or custom accessories.



Pioneer LX

- Integrated onboard computer
- Autonomous navigation software
- SICK S300 laser scanner
- Front bumper sensor
- Front and rear sonar sensors
- Color LED status indicator rings
- Accessory mounting deck (removable)
- Removable exterior body panels
- Recharging station
- Speakers & Voice Synthesis Software
- Pioneer Software Development Kit
- 5V, 12V, 20V Power Supplies

Integrated On-Board Computer

Intel D252 64-bit Dual Core 1.8 GHz Atom

Wireless Ethernet Communications

2GB DDR3-1066 RAM

Available with Windows or Ubuntu Linux

16 In / 16 Out Digital I/O

4 In / 4 Out Analog I/O

+1.603.881.7960 www.mobilerobots.com sales@mobilerobots.com

IEEE ROBOTICS & AUTOMATION MAGAZINE

Vol. 21, No. 3 SEPTEMBER 2014
 ISSN 1070-9932
<http://www.ieee-ras.org/publications/ram>

FEATURES

26 Vision-Controlled Micro Flying Robots

From System Design to Autonomous Navigation and Mapping in GPS-Denied Environments

By Davide Scaramuzza, Michael C. Achtelik, Lefteris Doitsidis, Friedrich Fraundorfer, Elias Kosmatopoulos, Agostino Martinelli, Markus W. Achtelik, Margarita Chli, Savvas Chatzichristofis, Laurent Kneip, Daniel Gurdan, Lionel Heng, Gim Hee Lee, Simon Lynen, Lorenz Meier, Marc Pollefeys, Alessandro Renzaglia, Roland Siegwart, Jan Carsten Stumpf, Petri Tanskanen, Chiara Troiani, and Stephan Weiss



©ISTOCKPHOTO.COM/NICOLAO

41 Developing an Aerial Manipulator Prototype

Physical Interaction with the Environment

By Matteo Fumagalli, Roberto Naldi, Alessandro Macchelli, Francesco Forte, Arvid Q.L. Keemink, Stefano Stramigioli, Raffaella Carloni, and Lorenzo Marconi



ON THE COVER

Autonomous microhelicopters will soon play a major role in search and rescue, environment monitoring, security surveillance, and other tasks. If they are further realized in small scale, they represent only a limited risk for people. See "Vision-Controlled Micro Flying Robots" on page 26 for more.

CAVE IMAGE: ©ISTOCKPHOTO.COM/PIOTRSOBCZYK

51 FILOSE for Svenning

A Flow Sensing Bioinspired Robot

By Otar Akanyeti, Jennifer C. Brown, Lily D. Chambers, Hadi el Daou, Maria-Camilla Fiazza, Paolo Fiorini, Jaas Ježov, David S. Jung, Maaria Kruusmaa, Madis Listak, Andrew Liszewski, Jacqueline L. Maud, William M. Megill, Lorenzo Rossi, Antonio Qualtieri, Francesco Rizzi, Taavi Salumäe, Gert Toming, Roberto Venturelli, Francesco Visentin, and Massimo De Vittorio

63 Survey of Geodetic Mapping Methods

Geodetic Approaches to Mapping and the Relationship to Graph-Based SLAM

By Pratik Agarwal, Wolfram Burgard, and Cyrill Stachniss

81 Optical Tweezers

Autonomous Robots for the Manipulation of Biological Cells
By Ashis Gopal Banerjee, Sagar Chowdhury, and Satyandra K. Gupta



If you like an article, click this icon to record your opinion. This capability is available for online Web browsers and offline PDF reading on a connected device.



(continued on p. 2)



FEATURES (continued)

89 **The Feel of MEMS Barometers**

Inexpensive and Easily Customized Tactile Array Sensors
By Yaroslav Tenzer, Leif P. Jentoft, and Robert D. Howe

96 **Robotic Dynamic Sculpture**

Architecture, Modeling, and Implementation of Dynamic Sculpture
By Tan Zhang, Kirk Backstrom, Richard E. Prince, Changli Liu, Zhiqin Qian, Dan Zhang, and Wenjun Zhang

105 **The CUIK Suite**

Analyzing the Motion of Closed-Chain Multibody Systems
By Josep M. Porta, Lluís Ros, Oriol Bohigas, Montserrat Manubens, Carlos Rosales, and Léonard Jaillet

115 **Vary Slow Motion**

Effect of Task Forces on Movement Variability and Implications for a Novel Skill Augmentation Mechanism
By Ozkan Celik and Marcia K. O'Malley

123 **Patient-Tailored Assistance**

A New Concept of Assistive Robotic Device That Adapts to Individual Users

By Ricardo Morales, Francisco J. Badesa, Nicolas Garcia-Aracil, Carlos Perez-Vidal, Jose M. Sabater, Eugenia Papaleo, Antonino Salerno, Loredana Zollo, and Eugenio Guglielmelli

134 **The Safety of Domestic Robots**

A Survey of Various Safety-Related Publications
By Tadele Shiferaw Tadele, Theo J.A. de Vries, and Stefano Stramigioli

143 **Rethinking the Machines in Which We Live**

A Multidisciplinary Course in Architectural Robotics
By Apoorva D. Kapadia, Ian D. Walker, Keith Evan Green, Joe C. Manganelli, Henrique Houayek, Adam M. James, Venkata Kanuri, Tarek Mokhtar, Ivan Siles, and Paul Yanik



Designed to set your ideas in motion.

The all-rounder: KUKA LBR iiwa

- **Safe:** Enables innovative cooperation between humans and machines.
- **Sensitive:** The torque sensors in each axis enable haptic solutions.
- **Flexible:** Its 7 axes provide human-like motion capabilities.
- **Programming ease:** C++, Java or any other code language can be used.
- **Soft and hard realtime applications:** Easy high level sensor integration.

KUKA



Experience our Service Robotics
KUKA LBR iiwa and KUKA youBot at
www.kuka-labs.com/en/service_robots



COLUMNS & DEPARTMENTS

- 6 FROM THE EDITOR'S DESK**
- 8 PRESIDENT'S MESSAGE**
- 10 HUMANITARIAN TECHNOLOGY**
- 18 REGIONAL**
- 20 INDUSTRIAL ACTIVITIES**
- 24 TC SPOTLIGHT**
- 152 EDUCATION**
- 154 SOCIETY NEWS**
- 160 WOMEN IN ENGINEERING**
- 162 CALENDAR**
- 164 ERRATA**
- 168 TURNING POINT**

IEEE ROBOTICS & AUTOMATION MAGAZINE

A Publication of the IEEE ROBOTICS AND AUTOMATION SOCIETY
Vol. 21, No. 3 September 2014 ISSN 1070-9932 <http://www.ieee-ras.org/publications/ram>

EDITORIAL BOARD

Editor-in-Chief
Eugenio Guglielmelli
(ram-eic@ieee.org)
Campus Bio-Medico
University, Roma (Italy)

Associate Editors

Antonio Franchi
Centre National de la Recherche
Scientifique, CNRS (France)

Yi Guo
Stevens Institute of Technology (USA)

Hesuan Hu
Xidian University (PR China)

Ferdinando Rodriguez Y Baena
Imperial College (UK)

Yu Sun
University of South Florida (USA)

Loredana Zollo
Campus Bio-Medico University, Roma
(Italy)

Past Editor-in-Chief
Peter Corke
Queensland University of Technology
Brisbane, Australia

Industry Editor
Raj Madhavan
University of Maryland College Park (USA)

RAM Editorial
Assistant and Column Manager
Rachel O. Warnick (USA)

COLUMNS
Competitions: Stephen Balakirsky
and Dan Popa (USA)

From the Editor's Desk: Eugenio
Guglielmelli (Italy)

ROS Topics: Steve Cousins
(USA)

On the Shelf: Alex Simpkins
RDP Robotics (USA)

Student Corner: Lauren Miller
Northwestern University (USA)

**IEEE RAS Vice-President
of Publication Activities**

Antonio Bicchi
University of Pisa (Italy)

RAM home page:
<http://www.ieee-ras.org/publications/ram>

**Robotics and Automation
Society Project Specialists**
Kathy Colabaugh
Rachel O. Warnick
ras@ieee.org

Advertising Sales
Susan Schneiderman
Business Development Manager
Tel: +1 732 562 3946
Fax: +1 732 981 1855
ss.ieemedia@ieee.org

**IEEE Periodicals
Magazines Department**
Debby Nowicki
Managing Editor
d.nowicki@ieee.org

Janet Duder
Senior Art Director
Gail A. Schnitzer
Assistant Art Director
Theresa L. Smith
Production Coordinator
Felicia Spagnoli
Advertising Production Manager
Peter M. Tuohy
Production Director

Dawn M. Melley
Editorial Director
Fran Zappulla
Staff Director,
Publishing Operations

**IEEE-RAS Membership
and Subscription Information:**
+1 800 678 IEEE (4333)
Fax: +1 732 463 3657
http://www.ieee.org/membership_services/membership/societies/ras.html

Digital Object Identifier 10.1109/MRA.2014.2334135

IEEE prohibits discrimination, harassment, and bullying. For more information, visit <http://www.ieee.org/web/aboutus/whatis/policies/p9-26.html>.

IEEE Robotics & Automation Magazine (ISSN 1070-9932) (IRAMEB) is published quarterly by the Institute of Electrical and Electronics Engineers, Inc. Headquarters: 3 Park Avenue, 17th Floor, New York, NY 10016-5997 USA, Telephone: +1 212 419 7900. Responsibility for the content rests upon the authors and not upon the IEEE, the Society or its members. IEEE Service Center (for orders, subscriptions, address changes): 445 Hoes Lane, P.O. Box 1331, Piscataway, NJ 08855 USA. Telephone: +1 732 981 0060. Individual copies: IEEE members US\$20.00 (first copy only), non-members US\$115.00 per copy. Subscription rates: Annual subscription rates included in IEEE Robotics and Automation Society member dues. Subscription rates available on request. Copyright and reprint permission: Abstracting is permitted with credit to the source. Libraries are permitted to



photocopy beyond the limits of U.S. Copyright law for the private use of patrons 1) those post-1977 articles that carry a code at the bottom of the first page, provided the per-copy fee indicated in the code is paid through the Copyright Clearance Center, 222 Rosewood Drive, Danvers, MA 01923 USA; 2) pre-1978 articles without a fee. For other copying, reprints or republication permission, write Copyrights and Permissions Department, IEEE Service Center, 445 Hoes Lane, Piscataway, NJ 08854. Copyright © 2014 by the Institute of Electrical and Electronics Engineers Inc. All rights reserved. Periodicals postage paid at New York and additional mailing offices. Postmaster: Send address changes to IEEE Robotics & Automation Magazine, IEEE, 445 Hoes Lane, Piscataway, NJ 08854 USA. Canadian GST #125634188
PRINTED IN THE U.S.A.





Webots™ 7

professional robot simulation software

 ROS
Enabled

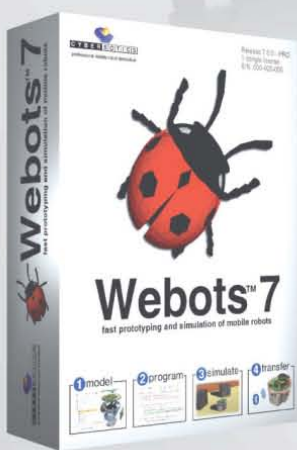
Enter the world of 3D simulation



Illustration created from a Webots screenshot. © 2012 Cyberbotics Ltd.

KEY FEATURES

- runs on Windows, Linux and Mac OS X
- full dynamic and kinematic simulations
- large libraries of robots, sensors, actuators and objects
- programming: ROS, C, C++, Java, Python, Matlab, URBI, etc.
- transfer to real robots: remote control & cross-compilation
- 950+ customers, rich documentation, technical support



www.cyberbotics.com



FROM THE EDITOR'S DESK

Robotics and Automation Science

By Eugenio Guglielmelli

Those of you who were in Hong Kong last June at the record edition of our annual IEEE International Conference on Robotics and Automation had the opportunity to enjoy the plenary talk about robotics research in the Human Brain Project (www.humanbrainproject.org). This is a ten-year, €1 billion research initiative recently launched in Europe as part of the Future Emerging Technologies Flagship program promoted by the European Commission.

Robotics and automation (R&A) technology has been selected as one of the pillars for building up what is supposed to become the most advanced integrated technological platform for tackling fundamental open challenges in simulating and understanding how the human brain works. This choice can be considered as evidence that our R&A disciplines have reached a high level of scientific maturity. Not surprisingly, if you look at the about 100 papers related to R&A topics published over the last 15 years in *Science* and *Nature*, two journals with scopes that span all of the modern scientific disciplines, you will find that nearly half of them address the use of robots as neuroscientific tools.

Other specific topics include design methods for R&A systems, applications of robots in remote and hazardous environments, R&A-based solutions for the severely disabled, and basic enabling technologies for R&A systems.

The IEEE Robotics and Automation Magazine Editorial Board fully sup-

ported the proposal for launching a special issue on replicable and measurable robotics research (see the "Call for Papers" on page 154 of this issue, also available on the magazine's Web site).

The underlying assumption behind the selection of this topic is that a significant portion of R&A research is still missing systematic application of the scientific method. We need careful experimental design, transparency, and many independent researchers worldwide double-checking interactively how the research was performed by other groups and following up by performing similar experiments to determine how dependable the research results are against the initial hypotheses.

The time has come for the R&A community to no longer rely only on the interpretation of the scientific method that has been consolidated over years in other fields such as neuroscience. We are ready to develop our own approaches by systematizing best practices and investing in the significant additional effort needed to develop new methods and tools. We need to spread such basic knowledge among the whole community while it is rapidly enlarging. This is why the IEEE Robotics and Automation Magazine Editorial Board believes that this new special issue fits well with the mission and within the scope of our magazine.

I would love to receive more regular articles focusing on enhancing experimental reproducibility, challenging the falsification of research outcomes generated by other labs, and sharing bench-



marks, data sets, and even remote access to local research platforms with other groups for running independent experiments.

When reading these lines, many of you will probably be on the way back from the 2014 IEEE/Robotics Society of Japan International Conference on Intelligent Robots and Systems in Chicago, which will be the first of our large conferences featuring only so-called interactive sessions. I believe that this format has a huge potential to become a powerful tool for fostering independent, interactive evaluation of experimental results, just like some centuries ago, when systematic application of the scientific method began with public demonstrations of major scientific experiments and related achievements.

After reading this column and maybe having attended many interactive sessions in Chicago, I am sure that some of you will derive from the many different features of this rich *IEEE Robotics and Automation Magazine* issue good hints for your next article on the reproduction of some of the experiments presented here. And do not miss the very interesting "Turning Point" column, which features an interview with Frank Park, the editor-in-chief (EiC) of *IEEE Transactions on Robotics* (*T-RO*). Park outlines how to best address the submission of your research results to *T-RO*, like Ken Goldberg, EiC of *IEEE Transactions on Automation Science and Engineering*, did in the same column in March. Enjoy the issue!

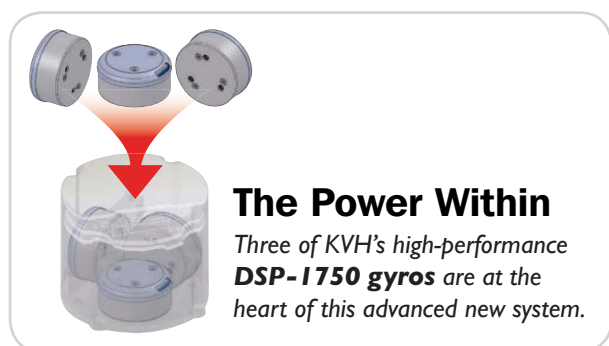
Digital Object Identifier 10.1109/MRA.2014.2347512
Date of publication: 10 September 2014

Price and performance in the palm of your hand



KVH 1750 IMU

- Bias instability of $\leq 0.1^\circ/\text{hr}$, 1σ
- Angle Random Walk (ARW) of $\leq 0.012^\circ/\sqrt{\text{hr}}$
- 3 axes of DSP-1750 FOGs combined with 3 MEMS accelerometers
- Easy integration with other sensors (GPS, DVL, ODO, etc.)
- Compact, precise & accurate
- Commercial-grade
- Breakthrough price & performance
- Available immediately



The Power Within
Three of KVH's high-performance **DSP-1750 gyros** are at the heart of this advanced new system.

Download the White Paper:
kvh.com/1750IMU



KVH Industries, Inc. World Headquarters: 50 Enterprise Center | Middletown, RI 02842 U.S.A. | info@kvh.com | +1 401.847.3327

©2013 KVH Industries, Inc. KVH is a registered trademark of KVH Industries, Inc.



PRESIDENT'S MESSAGE

25 Years of the IEEE Robotics and Automation Society, 30 Years of ICRA

By Raja Chatila

The year 2014 marks both the 25th anniversary of the creation of the IEEE Robotics and Automation Society (RAS) and the 30th anniversary of the IEEE International Conference on Robotics and Automation (ICRA).

On 13 December 1983, the Robotics and Automation Council was created by the IEEE, with operations starting in 1984, as a consequence of the increased interest in robotics and automation within several IEEE Societies, among which were the IEEE Control Systems Society and the IEEE Computer Society. Robotics and automation were fast-growing fields in the early 1980s, and there was a notable number of papers in these areas in the publications and conferences of the Societies.

The Council, chaired by George Saridis, enabled the creation of *IEEE Journal of Robotics and Automation* (with Editor-in-Chief George Bekey), published a newsletter, and organized the first International Conference on Robotics in Atlanta, Georgia, 13–15 March 1984, under the Technical Committee on Robotics of the IEEE Computer Society, with 75 papers in two parallel tracks. In 1985, the conference moved to Saint Louis, Missouri, United States, and became ICRA, with 165 papers in four parallel tracks.

Thanks to the continual efforts of the founding fathers, including George

Saridis, John Jarvis, Richard (Lou) Paul, Antal (Tony) Bejczy, and Larry Ho, the Council soon became a full Society, with an official name change on 15 May 1989. The first president was Arthur Sanderson. Today, robotics and automation are among the key technologies worldwide, and RAS has about 12,000 members.

Thirty years after the Atlanta event, ICRA 2014, held from 31 May to 7 June in Hong Kong, featured 1,016 papers in 227 technical sessions and 19 tracks. It was a wonderfully organized conference thanks to a dedicated committee, with Ning Xi as general chair and King W.C. Lai as local arrangements chair. There was an excellent technical program with a thorough selection process by the Conference Editorial Board chaired by Lynne Parker and the program committee chaired by Bill Hamel and cochaired by Jindong Tan. My warmest thanks go to them all and to their teams.

Today, along with its flagship ICRA, RAS fully sponsors nine conferences. That includes the IEEE International Conference on Automation Science and Engineering (CASE), which took place this year in Taipei, Taiwan, 18–22 August.

RAS financially cosponsors 14 conferences, the most important of which is the IEEE/Robotics Society of Japan (RSJ) International Conference on Intelligent Robots and Systems (IROS). This year, it will be held in Chicago, Illinois, 14–18 September. IROS started in 1988 and is cosponsored by the IEEE

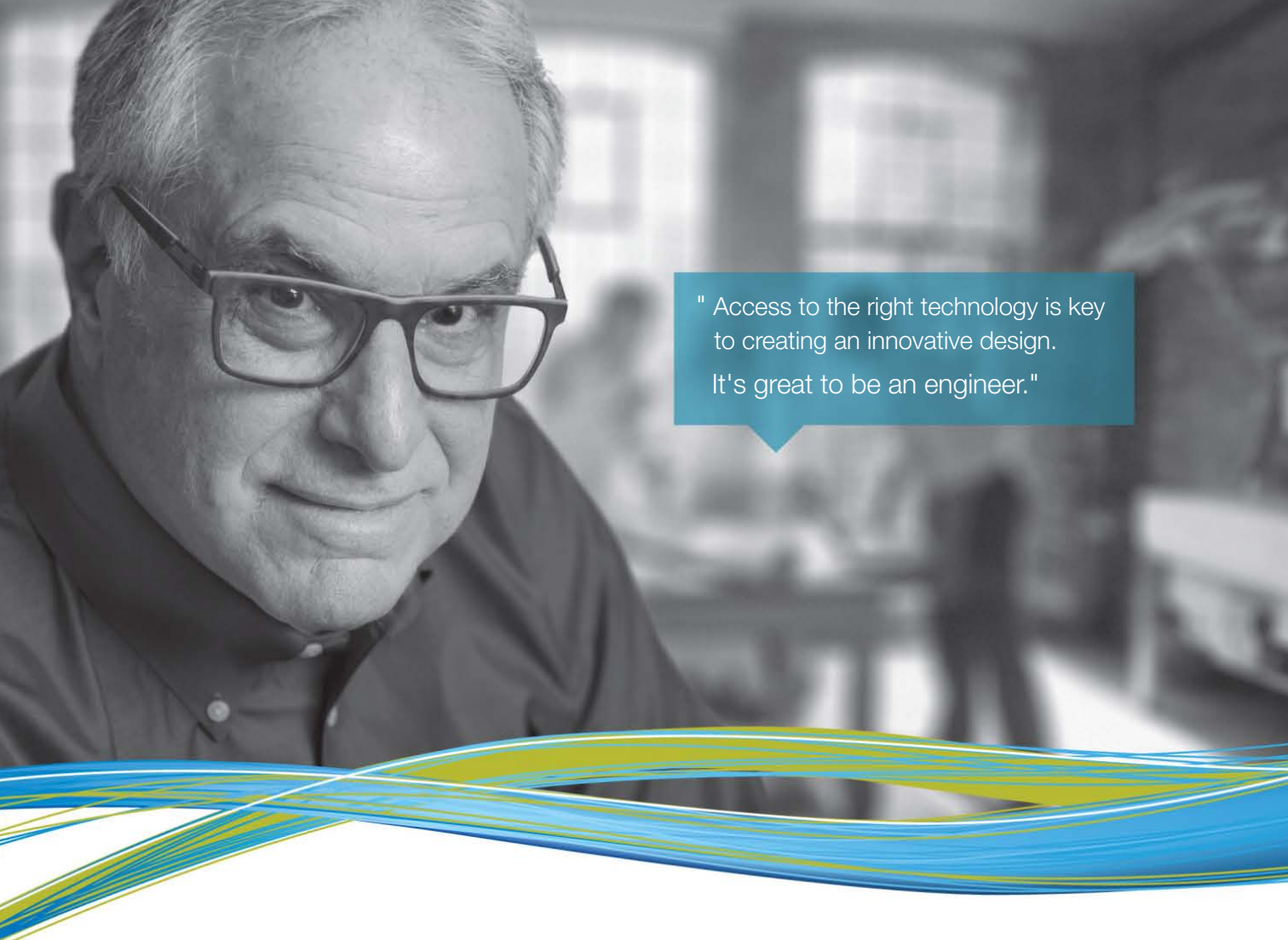
Industrial Electronics Society, RSJ, the Society of Instrument and Control Engineers, and the New Technology Foundation. Finally, RAS also technically cosponsors 13 other conferences.

This broad portfolio is a sign of the richness of our domain, but it requires a global approach and a shared policy for our conferences. Helping conference organizers to use common tools and pass the experience of the past conferences to the organizers of new ones—with the help of the Conference Activity Board, chaired by Oussama Khatib, and the IEEE Meetings, Conferences, and Events Service—can save time and money and make the organization more efficient and our service to members and conference attendees better. We want all conference participants, students and senior scientists alike, to be part of the technical and social activities, to better interact and share the unique experience that our conferences provide. And we want ICRA to be a focal point where all these conferences can be highlighted and promoted to the global community.

As our Society grows, our conferences must gain in scientific and technical quality with a thorough selection process, which is already in place, and innovative paper presentations. Conferences are the place where the members of the robotics and automation community congregate. We owe them the best environment in which to do so.

Digital Object Identifier 10.1109/MRA.2014.2339971
Date of publication: 10 September 2014





" Access to the right technology is key to creating an innovative design.
It's great to be an engineer."

ENGINEERS START HERE.

Research. Design. Prototype.

From data sheets to development kits & tools to components, Newark element14 offers what you need for every stage of your design. newark.com | 800.463.9275



 KEYSIGHT
TECHNOLOGIES

Featured Product:
33611A Trueform Waveform Generator
(29X7419)



element*14*



 HUMANITARIAN TECHNOLOGY

2014 Humanitarian Robotics and Automation Technology Challenge

By Raj Madhavan, Lino Marques, Edson Prestes, Prithviraj Dasgupta, Gonçalo Cabrita, David Portugal, Bruno Gouveia, Vitor Jorge, Renan Maffei, Guilherme Franco, and Jose Garcia

Robotics and automation (R&A) technologies have the potential to transform and improve the lives of people around the globe by addressing the world's toughest challenges. The IEEE Robotics and Automation Society (RAS) Special Interest Group on Humanitarian Technology (SIGHT) is engaging the academic and nonacademic community to propose viable solutions in R&A to address relevant world problems through the Humanitarian Robotics and Automation Technology Challenge (HRATC). The HRATC is an unprecedented opportunity for IEEE Members from around the world to collaborate using their skills and education to benefit humanity. The problems (challenges) are framed with the environmental, cultural, structural, political, socioeconomic, and resource constraints so that solutions can be developed, deployed, and sustained.

RAS is the first and only IEEE Society to have a SIGHT. The mission of the RAS SIGHT is the application of R&A technologies for promoting humanitarian causes around the globe and to leverage existing and emerging technologies for the benefit of humanity and toward increasing the quality of life in underserved, underdeveloped areas in collaboration with existing global communities and organizations.

According to the United Nations Mine Action Service, land mines kill 15,000–20,000 people every year (mostly children) and maim countless more across 78 countries. Demining efforts

cost US\$300–1,000 per mine, and, for every 5,000 mines cleared, one person is killed and two are injured. Thus, clearing postcombat regions of land mines has proven to be a difficult, risky, dangerous, and expensive task with enormous social implications for civilians. Motivated by these considerations, the first HRATC edition took place at the 2014 International Conference on Robotics and Automation (ICRA) in Hong Kong and remotely in Coimbra, Portugal. It focused on promoting the development of new strategies for autonomous land mine detection using a mobile (ground) robot.

Initially, 14 teams from eight countries submitted their entries. Based on the description papers where teams were asked to describe their experience and strategies, ten teams were short-listed to move forward with the three stages of HRATC 2014: simulation, testing, and finals. The 2014 edition was the first HRATC event where teams from around the globe had the chance to participate and remotely develop autonomous demining strategies for detection and classification in a physical outdoor robotic platform, the field and service robotics (FSR) Husky, as shown in Figure 1. This is an all-terrain, four-wheeler, skid-steering autonomous robot built around a Clearpath Husky A200 base, comprising several sensors, such as stereo cameras, a laser range finder, a global positioning system (GPS), an inertial measurement unit (IMU), and a



Figure 1. The HRATC 2014 robot platform.

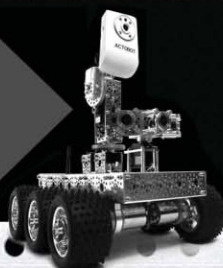
two-degrees-of-freedom (2-DoF) mine clearance arm equipped with a Vallon VMP3 metal detector.

For the simulation stage (March–April 2014), a software framework (hereafter referred to as the *HRATC framework*) that runs on a Linux-based operating system and uses the robot operating system (ROS) to communicate with the client and the robot was developed. Figure 2 presents the software architecture. In the simulation, as shown in Figure 2(a), the framework provides the simulated data to the client. The Gazebo Simulator, through the Husky modules, provides the data of the robot sensors, cameras, and its localization, while a custom simulator provides the metal detector readings based on data sets collected with the real metal detector. In the core of the framework is the HRATC Judge, which extracts several performance measures, such as the number of detected mines, false detections, and exploded unknown mines as well as the covered area and coverage time, and computes the scores of

Digital Object Identifier 10.1109/MRA.2014.2334953
Date of publication: 10 September 2014

Actobotics™

DREAM. DESIGN. BUILD. REPEAT.



DID YOU KNOW?

- ✓ We offer servo modifications
- ✓ We carry over 3,500 products
- ✓ We ship candy with orders
- ✓ We have a cat named Yoda
- ✓ We launched a blog
- ✓ We love seeing customer photos
- ✓ We've been in business for 20 years
- ✓ We ship internationally
- ✓ We appreciate our customers!



NEW MOBILE SITE

You asked, we listened. Now it's easy to browse and shop ServoCity on the go from your mobile device!



www.SERVOCITY.com
620.221.0123



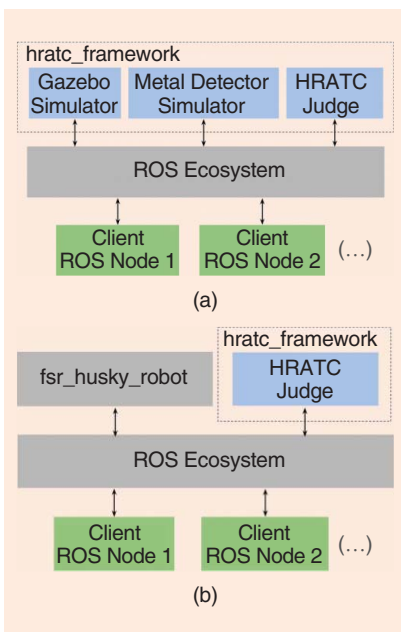


Figure 2. The software architecture for (a) the simulation and (b) the testing phase.

the teams. During experiments, these measures can be visualized in the HRATC framework main window, as

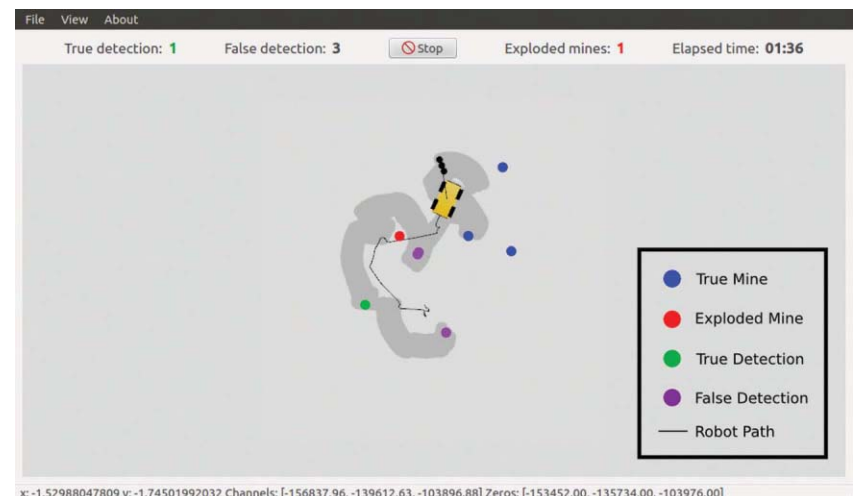
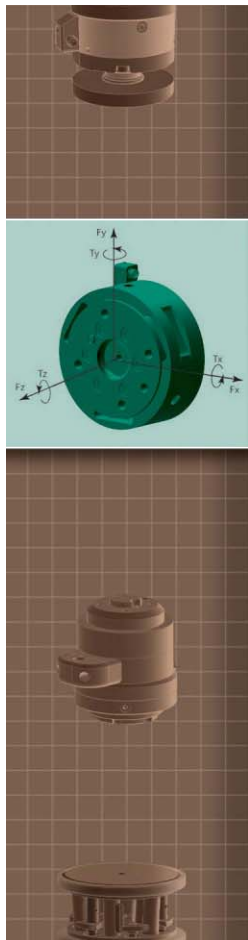


Figure 3. An HRATC framework main window.

shown in Figure 3, along with some additional information, such as the robot path.

The scoring metric used to evaluate the performance of the teams is a composition of three different components: the mine detection score, the total time score, and the swept area score. The mine detec-

tion score—the one with the largest weight of the three—is a ratio between the number of true detections and all guesses made by the competitor, and, therefore, each mistake decreases this score. In addition, mistakes considering previous knowledge (e.g., explosions of detected mines) are worse than mistakes without



Measure all six components of force and torque in a compact, rugged sensor.

Interface Structure—high-strength alloy provides IP60, IP65, and IP68 environmental protection as needed

Low-noise Electronics—interfaces for Ethernet, PCI, USB, EtherNet/IP, PROFINET, CAN, EtherCAT, Wireless, and more

Sensing Beams and Flexures—designed for high stiffness and overload protection



The F/T Sensor outperforms traditional load cells, instantly providing all loading data in every axis. Engineered for high overload protection and low noise, it's the ultimate force/torque sensor. Only from ATI.

ATI INDUSTRIAL AUTOMATION
Engineered Products for Robotic Productivity

25
YEARS

www.ati-ia.com/rft
919.772.0115

While the world benefits from what's new,
IEEE can focus you on what's next.



Develop for tomorrow with
today's most-cited research.

Over 3 million full-text technical documents
can power your R&D and speed time to market.

- IEEE Journals and Conference Proceedings
- IEEE Standards
- IEEE-Wiley eBooks Library
- IEEE eLearning Library
- Plus content from select publishing partners

IEEE Xplore® Digital Library

Discover a smarter research experience.

Request a Free Trial

www.ieee.org/tryieeexplore

Follow IEEE Xplore on  



IEEE
*Advancing Technology
for Humanity*

IEEE TRANSACTIONS ON ROBOTICS

A PUBLICATION OF THE IEEE ROBOTICS AND AUTOMATION SOCIETY

The IEEE TRANSACTIONS ON ROBOTICS (T-RO) publishes fundamental scientific papers covering all aspects of robotics. Papers reporting on results of major research significance that draw upon any combination of theoretical, algorithmic, experimental, and empirical analysis and validation, including design and fabrication, are welcome. Paper categories include regular papers, short papers, communications, and survey papers. Multimedia attachments are also welcome.

IEEE and T-RO support the evolutionary publication paradigm, in which early versions of a work may have appeared in conferences. Sources must be indicated during the submission procedure, explicitly cited in the manuscript, and any differences, changes, or additions discussed in the text of the paper.

Submission information : <http://ieee-ras.org/publications/t-ro>

EDITOR-IN-CHIEF : FRANK PARK, Seoul Nat.Univ. ,Seoul, Korea

EDITORS

DIETER FOX Univ. of Washington Seattle, WA, USA	ABDERRAHMANE KHEDDAR CNRS-AIST JRL Tsukuba, Japan	TODD MURPHEY Northwestern Univ. Evanston, IL USA	BRAD NELSON ETH Zurich Zurich, Switzerland	CARME TORRAS IRI CSIC-UPC Barcelona, Spain
---	---	--	--	--

ASSOCIATE EDITORS

TAMIM ASFOUR Karlsruhe Inst. Tech. Karlsruhe, Germany	AUDE BILLARD EPFL Lausanne, Switzerland	TIM BRETL UIUC Urbana, IL, USA	JOSE CASTELLANOS Univ. Zaragoza Zaragoza, Spain	RAVINDER DAHIYA Univ. Glasgow Glasgow, UK
RYAN EUSTICE Univ. Michigan Ann Arbor, MI, USA	TAREK HAMEL CNRS-UNSA Sophia-Antipolis, France	SHINICHI HIRAI Ritsumeikan Univ. Kusatsu, Japan	DAVID HSU Nat. Univ. Singapore Singapore	VOLKAN ISLER Univ. Minnesota Minneapolis, MN, USA
PATRIC JENSFELT KTH Stockholm, Sweden	SANGBAE KIM MIT Cambridge, MA, USA	JA CHOON KOO Sungkyunkwan Univ. Suwon, Korea	VENKAT KROVI SUNY Buffalo Buffalo, NY, USA	VILLE KYRKI Aalto Univ. Espoo, Finland
NICOLAS MANSARD LAAS-CNRS Toulouse, France	ANDREAS MUELLER Univ. Mich/SJTU J. Inst. Shanghai, China	CHRISTIAN OTT DLR Wessling, Germany	LUCIA PALLOTTINO Univ. of Pisa Pisa, Italy	JAN PETERS TU Darmstadt Darmstadt, Germany
STEPHANE REGNIER ISIR Paris, France	PAOLO ROBUFFO-GIORDANO CNRS at IRISA/INRIA Rennes, France	CRISTIAN SECCHI Univ. Modena and Reggio Emilia Reggio Emilia, Italy	NABIL SIMAAN Vanderbilt Univ. Nashville, TN, USA	PHILIPPE SOUREZ LAAS-CNRS Toulouse, France
FEDERICO THOMAS IRI CSIC-UPC Barcelona, Spain	ROBERT J. WEBSTER III Vanderbilt Univ. Nashville, TN, USA	PIERRE-BRICE WIEBER INRIA Grenoble Grenoble, France	EIICHI YOSHIDA CNRS-AIST JRL Tsukuba, Japan	





Figure 4. A challenge environment.

prior knowledge (e.g., explosions of undetected mines), and receive a large penalization. The swept area score, i.e., the percentage of the total area of the environment covered by the robot sensors, is of great importance since one of the goals in demining is cleaning the largest area. However, its importance is much smaller than the mine detection score because a large coverage without a good mine detection strategy can be useless and even dangerous. Finally, the total time score, although important, is not as critical as correct detection and, therefore, only adds a small contribution to the final score.

In the testing stage, as shown in Figure 2(b), the real robot is used through the `fsr_husky_robot` ROS metapackage. For consistency, in both stages, the same ROS topics are used to publish the data, which means that the code generated by the teams during the simulation stage can also work on the testing stage without major modifications. During the testing phase, which took place over the first three weeks of May 2014, each team had the possibility to refine its field coverage and mine detection strategies using ROS to control the FSR Husky. Flexibility was a priority, as the participants could make use of all of the robot's sensors as they saw fit to develop their own algorithms. The testing phase took place in an outdoor arena covered by low grass and ditches, as shown in Figure 4. A few surrogate mines, composed of a small plastic box with a metal sphere inside, were buried at a shallow depth, together with other metal debris, e.g., coke cans, metal pieces, and large screws. Three separate trials were allowed (staggered by a week each) for each team to evaluate and adjust their strategy. Participants had access in real time to precise localization

data fed by GPS, IMU, and odometry. In addition, during the trials, a data set for the teams to assess the sensibility of the metal detector over different types of soil was also provided, as well as several examples on how to control the robot and the sweeping arm with the ROS. Feedback, data sets, and video footage with the robot behavior were sent to all teams

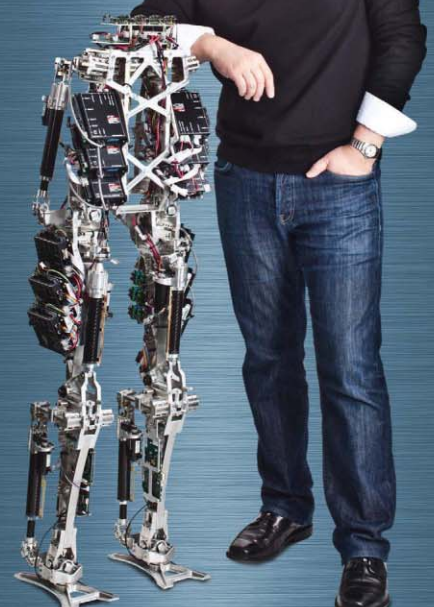
after each trial. This phase was crucial to allow the participants to have a “feel” of the differences between controlling a simulated platform, which they used for development and the real robot used in the finals. These differences mainly were in the localization system and the arm control. Likewise, the testing phase was a fundamental learning process for the

“For our high performance robots, we need high speed, light weight, high torque actuators. The only solution is maxon.”

— Dr. Dennis Hong
Professor of Mechanical & Aerospace Engineering and Director
of RoMeLa (Robots & Mechanism Laboratory) at UCLA

What drives Dr. Dennis Hong is his quest to create truly humanoid robots that can do useful work. What drives his robots are maxon motors and controllers. Where precision, consistency, and easy integration are critical, maxon provides the intelligent drive systems to bring tomorrow's designs to life. Learn how we can help you keep your projects moving. Visit us at maxonmotorusa.com.

Scan code to see video of Dr. Hong discuss working with Maxon Motors.



SAFFiR (Shipboard Autonomous FireFighting Robot)

maxon motor

driven by precision

maxon
PRECISION MOTORS



Figure 5. From left, Raja Chatila, RAS president; Sandesh Gowda and Dan Popa (winners from team ORION); and cochairs of HRATC 2014: Raj Madhavan (chair, RAS SIGHT and vice president, RAS Industrial Activities Board), Lino Marques, Edson Prestes, and Prithviraj Dasgupta.

challenge organization, as it allowed for checking the robustness of the robot in numerous field trials and during long periods of time, as well as optimizing the arm sweeping controlling parameters, carrying out timely replacement of hardware and pieces, and assessing weaker points of the platform so as to improve in upcoming trials.

After the testing phase, four teams participated in the finals at ICRA in

Hong Kong, consisting of two runs on 31 May and 1 June, which were video-streamed live over the Internet from Coimbra, Portugal. The final challenge environment was an open wooded area with a size of 10×5 m, as shown in Figure 4, and delimited by four GPS coordinates. The challenge area was marked by plastic tape for visualization purposes, and a virtual fence was deployed to stop the robots from going outside the chal-

lenge area. Five surrogate mines were buried in the field in addition to metal debris. The teams were evaluated according to the scoring metric on their best run.

Team ORION of the University of Texas at Arlington was declared as the grand winner. The second- and third-place finishers were the Team Geeks of the Square Table (University of Bremen, Germany) and Team USMiners (University of Southern Mississippi). Thanks to IEEE SIGHT sponsorship, the three best-ranked teams received a cash prize (US\$1,000, US\$500, and US\$250, respectively) together with a certificate and a plaque.

We see this challenge as a multiyear effort at the end of which it is our hope that, with the help of the academic and industrial communities, a sustainable, cost-effective, and meaningful solution would become available to this problem that has plagued several worldwide communities for a long while. In the next HRATC edition that will take place during ICRA 2015 in Seattle, Washington, we will continue to refine the development of new strategies for autonomous land mine detection.

In addition, the RAS SIGHT is currently investigating new challenges for the R&A community. If you are interested in participating and/or proposing a challenge, please send an e-mail to raj.madhavan@ieee.org. Additional information regarding challenges, deadlines, and a subscription for the next edition will be posted at <http://www.ieee-ras.org/educational-resources-outreach/humanitarian-efforts>. The challenge organizers thank Clearpath Robotics, Inc., the FP7-TIRAMISU project (<http://www.fp7-tiramisu.eu/>), the RAS Competitions Committee, and the RAS SIGHT for their support and partnership in organizing HRATC'14.

The HRATC 2014 organizers were Raj Madhavan (chair, RAS SIGHT), Lino Marques (University of Coimbra, Portugal), Edson Prestes (Federal University of Rio Grande do Sul, Brazil), and Prithviraj Dasgupta (University of Nebraska-Omaha). For more information and details on the challenge and scope, please visit <http://www.isr.uc.pt/HRATC2014/>. 

Butterfly Haptics

Magnetic Levitation Haptic Interfaces



Highest fidelity interaction
for teleoperation and virtual
environments

<http://butterflyhaptics.com>

sales@servocity.com

(620) 221-0123

SERVOCITY

MAKING THINGS MOVE

LINEAR ACTUATORS

12V HEAVY DUTY

Up to 180 lb thrust

Offered in 6 stroke lengths from 2" to 12"



Aluminum stroke rod and outer tube

Metal drive gears ensure tremendous durability

\$129.99



5/16" diameter mounting points that bolt up to our mounting brackets (sold separately)



12V SUPER DUTY

Up to 1,570 lb thrust

Offered in 6 stroke lengths from 4" to 24"

1.125" diameter extension shaft



Precision ball screw-drive

\$399.99



Powder-coated aluminum base

MOTOR SYSTEMS

These systems offer a simple way to reduce the speed and increase the torque of a gearmotor

\$59.99
Gearmotor Gearbox (full metal gears)\$59.99
Worm Drive Gearbox 30:1 Gear Reduction Ratio

Brand New!

DREAM.
DESIGN.
BUILD.
REPEAT.— DID YOU KNOW? —
We price match and pre-modify Hitec servos!

GEARMOTORS

3-12V Standard Gearmotors

\$24.99
6-12V Micro GearmotorBlocks

\$14.99

\$59.99
Robotzone Heavy Duty Gearmotors

6-12V Precision Gearmotors

SERVOS

Offset Gearmotors



\$49.99



\$34.99



SCAN THIS CODE TO VISIT SERVOCITY ON THE GO!

Rover Build Credit:
John Art
Robotics Teacher
Ellensburg, WA

WE SHIP WORLDWIDE



...and much more!



Channel & Brackets

Hub Mounts

Bearing Mounts

Gears & Sprockets

Shafting & Tubing

Hubs & Clamps

Channel Gearboxes

Wheels & Tires

Pulleys & Belts

One online store.
Thousands of products.
Millions of possibilities.

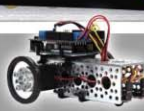
NEW

WWW.SERVOCITY.COM**HUGE SELECTION - LOW PRICES - FAST SHIPPING!**

Join our online community



Aluminum Frame

Introducing the ActoBitty Robot Kit -----
Simply snap on an Arduino or Raspberry Pi and you're ready to go!

just \$27.99

REGIONAL

Network Bridging Among Professionals

By Xiaorui Zhu

I am honored to deliver the opening remarks of a series on Chapter activities on behalf of the IEEE Robotics and Automation Society (RAS) Chapter and International Activities Committee. This committee is in charge of organizing and fostering international cooperation among scholars and students, mainly through the Chapters of the Society, which are an important means toward this goal. Kenji Suzuki from the University of Tsukuba, Japan, has made great efforts in his previous term leading the Committee. I, Xiaorui Zhu, am from the Harbin Institute of Technology Shenzhen Graduate School and have led the IEEE Women in Engineering committee within RAS over the last two years. Now, Kenji and I are cochairs of the Chapter and International Activities Committee, serving the membership for the next two years to make use of our experiences and advance the development of RAS membership, especially in local Chapters.

Like all IEEE Societies, the membership of RAS is made up of individual IEEE Members. RAS has over 12,000 members around the world and is the fastest-growing Society within the IEEE. RAS membership has seen dramatic growth at all levels over the past five years. Our goal is to provide aid in promoting close cooperation and exchange of technical information and opportunities among individual members, although they are scattered all around the world.

Many RAS members are relatively new to the Society, with 36% of mem-

bers in their first year, and only 34% of RAS members have been with the Society for over five years. Of the first-year members, 54% are student or graduate student members.

How can RAS form better connections and encourage long-term membership? Technical committees are an important network for these members in terms of the field of interest. Another essential network is provided through the local Chapters (Section/Branch Chapters, including joint Chapters with other IEEE Societies); they can unite the individual members according to geographic location. Through these Chapters, we strive to ensure that the members of all regions are well represented and feel equally at home in the diverse Society activities, such as conferences, summer/winter schools, and elections.

As can be seen in Figure 1, the number of local Chapters has increased since the birth of RAS and reached 78 Chapters this year. There has been a 30% increase in the number of local Chapters

since 2011. A sharp jump was also observed in the number of student Chapters, with 82 student Chapters in 2014 compared with the year of 2013. This growth is very encouraging for us, as we aim to provide more services to support RAS Chapters.

Therefore, in the next two years, we will take action in different ways to improve the network of the local Chapters and the Society. As usual, we will keep providing sufficient funding each year to support the diverse technical and educational activities organized by the Chapters. The opportunities include the following.

- Local Chapter support requests of up to US\$2,000 are granted, depending on the quality and quantity of the proposals. The application form can be found at <http://www.ieee-ras.org/images/Chapter%20Grant%20Application14-15.pdf>. Chapter grant proposals will be reviewed at each IEEE Conference on Robotics and Automation (ICRA) and IEEE/RSJ International Conference on Intelligent

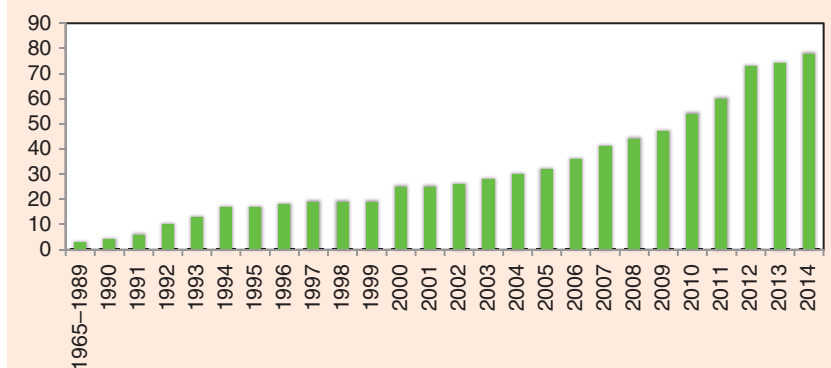


Figure 1. The history of RAS Section Chapter development, not accounting for Student Branch Chapters.

Digital Object Identifier 10.1109/MRA.2014.2334141
Date of publication: 10 September 2014

Robots and Systems (IROS), with the two application deadlines being 15 August and 15 April.

- RAS start-up Chapter grant requests are granted in the amount of US\$500 to encourage each new Chapter to initiate activities. Organizers need to fill out the application form at <https://adobeformscentral.com/?f=KYlSh2SSiHMmtHVJu-PZ-BwReview>.
- Distinguished Lecturer support of up to US\$3,000 is available, which is reviewed in conjunction with a related technical committee to jointly make recommendations. Please refer to http://www.ieee-ras.org/images/ras-resources/DL_Check_List_for_Chapter_Request14-15.pdf for the application form.

To communicate with the local Chapters, we will send eNews to Chapter Chairs quarterly to inform them of support available through RAS and the IEEE. We encourage Chapters to take full advantage of RAS support to benefit our

members. In addition, new members will be introduced to a local Chapter nearby when applicable. We hope every RAS member will belong to a local Chapter through our efforts!

A new program is in the early stages of formation. It will allow us to invite local Chapter representatives to the RAS flagship conference ICRA each year to meet with the Society leaders and share best practices and common issues. This initiative is expected to begin at ICRA 2015 in Seattle, Washington United States. We encourage more local Chapters to focus on quality rather than quantity. Good-quality Chapters will have more opportunities to receive our invitation letter and travel support, such as the winner of the Best Chapter of the Year. The detailed plan will be announced following IROS 2014 in October.

This column is also an important platform for the local Chapters to show off their successful activities and share their point of view in technical and educational aspects. If you have any experi-

ences or lessons to share or want to recognize your Chapter, please feel free to contact us and make the best use of this great platform. You are welcome to submit your articles to us at any time.

To summarize, the RAS Chapter and International Activities Committee wants to further develop the relationship between RAS leaders and RAS Chapters. Please take advantage of the following available resources:

- <http://www.ieee-ras.org/member-communities>
- <http://www.ieee-ras.org/member-communities/chapters>
- <http://www.ieee-ras.org/member-communities/chapters/section-chapters>
- <http://www.ieee-ras.org/member-communities/chapters/student-chapters>
- <http://www.ieee-ras.org/about-ras/society-resource-center/ras-resources>
- Chapter Resources: <http://www.ieee-ras.org/about-ras/society-resource-center/rasresources#>



youBot and more

youBot Store

www.youBot-Store.com

New soft two-finger gripper for the youBot!



youBot Store GmbH | Bergiusstr. 15 | D-86199 Augsburg | Germany | mailto: sales@youBot-Store.com



Draft Standards Development of Two Working Groups

By Raj Madhavan, Wonpil Yu, Craig Schlenoff, Edson Prestes, and Francesco Amigoni

The IEEE Robotics and Automation Society Standing Committee for Standards Activities (RAS-SCSA) strives to formally adopt and confirm the best practices in robotics and automation. In the last three years, the RAS-SCSA has been working closely with the academic and industrial

communities and with other standards developing organizations (SDOs) toward the standardization of map data representation and ontologies for robotics and automation within two working groups (WGs). This column provides an overview of the work carried out so far and of the draft standards

that are soon to be submitted for balloting and subsequent approval.

Being one of the essential elements toward a complete navigation function for mobile robots, maps for mobile robots (robot maps, for short) are diversified according to how a target environment is represented. Without a common representation of map data, however, variations in the implementation of robot maps readily deteriorate the compatibility of a robot map into limited use. Based on the observations on the

increase of robot products equipped with navigation functionality, the RAS-SCSA Map Data Representation Working Group (MDR WG) was formed to develop a standard for two-dimensional (2-D) maps to be used by mobile robots operating in indoor and outdoor environments. The standard provides the specifications for representing 2-D metric and topological maps and a recommended format for exchanging map data among robots, computers, and other devices. While facilitating the technological advancement for robot mapping, the standard does not cover the activities of maintaining, updating, and revising robot maps.

Since the official approval of the proposed project authorization request in November 2011 (<http://standards.ieee.org/develop/project/1873.html>), the MDR WG has been active in developing a draft specification of the MDR standard. First, the MDR WG conducted a survey of existing standards from other SDOs, such as the International Standards Organization and the Open Geospatial Consortium, which may be related to robot maps. Then the industry practices of robot map usage were examined in the form of a technical workshop held during the IEEE International Conference on Automation Science and Engineering 2012 conference week. Based on the findings and on the discussions during the follow-up meetings, the MDR WG specified a robot map hierarchy and terminologies related to robot maps (which are fully compatible with the standard ontology described later) and a corresponding

data model. As the draft standard is getting more specific, new experts have joined the WG this year to develop an XML schema for exchanging robot maps. In the meantime, the MDR WG WiKi site (<https://ieee-sa.centraldesktop.com/1873workinggrouppublic/>) was built to facilitate collaboration among WG members and to provide brief information of the MDR WG activities to the public.

At the heart of the MDR specifications lies the definition of a local map, which acts as a baseline (abstract) representation for metric and topological maps. Figure 1 shows a Unified Modeling Language (UML) diagram of a local map, which is still under construction and is largely self-explanatory. Class diagrams describing metric and topological maps have gone through several revisions within the MDR WG, and an associated XML schema has been developed based on them. Before submitting the draft standard to the IEEE Standards Association around the IEEE/RSJ International Conference on Intelligent Robots and Systems 2014 conference week, a reference implementation based on the developed MDR specifications will be developed within the MDR WG. The reference implementation will include compatibility check and translation tools between common robot map formats [for example, those employed in robot operating system (ROS)] and MDR specifications, and will cover grid, geometric, and topological maps. In addition, a map-merging application based on the MDR specifications will serve as further evidence for verification

While facilitating the technological advancement for robot mapping, the standard does not cover the activities of maintaining, updating, and revising robot maps.

that are soon to be submitted for balloting and subsequent approval.

Being one of the essential elements toward a complete navigation function for mobile robots, maps for mobile robots (robot maps, for short) are diversified according to how a target environment is represented. Without a common representation of map data, however, variations in the implementation of robot maps readily deteriorate the compatibility of a robot map into limited use. Based on the observations on the

Digital Object Identifier 10.1109/MRA.2014.2334971
Date of publication: 10 September 2014

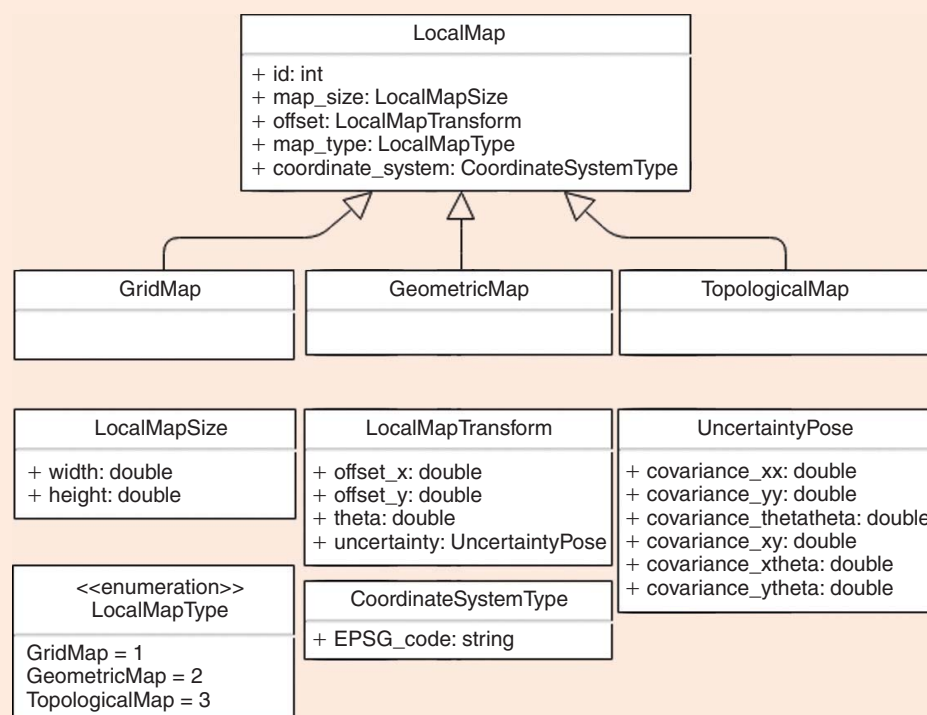


Figure 1. A UML diagram of a local map.

Robotnik
Advanced Robotic Solutions

KEY FEATURES:

- » ROS architecture
- » High mobility and modularity
- » Indoor / Outdoor Navigation
- » Suitable for research, security and inspection
- » Customized Solutions

Contact us today
info@robotnik.es

www.robotnik.eu

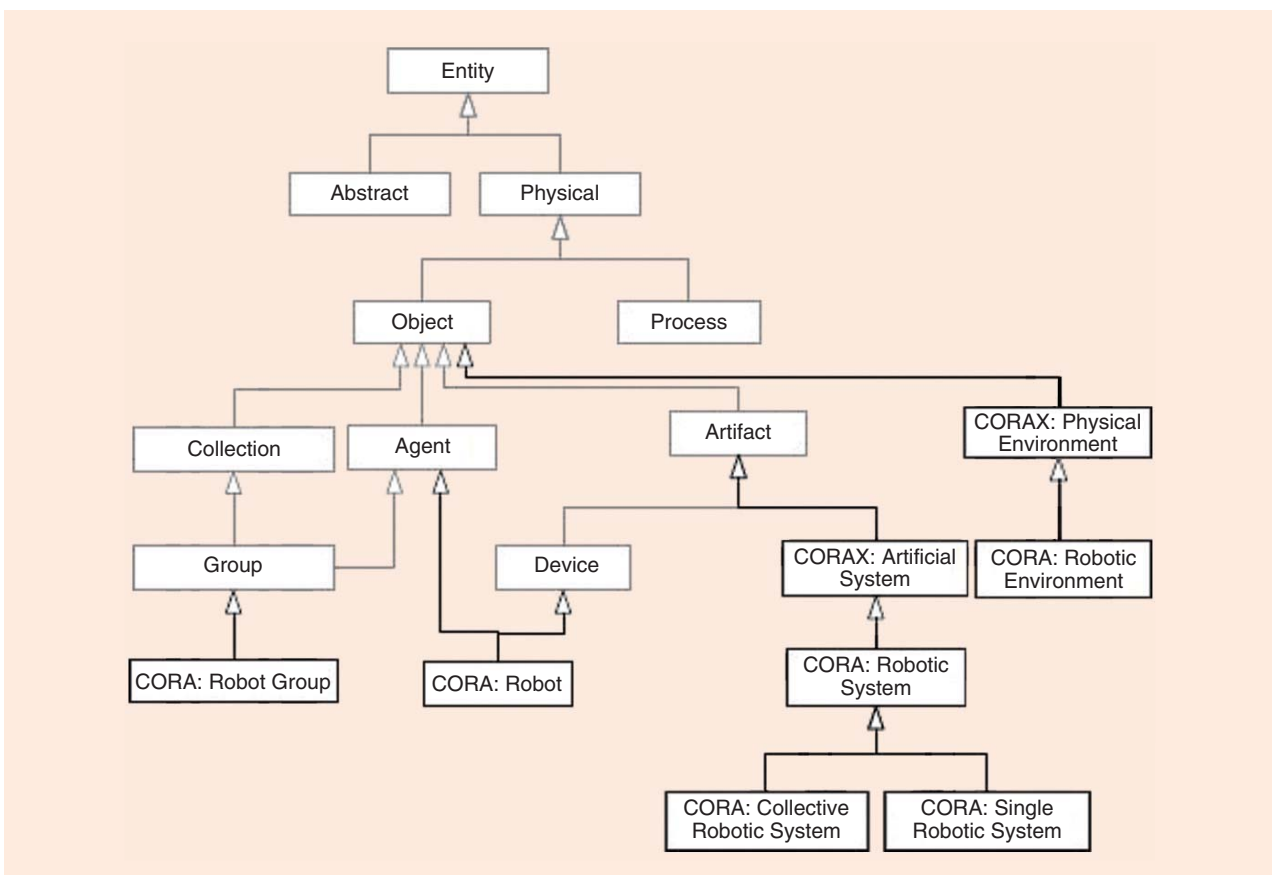


Figure 2. An overview of the main concepts of the CORA.

and validation of the developed MDR specifications.

The goal of the RAS-SCSA Ontologies for the Robotics and Automation Working Group (ORA WG) is to develop a standard to provide an overall ontology and associated methodology for knowledge representation and reasoning in robotics and automation, together with the representation of concepts in an initial set of application domains. It provides a unified way of representing knowledge and a common

set of terms and definitions, allowing for unambiguous knowledge transfer among any group of human, robots, and other artificial systems.

The recent efforts of the WG have been on the development of a core ontology for robotics and automation (CORA) standard, which focuses on the representation of funda-

mental concepts from which the more detailed concepts belonging to other ORA WG ontologies are constructed. A consensus has been reached among the WG participants, and the document is expected to be forwarded to the IEEE Standards Association to start the balloting process in the Summer of 2014.

The CORA aims to describe what a robot is and how this concept relates to other concepts (for more details, see [1]). It defines four broad entities: robot part, robot, complex robot, and robotic system. The term *robot* may have as many definitions as authors writing about the subject. The inherent ambiguity in this term might be an issue when one needs to specify an ontology for a broad community like ours. We acknowledge this ambiguity as an intrinsic feature of the domain, and, therefore, we decided to elaborate a definition based purely on necessary conditions, without specifying sufficient conditions. Thus, it is ensured that the CORA will cover all of the

entities that the community actually considers as robots, at the cost of classifying as a robot some entities that actually are not robots from the point of view of some roboticists. However, the concepts in our ontology could be specialized according to the needs of specific subdomains or applications of robotics and automation. More importantly, we decided on a definition of robot that emphasizes its functional aspects. For our general purposes, robots are agentive devices in a broad sense, purposed to act to accomplish a task. In some cases, the actions of a robot might be subordinated to the actions of other agents, such as software agents (bots) or humans. A robot is also a device, in the sense of the Suggested Upper Merged Ontology (SUMO) [2], composed of suitable mechanical and electronic parts. According to SUMO, a device is an artifact (i.e., a physical object product of making), which participates as a tool in a process. Being a device, a robot

At the heart of the MDR specifications lies the definition of a local map.

of the WG have been on the development of a core ontology for robotics and automation (CORA) standard, which focuses on the representation of funda-

inherits from SUMO the notion that devices have parts. As a consequence, the CORA allows one to represent complex robots with robot parts. A robot is also an agent. SUMO states that an agent is “something or someone that can act on its own and produce changes in the world.” Robots perform tasks by acting on the environment or themselves. Action is strongly related to agency in the sense that the acting defines the agent. Robots can form social groups, called *robotic groups*, where they interact to achieve a common goal. A robotic group is also an agent in the sense that its own agency emerges from its participants. This notion can be used to describe robot teams, or even complex robots formed by many independent robotic agents acting in unison. Robotic systems are systems composed of robots (or groups

of robots) and other devices that facilitate the operations of robots. A good example of a robotic system is a car assembly cell in a manufacturing site. It is located in an environment equipped with actuated structures that manipulate the car body in a way that industrial robots can act on them. An environment equipped with a robotic system is a robotic environment. Figure 2 shows an overview of the main concepts of the CORA.

If you are interested in getting involved in the MDR WG, please visit <https://ieee-sa.centraldesktop.com/1873workinggrouppublic/> or contact the chair, Wonpil Yu (ywp@etri.re.kr), or vice chair, Francesco Amigoni (francesco.amigoni@polimi.it). For the ORA WG, please visit <https://ieee-sa.centraldesktop.com/p1872public/> or contact the chair, Craig Schlenoff (craig.schlenoff@nist.gov), or vice chair, Edson Prestes (prestes@inf.ufrgs.br). For general questions about standards development within the IEEE RAS, please contact the chair, Raj Madhavan (raj.madhavan@ieee.org).

References

- [1] E. Prestes, J. L. Carbonera, S. R. Fiorini, V. A. M. Jorge, M. Abel, R. Madhavan, A. Locoro, P. Goncalves, M. E. Barreto, M. Habib, A. Chibani, S. Gérard, Y. Amirat, and C. Schlenoff, “Towards a core ontology for robotics and automation,” *Robot. Auton. Syst.*, vol. 61, no. 11, pp. 1193–1204, 2013.
- [2] A. Pease, I. Miles, and J. Li, “The suggested upper merged ontology: A large ontology for semantic web and its applications,” in *Proc. Working Notes AAAI-Workshop Ontologies Semantic Web*, Edmonton, AB, Canada, 2002.



IEEE Open Access

Unrestricted access to today's groundbreaking research via the IEEE Xplore® digital library

IEEE offers a variety of open access (OA) publications:

- Hybrid journals known for their established impact factors
- New fully open access journals in many technical areas
- A multidisciplinary open access mega journal spanning all IEEE fields of interest

Discover top-quality articles,
chosen by the IEEE peer-review
standard of excellence.



Learn more about IEEE Open Access
www.ieee.org/open-access



TC SPOTLIGHT

Model-Based Optimization for Robotics

By Katja Mombaur, Abderrahmane Kheddar, Kensuke Harada, Thomas Buschmann, and Chris Atkeson

Nature has demonstrated an incredible ability to optimize the designs and behaviors of humans, animals, and plants. Many areas of engineering have tried to copy the optimality principles of nature or optimize technical properties of systems, and mathematical optimization has been a very helpful tool in this context.

To promote the use of optimization methods in robotics, the IEEE Robotics and Automation Society (RAS) Technical Committee (TC) on Model-Based Optimization for Robotics was founded and approved by the IEEE RAS Technical Activities Board and the RAS Administrative Committee in October 2012 with Co-chairs

as their practical implementation. Optimization approaches are, in principle, applicable to any type of robot or robot behavior but are most interesting for robots with complex structures and dynamics, e.g., humanoid robots, or for high speeds, e.g., in mobile or agile manipulation (Figures 1–3). Optimization problems in robotics range from different tasks related to model identification (such as parameter estimation, optimum experimental design, inverse optimal control, and so on) over design optimization to optimal behavior generation (offline optimal control, model predictive control/online optimal control). Recent developments in optimization algorithms and, in particular, real-time optimization make a wider application of algorithmic optimization a realistic option even for real-time control in complex robotic applications in the near future.

There is a growing interest in optimization in the robotics community for behavior generation and control, as recent publications and workshops show. However, it can be observed that the level of optimization techniques used is often far behind the current state of the art within the optimization community and that only very simple optimization problems are solved. This prevents the optimization potential of existing robot platforms from being fully exploited, and current designs are often suboptimal. But some papers show very interesting optimization solutions for the most advanced robotic systems, even for complex tasks with impacts or varying constraints, such as

weight lifting or fast walking. At the same time, it is still a major challenge to actually apply these optimal solutions robustly to real robots and to handle modeling errors and uncertainties.

Important research areas in the scope of this TC include:

- the optimization-based generation of robot trajectories using dynamical models of the robot and its environment
- improving the behavior style of robots by optimization, in particular for humanoid robots (induce natural behavior)
- online motion control using real-time model-based optimization and model predictive control/receding horizon control
- optimizing the design of robots for given tasks (parameter optimization and structural optimization)
- the development of appropriate dynamical models for offline and online optimization
- learning/improving models during optimization
- inverse optimal control techniques for the identification of objective functions
- robust optimal control and the refinement of optimal control policies based on actual experience
- the combination of optimization and machine-learning approaches
- the combination of optimization and path-planning methods.

TC Activities

Since its foundation in late 2012, the following activities have been pursued

The vision of this IEEE RAS TC is to promote the research and education on this aspect as part of the efforts to provide better services to society.

Katja Mombaur, Abderrahmane Kheddar, Kensuke Harada, Thomas Buschmann, and Chris Atkeson. The TC focuses on optimization in robotics in the very general sense and, in particular, on the development and application of optimization methods for the design of robots and the generation and control of dynamic behaviors in robotics as well

Digital Object Identifier 10.1109/MRA.2014.2334973
Date of publication: 10 September 2014

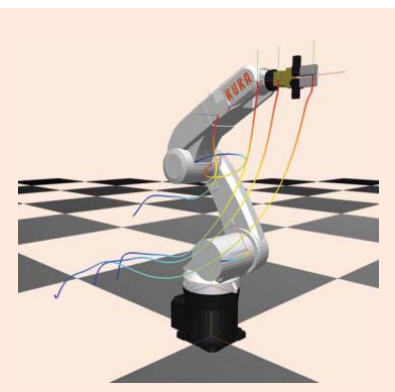


Figure 1. Optimal trajectories for a KUKA KRsixx R850 robot.

by the TC on Model-Based Optimization in Robotics.

Workshop Organization

- Workshop on Generating Optimal Paths in Humanoid and Industrial

Robotics at IEEE-RAS Humanoids 2012 (Osaka, Japan, November 2012)

- Workshop on Novel Methods for Learning and Optimization of Control Policies and Trajectories for Robotics at the IEEE International Conference on Robotics and Automation 2013 (Karlsruhe, Germany, May 2013)
- Workshop on Inverse Optimal Control and Robot Learning by Demonstration at Robotics: Science and Systems (RSS) 2013 (Berlin, Germany, June 2013)
- Workshop on Physical Assistive Devices: Model-Based Simulation and Optimization at IEEE/Robotics Society of Japan (RSJ) International Conference on Intelligent Robots and Systems (IROS) 2013 (Tokyo, Japan, November 2013)

- Workshop on Online and Offline Optimization for Humanoid Robots at IEEE/RSJ IROS 2013 (Tokyo, Japan, November 2013)
- Workshop on Optimization Techniques for Motion Generation in Robotics at RSS 2014 (Berkeley, United States, July 2014).

Tutorial Organization

- Heidelberg Collaboratory for Industrial Optimization (HCO) Workshop on Industrial Optimization—A tutorial workshop on nonlinear optimization and optimal control for participants from industry and academia, with optimization in robotics as a subtopic (Heidelberg, Germany, February 2014).

(continued on p. 161)

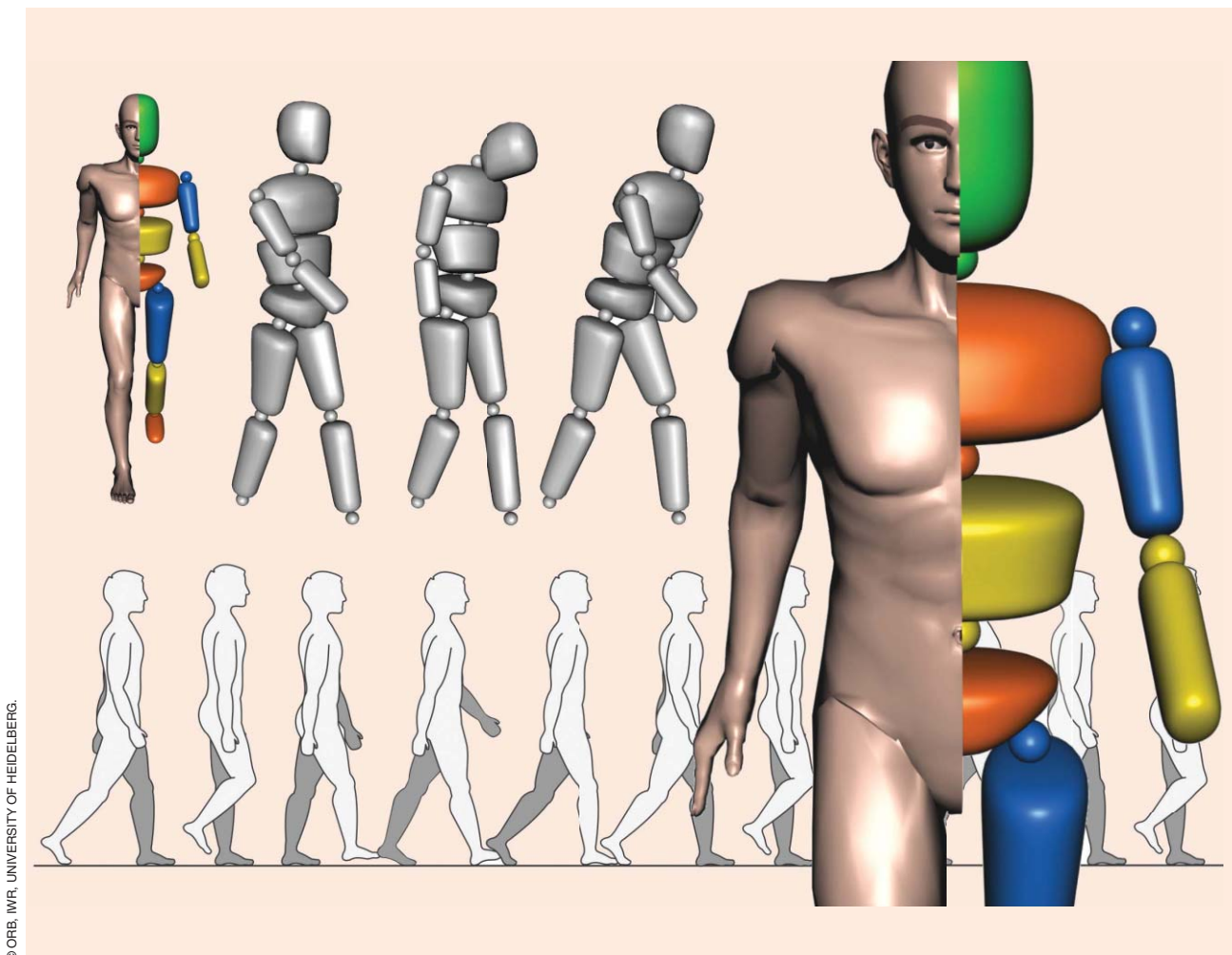
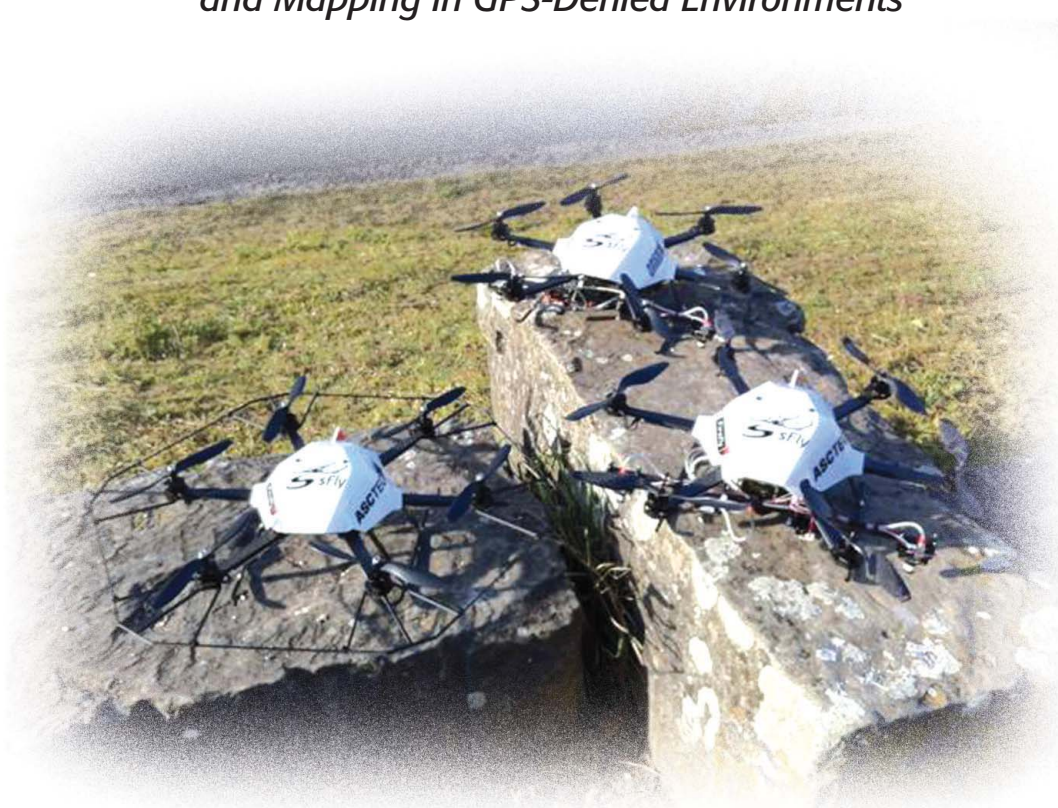


Figure 2. The generation of humanlike walking motions under different emotions by model-based optimization.

Vision-Controlled Micro Flying Robots

From System Design to Autonomous Navigation and Mapping in GPS-Denied Environments



By Davide Scaramuzza, Michael C. Achtelik, Lefteris Doitsidis, Friedrich Fraundorfer, Elias Kosmatopoulos, Agostino Martinelli, Markus W. Achtelik, Margarita Chli, Savvas Chatzichristofis, Laurent Kneip, Daniel Gurdan, Lionel Heng, Gim Hee Lee, Simon Lynen, Lorenz Meier, Marc Pollefeys, Alessandro Renzaglia, Roland Siegwart, Jan Carsten Stumpf, Petri Tanskanen, Chiara Troiani, and Stephan Weiss

Autonomous microhelicopters will soon play a major role in tasks like search and rescue, environment monitoring, security surveillance, and inspection. If they are further realized in small scale, they can also be used in narrow outdoor and indoor environments and represent only a limited risk for people. However, for such operations, navigating based only on global positioning system (GPS) information is not sufficient. Fully

autonomous operation in cities or other dense environments requires microhelicopters to fly at low altitudes, where GPS signals are often shadowed, or indoors and to actively explore unknown environments while avoiding collisions and creating maps. This involves a number of challenges on all levels of helicopter design, perception, actuation, control, and navigation, which still have to be solved. The Swarm of Micro Flying Robots (SFLY) project was a European Union–funded project with the goal of creating a swarm of vision-controlled microaerial vehicles (MAVs) capable of autonomous navigation, three-dimensional (3-D) mapping, and optimal

Digital Object Identifier 10.1109/MRA.2014.2322295

Date of publication: 20 August 2014

surveillance coverage in GPS-denied environments. The SFLY MAVs do not rely on remote control, radio beacons, or motion-capture systems but can fly all by themselves using only a single onboard camera and an inertial measurement unit (IMU). This article describes the technical challenges that have been faced and the results achieved from hardware design and embedded programming to vision-based navigation and mapping, with an overview of how all the modules work and how they have been integrated into the final system. Code, data sets, and videos are publicly available to the robotics community. Experimental results demonstrating three MAVs navigating autonomously in an unknown GPS-denied environment and performing 3-D mapping and optimal surveillance coverage are presented.

Motivation

Autonomous navigation of microhelicopters (where *micro* means up to the size of a few decimeters and fewer than 2 kg) has progressed significantly in the last decade thanks to the miniaturization of exteroceptive sensors (e.g., laser rangefinders and digital cameras) and to the recent advances in microelectromechanical systems, power supply, and vehicle design.

Microhelicopters—and, notably, multirotor helicopters—have several advantages compared with fixed-wing microaerial vehicles: they are able to take off and land vertically, hover on a spot, and even dock to a surface. This capability allows them to easily work in small indoor environments, pass through windows [1], traverse narrow corridors, and even grasp small objects [2].

A key problem in aerial-vehicle navigation is the stabilization and control in six degrees of freedom (DoF), i.e., attitude and position control. Today's systems handle the attitude control well. However, without a position control, they are prone to drift over time. In GPS-denied environments, this can be solved using offboard sensors (such as motion-capture systems or total stations) or onboard sensors (such as cameras and laser rangefinders). The use of offboard sensors allows research to focus on control issues without dealing with the challenges of onboard perception. Today's popular MAV testbeds are made by Vicon or OptiTrack motion-capture systems, which consist of multiple infrared static cameras tracking the position of a few highly reflective markers attached to the vehicle with millimeter accuracy and at a very high frame rate (several hundred hertz). These systems are very appropriate for testing and evaluation purposes [3], such as multirobot control strategies or fast maneuvers, and serve as a ground-truth reference for other localization approaches. Using this infrastructure, several groups have demonstrated aggressive maneuvers and impressive acrobatics [4], [5]. In the works mentioned previously, the MAVs are actually blind. To navigate, they rely on the highly precise position measurement provided by the external motion-tracking system. As a matter of fact, what is really autonomous is not the single MAV itself but the system comprising the MAVs plus the external cameras. Furthermore, these systems are limited to small, confined spaces, and require manual installation and calibration of the cameras, making it



Figure 1. The three SFLY hexacopters are designed for inertial-visual navigation in GPS-denied environments.

impossible to navigate autonomously in unknown, yet-unexplored environments. Therefore, for a MAV to be fully autonomous, sensors should be installed on board.

Contributions of SFLY

This article describes the technical challenges and results of the three-year European project SFLY (www.sfly.org) devoted to the implementation of a system of multiple microflying robots capable of autonomous navigation, 3-D mapping, and optimal coverage in GPS-denied environments. The SFLY MAVs can fly using only an onboard camera and an IMU. This article describes the major contributions of the SFLY, from hardware design and embedded programming to vision-based navigation and mapping. The first contribution is the development of a new hexacopter equipped with enough processing power for on board computer vision (Figure 1). The second contribution is the development of a local-navigation module based on monocular simultaneous localization and mapping (SLAM) that runs in real time on board the MAV. The output of the monocular SLAM is fused with inertial measurements and is used to stabilize and control the MAV locally without any link to a ground station. The third contribution is an offline dense-mapping process that merges the individual maps of each MAV into a single, global map that serves as input to the global navigation module. Finally, the fourth contribution is a cognitive, adaptive optimization algorithm to compute the positions of the MAVs, which allows the optimal surveillance coverage of the explored area.

Related Work

System Design

Extensive work has been carried out on quadrotor systems. The function principle of quadrotors can be found in [6] and [7]. A review of the state of the art on modeling, perception, and control of quadrotors can be found in [8]. The pitch angle of the propellers is typically fixed; an evaluation of variable-pitch propellers is presented in [9]. The platform described in this article, the AscTec FireFly, is an improvement of the previous and popular model known as AscTec Pelican. While

other groups often run the computation off board, by transmitting image data to a powerful ground-station computer, the SFLY platform runs most computer-vision algorithms fully on board. This demands high onboard-computation capabilities. In the first SFLY vehicle [10], a 1.6-GHz Intel Atom computer was used; however, in the latest platform, this was replaced with a Core 2 Duo onboard computer able to process all flight-critical data on board.

Autonomous Navigation

Autonomous navigation based on onboard two-dimensional (2-D) laser rangefinders has been largely explored for ground mobile robots [11]. Similar strategies have been extended to

To avoid drift over long periods of time, the system should be able to relocalize whenever it comes back to a previously visited location.

MAVs to cope with their inability to “see” outside the scan plane. This is usually done by varying the height and/or the pitch and roll of the helicopter as well as by incorporating readings from air-pressure and gyroscopic sensors [1], [12]–[16]. Although laser scanners are very reliable and robust, they are still too heavy and consume too much power for light-

weight MAVs. Therefore, vision sensors are very appealing; however, they require external illumination and a certain computing power to extract meaningful information for navigation.

Most of the research on vision-based control of MAVs has focused on optical flow [17]–[19]. But since optical flow can only measure the relative velocity of features, the position estimate of the MAV will inevitably drift over time. To avoid drift over long periods of time, the system should be able to relocalize whenever it comes back to a previously visited location. One possibility is offered by SLAM approaches.

Preliminary experiments for MAV localization using a visual extended Kalman filter (EKF)-based SLAM technique were described in [20]. However, the first use of visual SLAM to enable autonomous basic maneuvers, such as takeoff and landing, point-to-point navigation, and drift-free hovering on the spot, was done right within the framework of the SFLY project [21], [22]. Due to the use of a single camera, the absolute scale was initially determined manually or using a known-size object [23]. Later, the system was extended [24] to incorporate data from an IMU and, thus, estimate the absolute scale automatically while self-calibrating all the sensors (this approach will be outlined in the “Inertial-Aided Visual Navigation” section).

Optimal Coverage

Optimal coverage is the problem of computing the poses of a team of robots, which guarantee the optimal visibility of an area under the constraints that

- the part of terrain monitored by each robot is maximized [25], [26]
- for every point in the terrain, the closest robot is as close as possible to that point.

The second objective is necessary for two practical reasons: 1) the closer the robot is to a point in the terrain, the better its sensing ability to monitor this point, and 2) in many multirobot coverage applications, there is the necessity of being able to intervene as fast as possible in any of the points of the terrain with at least one robot. The optimal visibility problem is also related to the art-gallery problem, where the goal is to find the optimum number of guards in a nonconvex environment such that each point of the environment is visible by at least one guard [27], [28]. An incremental algorithm, which also considers a maximum monitoring distance, was presented in [29], while the optimal coverage of a 2-D region with a team of flying robots was studied in [30].

Most approaches for multirobot surveillance coverage concentrate on the second objective and tackle 2-D surfaces [31]–[35]. A method for nonplanar surfaces embedded in 3-D was presented in [36], while a study for multiple flying robots equipped with downward-looking cameras observing a planar 2-D environment was proposed in [30]. Multirobot optimal-coverage algorithms for convex environments were proposed in [31] and [32] using Voronoi partition, while in [33] the classical Voronoi coverage was combined with the Lloyd algorithm and the local path-planning TangentBug algorithm. In [32], a function indicating the relative importance of different areas in the environment using information from onboard sensors was used. An approach for nonconvex environments was proposed in [34] using Voronoi partition and in [35] using the potential-field method. Partition was obtained using the geodesic distance instead of the Euclidean one, considering the particular topology of the problem. In [35], the same problem was approached using the potential-field method. Another possible solution for convex environments with obstacles was proposed in [33]: the classical Voronoi coverage was combined with the Lloyd algorithm and the local path-planning TangentBug algorithm.

In all of the aforementioned approaches, the regions to monitor are considered in two dimensions. An approach for 3-D spaces was proposed in [36]. Conversely, the approach described in this paper is based on a new stochastic optimization method, called *cognitive-based adaptive optimization* (CAO). This method addresses 3-D environments and tackles the two aforementioned objectives simultaneously.

Microhelicopter Platform

Design Concept

One goal of the SFLY project was to have a vehicle as small, lightweight (fewer than 1.5 kg), and safe as possible, while being capable of carrying and powering an onboard computer and cameras. Since the SFLY helicopter was envisaged to operate in urban environments, the impact energy had to be reduced to a minimum. To limit the risk of injuries, studies

were made to evaluate the effects of having more than four (but smaller and safer) rotors on efficiency achievable dynamics and redundancy. These studies are presented in detail in [37]. In brief, it was found that the smaller the number of rotors, the better the efficiency of the vehicle. On the other hand, the achievable dynamics and, therefore, the maneuverability of the vehicle can be enhanced by a larger number of propellers and a smaller ratio between rotor surface and total weight. However, for safe operation, the most important aspect is redundancy against at least a single-rotor failure. In [37], it was shown that the minimum number of rotors with redundancy against a single failure could be reduced to six due to a new redundancy concept. To do so, different shapes of redundant multirotor vehicles were analyzed, and the maximum thrust in a redundancy situation was calculated. The results are shown in Table 1 (neglecting the additional margin needed to control the other axes). The hexagon-shaped six-rotor design was chosen as the best tradeoff. By deriving a control scheme for such a configuration, it can be concluded that, if all working motors are to spin at least at idle speed, a six rotor helicopter in hexagon shape cannot compensate for a single-motor failure. Undesired momentum around the yaw axis will be the result if pitch and roll are to be controlled (see [37] for more details). To overcome this disadvantage, a new and very simple control scheme was developed, which is shown in Figure 2.

The selected configuration can be built with propellers as small as the known safe propellers of the AscTec Hummingbird [10]. In addition, it can carry the demanded payload and is redundant against single-rotor failures, thus enabling safe operations in urban areas. Compared with an octocopter design, the thrust in a redundancy situation is smaller but the overall efficiency is higher due to the use of six rotors instead of eight.

Electronic Architecture

Except for the two additional motors, the electronic components and the software architecture are about the same as the AscTec Pelican described in [10].

To handle motor-failure situations, the communication protocols were extended for six motors, and the algorithms for failure detection and redundancy handling added. The control scheme for these failure situations is prescribed for each one of the possible six failure cases to be activated automatically if a failure is detected.

A distribution of the flight-control units (FCUs) main task between two microprocessors is shown in Figure 3. The so-called

Table 1. The theoretical maximum thrust in redundancy situations for different configurations.

System Configuration	Thrust in Failure Situation
Triangle hex	50%
Hexagon hex	66%
V-shape octo	62%
Octagon octo	70–73%

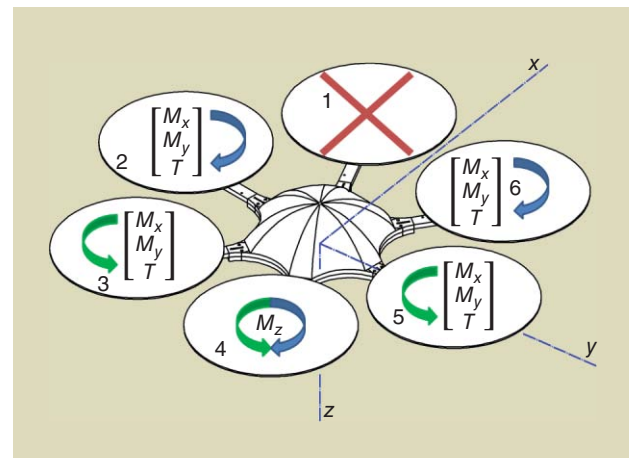


Figure 2. This illustration shows the redundancy against single-rotor failure. Assuming that motor 1 is failing, motors 2, 3, 5, and 6 are controlled by the thrust command and the roll and pitch controllers' output. Motor 4—on the opposite side of the failing motor—compensates and controls the yaw momentum by repeatedly changing its direction.

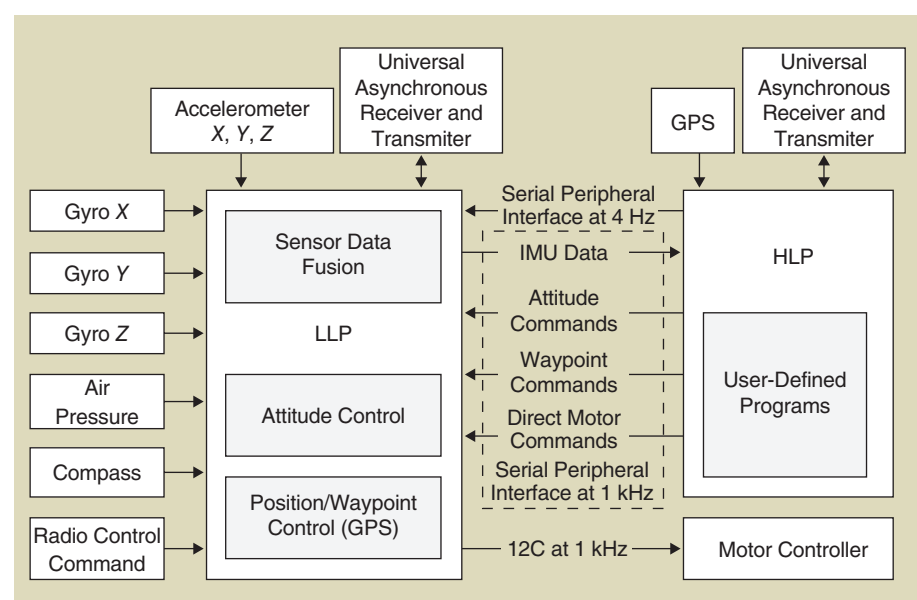


Figure 3. The electronic architecture: all sensors, except the GPS, are connected to the LLP, which communicates via I2C with the motor controllers and via the serial peripheral interface with the HLP. For this article, position control and state estimation for local navigation are implemented in the “user-defined programs” section of the HLP (see Figure 8). The position (waypoint) controller on the LLP is not used here since we work in GPS-denied environments.

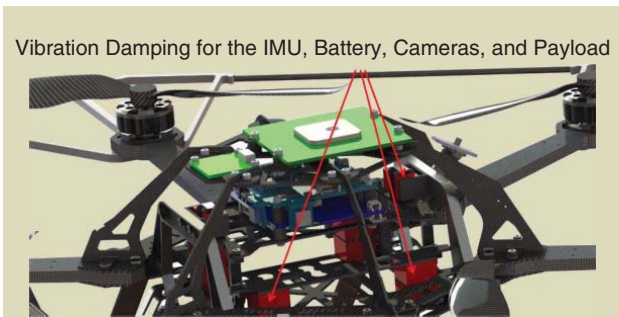


Figure 4. The computer-aided design (CAD) model illustrating the vibration damping between the two parts of the frame: the motors and the landing gear are connected to the outer frame, and the inner frame to the IMU, battery, and payload. The silicon dampers are highlighted in red.

low-level processor (LLP) handles all hardware interfaces; it is connected to the sensors and computes the attitude-data-fusion and flight-control algorithms at an update rate of 1 kHz. The high-level processor (HLP) is open for customized or experimental code. In the SFLY project, the HLP is used for state estimation and control. It has proven to be helpful to have the LLP as a safety backup while performing experiments in flight.

The SFLY MAVs do not rely on remote control, radio beacons, or motion-capture systems.

To integrate all computationally intense parts on board the vehicle, the initial Atom computer board of the Pelican platform was not sufficient. Therefore, the ongoing development of a new motherboard supporting the COM Express standard was pushed forward to support the integration of a Dual Core Atom, a Core 2 Duo, or a Core i7 central processing unit. These computer boards provide enough computational power to run all onboard software. Furthermore, additional interfaces like Firewire and hardware serial ports are supported. Specifically, the hardware serial ports are another step toward precise and fast state estimation on the onboard computer, as the latency is reduced to a minimum.

Mechanical Concept and Vibration Decoupling

One important requirement, raised from test flights of the previous vehicles, is a vibration decoupling. Just decoupling the IMU has proven to be insufficient. Instead, payloads such as cameras should be decoupled as well and, ideally, fixed to the IMU. Vibration damping is necessary to improve state estimation for position control as well as image quality. The damping system has to be designed so that there is a rigid connection between the cameras and IMU to avoid any dynamic misalignment. These requirements led us to a completely new concept. A so-called frame-in-frame concept was

built: the outer frame holds the motors, the landing gear, the canopy, and the propeller protection, while the inner frame carries the IMU, the battery, and the payload. As shown in Figure 4, both frames are connected using special silicon dampers, distributed in a pattern to intentionally influence the dynamics between both frames. This is necessary because the frame-in-frame concept leads to additional dynamics between both parts. The eigenmodes of this new dynamic system had to be adjusted so that no resonance oscillations between both frames occurred for a variety of payload configurations. Flight tests show an improvement of image and state-estimation quality, and all resonance oscillations are eliminated. Due to this new damping concept, the whole mechanical structure had to be redesigned.

To reduce the overall height and to concentrate the mass closer to the center of gravity, the battery was moved to the center of the frame. Furthermore, a landing gear was added to protect the payload, which is connected to the damped frame. A rollover bar protecting the electronic components and supporting the cover was added as well.

In addition to these additional features, another requirement was to enable fast component changes in case of a crash or modification during integration and testing. To put all these requirements and features together, a new combination of carbon fiber, carbon fiber sandwich, and aluminum was chosen.

Details of this concept can also be observed in Figure 4, and a complete computer-aided design (CAD) model, including a camera mount, is shown in Figure 5. Note that only one camera (downward looking) is used for navigation, while the other two, in stereo configuration, are used for obstacle avoidance (not described here) and dense matching (see the “3-D Mapping” section). Table 2 summarizes the main technical data.



Figure 5. The complete CAD model, including three cameras on the SFLY hexacopter.

Table 2. The main technical data.

Empty weight without battery	640 g
$I_{xx} \approx I_{yy}$	0.013 kg·m ²
I_{zz}	0.021 kg·m ²
Total thrust (at 10.5 V)	24 N
Maximum takeoff weight	1,090 g
Maximum payload	450 g
Maximum flight time	Up to 30 min

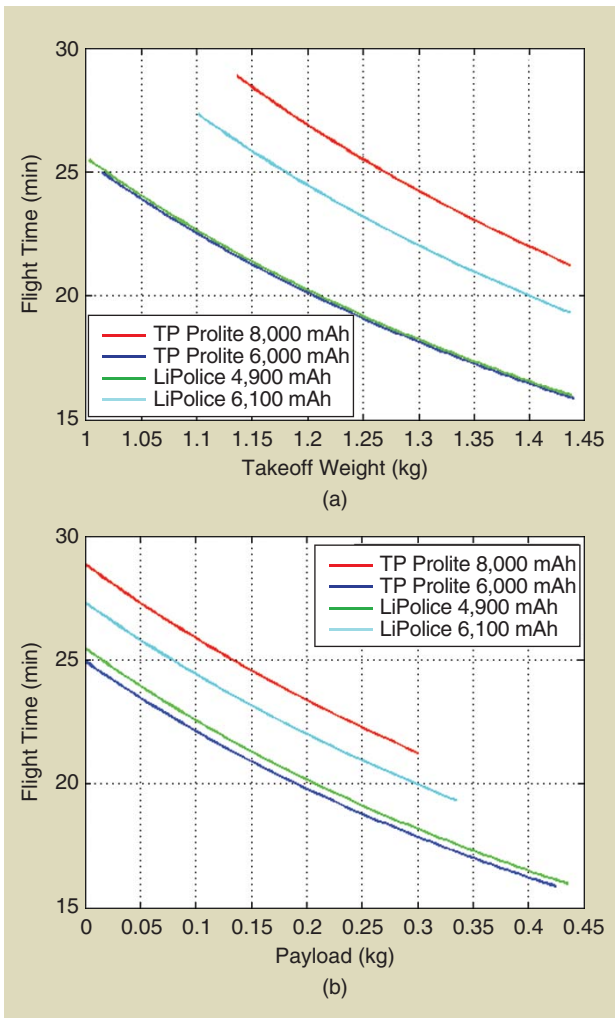


Figure 6. The calculated flight time is plotted versus (a) takeoff weight and (b) payload. The estimated flight time for a given payload with different batteries is shown. Thunder Power (TP) and LiPolice are LiPo battery manufacturers.

Flight-Time Estimation and Payloads

Based on test-bench data of the consequently improved motors and propellers as well as a final empty weight of 640 g, the flight time can be calculated for different payloads and batteries (Figure 6). The weight of the different batteries is considered, and the plots are limited to the maximum takeoff weight. The flight time is calculated for 85% of the battery capacity because lithium-polymer batteries must not be completely discharged. For the SFLY requirements, a 4,900-mAh battery was selected, resulting in an approximately 16-min flight time at a 400-g payload (neglecting the onboard-computer power consumption).

Inertial-Aided Visual Navigation

The navigation of the MAVs is handled by two different modules that are named *local navigation* and *global navigation*. The local-navigation module is responsible for flight stabilization, state estimation (including absolute-scale estimation), and waypoint-based navigation of each MAV. It runs on

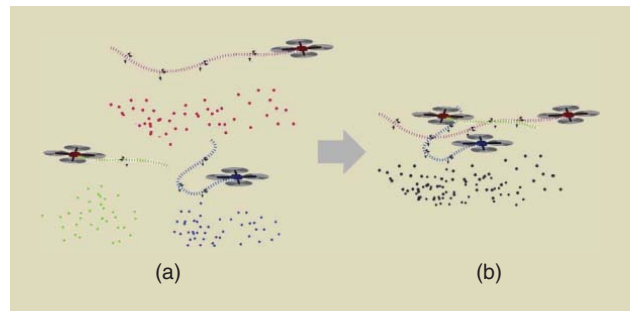


Figure 7. (a) The local-navigation module (running on board) estimates the pose of each MAV independently for each platform. (b) The global-navigation module (offboard) recognizes path intersections and uses them to express the MAVs' poses in the same, global coordinate frame and to reduce drift.

board each platform and estimates the pose of each MAV with respect to its starting position and, hence, does not rely on a persistent connection to the ground station. The state estimator and position controller are spread over the different computation platforms, according to the processing power and to reduce delay. The relative positions of the MAVs at start are unknown. The task of the global-navigation module (running off board the MAVs, on a ground-station computer) is to express the poses of all MAVs in a common, global coordinate frame and, possibly, to reduce both motion and map drifts. This is done by identifying both loop closures by the same MAV and path intersections between multiple MAVs (Figure 7). The interaction between these modules can be observed in Figure 8.

Local Navigation

In recent years, 5-DoF single-camera-based visual odometry (VO) has made significant progress. (a tutorial on monocular and stereo VO can be found in [38] and [39]). (Here, we refer to 5 DoF instead of 6 DoF because the absolute scale is not observable with a single camera.

However, the scale factor can be estimated by adding an IMU, as explained in this section.) Filter-based and key-frame-based off-the-shelf algorithms are publicly available. Because of its robustness, real-time performance, and position accuracy, the key-frame-based solution proposed in [40] was selected and tailored to the general needs of our computationally limited platform. However, nowadays, more recent VO algorithms, such as Semidirect Visual Odometry [41], represent a more robust, more accurate, and faster option for MAVs.

Our framework uses the Robot Operating System (ROS) middleware (www.ros.org) and runs on a standard Ubuntu operating system, facilitating the development of

The local-navigation module is responsible for flight stabilization, state estimation, and waypoint-based navigation of each MAV.

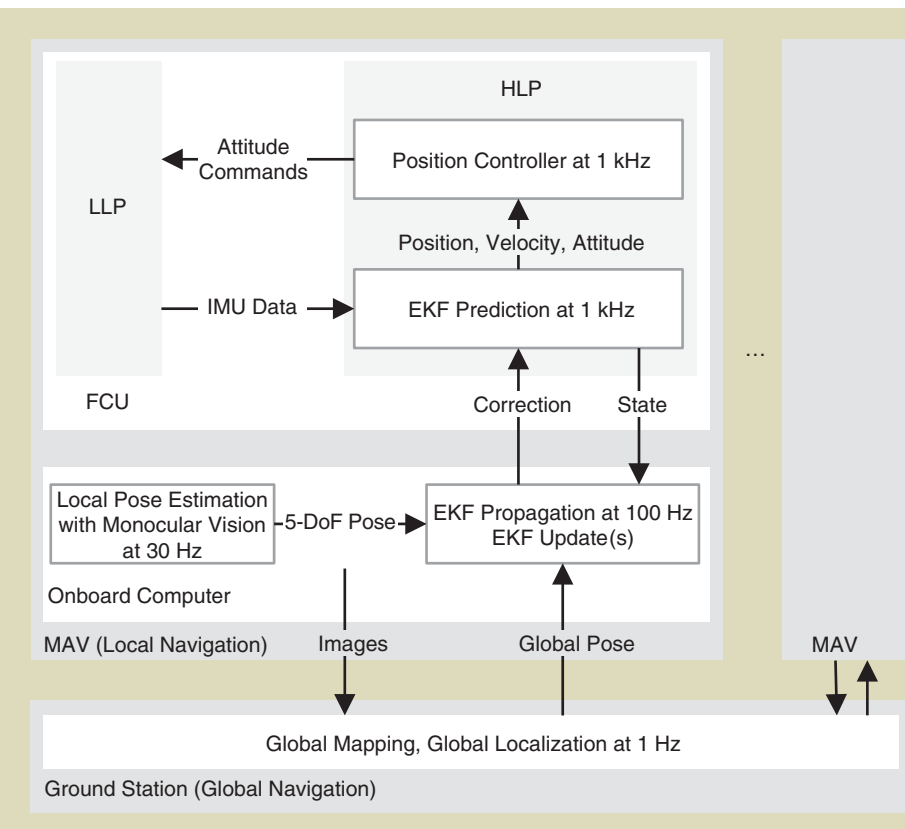


Figure 8. An overview of the different processing tasks and how these are distributed and interact with each other in our navigation framework. Waypoint commands are sent from the ground station to the onboard computer, which forward them to the position controller. The ground station and onboard computer communicate over a Wi-Fi connection. Note that all critical parts necessary to keep the helicopter airborne run entirely on board and do not rely on the Wi-Fi link. The parts on the HLP refer to the “user-defined programs” section in Figure 3.

new algorithms. The current implementation uses only 60% of one core of the Core 2 Duo processor at 30 Hz, leaving enough resources for future higher-level tasks. As a reference, the same implementation on an Atom 1.6-GHz single-core computer runs at 20 Hz using 100% of the processing power.

The 5-DoF pose of the MAV camera output by the visual-odometry algorithm was fused with the inertial measurements of an IMU using an EKF. More details are given in [42]. An

EKF framework consists of a prediction and an update step. The computational load required by these two steps is distributed among the different units of the MAV, as described in [43]. The state of the filter is composed of the position p_w^i , the attitude quaternion q_w^i , and the velocity v_w^i of the IMU in the world frame. The gyroscope and accelerometer biases b_ω and b_a as well as the missing scale factor λ are also included in the state vector. For

For safe operation, the most important aspect is redundancy against at least a single-rotor failure.

q_w^i , and the velocity v_w^i of the IMU in the world frame. The gyroscope and accelerometer biases b_ω and b_a as well as the missing scale factor λ are also included in the state vector. For

completeness, the extrinsic calibration parameters describing the relative rotation q_i^s and position p_i^s between the IMU and the camera frames were also added. Note that the calibration parameters could be omitted from the state vector and be set to a premeasured constant to increase robustness and faster state convergence. Having p_i^s as a constant and not as a filter state would increase the convergence performance of the visual scale. We did not notice significant performance improvement when removing q_i^s from the state vector. We assume that this is because the attitude is directly measured by the visual pipeline whereas the scale ambiguity occurs in both p_i^s and the MAV position p_w^i . In this article, we show that even with continuously estimating both parameters p_i^s and q_i^s , we can achieve good and robust results. This yields a 24-element state vector X :

$$X = \{p_w^{i^T} v_w^{i^T} q_w^{i^T} b_\omega^T b_a^T \lambda \ p_i^s \ q_i^s\}. \quad (1)$$

Figure 9 shows the setup with the IMU and camera coordinate frames and the state variables introduced above.

The equations of the EKF prediction step for the considered IMU-camera fusion are given in [42]. The equations of the update step are derived by computing the transformation from the world reference frame to the camera frame as follows. For the position z_p , we can write:

$$z_p = p_w^s = (p_w^i + C_{(q_w^i)}^T p_i^s) \lambda + n_p, \quad (2)$$

where $C_{(q_w^i)} \in SO(3)$ is the rotation matrix associated with the IMU attitude quaternion q_w^i in the world frame, z_p denotes the observed position (the output of the visual odometry), λ is the scale factor, and n_p the measurement noise. For the rotation measurement z_q , we apply the notion of error quaternion. Since the visual-odometry algorithm yields the rotation q_w^s from the world frame to the camera frame, we can write:

$$z_q = q_w^s = q_i^s \otimes q_w^i. \quad (3)$$

A nonlinear observability analysis [44] reveals that all state variables are observable, including the intersensor calibration parameters p_i^s and q_i^s . Note that the visual pose estimates are prone to drift in position, attitude, and scale with respect to the world-fixed reference frame. Since these quantities are observable (and, notably, roll, pitch, and scale), gravity-aligned metric navigation becomes possible even in long-term missions. This is true as long as the robot excites the IMU accelerometer and gyroscopes sufficiently, as discussed in [45]. Note that the estimated attitude and position of the MAV in the world frame is subject to drift over time. However, since the gravity vector measured by the IMU is always vertically aligned during hovering, this prevents the MAV from crashing due to gravity misalignment even during long-term operations.

Global Navigation

The task of the global-navigation module (running on the ground station) is to express the poses of all MAVs in a common, global coordinate frame and, possibly, to reduce both motion and map drifts. This is done by matching the current camera image to a 3-D environment map. The 3-D map consists of landmarks (3-D points and corresponding descriptors in each image) and the corresponding camera poses. The 3-D map is computed offline, as described in the “3-D Mapping” section and combines the maps of the individual MAVs into a single merged map. Map merging works by identifying both loop closures by the same MAV and path intersections between multiple MAVs (Figure 7). To reduce the computational load of the onboard computer, the global-navigation module runs on a ground station that constantly receives the images of the MAVs via Wi-Fi and sends back the updated global poses. To save bandwidth, a valid alternative to sending full camera frames is to have each MAV stream only features of selected key frames and relative-pose estimates, as recently proposed in [46].

Matching the current camera view to the 3-D map is done by vocabulary-tree-based image search, as described in [47] and [48]. For every frame, speeded-up robust Features [49] are extracted and then quantized into visual words using a vocabulary tree that was pretrained on a general image data set. The image IDs and the corresponding visual words are stored in a database that is organized as an inverted file for efficient data access. Additional metadata (pose estimates from the local-navigation module and IMU data) are stored with each image in the database. Whenever a new image is processed, it is ranked with all images in the database according to the similarity of the visual words. Geometric verification is performed on the top- N most similar frames using perspective three-point algorithm-based random sample consensus (RANSAC) [50]. A match is accepted if the inlier count exceeds a certain threshold. The initial pose from RANSAC is refined using nonlinear optimization and is sent back as global pose update. This approach allows for efficient localization and also scales to large maps.

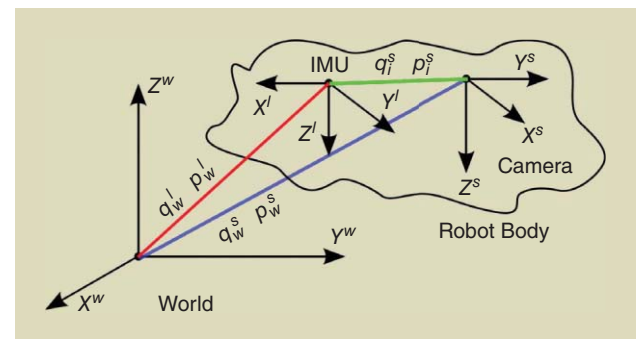


Figure 9. A setup depicting the robot body with its sensors with respect to a world reference frame. The system state vector is $X = \{p_w^s v_w^s q_w^s b_w^s b_a^s \lambda p_i^s q_i^s\}$, whereas p_w^s and q_w^s denote the robot's sensor measurements in (a possibly scaled) position and attitude, respectively, in a world frame.

3-D Mapping

For the 3-D mapping of the environment, an offboard ground station takes images from all MAVs and fuses them offline into a detailed map. The mapper is based on the general framework for graph optimization (g2o) framework [51]; it uses a pose-graph optimizer for prealignment of the data and then runs a bundle adjustment to get optimal results.

The maximum-likelihood estimates of the poses are computed by minimizing the Euclidean distances between the transformations in a pose graph. The nonlinear optimization is done by sparse Cholesky decomposition using the g2o framework. To improve the accuracy of the map, a bundle adjustment is run. The bundle adjustment optimizes the poses and the 3-D positions of all features at the same time by minimizing the image reprojection error. The corresponding graph of this problem consists of the MAV poses and the 3-D feature points as nodes. They are connected by edges that represent the projection of the 3-D feature point to images where the feature was detected. During the loop-detection phase, for every new frame, all image projections of the inlier features are added to the bundle-adjustment graph.

A dense map is built offline using the poses of the MAV computed from the bundle adjustment process and the corresponding stereo images. For each pose and corresponding stereo frame, a 3-D point cloud in global coordinates is computed via stereo triangulation and used to update a 3-D occupancy map. After all the data have been processed, a terrain map is extracted from the 3-D occupancy map by thresholding the occupancy value in each cell in the occupancy map. The terrain map is triangulated to create a dense mesh. Furthermore, a dense textured map is created by projecting all triangular faces in the mesh onto the images, from which the faces are entirely visible, and texturing each face with the image that has the smallest

**The outer frame holds
the motors, the landing
gear, the canopy, and the
propeller protection.**

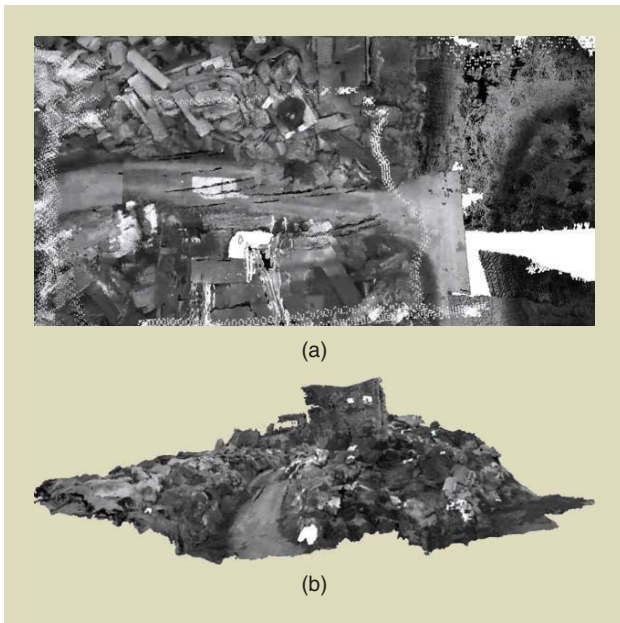


Figure 10. The textured visualization of the 3-D map of the firefighter area: (a) top and (b) side views.

incident angle relative to the face normal. This image-selection heuristic helps to minimize perspective distortion. A textured visualization of a 3-D map is shown in Figure 10. More details can also be found in [52].

Optimal Surveillance Coverage

The problem of deploying a team of flying robots to perform surveillance coverage missions over an unknown terrain of complex and nonconvex morphology was tackled using a novel CAO algorithm. The CAO algorithm was originally developed and analyzed for the optimization of functions for which an explicit form is unknown but measurements are

available as well as for the adaptive fine-tuning of large-scale nonlinear-control systems [53]. The many advantages of using stochastic gradient descent algorithms, like the simultaneous perturbation stochastic approximation algorithm [54], to

**The mapper is based on
the general framework
for graph optimization
framework.**

approach a sensor-based deployment problem have already been highlighted in [55].

Within SFLY, CAO was implemented for surveillance tasks in unknown 3-D terrains of complex and nonconvex morphology with obstacles using only onboard monocular vision. CAO possesses several advantages compared with the previous works described in the “Optimal Coverage” section: it is computationally simple to implement, scalable, and can easily embed any kind of physical constraints and limitations (e.g., obstacle avoidance, nonlinear sensor-noise models). CAO does not create an approximation or estimation of the

obstacles’ location and geometry; conversely, it produces an online local approximation of the cost function to be optimized. A detailed description of the CAO algorithm and its functionality for the case of a team of aerial robots can be found in [56] and [57].

In the context of the SFLY project, the CAO algorithm tackles two objectives simultaneously to assure that the robot team will perform optimal surveillance coverage:

- maximize the part of terrain monitored by each robot
- for every point in the terrain, the closest robot has to be as close as possible to that point.

If only the first objective were considered, the robots would fly as high as their visibility threshold allows (which is defined as the maximum distance the robot’s sensor can measure). Therefore, the second objective ensures that, among all possible configurations that maximize the visible area V , the robot team converges to the one that keeps as small as possible the average distance between each robot and the part of the terrain for which that particular robot is responsible. (Note that in the ideal case, where there are no limits for the robot’s maximum height, and the robot has unlimited sensing capabilities, it suffices to have a single robot at a very high position to monitor the whole terrain.) The second objective is also necessary for two practical reasons: first, the closer the robot is to a point in the terrain, the better, in general, its sensing ability to monitor this point; second, in many multirobot coverage applications, it is necessary to intervene as fast as possible in any of the points of the terrain with at least one robot.

The two aforementioned objectives are combined in an objective function that the robot team has to minimize [56], i.e.,

$$J(P) = \int_{q \in V} \min_{i \in \{1, \dots, M\}} \|x^{(i)} - q\|^2 dq + K \int_{q \in T - V} dq, \quad (4)$$

where M is the number of robots that are deployed to monitor a terrain T , $x^{(i)}$ is the position of the i th robot, $P = \{x^{(i)}\}_{i=1}^M$ denotes the configuration of the robot team, q is a point in the terrain T , V consists of all points $q \in T$ that are visible from the robots, and K is a user-defined positive constant.

The first term in (4) addresses the second objective. The second term addresses the first objective and relates to the invisible area of the terrain (i.e., $\int_{q \in T - V}$, which is the total part of the terrain that is not visible to any of the robots). The positive constant K serves as a weight to give more or less priority to one or the other objective. A detailed analysis of the effect of K is presented in [56].

The implementation of CAO within the SFLY framework ensures that the physical constraints are also met throughout the entire multirobot coverage application. Such physical constraints include, but are not limited to, the following:

- the robots remain within the terrain’s limits
- the robots satisfy a maximum-height requirement while not hitting the terrain
- the robots do not come closer to each other than a minimum allowable safety distance.

The above constraints can be easily formulated and incorporated in the optimization problem [56]. CAO uses function approximators for the estimation of the objective function at each time instant; therefore, a crucial factor for the successful implementation is the choice of the regressor vector, as described in [56]. Once the regressor vector has been set and the values of the cost function are available for measurement, it is possible to find at each time step the vector of parameter estimates and, thus, the approximation of the cost function.

Experimental Results

Flying Platform

The achievable dynamics and maneuverability are demonstrated by the accurate trajectory following and position control shown in Figure 11. To evaluate the redundancy capabilities, a switch disabling one motor was implemented to simulate a motor failure. There was no measurable deviation in the roll and pitch axes, but the maximum thrust is obviously limited during this failure situation.

Figure 12 shows the motor commands input to the four propellers during such a redundancy test. The motor commands are in the range $[-100, 200]$. As observed, at about 14 s, one motor is deactivated (the yellow plot drops to zero), and one motor command starts compensating for the yaw moment by slowly oscillating around zero (red plot). The other four motors are set feedforward to a higher thrust to compensate for the loss caused by the other two motors. Figure 12(b) shows the pilot's stick inputs. This plot looks absolutely normal for a manual flight, like Figure 12(c), which shows the attitude measure.

Vision-Based Navigation

Figures 13 and 14 show the evolution of the position and attitude of one MAV estimated by the EKF framework described in the “Local Navigation” section. The position plot (Figure 13) shows that the visual scale has been estimated correctly by the filter throughout the whole flight; as can be observed, the position and attitude drifts of the vision system are very low. For a rapidly drifting vision system, one would observe an increased difference between the GPS data and filter estimates. Note that GPS measurements were used during the initialization phase to align all states for a simpler comparison with ground truth. After this alignment phase (at about $t = 80$ s in Figures 13 and 14), GPS was no longer used as additional input in the EKF framework.

A 350-m trajectory estimated using this framework, resulting in an overall position drift of only 1.5 m, is shown in Figure 15. The presented framework was tested under a variety of challenging conditions, exhibiting robustness in the presence of wind gusts, strong light conditions causing saturated images, and large-scale changes in flight altitude. More details are given in [58].

3-D Mapping and Optimal Coverage

The platforms and the algorithms described in the previous sections were used to implement an autonomous-navigation

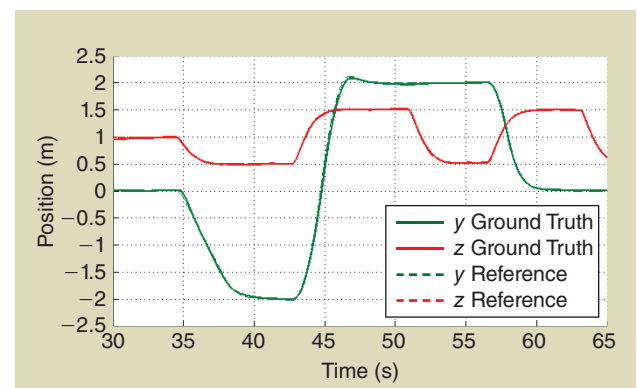


Figure 11. The plot shows the commanded reference trajectory and the measured ground truth.

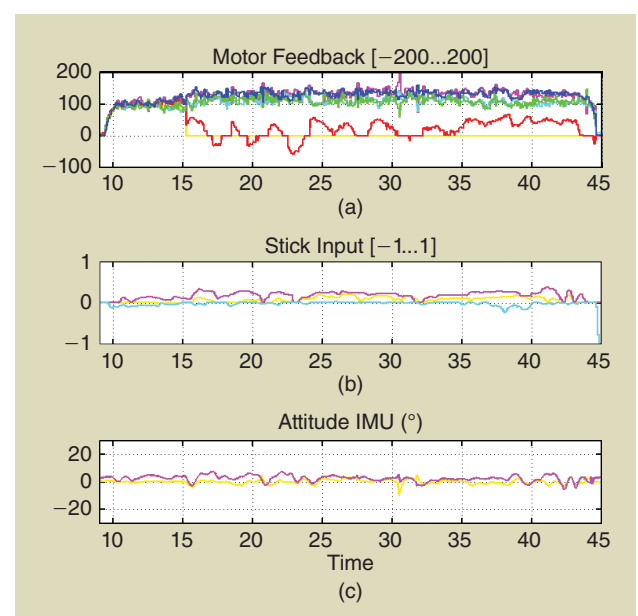


Figure 12. (a) The motor commands in a range $[-100, 200]$ are shown. At about 14 s, the yellow motor is disabled so that the redundancy controller can be activated. As observed, the red motor command slowly oscillates around zero to compensate for the yaw moment. (b) and (c) There is nearly no influence of the failing motor to the pilot's commands or the measured attitude.

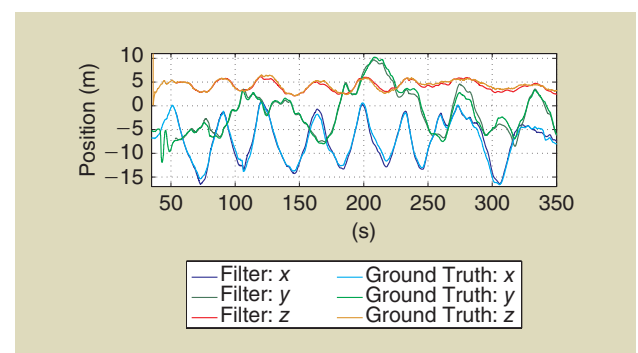


Figure 13. A comparison between EKF-based position estimate (filter: x, y, z) and raw GPS measurements (ground truth: x, y, z) during a 5-min interval of time. The plot suggests that the absolute scale is estimated correctly.

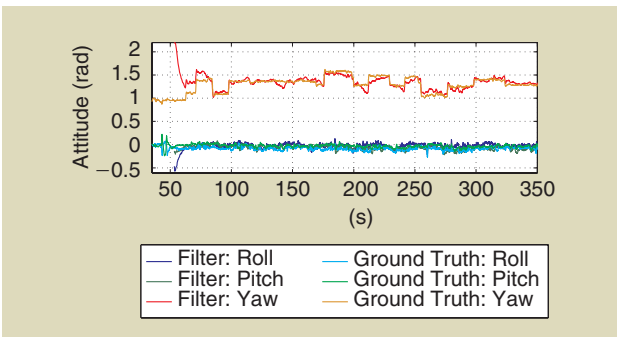


Figure 14. A comparison between EKF-based attitude estimate (filter: roll, pitch, yaw) and GPS-IMU based estimates from the AscTec internal state estimator (ground truth: roll, pitch, yaw) during a 5-min interval of time.

scenario that was publicly demonstrated at the firefighters' training area in Zürich, Switzerland (Figure 16). As described in the "Inertial-Aided Visual Navigation" section, a visual odometry algorithm ran on board each MAV and served for local stabilization as well as for trajectory estimation. At the same time, each MAV built a sparse 3-D map that was incrementally transmitted, together with images and pose estimates, over a Wi-Fi network to a ground-station computer. The ground station, a quad-core Lenovo W520 laptop, was in charge of combining all the received data to compute global position estimates of the three MAVs as well as a dense 3-D map.

Figure 17 shows the pose graphs built by the three MAVs during a flight over the area. These graphs are generated after visual odometry. Drift is visible, especially in the blue trajectory. There, the start and end points are marked with red arrows. The start and end points should overlap in this case, but they do not due to drift. Loop detection, however, recognized the loop closure.

Finally, the three individual submaps are merged into a single global map: first, loop closures are detected between the submaps; then, global bundle adjustment is run over the

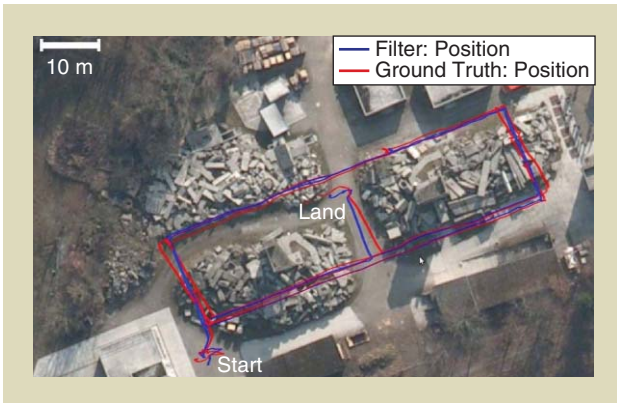


Figure 15. After a short initialization phase at the start, vision-based navigation (blue) was switched on for successful completion of a more than 350-m-long trajectory, until battery limitations necessitated landing. The comparison of the estimated trajectory with the GPS ground truth (red) indicates a very low position and yaw drift of the real-time onboard visual odometry.

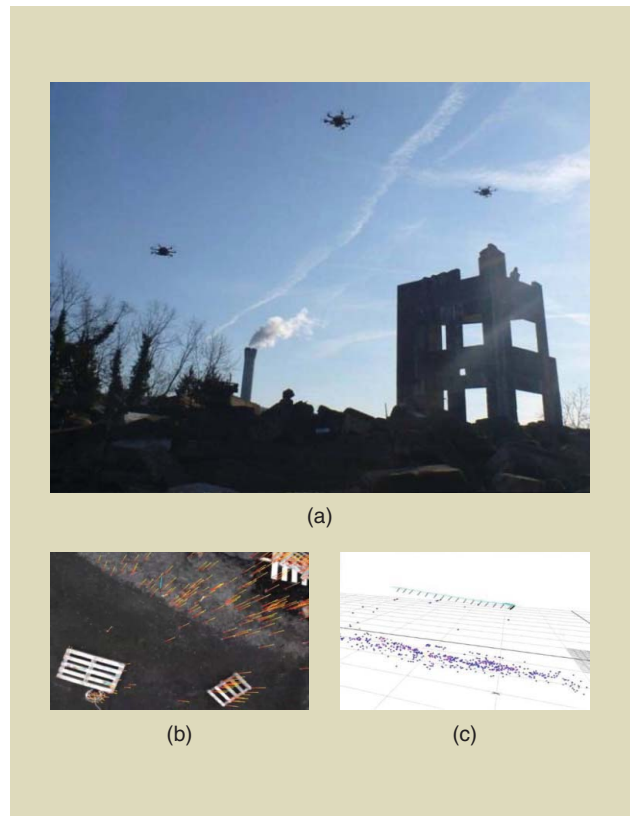


Figure 16. (a) The SFLY helicopters during a demonstration of autonomous exploration at the firefighters' training area in Zürich, (b) feature tracks, and (c) the online-built 3-D sparse map used for local navigation.

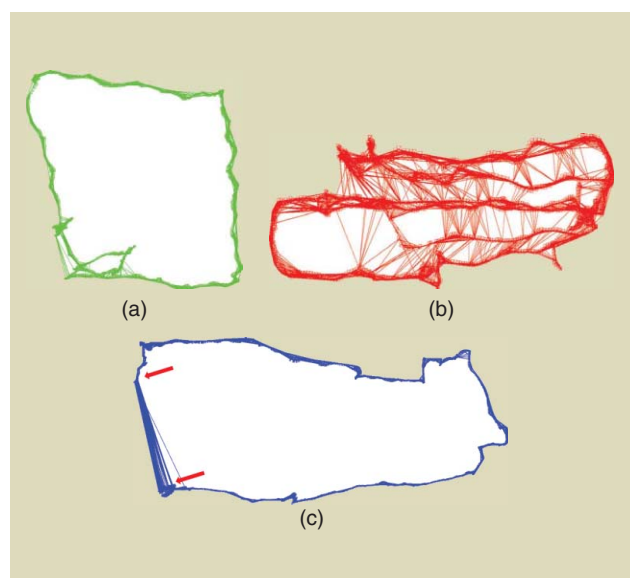


Figure 17. (a)–(c) The pose graphs of three flight trajectories that were used for 3-D mapping. The camera poses are plotted after visual odometry and windowed bundle adjustment. The connecting lines between the cameras show loop closures. As no global optimization is run, pose drift is visible. In (c) the blue trajectory, start and end points are marked with red arrows. The start and end points should overlap in this case, but they do not due to drift. Loop detection, however, recognized the loop closure, and pose-graph optimization will remove the drift (Figure 18).

whole map. Figure 18 shows the pose graph of the final map. The black lines between the cameras of different sub-maps show the detected loop closures. The global bundle adjustment is able to remove the drift in the individual sub-maps; and thus, the resulting global map is drift free and in the correct absolute (metric) scale.

A 3-D occupancy map was built, as described in the “3-D Mapping” section. Out of the 3-D occupancy grid, a height map was generated (Figure 19) and fed to the CAO algorithm to compute the optimal-coverage poses. The produced map covers a $42 \text{ m} \times 32 \text{ m}$ area with a maximum height of 8.3 m. The final poses for the optimal surveillance coverage of the area by the three MAVs are shown in Figure 20.

Figure 10 shows a textured visualization of the 3-D environment map of the firefighter area created from three MAVs.

Lessons Learned

Visual-Inertial Sensor Fusion

The flight of more than 350 m outdoors in an unprepared environment (Figure 15) revealed important insights about the system running under real-world conditions. First, the observability analysis of the system, described in the “Local Navigation” section, shows that the system requires excitation to render all states, and, in particular, the visual scale factor, observable. Our tests showed that, under real conditions, this requirement is generally fulfilled. We observed that initializing the visual scale factor correctly (up to about 10% of the true value) is crucial for proper state convergence. In our experiments, we initialized the scale factor either by GPS or by pres-

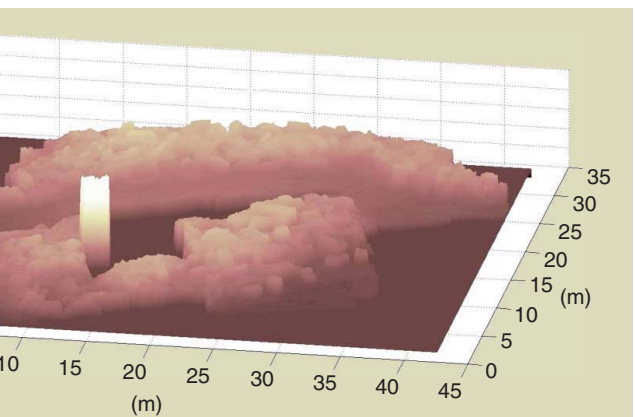


Figure 19. The height map of the Zürich firefighters’ training area.

sure-sensor height measurements. Second, recent work on visual-inertial sensor fusion proposes online calibration of the time offset between the two sensors [44], [45]. While such approaches have high theoretical value, in our experiments, we did not see noticeable differences when increasing or decreasing this offset of maximum 5 ms. This change is significantly larger than the accuracy of common time synchronization protocols like NTP, including jitter on universal serial bus (USB) connections. We estimated once a fixed delay in USB transmissions but did not adapt this estimate during flights or between missions. Third, in the beginning of the project, we experienced significant issues of the visual pipeline [original parallel tracking and mapping algorithm (PTAM)] in self-similar outdoor scenes. Map failures occurred often and marked the end of the mission. Our improvements, described in detail in [59], were key to ensuring continuous operation of the MAV. The most important adaptations include modifying PTAM to a visual odometry framework with constant computational complexity as well as improved feature handling, drastically reducing false positives in the map-building process and

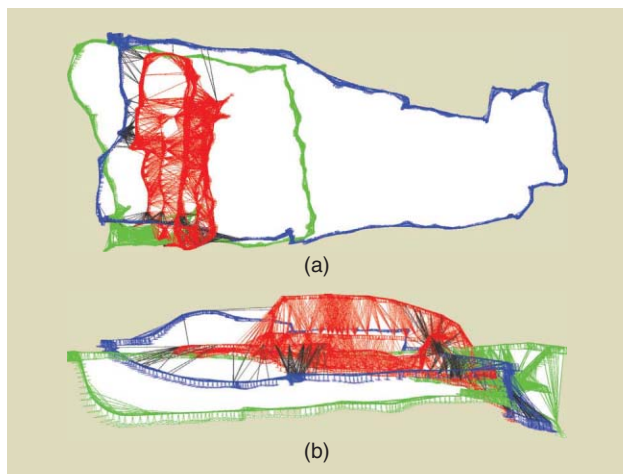


Figure 18. The (a) top and (b) front views of the pose graphs of the three flight trajectories in Figure 17 after map merging and global bundle adjustment. The black lines show the loop closures between the three submaps.

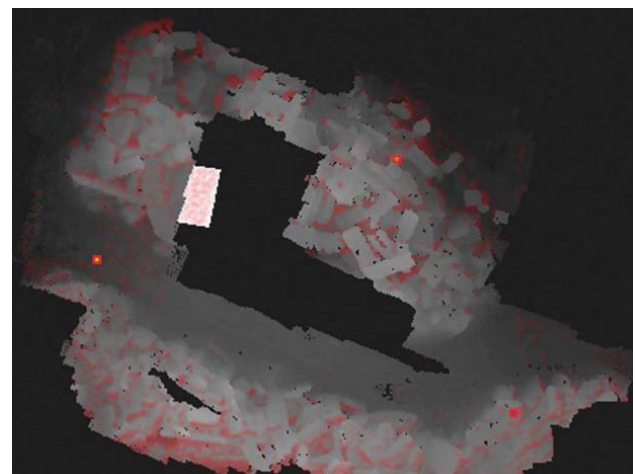


Figure 20. The final configuration of a robot team performing surveillance coverage: the red squares represent the final positions of the MAVs, while the red areas represent the invisible part of the map.

reducing the computational demand at the same time. However, today, more recent VO algorithms, such as SVO [41], represent a more robust, accurate, and faster option for MAVs.

Optimal Coverage

The implementation of the CAO algorithm within the SFLY framework proved the feasibility of an approach relying on an optimization procedure, where the explicit form of the function to be optimized is unknown. A key issue to the successful implementation is the fast and reliable generation of the appropriate inputs to the algorithm. In the case of the SFLY system, the lack of the online map generation resulted in the necessity of offline calculation. The implementation of CAO does not create an approximation or estimation of obstacle location and geometry; instead, it produces on line a local approximation of the unknown cost function that the robots are called to optimize. For this reason, it requires simple and, thus, scalable approximation schemes to be employed, which proved to be ideal for the real-time implementation of CAO.

3-D Mapping

The use of a stereo camera system for 3-D mapping proved to be beneficial. Having a fixed baseline eliminates scale drift in camera pose estimation and makes the dense 3-D reconstruction problem a depth-map fusion problem.

Leveraging the IMU measurements for the 3-D reconstruction task proved to be beneficial

The use of a stereo camera system for 3-D mapping proved to be beneficial.

as well. For feature matching, the relative rotations between two frames is used to predict feature locations and eliminate most of the outliers immediately. This leads to an efficient feature matching and motion estimation step. Our map merging system is based solely on visual information. Our experiments demonstrated successfully that visual map merging works across multiple platforms even with different camera systems. Performing map merging by pose-graph optimization followed afterward by full bundle adjustment showed to be an efficient way. For dense 3-D reconstruction, we chose to fuse the 3-D measurements into a 3-D grid map prior to digital elevation map generation and triangulation. This avoided problems in 3-D mesh fusion present in other works [60]. Overall, we could successfully demonstrate that it is possible to create large-scale dense 3-D reconstructions using low-weight, low-quality, and low-resolution cameras by fusing a high number of small-scale 3-D reconstructions.

Conclusions

This article described a framework that allows small-size helicopters to navigate all by themselves using only a single onboard camera and an IMU, without the aid of GPS or active range finders. This framework allows unprecedented MAV

navigation autonomy, with flights of more than 350-m length, in previously unexplored environments.

This article shared the experience earned during the three-year European project SFLY about visual-inertial real-time onboard MAV navigation, multirobot 3-D mapping, and optimal surveillance coverage of unknown 3-D terrains. Particular focus was devoted to the technical challenges that have been faced and the results achieved, with detailed insights of how all the modules work and how they have been integrated into the final system. Code, data sets, and videos were made publicly available to the robotics community.

This article highlighted four major contributions of SFLY. The first one is the development of a new six-rotor-based platform robust to single-rotor failures, equipped with enough processing power for onboard computer vision. The second contribution is the development of a local-navigation module based on monocular SLAM that runs in real time on board the MAV. The output of the monocular SLAM is fused with inertial measurements and is used to stabilize and control the MAV locally without any link to a ground station. The third contribution is an offline and offboard dense-mapping process that merges the individual maps of each MAV into a single, global map that serves as input to the global navigation module. Finally, the fourth contribution is a cognitive, adaptive optimization algorithm to compute the positions of the MAVs, which allows the optimal surveillance coverage of the explored area.

To the best of our knowledge, this article describes the first working visual-inertial system of multiple MAVs in real-world scenarios able to autonomously navigate while collaboratively building a rich 3-D map of the environment and performing optimal surveillance coverage. It is believed that the presented system constitutes a milestone for vision-based MAV navigation in large, unknown, and GPS-denied environments, providing a reliable basis for further research toward complete missions of search-and-rescue or inspection scenarios with multiple MAVs.

References

- [1] M. Achtelik, A. Bachrach, R. He, S. Prentice, and N. Roy, "Stereo vision and laser odometry for autonomous helicopters in GPS-denied indoor environments," in *Proc. SPIE Conf. Unmanned Systems Technology*, 2009, pp. 1–8.
- [2] N. Michael, J. Fink, and V. Kumar, "Cooperative manipulation and transportation with aerial robots," *Auton. Robot.*, vol. 30, no. 1, pp. 73–86, 2010.
- [3] N. Michael, D. Mellinger, Q. Lindsey, and V. Kumar, "The GRASP multiple micro UAV testbed," *IEEE Robot. Automat. Mag.*, vol. 17, no. 3, pp. 56–65, 2010.
- [4] S. Lupashin, A. Schöllig, M. Sherback, and R. D'Andrea, "A simple learning strategy for high-speed quadrocopter multi-flips," in *Proc. IEEE Int. Conf. Robotics Automation*, May 2010, pp. 1642–1648.
- [5] D. Mellinger and V. Kumar, "Minimum snap trajectory generation and control for quadrotors," in *Proc. IEEE Int. Conf. Robotics Automation*, 2011, pp. 2520–2525.
- [6] S. Bouabdallah, P. Murrieri, and R. Siegwart, "Design and control of an indoor micro quadrotor," in *Proc. IEEE Int. Conf. Robotics Automation*, 2004, pp. 4393–4398.

- [7] R. Mahony, V. Kumar, and P. Corke, "Multirotor aerial vehicles-modeling, estimation, and control of quadrotor," *IEEE Robot. Automat. Mag.*, vol. 19, no. 3, pp. 20–32, 2012.
- [8] N. Michael, D. Scaramuzza, and V. Kumar, "Special issue on micro-UAV perception and control," *Auton. Robot.*, vol. 23, nos. 1–2, pp. 1–3, 2012.
- [9] M. Cutler, N. Ure, B. Michini, and J. P. How. (Aug. 2011). Comparison of fixed and variable pitch actuators for agile quadrotors. presented at AIAA Guidance, Navigation, Control Conf., Portland, OR. [Online]. Available: http://acl.mit.edu/papers/GNC11_Cutler_uber.pdf
- [10] M. C. Achtelik, J. Stumpf, D. Gurdan, and K.-M. Doth, "Design of a flexible high performance quadcopter platform breaking the MAV endurance record with laser power beaming," in *Proc. IEEE Int. Conf. Intelligent Robots Systems*, 2011, pp. 5166–5172.
- [11] S. Thrun, M. Montemerlo, H. Dahlkamp, D. Stavens, A. Aron, J. Diebel, P. Fong, J. Gale, M. Halpenny, G. Hoffmann, K. Lau, C. Oakley, M. Palatucci, V. Pratt, P. Stang, S. Strohband, C. Dupont, L.-E. Jendrossek, C. Koelen, C. Markey, C. Rummel, J. van Niekerk, E. Jensen, P. Alessandrini, G. Bradski, B. Davies, S. Ettinger, A. Kaehler, A. Nefian, and P. Mahoney, "Stanley, the robot that won the DARPA grand challenge," *J. Field Robot.*, vol. 23, no. 9, pp. 661–692, 2006.
- [12] A. Bachrach, R. He, and N. Roy, "Autonomous flight in unstructured and unknown indoor environments," in *Proc. European Conf. Micro Air Vehicles*, 2009, pp. 1–8.
- [13] A. Chambers, S. Achar, S. Nuske, J. Rehder, B. Kitt, L. Chamberlain, J. Haines, S. Scherer, and S. Singh, "Perception for a river mapping robot," in *Proc. IEEE/RSJ Int. Conf. Intelligent Robots Systems*, 2011, pp. 227–234.
- [14] S. Grzonka, G. Grisetti, and W. Burgard, "A fully autonomous indoor quadrotor," *IEEE Trans. Robot.*, vol. 28, no. 1, pp. 90–100, 2012.
- [15] S. Shen, N. Michael, and V. Kumar, "Autonomous multi-floor indoor navigation with a computationally constrained MAV," in *Proc. IEEE Int. Conf. Robotics Automation*, 2011, pp. 20–25.
- [16] S. Shen, N. Michael, and V. Kumar, "Autonomous indoor 3D exploration with a micro-aerial vehicle," in *Proc. IEEE Int. Conf. Robotics Automation*, 2012, pp. 20–25.
- [17] D. Floreano, J. Zufferey, M. Srinivasan, and C. Ellington, *Flying Insects and Robots*. Berlin Heidelberg, Germany: Springer-Verlag, 2010.
- [18] S. Hrabar, G. S. Sukhatme, P. Corke, K. Usher, and J. Roberts, "Combined optic-flow and stereo-based navigation of urban canyons for a UAV," in *Proc. IEEE/RSJ Int. Conf. Intelligent Robots Systems*, 2005, pp. 3309–3316.
- [19] J. Zufferey and D. Floreano, "Fly-inspired visual steering of an ultralight indoor aircraft," *IEEE Trans. Robot.*, vol. 22, no. 1, pp. 137–146, 2006.
- [20] S. Ahrens, D. Levine, G. Andrews, and J. How, "Vision-based guidance and control of a hovering vehicle in unknown, GPS-denied environments," in *Proc. Int. Conf. Robotics Automation*, 2009, pp. 2643–2648.
- [21] M. Bloesch, S. Weiss, D. Scaramuzza, and R. Siegwart, "Vision based MAV navigation in unknown and unstructured environments," in *Proc. IEEE Int. Conf. Robotics Automation*, 2010, pp. 21–28.
- [22] S. Weiss, D. Scaramuzza, and R. Siegwart, "Monocular-SLAM-based navigation for autonomous micro helicopters in GPS-denied environments," *J. Field Robot.*, vol. 28, no. 6, pp. 854–874, 2011.
- [23] D. Eberli, D. Scaramuzza, S. Weiss, and R. Siegwart, "Vision based position control for MAVs using one single circular landmark," *J. Intell. Robot. Syst.*, vol. 61, nos. 1–4, pp. 495–512, 2011.
- [24] S. Weiss, M. Achtelik, S. Lynen, M. Chli, and R. Siegwart, "Real-time onboard visual-inertial state estimation and self-calibration of MAVs in unknown environments," in *Proc. IEEE Int. Conf. Robotics Automation*, 2012, pp. 957–964.
- [25] A. Ganguli, J. Cortés, and F. Bullo, "Maximizing visibility in nonconvex polygons: Nonsmooth analysis and gradient algorithm design," in *Proc. American Control Conf.*, 2005, vol. 2, pp. 792–797.
- [26] A. Ganguli, J. Cortés, and F. Bullo, "Visibility-based multi-agent deployment in orthogonal environments," in *Proc. American Control Conf.*, 2007, pp. 3426–3431.
- [27] P. Agarwal and M. Sharir, "Efficient algorithms for geometric optimization," *ACM Comput. Surv.*, vol. 30, no. 4, pp. 412–458, 1998.
- [28] T. Shermer, "Recent results in art galleries," *Proc. IEEE*, vol. 80, no. 9, pp. 1384–1399, 1992.
- [29] A. Howard, M. Matarić, and G. Sukhatme, "Distributed coverage control on surfaces in 3D space," in *Proc. IEEE Int. Conf. Robotics Intelligent System*, Lausanne, Switzerland, 2002, pp. 2849–2854.
- [30] M. Schwager, B. Julian, and D. Rus, "Optimal coverage for multiple hovering robots with downward facing camera," in *Proc. IEEE Int. Conf. Robotics Automation*, Kobe, Japan, 2009, pp. 3515–3522.
- [31] J. Cortés, S. Martínez, T. Karataş, and F. Bullo, "Coverage control for mobile sensing networks," *IEEE Trans. Robot. Automat.*, vol. 20, no. 2, pp. 243–255, 2004.
- [32] M. Schwager, J. McLurkin, and D. Rus, "Distributed coverage control with sensory feedback for networked robots," in *Proc. Robotics: Science Systems*, Philadelphia, PA, 2006.
- [33] A. Breitenmoser, M. Schwager, J. Metzger, R. Siegwart, and D. Rus, "Voronoi coverage of non-convex environments with a group of networked robots," in *Proc. IEEE Int. Conf. Robotics Automation*, Anchorage, AK, 2010, pp. 4982–4989.
- [34] L. Pimenta, V. Kumar, R. Mesquita, and G. Pereira, "Sensing and coverage for a network of heterogeneous robots," in *Proc. IEEE 47th Conf. Decision Control*, Cancun, Mexico, 2008, pp. 3947–3952.
- [35] A. Howard, M. Matarić, and G. Sukhatme, "Mobile sensor network deployment using potential fields: A distributed, scalable solution to the area coverage problem," in *Proc. 6th Int. Conf. Distributed Autonomous Robotic System*, 2002, pp. 299–308.
- [36] A. Breitenmoser, J. Metzger, R. Siegwart, and D. Rus, "Distributed coverage control on surfaces in 3D space," in *Proc. IEEE Int. Conf. Robotics Intelligent System*, 2010, pp. 1–8.
- [37] M. Achtelik, K.-M. Doth, D. Gurdan, and J. Stumpf, "Multi-rotor-mavs—A trade off between efficiency, dynamics and redundancy," in *Proc. Guidance, Navigation, Control*, Aug. 2012, pp. 1–8.
- [38] D. Scaramuzza and F. Fraundorfer, "Visual odometry: Part I—The first 30 years and fundamentals," *IEEE Robot. Automat. Mag.*, vol. 18, no. 4, pp. 80–92, 2011.
- [39] F. Fraundorfer and D. Scaramuzza, "Visual odometry: Part II—Matching, robustness, and applications," *IEEE Robot. Automat. Mag.*, vol. 19, no. 2, pp. 78–90, 2012.
- [40] G. Klein and D. Murray, "Parallel tracking and mapping for small AR workspaces," in *Proc. Int. Symp. Mixed Augmented Reality*, 2007, pp. 1–10.
- [41] C. Forster, M. Pizzoli, and D. Scaramuzza, "SVO: Fast semi-direct monocular visual odometry," in *Proc. IEEE Int. Conf. Robotics Automation*, 2014, pp. 1–8.
- [42] S. Weiss and R. Siegwart, "Real-time metric state estimation for modular vision-inertial systems," in *Proc. IEEE Int. Conf. Robotics Automation*, 2011, pp. 4531–4537.
- [43] S. Weiss, M. W. Achtelik, M. Chli, and R. Siegwart, "Versatile distributed pose estimation and sensor self-calibration for an autonomous MAV," in *Proc. IEEE Int. Conf. Robotics Automation*, 2012, pp. 31–38.
- [44] A. Martinelli, "Vision and IMU data fusion: Closed-form solutions for attitude, speed, absolute scale, and bias determination," *IEEE Trans. Robot.*, vol. 28, no. 1, pp. 44–60, 2012.

- [45] J. Kelly and G. S. Sukhatme, "Visual-inertial sensor fusion: Localization, mapping and sensor-to-sensor self-calibration," *Int. J. Robot. Res.*, vol. 30, no. 1, pp. 56–79, 2011.
- [46] C. Forster, S. Lynen, L. Kneip, and D. Scaramuzza, "Collaborative monocular SLAM with multiple micro aerial vehicles," in *Proc. IEEE/RSJ Int. Conf. Intelligent Robots a Systems*, 2013, pp. 3962–3970.
- [47] D. Nistér and H. Stewénius, "Scalable recognition with a vocabulary tree," in *Proc. IEEE Conf. Computer Vision Pattern Recognition*, New York, 2006, pp. 2161–2168.
- [48] F. Fraundorfer, C. Engels, and D. Nister, "Topological mapping, localization and navigation using image collections," in *Proc. IEEE/RSJ Int. Conf. Intelligent Robots Systems*, 2007, pp. 3872–3877.
- [49] H. Bay, T. Tuytelaars, and L. V. Gool, "SURF: Speeded up robust features," in *Proc. European Conf. Computer Vision*, 2006, pp. 404–417.
- [50] L. Kneip, D. Scaramuzza, and R. Siegwart, "A novel parametrization of the perspective-three-point problem for a direct computation of absolute camera position and orientation," in *Proc. IEEE Conf. Computer Vision Pattern Recognition*, 2011, pp. 2969–2976.
- [51] R. Kuemmerle, G. Grisetti, H. Strasdat, K. Konolige, and W. Burgard, "G2o: A general framework for graph optimization," in *Proc. IEEE Int. Conf. Robotics Automation*, 2011, pp. 3607–3613.
- [52] L. Heng, G. Lee, F. Fraundorfer, and M. Pollefeys, "Real-time photorealistic 3D mapping for micro aerial vehicles," in *Proc. IEEE Int. Conf. Robotics Intelligent System*, 2011, pp. 4012–4019.
- [53] E. Kosmatopoulos and A. Kouvelas, "Large-scale nonlinear control system fine-tuning through learning," *IEEE Trans. Neural Netw.*, vol. 20, no. 6, pp. 1009–1023, 2009.
- [54] J. Spall, *Introduction to Stochastic Search and Optimization*. New York: Wiley, 2003.
- [55] J. L. Ny and G. Pappas, "Sensor-based robot deployment algorithms," in *Proc. 49th IEEE Conf. Decision Control*, Atlanta, GA, 2010, pp. 5486–5492.
- [56] A. Renzaglia, L. Doitsidis, A. Martinelli, and E. Kosmatopoulos, "Multi-robot three-dimensional coverage of unknown areas," *Int. J. Robot. Res.*, vol. 31, no. 6, pp. 738–752, 2012.
- [57] L. Doitsidis, S. Weiss, A. Renzaglia, M. W. Achtelik, E. Kosmatopoulos, R. Siegwart, and D. Scaramuzza, "Optimal surveillance coverage for teams of micro aerial vehicles in GPS-denied environments using onboard vision," *Auton. Robot.*, vol. 33, nos. 1–2, pp. 173–188, 2012.
- [58] M. Achtelik, S. Lynen, S. Weiss, L. Kneip, M. Chli, and R. Siegwart, "Visual-inertial SLAM for a small helicopter in large outdoor environments," in *Video Proc. IEEE/RSJ Int. Conf. Intelligent Robots Systems*, 2012, pp. 2651–2652.
- [59] S. Weiss, M. W. Achtelik, S. Lynen, M. Chli, and R. Siegwart, "Real-time onboard visual-inertial state estimation and self-calibration of MAVs in unknown environments," in *Proc. IEEE Int. Conf. Robotics Automation*, 2012, pp. 957–964.
- [60] M. Pollefeys, D. Nister, J. M. Frahm, A. Akbarzadeh, P. Mordohai, B. Clipp, C. Engels, D. Gallup, S. J. Kim, P. Merrell, C. Salmi, S. Sinha, B. Talton, L. Wang, Q. Yang, H. Stewénius, R. Yang, G. Welch, and H. Towles. (2008, July). Detailed real-time urban 3D reconstruction from video. *Int. J. Comput. Vision.* [Online]. 78(2–3), pp. 143–167. Available: <http://dx.doi.org/10.1007/s11263-007-0086-4>

Davide Scaramuzza, University of Zürich, Zürich 8050, Switzerland. E-mail: davide.scaramuzza@ieee.org.

Michael C. Achtelik, Ascending Technologies GmbH, Krailling D82152, Germany. E-mail: michael@achtelik.net, michael.achtelik@asctec.de.

Lefteris Doitsidis, Technological Educational Institute of Crete, Chania 73100, Greece. E-mail: ldoitsidis@chania.teicrete.gr.

Friedrich Fraundorfer, Technische Universität München, München 80333, Germany. E-mail: friedrich.fraundorfer@tum.de.

Elias Kosmatopoulos, Democritus University Thrace and ITI/CERTH, Xanthi 67100, Greece. E-mail: kosmatop@dssl.tuc.gr.

Agostino Martinelli, INRIA Grenoble-Rhone-Alpes, Grenoble 38334, France. E-mail: agostino.martinelli@inria.fr.

Markus W. Achtelik, Autonomous Systems Lab, ETH Zürich, Zürich 8092, Switzerland. E-mail: markus.achtelik@mavt.ethz.ch.

Margarita Chli, University of Edinburgh, Edinburgh EH8 9AB, United Kingdom. E-mail: margarita.chli@mavt.ethz.ch.

Savvas Chatzichristofis, Democritus University Thrace and ITI/CERTH, Xanthi 67100, Greece. E-mail: schatzic@ee.duth.gr.

Laurent Kneip, Australian National University, Canberra 0200, Australia. E-mail: laurent.kneip@anu.edu.au.

Daniel Gurdan, Ascending Technologies GmbH, Krailling 82152, Germany. E-mail: daniel@gurdan.de.

Lionel Heng, ETH Zürich, Zürich 8092, Switzerland. E-mail: hengli@inf.ethz.ch.

Gim Hee Lee, ETH Zürich, Zürich 8051, Switzerland. E-mail: lgimhee@gmail.com, glee@student.ethz.ch.

Simon Lynen, ETH Zürich, Zürich 8092, Switzerland. E-mail: simon.lynen@mavt.ethz.ch.

Lorenz Meier, ETH Zürich, Zürich 8092, Switzerland. E-mail: lm@inf.ethz.ch.

Marc Pollefeys, ETH Zürich, Zürich 8006, Switzerland. E-mail: marc.pollefeys@inf.ethz.ch.

Alessandro Renzaglia, University of Minnesota, Minnesota 55455, USA. E-mail: a.renzaglia@gmail.com, arenzagl@umn.edu.

Roland Siegwart, ETH Zürich, Zürich 8092, Switzerland. E-mail: rsiegwart@ethz.ch.

Jan Carsten Stumpf, Ascending Technologies GmbH, Krailling 82152, Germany. E-mail: jan@asctec.de.

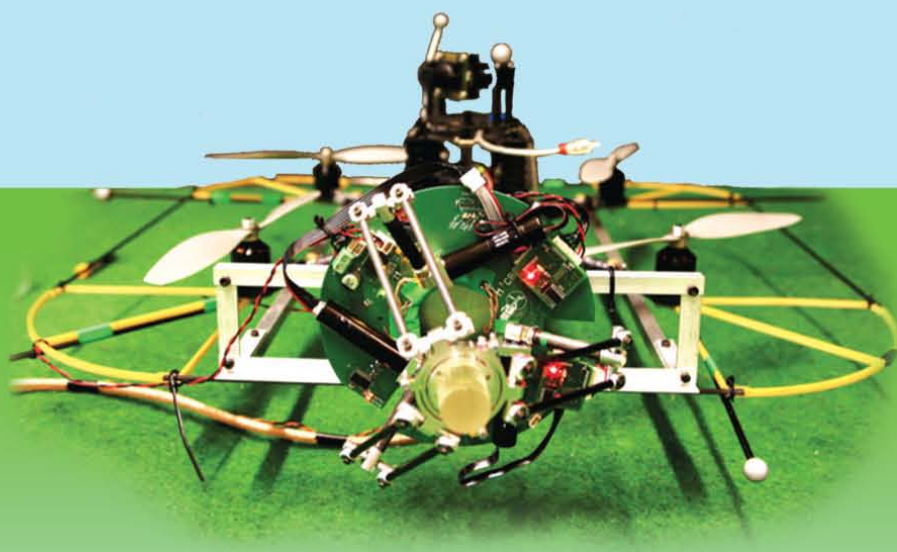
Petri Tanskanen, ETH Zürich, Zürich 8092, Switzerland. E-mail: tpetri@student.ethz.ch.

Chiara Troiani, INRIA Rhone Alpes, Grenoble 38334, France. E-mail: chiara.troiani@inrialpes.fr, t.chiara@gmail.com.

Stephan Weiss, NASA Jet Propulsion Laboratory and California Institute of Technology, Pasadena 91109, California, USA. E-mail: stephan.weiss@ieee.org.

Developing an Aerial Manipulator Prototype

Physical Interaction with the Environment



By Matteo Fumagalli, Roberto Naldi, Alessandro Macchelli, Francesco Forte, Arvid Q.L. Keemink, Stefano Stramigioli, Raffaella Carloni, and Lorenzo Marconi

This article focuses on the design, modeling, and control of an aerial manipulator prototype, i.e., an innovative configuration consisting of a miniature quadrotor helicopter endowed with a robotic manipulator. The overall system is designed to accomplish operations that require physical interaction with the surrounding environment while remaining airborne. To investigate the dynamical model of the aerial manipulator, a simple planar benchmark is used to analyze the interactions between the quadrotor, the robotic manipulator, and the

environment. A control strategy for the planar system is designed to guarantee robustness in the presence or absence of contacts. Experiments on a real setup validate the control in the two different scenarios in which the aerial manipulator is either freely flying or physically interacting with the environment.

Aerial Interaction

The physical interaction between unmanned aerial vehicles (UAVs) and their surrounding environment is a new research trend that is currently receiving considerable attention in the field of aerial robotics [1]. The goal is to exploit, in real applicative scenarios, the potentialities of systems that are not only able to fly autonomously but also to safely interact with

Digital Object Identifier 10.1109/MRA.2013.2287454
Date of publication: 11 August 2014

remote objects to accomplish tasks such as data acquisition by contact, sample picking, and repairing and assembling objects. To achieve this, several methodological and technological challenges have to be faced. In particular, most aerial configurations, including quadrotors [2], [3], helicopters [4], or ducted fans [5], are underactuated mechanical systems [6],

which means that not all of their degrees of freedom (DoF) can be controlled simultaneously. This feature affects the design of the control law, particularly because stability has to be preserved even in the presence of disturbances derived from physical interaction.

Several recent contributions to the literature

attest to the interest in such challenging control scenarios. For instance, grasping and transportation using a fleet of quadrotors are considered in [7] and extended in [8] to assembling an infrastructure. A control law to allow an autonomous aerobatic airplane to land on a vertical surface is proposed in [9] and [10]. In [11], a quadrotor helicopter is employed to clean a surface while hovering, where an additional propeller is employed to counteract contact forces while maintaining the stability of the vehicle. In [12], the physical interaction between a ducted-fan aerial vehicle and the environment is considered, and a switching control law is proposed that considers the possible constraints due to the presence of contacts. Aerial grasping using an autonomous helicopter endowed with a manipulator is discussed in [13]. In this case, the analysis focuses on the stability of the vehicle during the interaction with a compliant environment. A prototype of a miniature aerial manipulator is proposed in [14].

Within this research scenario is the European project Innovative Aerial Service Robots for Remote Inspections by Contact (AIRobots) [15]. The goal of AIRobots is to develop a new generation of service robots capable of supporting human beings in all those activities that require the ability to

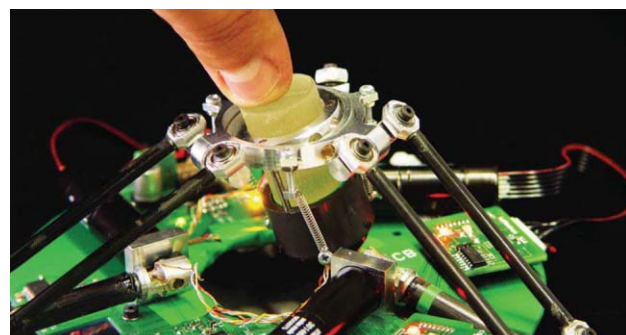


Figure 1. The compliant structure of the end effector of the robotic manipulator. (Photo courtesy of the Robotics and Mechatronics Lab at the University of Twente.)

interact actively and safely with environments not constrained on the ground but airborne.

Contribution

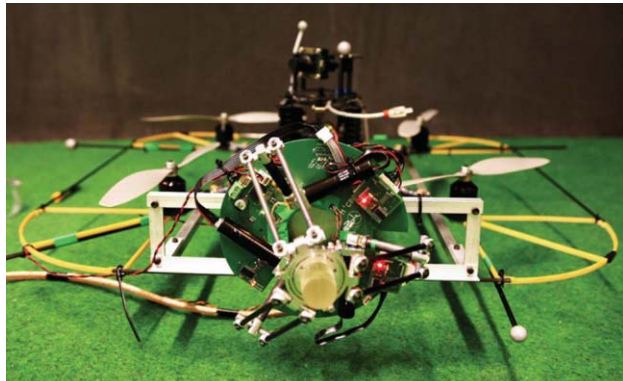
Inspired by the application scenario in [15], this article presents the design, modeling, and control of an aerial manipulator consisting of a miniature quadrotor helicopter endowed with a robotic manipulator.

The airframe of a generic quadrotor helicopter has been adapted to carry a miniature robotic manipulator, which has been specifically designed for aerial inspection of industrial plants [16]. The mechanical design of the robotic manipulator consists of an arm based on a 3-DoF delta structure, and a 3-DoF end effector based on a Cardan gimbal.

The selected configuration presents some remarkable advantages. On one side, the additional DoF of the robotic manipulator decouple the position and the orientation of the end effector from those of the aerial vehicle and, therefore, they improve the effectiveness of the overall aerial manipulator well beyond the standard quadrotor capabilities. On the other side, since the aerial vehicle configuration has not been substantially modified, all of the main advantages of the well-known quadrotor design, such as the reduced aeromechanical complexity and the high aerodynamic efficiency, are preserved.

By analyzing the interaction between the quadrotor, the manipulator, and the environment, the dynamical properties of the aerial manipulator are investigated near hovering both during free flight and during a docking maneuver with a vertical surface, i.e., when the end effector is in contact with the environment. Building upon this analysis, an energy-based control strategy is proposed [17], [18]. The main idea is to make the position dynamics of the vehicle passive [19] by relying upon a cascade control strategy [20] in which the attitude is considered a virtual available control input. The closed-loop passive system can then be controlled as a standard robotic manipulator, implementing impedance control strategies [21], suitable to handle both contact and no-contact cases.

To show the effectiveness of the overall design, two main experiments are proposed. The first shows how a position controller for the manipulator can be employed to track certain references in the Cartesian space, maintaining a constant position despite the fluctuations that the aerial vehicle, affected by aerodynamic disturbances, induces on the manipulator's end effector. This experiment reveals how, in free flight, the DoF of the manipulator can be employed to improve the accuracy in positioning the end effector without significantly affecting the dynamics of the aerial vehicle. The second experiment considers a docking maneuver in which the manipulator's end effector applies a force to a vertical surface. This experiment reveals how the quadrotor, which plays the role that a fixed base does for a standard manipulator, has to tilt to compensate for the reaction forces and, therefore, maintain the aerial manipulator's contact with the environment.



© ASCENDING TECHNOLOGIES

Figure 2. The aerial manipulator: the Pelican quadrotor by Ascending Technologies (AscTec) and the robotic manipulator. The AscTec Pelican is developed by Ascending Technologies GmbH, <http://www.asctec.de>.

Aerial Manipulator

The aim of this article is to realize an aerial manipulator that is able to interact safely with the environment and to robustly perform docking maneuvers at locations inaccessible to humans. The aerial manipulator integrates a miniature commercial helicopter, an AscTec Pelican quadrotor (Ascending Technologies GmbH, Germany), with a custom-made robotic manipulator.

The prototype of the robotic manipulator has been designed to perform Cartesian movements to compensate for the quadrotor's dynamics, both in free flight and during contact, and to realize safe and robust interaction. The mechanical innovation of the robotic manipulator lies in the use of a delta structure with three active DoF and a three-passive-DoF end effector, which is realized by a Cardan gimbal and a set of springs [16].

The delta structure is ideal since it provides the Cartesian end effector motion through three rotary motor motions, and it can supply a significant amount of force to the end effector while keeping the overall weight low. As shown in Figure 1, the motors are placed on a base plate, i.e., the electronic board, close to the UAV's center of gravity (CG). This induces a small torque disturbance on the UAV and, hence, requires less counterbalancing, especially during free flight.

The Cardan gimbal and the springs of the end effector allow a passive adaptation to the contact surface and an absorption of impacts. As shown in Figure 1, the Cardan gimbal has been designed to be a socket for the modular end effectors, e.g., a nondestructive ultrasound sensor, necessary to achieve the tasks required by the inspection through contact, as required in [15]. The complete aerial manipulator, which is used as the experimental platform in the tests of the "Experimental Validation" section, is shown in Figure 2.

In this article, the dynamical properties of the aerial manipulator are analyzed, and a control is designed during free flight and in an interaction scenario. More precisely, the end effector's orientation is neglected in the design of the controller and only the end effector's position is considered.

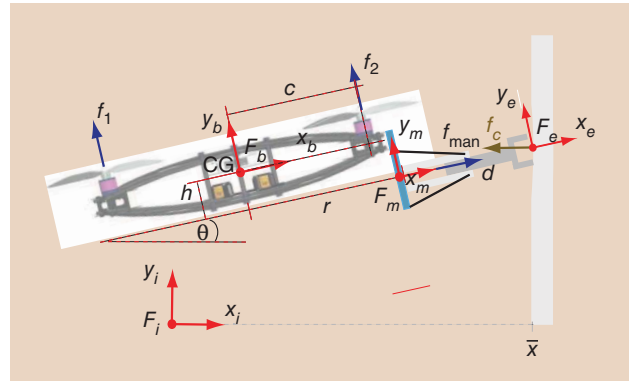


Figure 3. The reference picture for the modeling of the planar aerial manipulator. Four reference frames are defined, namely the inertial frame F_i , a body frame F_b attached to the CG of the aerial vehicle, a frame F_m attached to the base plate of the manipulation system, and a frame F_e attached to the end effector. (Photo courtesy of the Robotics and Mechatronics Lab at the University of Twente.)

Control and Experimental Validation

We present a control architecture for the aerial manipulator that is robust with respect to both the uncertainties of the dynamical model of the system and of the environment. In general, classical control strategies, synthesized without explicitly considering the interaction, cannot deal with all of the situations the aerial vehicle may incur due to the remarkably different dynamics underlying the system behavior in free flight and in the presence of contact with the environment.

The proposed control law is formally designed in a two-dimensional benchmark able to capture the basic dynamical properties of the system near hovering and validated, through experiments, in three dimensions on the aerial manipulator. The behavior of the overall system is tested in two different scenarios.

First, the performance of the controller while the system is in free flight is analyzed. The end effector of the robotic manipulator is required to track a desired fixed point p_{ee}^* in the workspace. The goal of this experiment is to show that the performances in tracking the fixed point are improved if the DoF of the manipulator are employed to decouple the dynamics of the end effector from those of the aircraft. In the second experiment, the system is controlled to realize a safe interaction with a vertical wall.

The analysis focuses on
the stability of the vehicle
during the interaction with
a compliant environment.

System Model

The interaction between the aerial vehicle, the robotic manipulator, and the environment can be captured by means of a simple reduced-order benchmark, denoted as the *planar aerial manipulator*. This benchmark, shown in Figure 3, consists of a robot composed of a prismatic joint

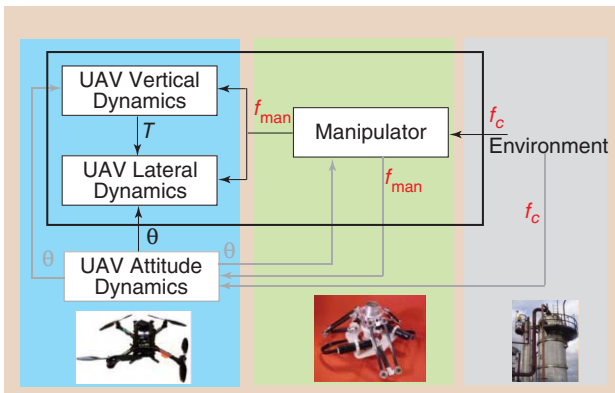


Figure 4. The planar aerial manipulator as the interconnection of different subsystems given by the environment, the manipulator and, for the quadrotor, the vertical, the lateral, and the attitude dynamics. The AscTec Pelican is developed by AscTec GmbH, <http://www.asctec.de>. (Photos courtesy of the Robotics and Mechatronics Lab at the University of Twente.)

manipulator linked to a planar model of the quadrotor. The planar aerial manipulator is an underactuated mechanical system since it has 4 DoF and three control inputs [6], [22], [23]. The former is given by the lateral position, the longitudinal position, the attitude orientation of the quadrotor, and the position of the prismatic joint; the latter is the two forces produced by the propellers and the actuation force governing the robotic manipulator.

- For the planar benchmark, we use the following notation:
- the relative pose between F_b and F_i is described by means of x and y , i.e., the lateral and longitudinal position of the aerial vehicle's CG expressed in the inertial frame F_i , and θ , i.e., the vehicle attitude orientation
 - the relative pose between F_e and F_m is described by means of d , i.e., the position of the manipulator joint expressed in the reference frame F_m
 - the relative pose between F_e and F_i is described by means of x_{ee} and y_{ee} , i.e., the lateral and vertical position of the end effector with respect to the inertial frame F_i
 - the relative pose between F_m and F_b is described by means of the constant parameters h and r , which are the vertical and lateral position of the point in which the manipulator is linked to the vehicle, respectively
 - f_1 and f_2 are the forces generated by the two propellers; f_{man} is the actuation force of the manipulator; f_c is the force applied by the environment to the end effector
 - c is the lever arm of the forces f_1 and f_2
 - M , J_{uav} , m , and J_{man} are the mass and the inertia of the aerial vehicle and the manipulator, respectively
 - g denotes the gravity acceleration.

Approximated Dynamical Model of the Planar Aerial Manipulator in the Interaction Scenario

As shown in Figure 4, the dynamical model of the planar aerial manipulator results from the interconnection of three different main subsystems: the environment, the robotic manipulator, and the quadrotor. As shown in Figure 3, the end

effector installed on the planar aerial manipulator may come into contact with the environment, modeled as a vertical compliant surface. When the lateral position of the end effector penetrates the wall, the environment applies to the end effector a force f_c orthogonal to the wall. By modeling the surface as a spring, the force f_c turns out to be proportional to the deformation of the contact material, i.e.,

$$f_c := \begin{cases} -k_x \eta & \text{if } \eta > 0 \\ 0 & \text{if } \eta \leq 0, \end{cases} \quad (1)$$

where k_x is the stiffness of the vertical surface and $\eta = (x_{ee} - \bar{x})$ represents the penetration of the end effector lateral position x_{ee} into the vertical surface located at \bar{x} .

As far as the manipulator is concerned, the following approximated dynamical model can be obtained

$$m\ddot{d} = f_{\text{man}} + f_c \cos \theta. \quad (2)$$

Observe that the manipulator position is driven by the control force f_{man} , and it is affected by the force f_c applied by the environment, and by the attitude θ of the vehicle.

The last subsystem is given by the quadrotor dynamics that are driven by the resultant thrust $T := f_1 + f_2$ and torque $\tau := c(f_2 - f_1)$ produced by the two propellers. By assuming that the mass m of the manipulator is concentrated at the end effector position and that it is negligible compared with the mass M of the quadrotor (in our setup, $M \approx 1.8$ kg, $m \approx 0.1$ kg), the lateral, longitudinal, and attitude dynamics can be approximated as

$$\begin{aligned} M\ddot{x} &= -f_{\text{man}} \cos \theta - T \sin \theta \\ M\ddot{y} &= -f_{\text{man}} \sin \theta + T \cos \theta - Mg \\ J_{\text{uav}}\ddot{\theta} &= \tau - hf_{\text{man}} - (r+d)f_c \sin \theta - (r+d)mg \cos \theta. \end{aligned} \quad (3)$$

Note that the above quadrotor dynamics are affected by the force f_{man} governing the manipulator, by the contact force f_c , and by the position d of the manipulator. As shown in Figure 4, in the above equations, the environment, the manipulator, and the lateral/vertical dynamics of the vehicle form a cascade interconnection in which the environment influences the manipulator dynamics by means of the force f_c , and this affects the lateral and vertical dynamics of the quadrotor through the control force f_{man} .

Control Architecture

Basic Properties

One of the distinguishing features of the proposed planar aerial manipulator is that the robotic manipulator is linked to an underactuated vehicle, i.e., the quadrotor, rather than to a fixed base. In classical robotic manipulation [24], both position and force control of the end effector are synthesized by assuming that the reaction forces and torques applied to the base as a consequence of the motion of the manipulator are perfectly rejected. On the other hand, when the manipulator is linked to a mobile platform, a similar design paradigm can

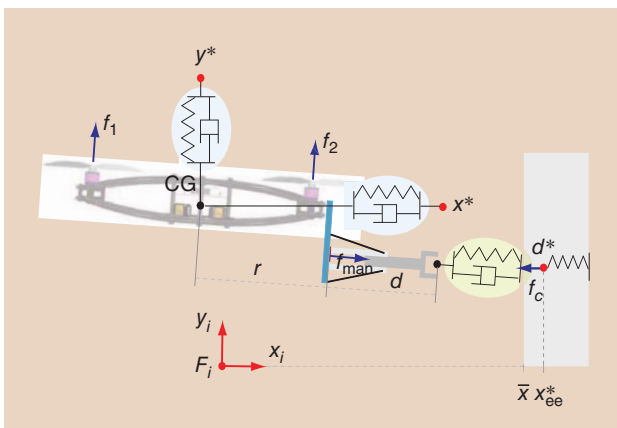


Figure 5. The passivity-based control architecture for the planar aerial manipulator. Intuitively the lateral, vertical, and the manipulator dynamics of the system are transformed by feedback into passive subsystems able to dissipate energy reaching the desired set points (y^* , x^* , d^* , x_{ee}^*) when no external forces are applied or to apply forces to the environment when the end effector enters in contact with the surface.

be employed only if the platform itself can be controlled to reject the reaction forces and torques applied to it by means of its own actuators, i.e., it can be transformed into a fixed base by feedback. Examples of such control approaches can also be found in the field of space robotics [25].

For an underactuated dynamical system, such as the planar aerial manipulator derived in the previous section, this approach may not be feasible, as the lack of available control inputs prevents the exact compensation for all of the reaction forces and torques while maintaining a constant desired configuration. Inspired by the control approaches in [20], where position controllers for underactuated aerial vehicles are proposed, we concentrate on a cascade control structure in which the attitude dynamics of the vehicle play the role of the inner loop to stabilize the lateral position of the vehicle, which is then designed as the outer loop. In this way, as far as the control design is concerned, it is possible to consider the attitude of the vehicle as a virtual input to apply forces in the lateral direction and, in turn, to counteract the reaction force proportional to f_{man} . The attitude controller will then be designed as a fast high-gain feedback loop [26] such that the attitude $\theta \approx \theta^*$, θ^* being the reference attitude to be used as virtual control input for the lateral dynamics of the vehicle.

When such an approach is adopted, an important issue is the actual controllability of the attitude in the presence of physical interaction. As shown in Figure 4, when the manipulator and environment are in contact, torque disturbances are produced and have to be compensated to avoid the system losing controllability of the attitude and, as a consequence, of the lateral dynamics. Since the environment

is not perfectly known, a really high-gain attitude controller may be required, unless the contact forces are kept reasonably small; this appears of paramount importance for a practical implementation of the proposed controller.

Control Approach

Inspired by the application scenario in [15], we consider a control problem in which the planar aerial manipulator is required to enter into contact with the vertical surface to perform an inspection by contact using the tool installed on the end effector. To succeed in this complex task, the goal of the con-

tral design is twofold. On one hand, the controller should be able to stabilize a given free-flight configuration, maintaining the end effector in the desired vertical and lateral positions. This feature can be employed, for instance, to move the tool installed on the end effector close to the area to be inspected before entering into contact with the surface. On the other hand, the control law should be designed to perform docking maneuvers, i.e., it should be able to stabilize the aerial manipulator while applying certain forces to the vertical surface by means of the end effector. This last feature is required to actually perform the inspection-by-contact operations.

Motivated by the effectiveness of the energy-based approaches [27] in applications pertaining to the physical interaction between robots and the environment [28], an impedance controller [21] is proposed to meet the two control goals simultaneously. The first step, discussed in the next section, consists of designing a passivity-based controller for the planar aerial manipulator by taking advantage of the cascade control structure introduced so far. This goal is achieved by considering standard passivity-based feedback design techniques [27], where the stability of a desired equilibrium point is obtained by shaping the energy function of

The airframe of a generic quadrotor helicopter has been adapted to carry a miniature robotic manipulator.

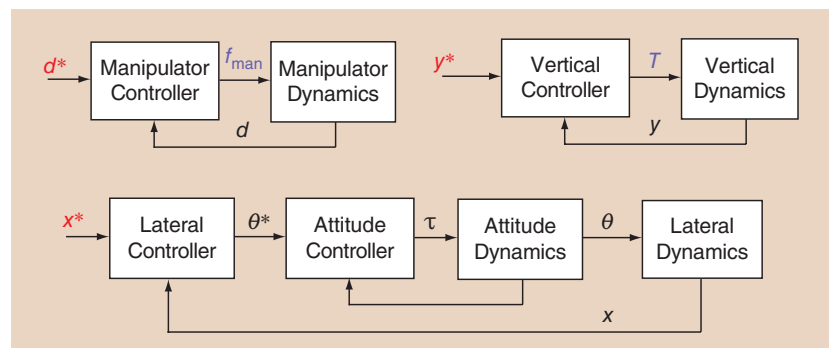


Figure 6. The overall control architecture with the cascade control structure employed to govern the attitude and the lateral position of the aerial vehicle.

the system to have a desired minimum (energy shaping), and then by dissipating energy to asymptotically converge to it (damping injection). A graphical representation of the overall passivity-based controller for the planar aerial manipulator is shown in Figure 5, whereas the overall control structure is shown in Figure 6. The overall behavior of the robotic device in the free-flight and docking scenarios is then discussed in the “Free-Flight Scenario” and “Docking Scenario” sections, respectively.

By modeling the surface as a spring, the force f_c turns out to be proportional to the deformation of the contact material.

“Free-Flight Scenario” and “Docking Scenario” sections, respectively.

Passivity-Based Control Design

From Figure 6, assume that the attitude controller is designed such that $\theta \approx \theta^*$. In addition, assume that the aerial robot dynamics, during the overall inspection-by-contact operation, remain close to the hovering condition, i.e., with small θ^* such that $\cos \theta^* \approx 1$, $\sin \theta^* \approx \theta^*$, and with $T \approx Mg$. Let the inputs f_{man} , T , and the virtual input θ^* be chosen as

$$f_{\text{man}} = mu_d, \quad T = M(u_y + g), \quad \theta = \frac{1}{g}u_x, \quad (4)$$

where u_d , u_y , and u_x are new inputs. Accordingly, in the hovering condition, the manipulator, the vertical, and the lateral dynamics in (1)–(3), can be approximated as

$$\ddot{\gamma} = u_\gamma + d_\gamma, \quad (5)$$

where $\gamma \in \{d, y, x\}$, where $d_d := f_c/m$, $d_y := -f_{\text{man}}\theta/M$, and $d_x := -f_{\text{man}}/M$ are exogenous disturbances.

Observe that (5) is a linear system driven by the control input u_γ and affected by the exogenous disturbance d_γ . Now, let $\gamma^* \in \{d^*, y^*, x^*\}$ be the desired constant reference for the manipulator, the vertical and the lateral position of the vehicle. In addition, let the control input u_γ be designed as

$$u_\gamma = -k_p^\gamma(\gamma - \gamma^*) - k_d^\gamma \dot{\gamma} \quad (6)$$

with $k_p^\gamma > 0$ and $k_d^\gamma > 0$ control parameters. The above linear controller can be interpreted as a passivity-based control law. In fact, observe that the resulting closed-loop system turns out to be output strictly passive [29] by choosing input d_γ , output $\dot{\gamma}$ and storage function

$$V = \mathcal{K} + \mathcal{P}$$

in which $\mathcal{K} = 1/2 M_\gamma \dot{\gamma}^2$ denotes the kinetic energy, with $M_\gamma = m$ if $\gamma = d$ or $M_\gamma = M$ otherwise, and $\mathcal{P} = 1/2 k_p^\gamma(\gamma - \gamma^*)^2$ denotes the potential energy having a minimum at the desired position γ^* .

As shown, for instance in [29, Lemma 6.7], the above property of output strict passivity can be linked to zero-input

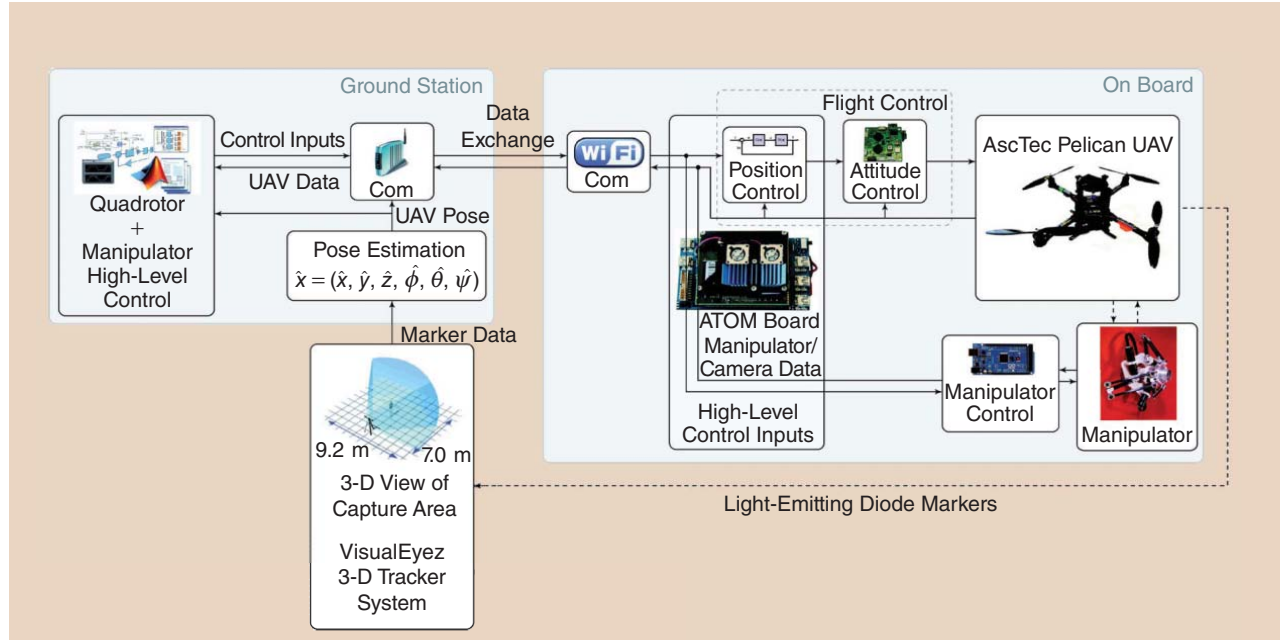


Figure 7. System overview: the overall system consists of the AscTec Pelican quadrotor, endowed with on-board sensors and electronics for the low-level control of the position and attitude control, and the robotic manipulator, whose low-level controller is embedded in custom-made electronics. An external tracker, VisualEyez VZ 4000, is used to detect some marker positions, which are used to estimate the absolute pose of the vehicle. The ground station allows the intercommunication between the different submodules and devices. The communication between the different software modules and the on-board electronics is performed using the robot operating system. The AscTec Pelican is developed by Ascending Technologies GmbH, <http://www.asctec.de>. (Used with permission.)

asymptotic stability via zero-state observability. This property can be shown to hold for the closed-loop system. It must now be shown that the linear controller (6) is actually able to perform both the control goals to be suitable to perform the inspection-by-contact operations.

Free-Flight Scenario

The free-flight scenario describes the situation in which the end effector is not in contact with the environment. The stability properties of the overall system can then be investigated by analyzing the cascade interconnection of the manipulator with the vertical and lateral dynamics of the vehicle shown in Figure 4. In particular, when the contact force is close to zero, i.e., $f_c \equiv 0$, also the exogenous input d_d affecting the manipulator subsystem is zero. From the passivity property highlighted previously, the position of the manipulator asymptotically converges to d^* , and, from the definition of u_d in (6), d_y and d_x also asymptotically converge to zero. As a consequence, the passivity properties of the vertical and lateral subsystems can be employed to show that the desired positions y^* and x^* are asymptotically stabilized.

In free flight, the manipulator can also be employed to track a reference trajectory $d^*(t)$ rather than a constant position. In case of perfect tracking of the reference, the manipulator influences the lateral and vertical dynamics of the vehicle by applying disturbances d_x and d_y , which turn out to be proportional to $(m/M)d^*(t)$. Since $m \ll M$, the influence of the manipulator on the vehicle motion can be reasonably ignored in all free-flight operations. Interestingly, this property implies that during all free-flight operations, the manipulator can be controlled without considering its influence on the aerial base; hence, the aerial vehicle and the manipulator can be controlled separately.

Docking Scenario

In the docking scenario, the goal is to stabilize the end effector in contact with the vertical surface. With an eye on Figure 5, this can be achieved by properly choosing the set points x^* and d^* in such a way that the desired end effector position $x_{ee}^* := x^* + d^* + r$ is greater than \bar{x} . This fact implies that the end effector in finite time impacts the vertical surface, and then the contact force f_c is

applied to it. In this condition, the stability properties of the system can be investigated by analyzing the overall cascade interconnection of the environment, the manipulator, and the vertical and lateral dynamics that are shown in Figure 4. By taking advantage of the passivity properties of the closed-loop system, an impedance controller is implemented [21] to regulate either the applied forces to the environment or the final equilibrium configuration. This is achieved by properly choosing the desired lateral and manipulator set points, and the stiffness of the passivity-based controllers to shape the disturbance response of the closed-loop system, i.e., the effects of the controlled aerial manipulator in the presence of the contact force f_c .

Experimental Validation

The overall system architecture, used to perform the experiments for the validation of the proposed passivity-based control law, is shown in Figure 7.

The aerial platform, i.e., the Pelican quadrotor, is equipped with an inertial measurement unit, which provides information about the roll, pitch, and yaw angles of the vehicle. In addition, a built-in controller regulates the attitude, the angular speed of the yaw angle, and the overall thrust. This controller

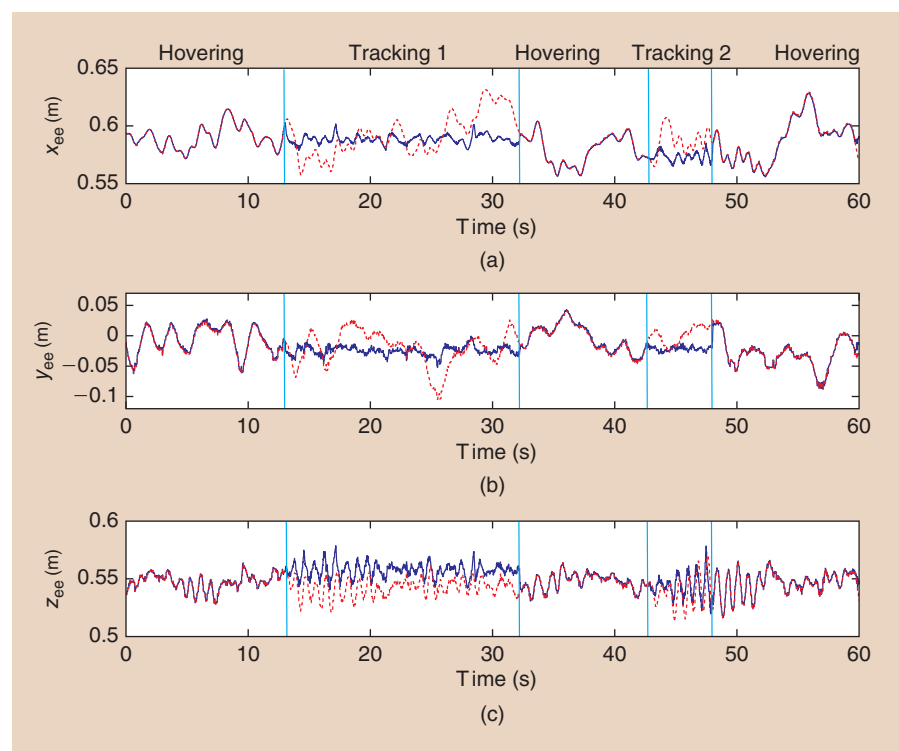


Figure 8. The tracking of a fixed point p_{ee} in the inertial frame. The figure compares the performances of the aerial manipulator while tracking a fixed point p_{ee} either by means of a manipulator used as a rigid tool or by exploiting the manipulator's DoF. When the system is hovering, the manipulator is used as a rigid tool. When the tracking task starts (corresponding to an external user input from a joystick interface), the manipulation system is controlled. The blue line corresponds to the motion of the end effector in the inertial frame F_i , while the red dashed line corresponds to the motion of the manipulator as a rigid tool. (a) The x coordinate of the end effector with respect to the inertial frame F_i . (b) The y coordinate of the end effector with respect to the inertial frame F_i . (c) The z coordinate of the end effector with respect to the inertial frame F_i .

runs on an on-board ATOM processor of 1.6 GHz and 1 GB of RAM, and it can be tuned to obtain sufficiently fast closed-loop attitude dynamics to support the cascade control approach adopted in this article. The robotic manipulator is endowed with a custom-made electronic board, which runs

the low-level control.

Stability has to be preserved even in the presence of disturbances derived from physical interaction.

Canada), runs on the ground station, with Linux as the operating system. The communication between the different software modules is performed using the robot operating system. The low-level control of both the aerial vehicle and the robotic manipulator communicates with the ground station over a Wi-Fi data link (802.11n standard).

Experiment 1: Tracking a Fixed Point

As previously discussed, two main experiments have been performed on the aerial manipulator.

The first experiment consists of tracking a point p_{ee}^* , which is fixed in the workspace with respect to the inertial frame F_i . Two different cases are compared: 1) the manipulation system is kept rigid at a certain configuration as if it were a rigid tool, meaning that there is no relative motion between F_{ee} and F_m , and 2) the manipulation system is exploited in all of its 6 DoF, i.e., three active DoF of the delta structure and three passive DoF of the end effector. More precisely, this means that only the relative linear motion between F_{ee} and F_m can be controlled.

In case 1, by controlling the quadrotor with (6) and keeping the manipulator rigid, small linear and angular displace-

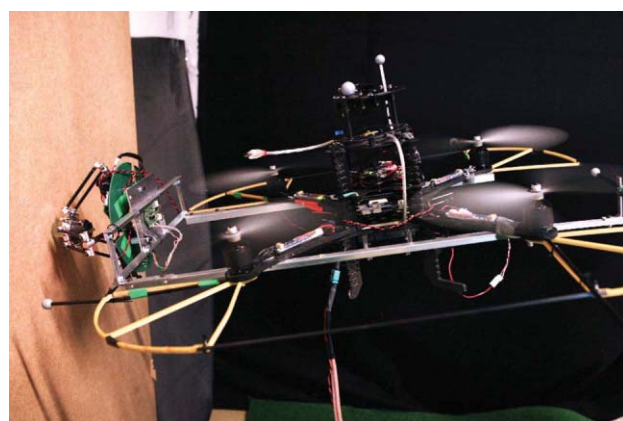


Figure 9. An AscTec Pelican quadrotor interacts with a wall by means of the manipulation system. The Ascending Technologies (AscTec) Pelican is developed by AscTec GmbH, <http://www.asctec.de>. (Photo courtesy of the Robotics and Mechatronics Lab at the University of Twente.)

Table 1. Tracking errors of the manipulation system used as a rigid tool and as a controlled manipulator.

	\bar{e}_x (mm)	\bar{e}_y (mm)	\bar{e}_z (mm)	$\ \bar{e}\ $
Rigid tool	0.92	4.9	-15	34
Manipulator	-0.18	0.34	0.97	9.3
	σ_x (mm)	σ_y (mm)	σ_z (mm)	$\sigma\ \bar{e}\ $
Rigid tool	16	28	8.0	14
Manipulator	3.9	7.7	6.2	5.3

ments due to the attitude and position control lead to large displacements of the end effector with respect to the fixed point p_{ee}^* . In case 2, the manipulator is also controlled and, therefore, it can compensate for the linear position tracking errors introduced by the vehicle and, therefore, it enhances the performances of the tracking of the fixed point p_{ee}^* .

As discussed in the “System Model” section, since the mass of the end effector and of the links of the manipulator is small compared with the mass of the quadrotor, the influence of the motion of the robotic manipulator on the dynamics of the aerial vehicle can be reasonably neglected.

Different stages of the experiment are shown in Figure 8. At the beginning, the system is hovering, i.e., the quadrotor’s CG is controlled in a certain position of the inertial frame F_i , while the manipulator is kept rigid with respect to its base. After this phase, the manipulator is also controlled and, while the quadrotor is still hovering, the end effector of the manipulator starts tracking the fixed point p_{ee}^* .

The experiment has been repeated several times, and the data are reported in Table 1. The results show a lower tracking error when the manipulator is controlled and not used as a

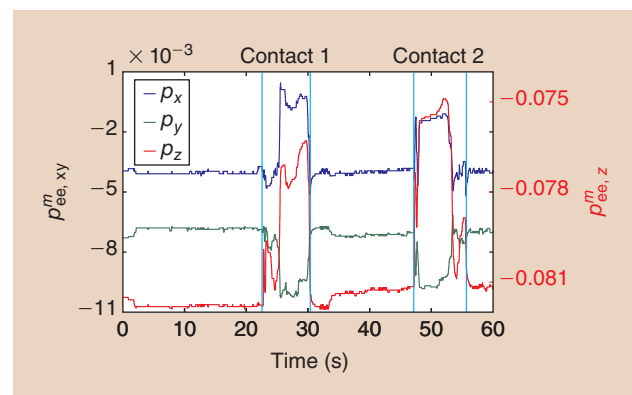


Figure 10. The figure represents the position $p_{ee}^m := [x_{ee}^m, y_{ee}^m, z_{ee}^m]$ of the end effector, expressed in the local manipulator base frame F_m during the interaction with a wall. The end effector position, initially in a certain configuration, responds to the forces produced by the wall during the contact, with a displacement. The end effector responds to external perturbation in a compliant manner, due to the low-level joint impedance control behavior. The motion of the end effector is estimated through the forward kinematics, from the measured encoder angles.

rigid tool. Figure 8 shows the overall motion that the manipulator needs to perform to track the fixed point p_{ee}^* . The coordinates x_{ee}^m , y_{ee}^m and z_{ee}^m of the end effector, with respect to the local base frame F_m , are shown. Note that the range of motion of the manipulator is within its reachable workspace.

Experiment 2: Contact

In the second experiment, the system is controlled to realize an interaction with a vertical wall by means of the robotic manipulator, as shown in Figure 9.

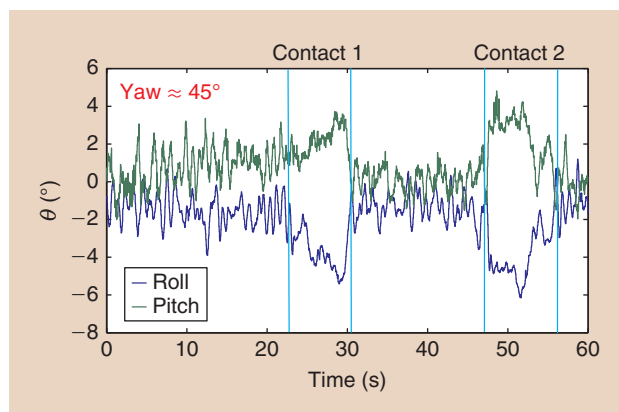


Figure 11. The measured attitude of the quadrotor at the reference frame F_b : during the task, the yaw reference of the Pelican is set to 40° to have the manipulator reference frame F_b axes parallel to (but not oriented as) the inertial frame F_i axes. Note the importance of the attitude regulation to counteract the contact force.

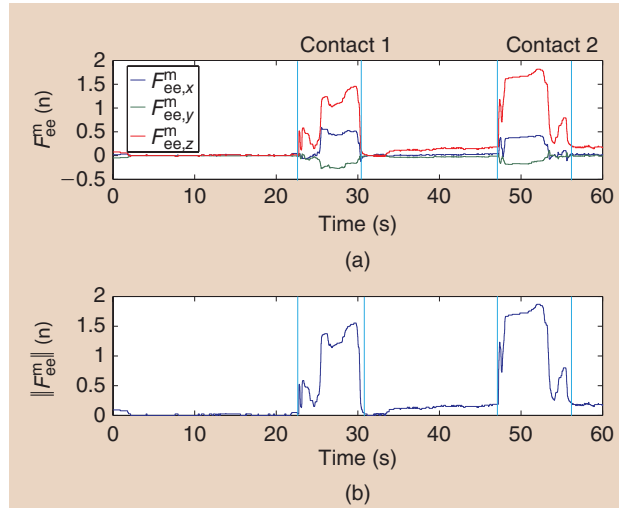


Figure 12. The contact forces during the interaction task are estimated. (a) The three components of the estimated external force during the task. The forces have been estimated off-line using the displacements from the reference position of the joint angles, while the manipulator is governed by the impedance control, and the knowledge on the model and on the control gain. (b) The norm of the overall force acting at the end effector. Note that between the two contacts, a certain amount of force is estimated, even though there is not a real contact. The reason for that comes from the joint friction that is not completely compensated, thus generating some joint position error that results in a small amount of residual force after interaction.

During the experiment, the quadrotor approaches a vertical surface, placed at about $\bar{x} = 1.2$ m. The reference position of the robotic manipulator is fixed with respect to F_m . A reference position is set to the quadrotor, such that the system enters in contact with the wall. When the system touches the wall, the robotic manipulator moves as a consequence of the intrinsic compliance of the low-level control and of the intrinsic compliance of its end effector. By design, the impedance behavior of the quadrotor generates a virtual force on the vehicle that depends on its position and velocity error.

Due to the interaction with the surface, a displacement of the joints of the manipulator, which is impedance controlled, can be observed. Figure 10 shows the coordinates x_{ee}^m , y_{ee}^m , and z_{ee}^m of the end effector, estimated using the joint angles and the forward kinematic of the delta structure, expressed in the local manipulator base frame F_m .

Figure 11 shows the attitude angle θ of the quadrotor when a certain contact force arises between the wall and the aerial manipulator at the end effector. When the reference position of the quadrotor is such that the manipulator impacts the wall, the position tracking error increases due to the constraint introduced by the environment, i.e., the wall. Due to the impedance behavior that characterizes the controlled system, the aerial manipulator tries to reduce the tracking error by generating actuation forces, which imitate the effect of an equivalent mass-spring-damper system between the actual position and the reference position. From the figure, it is clear that the quadrotor contributes with both roll and pitch motion to the generation of the actuation force and, as a consequence, to guarantee the interaction force between the end effector and the wall. If the attitude angles remain limited in their range, the aerial manipulator does not lose controllability and the system remains stable in interaction, as long as the propellers rotation is not disturbed.

Figure 12 shows an estimation of the interaction forces at the end effector, in x , y , and z with respect to the manipulator frame F_m . The force estimation values have been computed by using the displacements from the reference position of the joint angles and the knowledge on the system model and of the control gains. Note that to guarantee this force against the wall, the quadrotor is tilted by the controller to compensate for the reaction forces and then enforce a stable equilibrium.

Conclusions

This article presented the design, modeling, and control of an innovative aerial vehicle, the aerial manipulator, deriving from the combination of a quadrotor helicopter with a robotic manipulator. After investigating the interaction between the aerial vehicle, the manipulator, and the environment, a control

The prototype of the robotic manipulator has been designed to perform Cartesian movements.

strategy able to handle both the case in which the end effector is in contact or not with the environment has been proposed. The effectiveness of the overall design is then evaluated in two main experiments. The first considers a free-flight scenario, in which the end effector is required to track a constant reference position. The second considers a docking maneuver, in which the aerial manipulator exerts forces on the environment.

References

- [1] E. Feron and E. Johnson, "Aerial robotics," in *Handbook of Robotics*, B. Siciliano and O. Khatib, Eds. New York: Springer-Verlag, 2008, pp. 1009–1027.
- [2] P. Pounds, R. Mahony, and P. Corke, "Modelling and control of a quadrotor robot," in *Proc. Australasian Conf. Robotics Automation*, 2006.
- [3] S. Bouabdallah and R. Siegwart, "Design and control of a miniature quadrotor," in *Advances in Unmanned Aerial Vehicles*. New York: Springer-Verlag, 2007, ch. 6.
- [4] V. Gavrilets, "Aerobatic maneuvering of miniature helicopters," Ph.D. dissertation, Dept. Aeronaut. Astron., Massachusetts Inst. Technol., Cambridge, MA, 2003.
- [5] J. Pfleimlin, P. Soueres, and T. Hamel, "Hovering flight stabilization in wind gusts for ducted fan UAV," in *Proc. IEEE Int. Conf. Decision Control*, 2004, pp. 3491–3496.
- [6] M. W. Spong, *Underactuated Mechanical Systems*. New York: Springer-Verlag, 1998.
- [7] N. Michael, J. Fink, and V. Kumar, "Cooperative manipulation and transportation with aerial robots," in *Autonomous Robots*, New York: Springer-Verlag, 2010.
- [8] Q. Lindsey, D. Mellinger, and V. Kumar, "Construction of cubic structures with quadrotor teams," in *Proc. Robotics: Science Systems Conf.*, 2011.
- [9] A. Desbiens and M. Cutkosky, "Landing and perching on vertical surfaces with microspines for small unmanned air vehicle," *J. Intelli. Robot. Syst.*, vol. 1, no. 4, pp. 313–327, 2009.
- [10] A. Frank, J. McGrew, M. Valenti, D. Levine, and J. How, "Hover, transition, and level flight control design for a single-propeller indoor airplane," in *Proc. AIAA Guidance, Navigation Control Conf.*, 2007, pp. 1–18.
- [11] A. Albers, S. Trautmann, T. Howard, T. Nguyen, M. Frietsch, and C. Sauter, "Semi-autonomous flying robot for physical interaction with environment," in *Proc. IEEE Int. Conf. Robotics Automation Mechatronics*, 2010, pp. 441–446.
- [12] L. Marconi, R. Naldi, and L. Gentili, "Modeling and control of a flying robot interacting with the environment," *Automatica*, vol. 47, no. 12, pp. 2571–2583, 2011.
- [13] P. Pounds, D. Bersak, and A. Dollar, "Grasping from the air: Hovering capture and load stability," in *Proc. IEEE Int. Conf. Robotics Automation*, 2011, pp. 2491–2498.
- [14] C. Korpela, T. Danko, and P. Oh, "MM-UAV: Mobile manipulating unmanned aerial vehicle," *J. Intelli. Robot. Syst.*, vol. 65, nos. 1–4, pp. 93–101, 2012.
- [15] L. Marconi, L. Basile, G. Caprari, R. Carloni, P. Chiacchio, C. Huerzeler, V. Lippiello, R. Naldi, J. Nikolic, B. Siciliano, S. Stramigioli, and E. Zwicker, "Aerial service robotics: The AIRobots perspective," in *Proc. Int. Conf. Applied Robotics Power Industry*, 2012, pp. 64–69.
- [16] A. Keemink, M. Fumagalli, S. Stramigioli, and R. Carloni, "Mechanical design of a manipulation system for unmanned aerial vehicles," in *Proc. IEEE Int. Conf. Robotics Automation*, 2012, pp. 3147–3152.
- [17] M. Fumagalli, R. Naldi, A. Macchelli, R. Carloni, S. Stramigioli, and L. Marconi, "Modeling and control of a flying robot for contact inspection," in *Proc. IEEE/RSJ Int. Conf. Intelligent Robots Systems*, 2012, pp. 1943–1948.
- [18] J. Scholten, M. Fumagalli, S. Stramigioli, and R. Carloni, "Interaction control of an UAV endowed with a manipulator," in *Proc. IEEE Int. Conf. Robotics Automation*, 2013, pp. 4895–4900.
- [19] A. van der Schaft, *L2-Gain and Passivity Techniques in Nonlinear Control*. New York: Springer-Verlag, 2000.
- [20] A. Isidori, L. Marconi, and A. Serrani, *Robust autonomous guidance: An internal model approach* (Series Advances in Industrial Control). London: Springer-Verlag, 2003.
- [21] N. Hogan, "Impedance control: An approach to manipulation: Part III," *ASME J. Dyn. Syst. Meas. Control*, vol. 107, no. 1, pp. 1–24, 1985.
- [22] M. Reyhanoglu, A. van der Schaft, N. McClamroch, and I. Kolmanovsky, "Dynamics and control of a class of underactuated mechanical systems," *IEEE Trans. Autom. Contr.*, vol. 44, no. 9, pp. 1663–1671, 1999.
- [23] R. Olfati-Saber, "Nonlinear control of underactuated mechanical systems with application to robotics and aerospace vehicles," Ph.D. dissertation, Dept. Electr. Eng. Comput. Sci., Massachusetts Inst. Technol., Cambridge, MA, 2001.
- [24] R. Murray, *A Mathematical Introduction to Robotic Manipulation*. Boca Raton, FL: CRC Press, 1994.
- [25] Y. Xu, *Space Robotics: Dynamics and Control*. Norwell, MA: Kluwer, 1993.
- [26] A. Isidori, *Nonlinear Control Systems II* (Series Communication and Control Engineering Series). London: Springer-Verlag, 1998.
- [27] R. Ortega, A. van der Schaft, I. Mareels, and B. Maschke, "Putting energy back in control," *IEEE Control Syst. Mag.*, vol. 21, no. 2, pp. 18–33, 2001.
- [28] B. Brogliato, *Nonsmooth Mechanics Model, Dynamics and Control*. New York: Springer-Verlag, 1996.
- [29] H. K. Khalil, *Nonlinear Systems*. Englewood Cliffs, NJ: Prentice Hall, 1996.

Matteo Fumagalli, Faculty of Electrical Engineering, Mathematics, and Computer Science, University of Twente, The Netherlands. E-mail: m.fumagalli@utwente.nl.

Roberto Naldi, Faculty of Engineering, University of Bologna, Italy. E-mail: roberto.naldi@unibo.it.

Alessandro Macchelli, Faculty of Engineering, University of Bologna, Italy. E-mail: alessandro.macchelli@unibo.it.

Francesco Forte, Faculty of Engineering, University of Bologna, Italy. E-mail: francesco.forte@unibo.it.

Arvid Q.L. Keemink, Faculty of Electrical Engineering, Mathematics, and Computer Science, University of Twente, The Netherlands. E-mail: a.q.l.keemink@utwente.nl.

Stefano Stramigioli, Faculty of Electrical Engineering, Mathematics, and Computer Science, University of Twente, The Netherlands. E-mail: s.stramigioli@utwente.nl.

Raffaella Carloni, Faculty of Electrical Engineering, Mathematics, and Computer Science, University of Twente, The Netherlands. E-mail: r.carloni@utwente.nl.

Lorenzo Marconi, Faculty of Engineering, University of Bologna, Italy. E-mail: lorenzo.marconi@unibo.it.

FILOSE for Svenning

A Flow Sensing Bioinspired Robot



© ISTOCKPHOTO.COM/NICOLAO

By Otar Akanyeti, Jennifer C. Brown, Lily D. Chambers,
Hadi el Daou, Maria-Camilla Fiazza, Paolo Fiorini, Jaas Ježov,
David S. Jung, Maarja Kruusmaa, Madis Listak, Andrew Liszewski,
Jacqueline L. Maud, William M. Megill, Lorenzo Rossi,
Antonio Qualtieri, Francesco Rizzi, Taavi Salumäe, Gert Toming,
Roberto Venturelli, Francesco Visentin, and Massimo De Vittorio

The trend of biomimetic underwater robots has emerged as a search for an alternative to traditional propeller-driven underwater vehicles. The drive of this trend, as in any other areas of bioinspired and biomimetic robotics, is the belief that exploiting solutions that evolution has already optimized leads to more advanced technologies and devices. In underwater robotics, bioinspired design is expected to offer more energy-efficient, highly maneuverable,

Digital Object Identifier 10.1109/MRA.2014.2322287

Date of publication: 10 September 2014

agile, robust, and stable underwater robots. The 30,000 fish species have inspired roboticists to mimic tuna [1], rays [2], boxfish [3], eels [4], and others. The development of the first commercialized fish robot Ghostswimmer by Boston Engineering and the development of fish robots for field trials with specific applications in mind (<http://www.roboshoal.com>) mark a new degree of maturity of this engineering discipline after decades of laboratory trials.

So far, all fish robots have been equipped with off-the-shelf robotic sensors, such as cameras and sonars, whereas real fish have a dedicated sensing organ, the lateral line, for sensing flow. This sensing organ does not have a direct analogy in robotics. Neither do any of the human senses (e.g., smell and taste) have a direct counterpart to a flow sensor or even an English word for it (as there is for hearing or tasting). The word *svenning* was therefore proposed to describe flow sensing with the lateral line (in honor of Swedish biologist Sven Dijkgraaf [5]) [6]. Fish svenning is involved in a great variety of behaviors. Rheotactic behavior is navigation with respect to flow. Fish hold position or orient themselves toward or away from the current, and it is assumed that this behavior helps fish detect odors and food as well as possibly migrate upstream. Lateral line sensing helps fish catch prey by detecting the wake of a swimming fish [7]. It is also used in mediating schooling behavior and possibly helps with building cognitive flow maps. Tropomorphism (the reaction of the fish to flow stimuli) is common to all fish species [7].

All fish species and many sea mammals have flow-sensitive organs, but no underwater robot so far has made use of local flow sensing. Such an obvious discrepancy has inspired several research groups to develop artificial lateral line sensors [8] using different, often bioinspired, working principles. In [9], hot-wire anemometry-based flow sensors are used to detect a trail in still water left by a vibrating object (a so-called dipole source). A strongly bioinspired artificial flow sensor for flow speed detection is described in [10]. Whereas these artificial lateral line sensors are sensitive to flow speed (cantilever structures bending in flow), the sensors used to detect and identify the flow signatures of objects in [11] are pressure sensitive.

Traditionally, underwater robotics regards flow as a disturbance to be compensated by a vehicle's control algorithms. At the same time, biological evidence suggests that the ability to detect hydrodynamic events makes it possible to take advantage of the flow. An example is fishes' behavior in the periodic wake of a bluff object, where fish have been observed favoring certain hydrodynamically distinct locations. Fish swimming in those locations tire less quickly than those swimming in the steady flow. There are two behaviors that fish can exploit to reduce energy consumption in periodic turbulence. The first is the so-called Kármán gaiting, where fish adjust their tail beat frequency to the vortex shedding frequency of the object so that they can almost passively interact with the vortices. The second is the so-called flow refuging, where fish seek shelter in the object's hydrodynamic shadow in the reduced flow zone [12].

None of the underwater vehicles developed so far are capable of controlling themselves with respect to flow. Here we

describe, to the best of our knowledge, the design of the first flow-sensitive underwater robot capable of flow-aided control. This article is an overview of the project Fish Locomotion and Sensing (FILOSE). It describes the research methodology, summarizes the main findings, and discusses and interprets the results of the project and the bioinspired approach.

Method of Bioinspired Robot Design

The general goal of the FILOSE project was to understand how fish sense flow and react to the flow stimuli, extract the underlying principles of this interaction, and then build robots with minimal complexity that react to the flow in the same way.

According to a classification by [13], the FILOSE project used a solution-driven approach to bioinspired design. We first identified an interesting biological phenomenon: fish interaction with the flow and its implication for fish energy consumption. We then identified two core principles that led to robust and energy-efficient behavior in flow.

- 1) Fish have flow-sensitive organs that can perceive flow information. This led to the design of flow-sensitive sensor systems.
- 2) Fish have compliant bodies that make it possible to adjust their motion in vortices and use the environment to facilitate motion. This led to the design of a compliant soft-bodied robot.

The biological data were obtained from both the biology literature and experiments. The model animal used for the biological experiments was a rainbow trout. Fish behavior was recorded in a controlled hydrodynamic environment with a high-speed video camera and a digital particle image velocimetry (DPIV) system (Figure 1). Various flow conditions were investigated to measure the response of animals to variations in the sizes and strengths of wakes. The DPIV data and fish motion were later analyzed with the specially developed MathWorks freeware (<http://www.mathworks.com/matlabcentral/fileexchange/37323>).

An additional constraint posed to the bioinspired solution was the application of a reductionist approach: flow-relative behavior of an underwater robot with a minimal complexity of its mechanical design, sensor design, and control.

As is usually the case for research and development projects, the robot prototypes underwent several development stages in a frequent testing and developing cycle. The project also developed two alternative lateral line systems, only one of which was eventually tested onboard a moving robot.

Fish Robot Actuation

The underlying principle of the FILOSE mechanical design was the exploitation of the shape and material properties of the body to create mechanically simple but energetically favorable and robust robots. As such, we explored the extendibility of the soft robotics paradigm to underwater robotics. There are several successful examples of using the properties of soft materials to implement the principle of morphological computations—a design principle where the

design parameter space includes material properties and body geometry to reduce the system's complexity and increase robustness [14]. No underwater robots currently explicitly account for hydrodynamic effects to exploit the principles of morphological computation.

Direct application of a bioinspired design would imply replicating the highly distributed system of muscle fibers, which, with a current technology of electromechanical (EM) devices, would lead to large and complicated machines. Currently, the undulating motion of fish robots is achieved using serial chain kinematics of a caudal tail consisting of rigid links and rotational joints [1]–[4]. Those design approaches would contradict with our first identified design principle: using a soft and compliant body to facilitate interaction with flow. An alternative approach was first explored in [15], where the undulating motion was created with a soft body and a single motor. This article uses these findings and designs to build a bioinspired fish robot driven by a compliant part with some modifications to the mechanical design.

From a modeling point of view, a system with flexible links has infinite degrees of freedom. Unlike multibody rigid systems, exact solutions for modeling the dynamics are not feasible, so numerical methods are used instead. We extended the approach in [15] for modeling a nonhomogeneous body with the assumed modes method to derive the equations of motion. In contrast to [15] and [16], the modeling objectives are different: the model in [15] and [16] was developed to mimic the deformation of fish tails by taking the fish motion as an input and the torque amplitude as an output. In this article, the assumed method is used to derive the relationship between the applied forces/momenta and the resulting deformations. Our model predicted, in accordance with the theory of vibration, that a compliant body excited by an external force can deform in defined modes that are dependent on its actuation and natural frequencies. The use of a rigid plate for actuation and the effects of internal damping are considered. Lighthill's elongated body theory is used to model the interaction between the robot and the surrounding water [17]. When mimicking the geometry, stiffness, and stiffness distribution of a rainbow trout, the kinematics of the fish can be achieved when the tail is actuated only by a single servo motor [18]. This is consistent with biological findings suggesting that, at the cruising speeds of 1–2 body length per second (BL/s), a fish uses mainly the anterior muscles of its body while the rest of the tail is passive and functions as a carrier of the traveling wave [19]. Our experiments showed good agreement between the predicted and measured motions [17]. They also demonstrated that such a system, as expected, was most efficient when actuated at its natural frequencies. We, therefore, further adopted a control mechanism where the tail beat frequency was fixed and the swimming speed of the robot was controlled by changing the tail beat amplitude. Another option would be to vary the stiffness of the tail, which is currently left for future work. Biological evidence also shows that fish change their swimming speed by controlling the frequency, actuation amplitude, and body stiffness [20]. Thus,

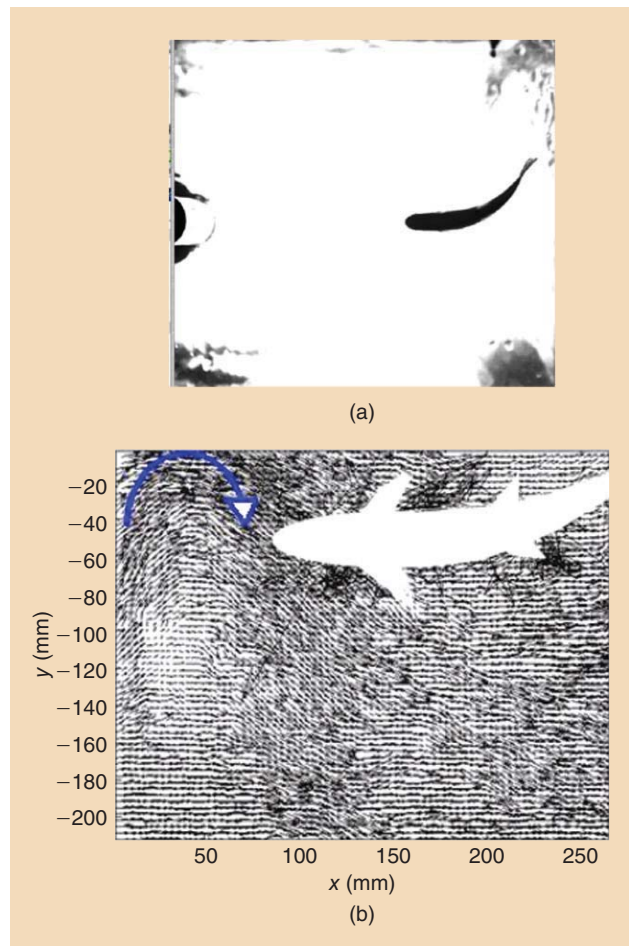


Figure 1. (a) A snapshot of a high-speed overview camera used to detect fish motion in a Kármán vortex street (KVS). A cylinder, partially visible on the left edge, is used to create periodic turbulence. (b) A DPIV image of the flow around a fish postprocessed to obtain the velocity vector field around the fish. The blue arrow indicates a vortex approaching the fish.

our simulations and experiments have implications for the soft-bodied robot design, showing that the kinematic envelope of a real fish is not always possible to achieve if the elasticity profile of the robot is static. The general theoretical framework developed for modeling a nonhomogeneous fin propulsor is, in the future, also suitable for analyzing the swimming modes of a swimmer with a stiffness control. A FILOSE robot prototype is shown in Figure 2, and its specifications are listed in Table 1. It consists of a rigid head and a compliant tail actuated by a servomotor that pulls two steel cables of an actuation plate. Flow sensors are mounted on the rigid head. Onboard data acquisition and servomotor control are implemented with an ARM processor with a Linux kernel. Flow sensing is analyzed in two dimensions, and, therefore, the robot has no buoyancy control. It is operated in a tethered mode to permit run-time debugging and data analysis.

Lateral Line Sensing

The sensing unit of a fish's lateral line is the neuromast, a hair cell that bends in the flow. The lateral line is a dual system

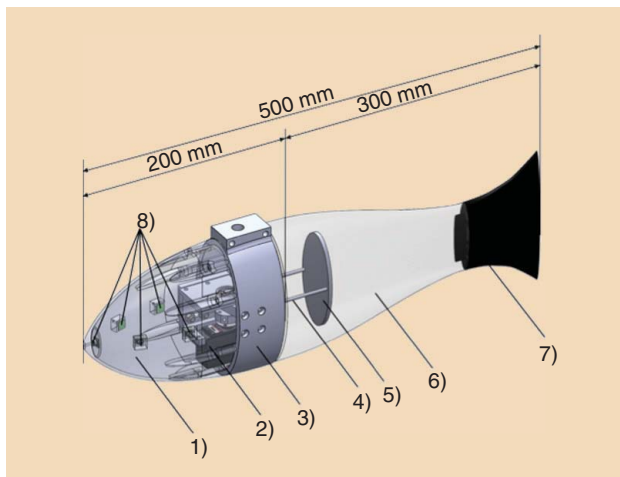


Figure 2. The FILOSE robot prototype. 1) Rigid head of the robot. 2) Servo-motor. 3) Middle section. 4) Steel cables. 5) Actuation plate. 6) Compliant tail. 7) Rigid fin. 8) Pressure sensors.

consisting of superficial and canal subsystems. Superficial neuromasts react to the flow speed on the surface of the fish's skin. Canal neuromasts are situated in the canals under the skin, and each of them measures the pressure difference between adjacent points where the canal emerges at the surface of the skin. This project has created several variations of two types of lateral line systems. The first type is based on microelectromechanical system (MEMS) stress-driven nitride-based bilayer design (Figure 3), equipped by a strain gauge. It consists of a multilayered cantilever beam, whose stress gradient along its cross section allows it to bend upward, mimicking a natural single hair cell of a neuromast in its EM characteristics and in its shape. Waterproofing is achieved by Parylene conformal coating. This Parylene encapsulation was demonstrated to be an efficient method to control the mechanical and sensory properties of a bioinspired artificial hair cell in a similar way as the natural hair cell [21]. The MEMS architecture easily adapts to flow variations due to its deformability in all points along

the cantilever beam and shows robustness up to 1 BL/s. These lateral line sensors have been demonstrated to respond to flow fluctuations in the air and water but have not yet been demonstrated on an underwater robot.

The other lateral line system consists of commercial pressure sensors, complemented by specialized acquisition electronics, to improve its sensitivity and accuracy (Figure 4). The sensors were mounted on the rigid head of the fish robot prototypes while the complexity of the sensor systems varied from a simple two-sensor system to a three-dimensional (3-D) lateral line consisting of 16 sensors. The two-sensor systems demonstrate two approaches to apply a biomimetic approach on a different level of abstraction. The first one (a MEMS cantilever-based lateral line) is an approach of more directly applying the biological analogy. It directly copies the sensor mechanics of a neuromast—an erect mechanical structure that bends in flow. Also, it has a similar height to a real superficial neuromast—just about the length to reach through the boundary layer.

The other system represents a bioinspired design on a more abstract level. At this level of the abstraction, the direct analogy to neuromasts does not matter and, in fact, is also not applied. Real fish do not have neuromasts that directly measure pressure; instead, the canal lateral line is realized by using flow-sensitive neuromasts embedded into a canal system. In contrast, our system uses sensors that measure absolute pressure, and this has no direct analogy in fish biology. As such, the bioinspired approach adopts the solution to the problem rather than a direct biological analogy [22]. In this case, the problem is more efficient control in flow and the solution is to use flow sensing.

Hydrodynamic Environments

Live fish as well as underwater field robots operate in complicated hydrodynamic environments with turbulence, currents, and waves. These environments are too complicated to use as a testbed for a developing technology, and they are difficult to quantify and control. We, therefore, limited our problem to simply reproducible but still sufficiently complex and variable environments of periodic turbulence. Periodic turbulence occurs behind bluff objects in flow at moderate Reynolds numbers. It is characterized by a distinct repeating pattern of swirling vortices, known as the KVS. On the one hand, KVS is a well-studied hydrodynamic effect that can be realized in laboratory conditions with high repeatability. On the other hand, it is also a sufficiently common natural phenomenon, appearing, for example, in rivers behind rocks or other objects obstructing the flow or in oceans on a global scale as gyres.

Under laboratory conditions, KVS is created in a flume where the stream is obstructed with a cylinder. A cylinder or half-cylinder creates a well-defined periodic wake, whose characteristics can be adjusted by changing the incoming laminar flow speed or the diameter of the cylinder. The turbulence patterns can be visualized using a DPIV system. The mean velocity field and its standard deviation, vorticity field, wake width, the location of the vortex formation point, vortex

Table 1. The FILOSE robot design specifications.

Length	0.5 m
Maximum width	0.085 m
Maximum height	0.156 m
Weight	3.04 kg
Motor	Futaba BLS152 brushless servo
Maximum torque	3 Nm
Controller	400-MHz ARM
Power source	External 24 V
Tail material	Dragon Skin 20 + Slacker additive by Smooth On
Young's modulus	83 kPa
Density	1,080 kg/m ³

shedding frequency, and wavelength are some of the features that can be extracted and visualized.

Figure 5(a) shows the schematic of the periodic turbulence together with the experimentally obtained DPIV image in Figure 5(b). Figure 5(c) and (d) shows postprocessed DPIV data that represents, respectively, the vorticity and the velocity values. In Figure 5(c), blue and red clearly show the street of opposite signed vortices. The velocity graph in Figure 5(d) shows the suction zone and the reduced flow zone behind the cylinder. The reduced flow zone is the energetically favorable place that fish have been observed to prefer.

Characterization of Hydrodynamic Environments and Detecting Hydrodynamic Events

To develop new control algorithms for our biomimetic robot, we first needed to analyze the hydrodynamic environments in which the robot was situated. The DPIV analysis of the flow field made it possible to visualize these environments globally from the observer's perspective, whereas the pressure recordings from the immersed platform provided a local picture of the flow from a situated perspective. This platform was static and attached on a force gauge, which gave information about the hydrodynamic forces acting on the platform [23]. The force measurements taken at different locations in the vortex streets showed that the magnitude of lateral forces (perpendicular to the flow stream) was significantly larger in vortex streets and the measurements were oscillating with the vortex shedding frequency. In contrast, the drag (force along the flow stream) was 42% less than the one measured in uniform flow. This drag reduction was mainly due to the shadowing effect of the cylinder. These measurements provided insights on what a mobile robot would experience in vortex streets.

By correlating pressure data with ground-truth DPIV data, we were able to identify distinct pressure cues that signaled interesting hydrodynamic events taking place around the robot. First, we identified vortex streets. The key feature that separates vortex streets from other flow regimes is the regular pattern of vortices in space and time [24]. This regularity was reflected in the pressure measurements and was identified through Fourier decomposition [24]. When the robot was in the vortex street, pressure readings from all of the sensors detected the vortex shedding frequency as the dominant frequency [Figure 6(a)]. The number of sensors having a consensus on the dominant frequency decreased gradually when the robot was systematically moved away from the vortex street. Besides analyzing absolute pressure measurements, we found it advantageous to compare pressure at different locations. For instance, the pressure difference between the nose and side sensors was distinct in vortex streets and uniform flows. In uniform flows, the pressure recordings from the nose sensor were higher than those from the side sensors, whereas, in vortex streets, the opposite was true [25] [Figure 6(b)]. When the robot was moved away from the vortex street laterally, the pressure difference between the nose and side sensors increased gradually with the distance and

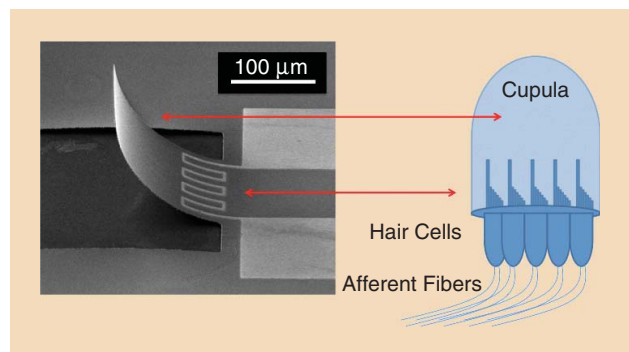


Figure 3. The bioinspired MEMS artificial lateral line flow sensor.

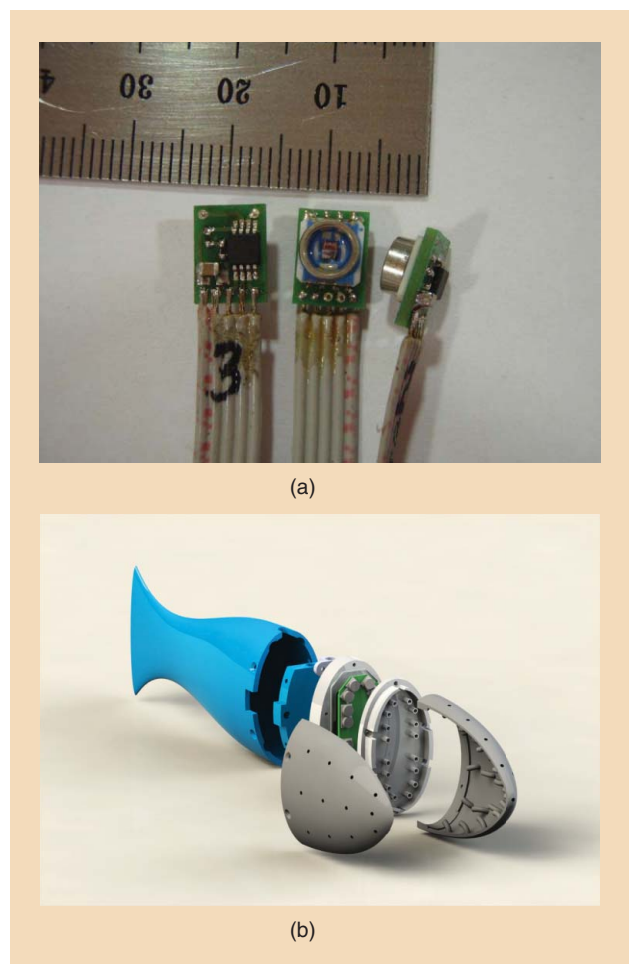


Figure 4. (a) The pressure sensors mounted on circuit boards with onboard electronics. The pressure sensors of an artificial lateral line use MS5407-AM diver's watch sensors by Intersema Sensoric SA. The sensing unit is connected as a Wheatstone bridge to give the sensor a high sensitivity of 56 mV/bar in the full scale (0–7 bar). We are using a 22-b differential analog-to-digital converter (ADC) with 124.5-mV reference voltage so that we can measure pressure with a least significant bit (LSB) of about (0.106 Pa). (b) The schematic of a fish robot prototype with a 3-D pressure-sensing lateral line.

finally reached normal values observed in uniform flows. The direction of motion (moving to the right or left) was determined by comparing the pressure values between the two sides of the robot.

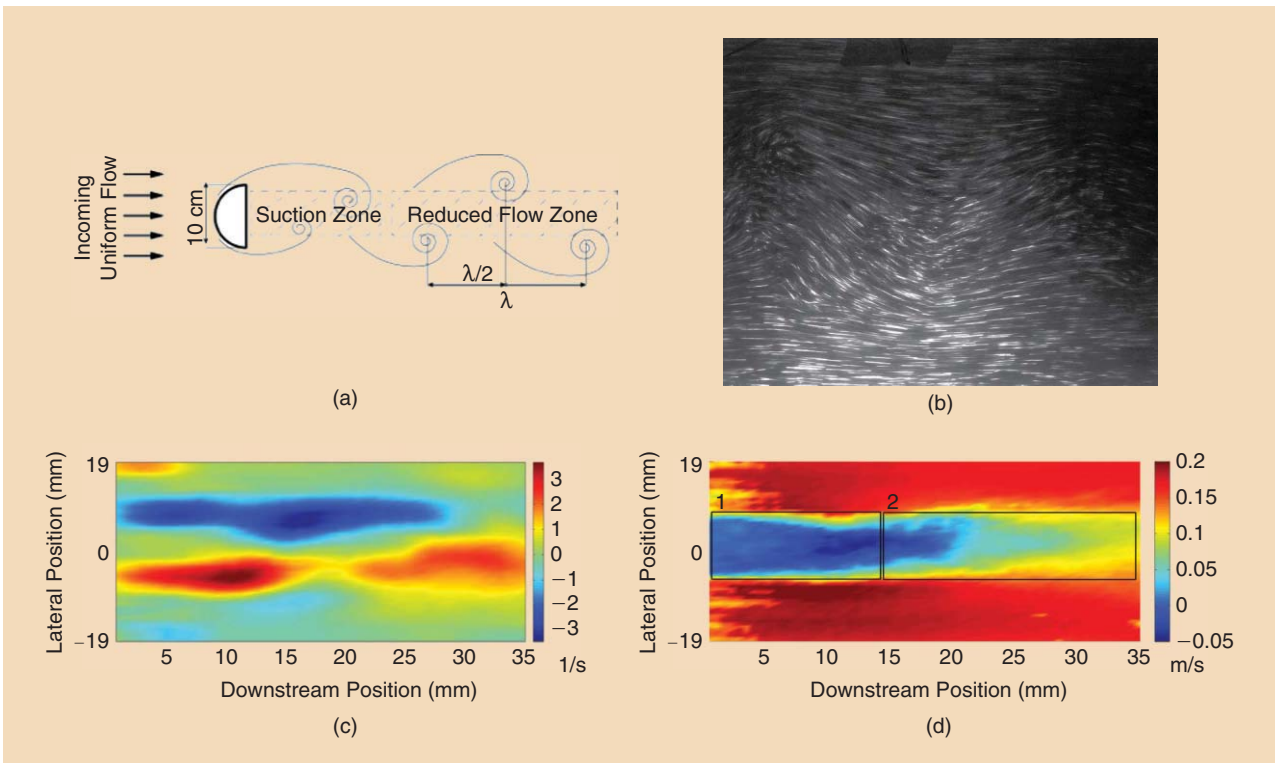


Figure 5. The KVS. (a) Schematics λ is the wavelength of the KVS. (b) A snapshot of a DPIV image of the flow obtained during fluid dynamics experiments. This data gets analyzed using (<http://www.mathworks.com/matlabcentral/fileexchange/37323>) and is an input for (c) and (d). (c) Instantaneous vorticity obtained from the DPIV image. The plot is obtained from two consequent DPIV snapshots, and a Gaussian filter is applied to smoothen the plot [25]. (d) Velocity readings averaged more than 10 s (500 frames obtained with 50-Hz frequency): 1) suction zone and 2) reduced flow zone.

After recognizing the presence of the vortex street, the next problem was to estimate the position and orientation of the robot with respect to the object's wake. The robot's distance from the cylinder was determined unambiguously by monitoring the turbulence intensity (calculated as the ratio of the standard deviation of the sensor readings to the mean value over an appropriate time window), and the amplitude of the dominant frequency [Figure 6(c)]. When the robot was moved closer to the suction zone, fewer sensors detected the vortex shedding frequency as the dominant frequency and the pressure at the tip of the robot was significantly lower. We found that the pressure difference between the left and right sensors was correlated with the orientation of the robot [Figure 6(d)].

Next, we extracted the robot's relative swimming velocity (i.e., flow velocity for a static robot) from the pressure measurements. In uniform flows, absolute pressure measurements as well as the pressure difference between the nose and side sensors increased quadratically with the flow velocity [24]–[26]. In vortex streets, we looked at the cross-correlation between sensor pairs randomly chosen from the same side of the robot. The peak values in the cross-correlation graphs indicated the amount of time required for a vortex to travel further down the body from one sensor to the next. The velocity of the vortex was then computed by dividing the distance between the two sensors to the estimated traveling time [27].

Up until now, our analysis was based on the pressure recordings obtained from a static robot configuration. To extract relevant flow information from the moving craft, we first need to understand how the pressure signals are impaired by the self-motion of the robot. For this purpose, we analyzed the motion of the robot in uniform flow by externally moving the robot with a robotic arm and recording pressure data and the robot's motion simultaneously. Two motion types were investigated: forward-backward motion along the direction of the flow and side-to-side motion perpendicular to the flow. We obtained two second-order polynomial models, which incorporated the position of the sensors, velocity, and acceleration of the robot to predict pressure distribution around the robot. The first model was presented in [26]. Through analysis of these models, we determined that, when the robot was moving with a velocity smaller than 0.2 BL/s, the self-motion effects on pressure sensing were negligible; the signal-to-noise ratio (the amplitude of pressure signals from hydrodynamic events divided by the amplitude of pressure signals generated by the self-motion of the robot) was adequate to characterize the hydrodynamic environments, as described in a static configuration. This method is also used to identify parameters of the hydrodynamic environment in the section “Flow-Aided Control and Navigation” (Experiment 5) for flow-aided control. However, at higher

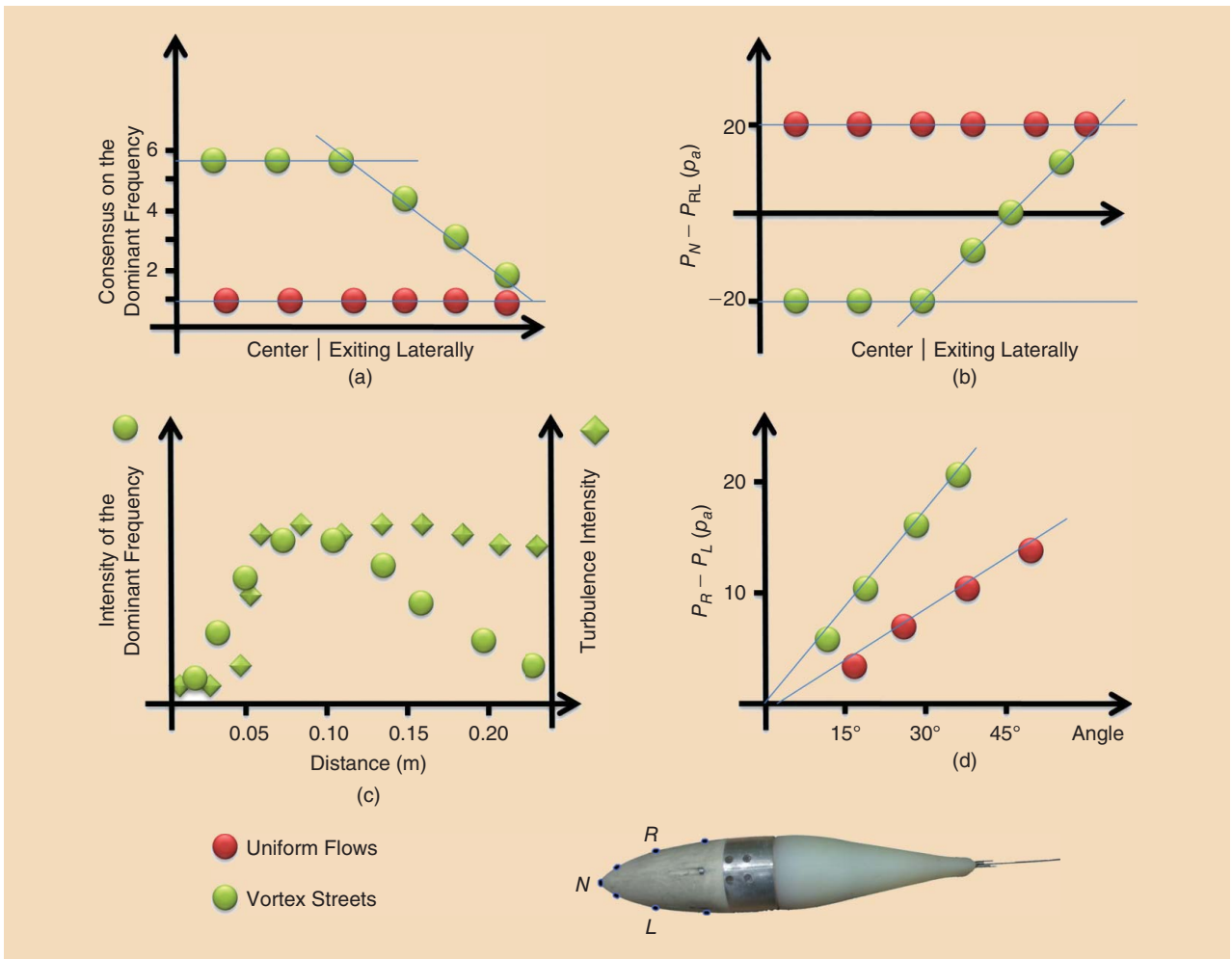


Figure 6. The pressure cues recorded from a robotic platform immersed in uniform flows (red-filled circle) and vortex streets (green-filled circle). (a) In vortex streets, most of the pressure signals were dominated by the vortex shedding frequency. The number of sensors detecting vortex shedding frequency decreased gradually when the robot was moved away from the vortex street. In contrast, in uniform flows, each pressure measurement had a different frequency with maximum amplitude, so there was no agreement among sensors. (b) The pressure difference between nose and side sensors is distinct between uniform flows and vortex streets. (c) Through an analysis of the turbulence intensity and amplitude of the dominant frequency, we were able to estimate the position of the robot with respect to the cylinder unambiguously. (d) The amplitude of the pressure difference between the right and left sides of the robot was linearly correlated to the robot's orientation with respect to the oncoming flow. The slope of the lines was different in uniform flows and vortex streets.

swimming velocities, the self-generated pressures would impair the perception of the environment. To minimize the self-motion effects, new filtering algorithms are needed so that external hydrodynamic events relevant to the robot's mission can be identified.

The robot's motion itself can be advantageous for sensing. For a stationary robot, the useful information has to be recovered from the analysis of a pressure pattern measured at one particular location. The moving robot can sample the hydrodynamic environment at multiple locations. By comparing multiple sensing patterns, it is possible to better evaluate the robot's current state. For instance, if the turbulence intensity and amplitude of the dominant frequency decrease as the robot moves from one arbitrary point to the next, we can deduce from Figure 6(c) that the robot would approach the cylinder. In Experiment 5, pressure gradients are used to guide the moving robots toward the control set point in the reduced flow zone.

Flow-Aided Control and Navigation

The experiments of flow-aided control of the FILOSE robot are conducted in uniform flow and in KVS in a flow tank, where the flow and the trajectories of the robot are recorded (Figure 7). The experimental setup is described in Figure 8. Experiments are conducted in a flow tunnel with a 0.5-m wide, 0.5-m high, and 1.5-m long working section. The robot is freely swimming but its motion is limited to two dimensions to permit trajectory tracking and motion analyses using an overview camera. The following experiments of flow-aided control were conducted.

Experiment 1: Detection of Flow Direction and Swimming Against the Flow

The direction of the uniform flow is detected by measuring the pressure difference between two sensors on the sides of the robot. A simple Braatenberg controller turns the robot

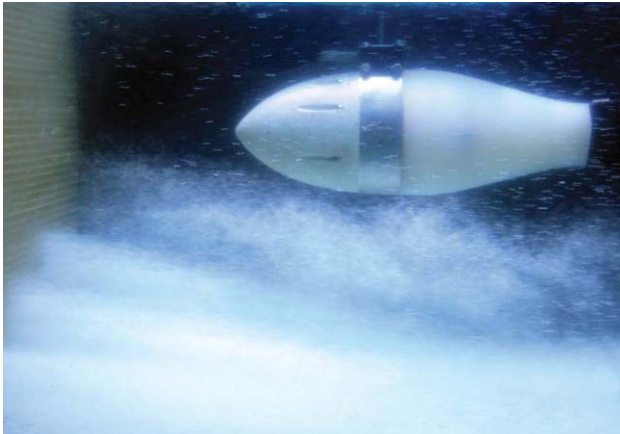


Figure 7. The FILOSE robot in flow in the DPIV flume pipe. The white dust is DPIV particles used to visualize the flow. A collimator, which is visible to the left, is used to create a uniform flow in the flow pipe. (Photo courtesy of the Centre of Biorobotics, Tallinn University of Technology)

toward the side with a higher pressure by adding an offset to the tail actuation signal. In uniform flow, two sensors and a simple Braatenberg controller were demonstrated to be sufficient to keep the fish robot oriented into the flow [28]. Figure 9 demonstrates the trajectories of the robot with and without feedback control and those compared with feedback control with the overview camera.

Experiment 2: Flow-Aided Trajectory Following

The robot in uniform flow uses a sideslipping maneuver. Sideslipping permits the robot to move laterally with respect to the incoming flow by exploiting its passive dynamics. Sideslipping is controlled by adjusting the heading of the robot

with respect to the flow when following a closed trajectory in a stream. A simple proportional-integral-derivative (PID) controller was implemented for controlling the motion of side slipping laterally and transversely [29]. Traditionally, when an underwater robot follows a trajectory, the coordinates of the waypoints are given in the global coordinates and also the speed of the robot is calculated with respect to Earth's reference frame. This experiment suggests that it is advantageous to know the flow-relative speed. It leads to reduced energy consumption and more stable trajectories. Figure 10(a) shows the trajectory of an underwater robot in the flow compared with the desired trajectory and the trajectory where the robot is not aware of the flow conditions (the standard case for underwater robot control). The average deviation from the desired trajectory is reduced by 3% for trajectory 1 (where the parallel flow disturbs the vehicle a little) and 82% for trajectory 2 where the flow is mostly perpendicular to the desired trajectory. Figure 10(b) shows a more complicated case of following a closed trajectory in the flow that the robot traverses without sharp turns in the waypoints.

Experiment 3: Station-Holding in a Steady Stream

The robot estimated the flow speed from the pressure readings at the sides of the head. The flow speed is calibrated with respect to the sensor readings at 0 m/s velocity. We used these signals as short-term odometry to compensate for the downstream drift using a PID controller. Our experiments using the setup in Figure 8 showed that the odometry reading from pressure sensors estimated the robot's relative position with respect to the flow, with an accuracy less than one body length of the robot over a duration of 270 s with varying flow speeds. (The initial flow speed was 11 cm/s and it was increased after every 30 s by 1 cm/s up to 19 cm/s.) The

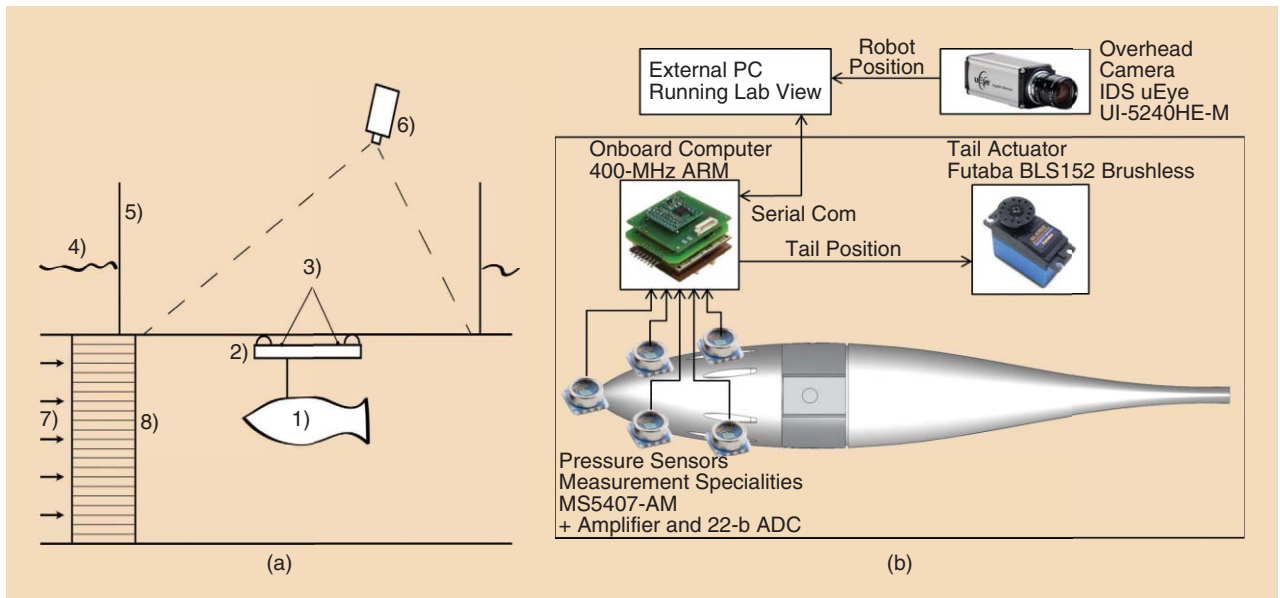


Figure 8. (a) The experimental setup [25] and side view of the flow tunnel. 1) Robotic fish. 2) Floater. 3) LEDs on the floater for position tracking. 4) Water level. 5) Transparent glass box on top of the tunnel for filming. 6) Camera for position tracking. 7) Flow direction. 8) Collimators. (b) Control schematics of the robot and the experiment.

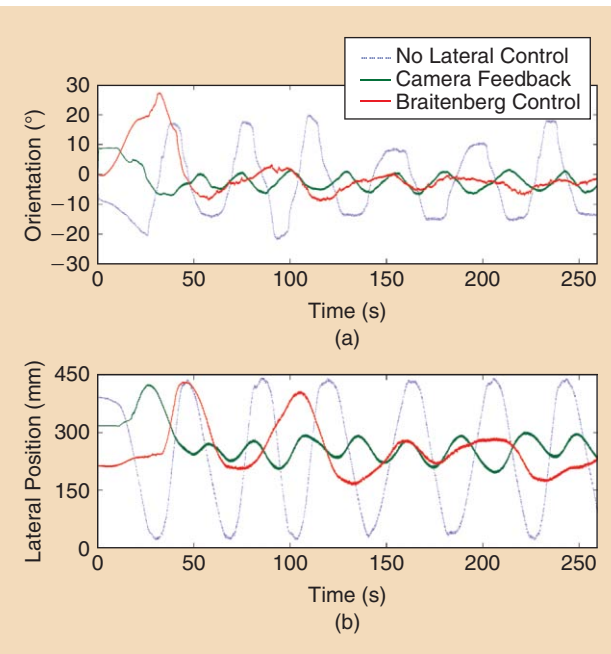


Figure 9. (a) The orientation and lateral displacement of the robot recorded with an overview camera [25]. (b) The robot is held in its longitudinal position with the feedback control from the camera for recording while the orientation is controlled by the Braitenberg controller using flow sensors or by the camera (for comparison). With no heading control, the robot is bouncing between the flow tank's walls (blue line) while the precision of the heading control based on flow sensing (red) and camera feedback (green) are almost comparable.

downstream drift at the end of the experiment was 1/5 of the robot's body length [25]. Currently, a standard method in underwater robotics is to use an acoustic Doppler current profiler (ADCP) to estimate the bulk flow speed. ADCPs are bulky, costly, and energy-consuming devices that are not suitable for small underwater vehicles. The lateral-line-based odometry can here provide a low-cost alternative for estimating the flow-relative speed and providing the velocity estimate in the absence of a global reference.

Experiment 4: Reducing Energy Consumption in Turbulence by Exploiting Vorticity

The experimental setup of this experiment is different than that shown in Figure 8 in that the robot is harnessed to a force plate for force measurements. The lateral line signals are used to control the tail beat timing. A motion pattern similar to Kármán gaiting is achieved by adjusting the frequency of the tail beat to the vortex shedding frequency and fine-tuning the tail beat timing. The tail bends against the high-pressure zone created by the vortex, and the robot takes advantage of the increased perpendicular component of the lift force created by pressure differences on both sides of the flexing tail (Figure 11). The results are compared with those of the tail fin propulsion in the steady flow with the same incoming flow speed. In comparison, 100% more thrust is created in KVS with the appropriate tail beat timing than in steady flow [30].

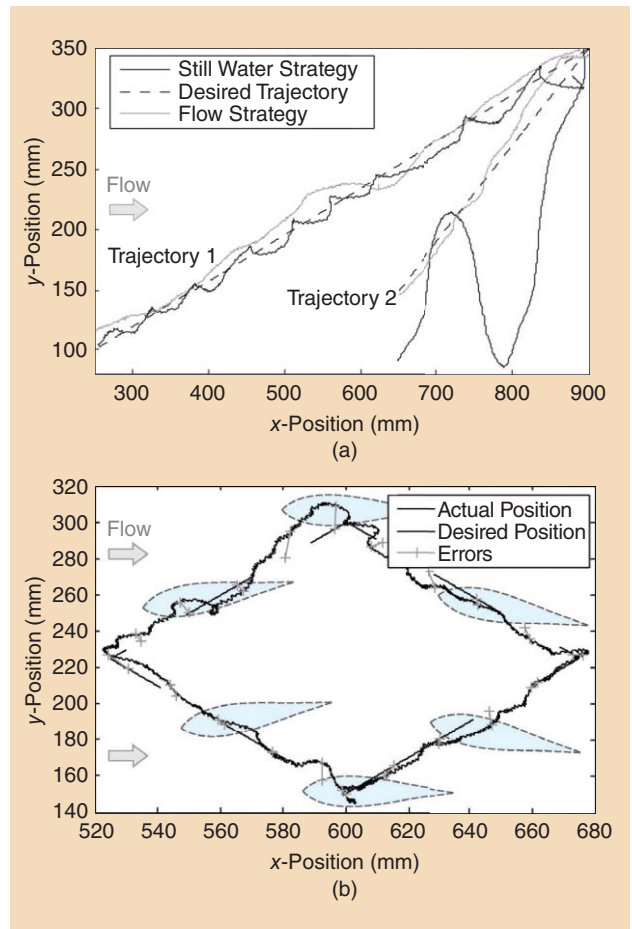


Figure 10. A flow-aided trajectory following [29]. (a) A straight line in the flow (dashed line) using the sideslipping maneuver and flow information (thin line) and without flow information (thick line). (b) A closed trajectory in the flow. Laminar flow is directed from left to right, and the robot's pose in the flow is marked in light blue.

Experiment 5: Reducing Energy Consumption by Holding Station in a Hydrodynamic Shadow

We first identified the reduced flow zone [zone 2 in Figure 5(d)] behind the object from DPIV images and adjusted the thresholds of pressure readings to identify the point of reference for station-holding. The robot compensates for the lateral and longitudinal drift using PID controllers and keeping the station in the hydrodynamic shadow. Monitoring the motor current consumption reveals that swimming in the reduced flow zone consumes 7% less energy behind the cylindrical object. The standard deviation of the downstream position behind the cylinder is 40.5 mm, and that of the lateral position is 12.7 mm. When the cylinder was replaced by the cuboid, creating a sharper pressure drop between the suction zone and the reduced flow zone, the energy consumption reduced by 17%. The standard deviation of the downstream position was 21.2 mm, and that of the lateral position was 13.3 mm in this experiment. The duration of both experiments was 270 s [25]. The trajectories of the robots are plotted in Figure 12.

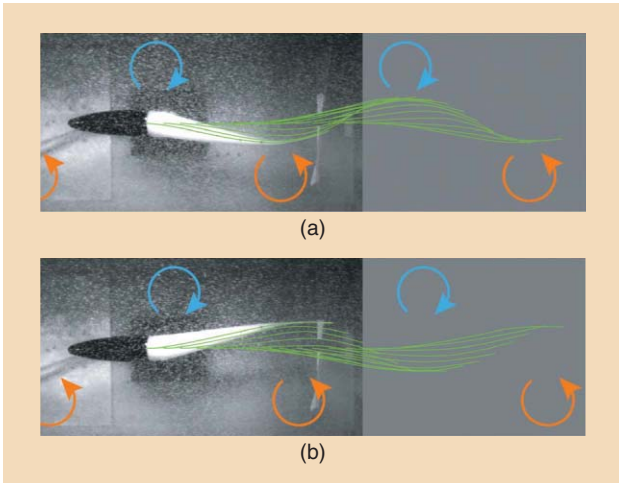


Figure 11. The fish tail position with respect to the vortex when the craft produces (a) max thrust and (b) minimal thrust.

Experiment 6: Comparative Experiments

Trajectories of a real fish and the robot were recorded in a uniform flow and when swimming behind in an object's wake. A swim path analysis to determine path tortuosity (as a measure of the complexity of the trajectory) was performed on data extracted from high-speed video recordings of four rainbow trout (*Oncorhynchus mykiss*) with a total body length (L) of 18 ± 3 cm swimming. Two different points on the fish midlines were used to track the path at 10 and 30% body length points, in flow speeds of 10, 20, and 30 cm/s and behind a range of cylinders with diameters of 2.5, 4.5, and 10 cm.

All fish species and many sea mammals have flow-sensitive organs, but no underwater robot so far has made use of local flow sensing.

Path tortuosity was determined from the fractal dimension or fractal d , one of a number of possible tortuosity estimators. Path analysis using the fractal dimension (D) data (estimated by the dividers method to determine the path length at varying step sizes) indicates that trout swimming in the unsteady KVS had a significantly

lower path tortuosity than the steady uniform flow ($P < 0.05, n = 45$). Within the KVS environment, the path tortuosity of the largest-cylinder-diameter swim paths was significantly lower than that of the smaller cylinder diameters ($P < 0.05, n = 45$). A similar decrease in path tortuosity was measured when comparing the robot's trajectories in uniform flow and behind the cylinder.

This suggests that the path tortuosity is influenced by the hydrodynamic forces in the environment. Fish and robots in KVS appear to have smoother trajectories than those in uniform flow. We hypothesize that the hydrodynamic forces within the KVS drive the fish/robot toward the center of the

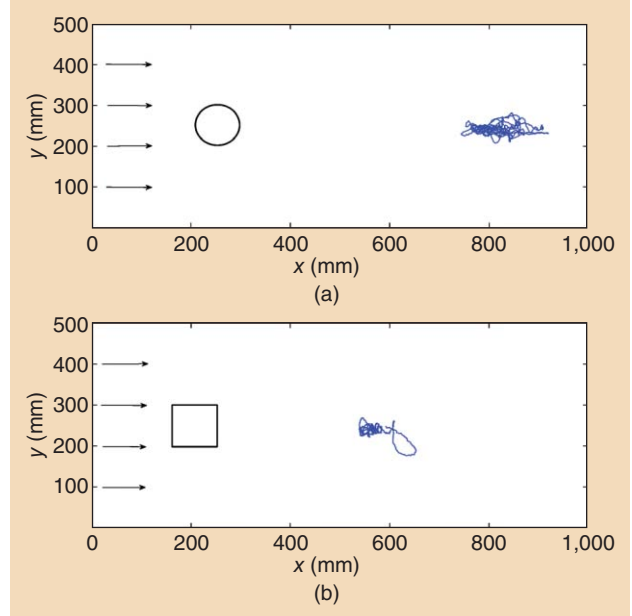


Figure 12. The center of mass trajectory of a robotic fish over 270 s in a reduced flow zone [Zone 2 in Figure 5(d)] generated by the (a) cylinder and (b) cuboid with the experimental setup in Figure 8 [25].

wake and thereby reduce the complexity of the trajectories, whereas, in the steady flow, the environment has no such environmental cues that help to stabilize the fish or the robot. This explanation is supported by measurements in [23], where we show that the drag profile in KVS has a single local minimum at the midline of the wake.

Discussion

Though all 30,000 fish species have a lateral line organ, so far, there have been no technological counterparts to lateral line sensing in use for controlling underwater robots. The contribution of this article is to give a new sense, svanning, to aid the control of underwater vehicles. Once flow can be perceived, it can be analyzed and exploited for a variety of purposes. Traditionally, flow is treated as a disturbance in underwater robotics, to be compensated by the vehicle's control algorithms. With flow sensing, flow becomes a source of information, and, with clever sensing–actuation coupling, flow becomes a source of energy. Flow information can be fused with other sensor modalities and used for vehicle control. Knowing flow direction and strength permits movement with respect to the flow-relative reference frame as opposed to the global reference frame.

Flow information can also be incorporated into higher-level behaviors. Salient flow features, such as wakes of objects or steady currents, could be identified and classified and used as landmarks. Again, this information can be fed into a vehicle's navigation algorithm and used for map building and localization. Flow sensing permits identification of flow conditions where a vehicle's control is more stable and energy efficient. Coupling of flow sensing and actuation opens up

new opportunities to exploit flow for energy-efficient motion. Flow-relative control could also make traditional rigid hull underwater robots more efficient, but there is more to gain from flow perception and robot–fluid interaction from small devices, with flexible fins or rudders.

This aligns flow-sensing robots with the increasingly popular trend of soft robotics. Hydrodynamic forces can be best exploited if the craft is continuous, flexible, and able to vary its stiffness to adapt to different conditions. For example, our FILOSE robot would need a stiffer tail to produce enough thrust in uniform flow and a floppy passive tail to bend in KVS between the vortices. Designing such a robot can be a challenging problem for mechanical engineering. Moreover, we still have a limited understanding of the theoretical foundations of coupled compliant body-fluid motion; the hydrodynamic effects in turbulence are complex and highly nonlinear and do not lend themselves well to real-time control. Our work shows that, in many cases, approximate linear control laws are sufficient, but it is unclear as to how well they scale up to more complicated tasks and environments.

Another challenge is to develop suitable lateral line sensors that would tremendously improve the perception and analysis of the fluid environment. Although several promising solutions exist, the FILOSE robot is the first one to exploit the lateral line sensors onboard a moving craft. The project developed in parallel two sensing systems, one based on MEMS technology and direct biological analogy, and another based on the commercial sensors and functional similarity. The first system was more complicated, and improving its reliability for onboard control is still an ongoing work. The other system was successfully demonstrated for control of the robot. However, its sensitivity does not compare with the one of the biological systems and may not be sufficient for complex real-world environments. For comparison, the sensitivity of fish canal lateral line neuromasts is four orders of magnitude higher than that of the FILOSE pressure sensors, which inevitably sets a limit to what the swimming robot can perceive compared with fish [31]. From the point of view of bioinspired design methodology, conclusions can be drawn for designing bioinspired robots in the future. The success of biologically inspired design critically depends on establishing an analogy at the appropriate level of abstraction [22]. This was well evident from comparing the application of two different flow-sensing systems as well as the design of the compliant tail, where functional similarity was preferred over a direct analogy of a real-fish highly distributed actuation system. Finally, the bioinspired locomotion and lateral line sensing offer possibilities to better understand how real fish sense the world and react to hydrodynamic stimuli and to use those findings to build better technology on the next development iteration. From the experiments conducted with the robot, we know what the flow looks like from the situated perspective and what information is there to sense. We also understand from comparative experiments as to how the stability and efficiency of the robot or a fish arise from the interplay with the environmental conditions. If a rigid methodology is used to conduct comparative experiments with fish

and robots, that will both enhance our understanding of nature and enable the development of better technology.

Acknowledgments

This work was financed by the European Commission 7th Framework program under FP7-ICT-2007-3 STREP project FILOSE. We would like to thank Prof. John Long from Vassar College and Prof. Thor I. Fossen from the Norwegian University of Science and Technology for their valuable feedback throughout the project.

References

- [1] D. Barrett, M. Grosenbaugh, and M. Triantafyllou, "The optimal control of a flexible hull robotic undersea vehicle propelled by an oscillating foil," in *Proc. Symp. Autonomous Underwater Vehicle Technology*, 1996, pp. 1–9.
- [2] K. H. Low, "Modelling and parametric study of modular undulating fin rays for fish robots," *Mech. Mach. Theory*, vol. 44, no. 3, pp. 615–632, 2009.
- [3] P. Kodati, J. Hinkle, A. Winn, and X. Deng, "Microautonomous robotic ostraciiform (MARCO): Hydrodynamics, design, and fabrication," *IEEE Trans. Robot.*, vol. 24, no. 1, pp. 105–117, 2008.
- [4] K. A. McIsaac and J. P. Ostrowski, "Experiments in closed-loop control for an underwater eel-like robot," in *Proc. IEEE Int. Conf. Robotics Automation*, 2002, vol. 1, pp. 750–755.
- [5] S. van Netten, Private communication. Groningen, The Netherlands, Nov. 2012.
- [6] S. Coombs, P. Görner, and H. Münz, *The Mechanosensory Lateral Line: Neurobiology and Evolution*. New York: Springer-Verlag, 1989.
- [7] J. Mogdans and H. Bleckmann, "Coping with flow: Behavior, neurophysiology and modeling of the fish lateral line system," *Biol. Cybern.*, vol. 106, nos. 11–12, pp. 627–642, 2012.
- [8] J. Tao and X. B. Yu, "Hair flow sensors: From bio-inspiration to bio-mimicking—A review," *Smart Mater. Struct.*, vol. 21, no. 11, p. 113001, 2012.
- [9] Y. Yang, J. Chen, J. Engel, S. Pandya, N. Chen, C. Tucker, S. Coombs, D. L. Jones, and C. Liu, "Distant touch hydrodynamic imaging with an artificial lateral line," *Proc. Natl. Acad. Sci.*, vol. 103, no. 50, pp. 18891–18895, 2006.
- [10] M. E. McConney, N. Chen, D. Lu, H. A. Hu, S. Coombs, C. Liub, and V. V. Tsukruk, "Biologically inspired design of hydrogel-capped hair sensors for enhanced underwater flow detection," *Soft Matter*, vol. 5, no. 2, pp. 292–295, 2009.
- [11] V. I. Fernandez, A. Maertens, F. M. Yaul, J. Dahl, J. H. Lang, and M. S. Triantafyllou, "Lateral-line-inspired sensor arrays for navigation and object identification," *Mar. Technol. Soc. J.*, vol. 45, no. 4, pp. 130–146, 2011.
- [12] J. Liao and A. Cotel, "Effects of turbulence on fish swimming in aquaculture," in *Swimming Physiology of Fish*, A. P. Palstra and J. V. Planas, Eds. Berlin Heidelberg, Germany: Springer-Verlag, 2013, pp. 109–127.
- [13] M. Helms, S. Vattam, and A. K. Goel, "Biologically inspired design: Process and products," *Des. Stud.*, vol. 30, no. 5, pp. 606–622, 2009.
- [14] R. Pfeifer, M. Lungarella, and F. Iida, "The challenges ahead for bioinspired 'soft' robotics," *Commun. ACM*, vol. 55, no. 11, pp. 76–87, 2012.
- [15] B. P. Epps, P. Valdivia y Alvarado, K. Youcef-Toumi, and A. H. Techet, "Swimming performance of a biomimetic compliant fish-like robot," *Exp. Fluids*, vol. 47, no. 6, pp. 927–939, 2009.
- [16] P. P. A. Valdivia y Alvarado, "Design of biomimetic compliant devices for locomotion in liquid environments," Ph.D. dissertation, Dept. Mech. Eng., Massachusetts Inst. Technol., Cambridge, MA, 2007.

- [17] H. E. Daou, T. Salumäe, L. D. Chambers, W. M. Megill, and M. Kruusmaa, "Modelling of a biologically inspired robotic fish driven by compliant parts," *Bioinspir. Biomim.*, vol. 9, no. 1, p. 016010, 2014.
- [18] T. Salumäe and M. Kruusmaa, "A flexible fin with bioinspired stiffness profile and geometry," *J. Bionic Eng.*, vol. 8, no. 4, pp. 418–428, 2011.
- [19] L. G. John, J. H. Long, M. J. McHenry, and N. C. Boetticher, "Undulatory swimming: How traveling waves are produced and modulated in sunfish (*Lepomis gibbosus*)," *J. Exp. Biol.*, vol. 192, no. 1, pp. 129–145, 1994.
- [20] M. J. McHenry, C. A. Pell, and J. H. Long, Jr., "Mechanical control of swimming speed: Stiffness and axial wave form in an undulatory fish model," *J. Exp. Biol.*, vol. 198, pp. 2293–2305, Nov. 1995.
- [21] F. Rizzi, A. Qualtieri, L. D. Chambers, W. M. Megillb, and M. de Vittorioac, "Parylene conformal coating encapsulation as a method for advanced tuning of mechanical properties of an artificial hair cell," *Soft Matter*, vol. 9, no. 9, pp. 2584–2588, 2013.
- [22] J. Yen and M. Weissburg, "Perspectives on biologically inspired design: Introduction to the collected contributions," *Bioinspir. Biomim.*, vol. 2, no. 4, 2007.
- [23] G. Toming, T. Salumae, A. Ristolainen, F. Visentin, O. Akanyeti, and M. Kruusmaa, "Fluid dynamics experiments with a passive robot in regular turbulence," in *Proc. IEEE Int. Conf. Robotics Biomimetics*, 2012, pp. 532–537.
- [24] O. Akanyeti, R. Venturelli, F. Visentin, L. Chambers, W. M. Megill, and P. Fiorini, "What information do Kármán streets offer to flow sensing?" *Bioinspir. Biomim.*, vol. 6, no. 3, p. 036001, 2011.
- [25] T. Salumäe and M. Kruusmaa, "Flow-relative control of an underwater robot," *Proc. Royal Soc. A: Math. Phys. Eng. Sci.*, vol. 469, no. 2153, pp. 20120671–20120671, 2013.
- [26] O. Akanyeti, L. D. Chambers, J. Ježov, J. Brown, R. Venturelli, M. Kruusmaa, W. M. Megill, and P. Fiorini, "Self-motion effects on hydrodynamic pressure sensing: Part I. Forward-backward motion," *Bioinspir. Biomim.*, vol. 8, no. 2, p. 026001, 2013.
- [27] R. Venturelli, O. Akanyeti, F. Visentin, J. Ježov, L. D. Chambers, and G. Toming, "Hydrodynamic pressure sensing with an artificial lateral line in steady and unsteady flows," *Bioinspir. Biomim.*, vol. 7, no. 3, p. 036004, 2012.
- [28] T. Salumae, I. Rano, O. Akanyeti, and M. Kruusmaa, "Against the flow: A Braatenberg controller for a fish robot," in *Proc. IEEE Int. Conf. Robotics Automation*, 2012, pp. 4210–4215.
- [29] D. Jung, P. Pott, T. Salumäe, and M. Kruusmaa, "Flow-aided trajectory following of an underwater robot," in *Proc. IEEE Int. Conf. Robotics Automation*, 2013, pp. 4602–4607.
- [30] J. Jezov, O. Akanyeti, L. D. Chambers, and M. Kruusmaa, "Sensing oscillations in unsteady flow for better robotic swimming efficiency," in *Proc. IEEE Int. Conf. Systems, Man Cybernetics*, 2012, pp. 91–96.
- [31] S. Netten, "Hydrodynamic detection by cupulae in a lateral line canal: Functional relations between physics and physiology," *Biol. Cybern.*, vol. 94, no. 1, pp. 67–85, 2006.

Otar Akanyeti, University of Verona, Italy (now with University of Florida, Gainesville). E-mail: otar@whitney.ufl.edu.

Jennifer C. Brown, University of Bath, United Kingdom. E-mail: j.c.brown@bath.ac.uk.

Lily D. Chambers, University of Bath, United Kingdom (now with University of Bristol, United Kingdom). E-mail: L.Chambers@bristol.ac.uk.

Hadi el Daou, Centre for Biorobotics, Tallinn University of Technology, Estonia (now with Imperial College London, United Kingdom). E-mail: hadi.eldaou@gmail.com.

Maria-Camilla Fiazza, University of Verona, Italy. E-mail: tokhami@gmail.com.

Paolo Fiorini, University of Verona, Italy. E-mail: pao.lo.fiorini@univr.it.

Jaas Ježov, Centre for Biorobotics, Tallinn University of Technology, Estonia. E-mail: jaas.jezov@ttu.ee.

David S. Jung, Centre for Biorobotics, Tallinn University of Technology (now with University of Nottingham, United Kingdom). E-mail: david.s.jung@web.de.

Maarja Kruusmaa, Centre for Biorobotics, Tallinn University of Technology, Estonia. E-mail: Maarja.Kruusmaa@ttu.ee.

Madis Listak, Marine Systems Institute, Tallinn University of Technology, Estonia. E-mail: Madis.Listak@ttu.ee.

Andrew Liszewski, University of Bath, United Kingdom. E-mail: andyliszewski@gmail.com.

Jacqueline L. Maud, Plymouth Marine Laboratory, United Kingdom (now with Plymouth Marine Laboratory). E-mail: jama@pml.ac.uk.

William M. Megill, University of Bath, United Kingdom (now with Rhine-Waal University of Applied Sciences, Germany). E-mail: william.megill@hsrw.eu.

Lorenzo Rossi, Italian Institute of Technology. E-mail: lorenzo.rossi@iit.it.

Antonio Qualtieri, Center for Bio-Molecular Nanotechnologies, Italian Institute of Technology. E-mail: antonio.qualtieri@iit.it.

Francesco Rizzi, Center for Bio-Molecular Nanotechnologies, Italian Institute of Technology. E-mail: francesco.rizzi@iit.it.

Taavi Salumäe, Centre for Biorobotics Tallinn University of Technology, Estonia. E-mail: Taavi.Salumäe@ttu.ee.

Gert Toming, Centre for Biorobotics Tallinn University of Technology, Estonia. E-mail: Gert.Toming@ttu.ee.

Roberto Venturelli, University of Verona, Italy. E-mail: venturelli.roberto@gmail.com.

Francesco Visentin, University of Verona, Italy. E-mail: francesco.visentin@univr.it.

Massimo De Vittorio, University of Salento and Italian Institute of Technology, Italy. E-mail: massimo.devittorio@unisalento.it.



© ISTOCKPHOTO.COM/PALTO

Survey of Geodetic Mapping Methods

*Geodetic Approaches
to Mapping and
the Relationship to
Graph-Based SLAM*

By Pratik Agarwal, Wolfram Burgard,
and Cyrill Stachniss

The ability to simultaneously localize a robot and build a map of the environment is central to most robotics applications, and the problem is often referred to as simultaneous localization and mapping (SLAM). Robotics researchers have proposed a large variety of solutions allowing robots to build maps and use them for navigation. In addition, the geodetic community has addressed large-scale map building for centuries, computing maps that span across continents. These large-scale mapping processes had to deal with several challenges that are similar to those of the robotics community. In this article, we explain key geodetic map building methods that we believe are relevant for robot mapping. We also aim at providing a geodetic perspective

on current state-of-the-art SLAM methods and identifying similarities both in terms of challenges faced and the solutions proposed by both communities. The central goal of this article is to connect both fields and enable future synergies between them.

Geodetic Mapping

SLAM is essential for several robotic applications in which the robot is required to autonomously navigate. A mobile robot needs a map of its environment to plan appropriate paths toward a goal. Furthermore, following the planned paths requires the robot to localize itself on its map. Many modern SLAM methods follow the graph-based SLAM paradigm [1]–[4]. In this approach, each pose of the robot or landmark position is represented as a node in a graph. A constraint between two nodes, which results from observations, is represented by an edge in the graph. The first part of the overall

Digital Object Identifier 10.1109/MRA.2014.2322282
Date of publication: 10 September 2014

problem is to create the graph, based on sensor data, and such a system is often referred to as the *front end*. The second part deals with finding the configuration of the nodes that best explains the constraints modeled by the edges. This step corresponds to computing the most likely map (or the distribution over possible maps), and a system solving it is typically referred to as a *back end*.

In the geodetic mapping community, one major goal has been to build massive survey maps, some even spanning across continents. These maps were then supposed to be used either directly by humans or for studying large-scale properties of the Earth. In principle, geodetic maps are built in a similar way to the front-end/back-end approach used in SLAM. Constraints are acquired through observations between physical observation towers. These towers correspond to positions of the robot as well as the landmarks in the context of SLAM. Once the constraints between observation towers are obtained, the goal is to optimize the resulting system of equations to get the best possible locations of the towers on the surface of the Earth.

The aim of this article is to survey key approaches of the geodetic mapping community and discuss them in relation to recent SLAM research. This mainly relates to the back ends of graph-based SLAM systems. We believe that this step will enable further collaborations and exchanges between both fields. As we will illustrate during this survey, both communities have come up with sophisticated approximations to the full least-square approach for computing maps with the aim of reducing memory and computational resources. A central starting point for the survey of the geodetic approaches is the “North American Datum of 1983 (NAD 83)” by Schwarz [5], and we go back to the work by Helmert [6]. This article extends [7] and presents a comprehensive review of the geodetic mapping techniques that we believe are related to SLAM.

Common Challenges in Geodetic and Robotic Mapping

SLAM and geodetic mapping have several problems in common. The first challenge is the large size of the maps. The map size in the underlying estimation problems is represented by the number of unknowns. In geodetic mapping, the unknowns are the positions of the observation towers, while, for robotics, the unknowns correspond to the robot positions and observed landmarks. For example, the system of equations for the North American Datum of 1927 (NAD 27) required solving for 25,000 tower positions and the NAD 83 required solving for 270,000 positions [8]. The largest real-world SLAM data sets have up to 21,000 poses [9], while simulated data sets with 100,000 poses [10] and 200,000 poses [4] have been used for evaluation. At the time of NAD 27 and 83, the map building problems could not be solved by standard least-square methods as no computer was capable of handling such large problems. Even today, computational constraints are challenging in robotics. SLAM algorithms often need to run on real mobile robots, including battery-powered wheeled platforms,

small flying robots, and low-powered underwater vehicles. For autonomous operation, the memory and computational requirements are often constrained so that approximate but online algorithms are often preferred over those that are more precise but are offline.

The second challenge results from outliers or spurious measurements. The front ends for robotics and geodetic mapping are affected by outliers and noisy measurements. In robotics, the front end is often unable to distinguish between similar-looking places, which leads to perceptual aliasing. A single outlier observation generated by the front end can lead to a wrong solution, which, in turn, results in a map that is not suitable to perform navigation tasks. To deal with this problem, recently, there has been more intense research for reducing the effect of outliers on the resulting map using extensions to the least-squares approach [11]–[14]. For geodetic mapping, the front end consisted of humans carefully and meticulously acquiring measurements. However, even this process was prone to mistakes [5].

The third challenge comes from the nonlinearity of constraints, which is frequently the case in SLAM as well as geodetic mapping. A commonly used approximation is to linearize the problem around an initial guess. However, this approximation to the nonlinear problem may lead to a suboptimal solution if the initial guess is not in the basin of convergence. There are various methods that enable finding a better initial guess, but this still remains a challenge [15], [16]. The importance of the initial guess in SLAM has also motivated the study of the convergence properties of the corresponding nonlinear optimization problem [17]–[20].

Fourth, geodetic mapping and SLAM ideally require an incremental and online optimization algorithm. In robotics, a robot is constantly building and using the map. It is advantageous if the system is capable of optimizing the map incrementally [21], [22]. In geodetic mapping, new survey towers are built and new constraints are obtained as and when required. It is not feasible to optimize the full network from scratch when new areas or constraints are added. Thus, geodetic methods must also be able to incorporate new information into the existing solutions with minimum computational demands.

Given these similarities, we believe that studying the achievements of the geodetic scholars is likely to inspire novel solutions to large-scale autonomous robotic SLAM.

Graph-Based SLAM

In the robotics community, Lu and Milios [1] were the first to introduce a least-squares-based direct method for SLAM. In their seminal paper, they proposed the graph-based framework in which each node models a robot pose and each edge represents a constraint between the poses of the robot. These constraints can represent odometry measurements between sequential robot poses produced by wheel encoders and inertial measurement units or by sensor fusion techniques such as scan matching [23]–[26].

Graph-based SLAM back ends aim at finding the configuration of the nodes that minimize the error induced by

constraints. Let $x = (x_1, \dots, x_n)^T$ be the state vector, where x_i describes the pose of node i . This pose x_i is typically three-dimensional (3-D) for a robot living in the two-dimensional (2-D) plane. We can describe the error function $e_{ij}(x)$ for a single constraint between the nodes i and j as the difference between the obtained measurement z_{ij} and the expected measurement $f(x_i, x_j)$ given the current state

$$e_{ij}(x) = f(x_i, x_j) - z_{ij}. \quad (1)$$

The actual realization of the measurement function f depends on the sensor setup. For pose-to-pose constraints, one typically uses the transformation between the poses. For pose-to-landmark constraints, we minimize the reprojection error of the observed landmark into the frame of the observing pose. The error minimization can be written as

$$x^* = \operatorname{argmin}_x \sum_{ij} e_{ij}(x)^T \Omega_{ij} e_{ij}(x), \quad (2)$$

where Ω_{ij} is the information matrix associated with a constraint and x^* is the optimal configuration of nodes with minimum sum of error induced by the edges. The solution to (2) is based on successive linearization of the original nonlinear cost typically around the current estimate. The nonlinear error function is linearized using Taylor series expansion around an initial guess \check{x}

$$e_{ij}(\check{x} + \Delta x) \simeq e_{ij}(\check{x}) + J_{ij} \Delta x, \quad (3)$$

with the Jacobian

$$J_{ij} = \frac{\partial e_{ij}(\check{x} + \Delta x)}{\partial \Delta x} \Big|_{\Delta x=0}. \quad (4)$$

This leads to a quadratic form. In the end, the Jacobians from all constraints can be stacked into a matrix and the minimum of the quadratic form can be found through direct methods, such as Gauss–Newton, by solving the linear system

$$H \Delta x^* = -b, \quad (5)$$

where $H = \sum_{ij} J_{ij}^T \Omega_{ij} J_{ij}$ and $b = \sum_{ij} J_{ij}^T \Omega_{ij} e_{ij}$ are the elements of the quadratic form that results from the linearized error terms and Δx^* is the increment to the nodes in the graph configuration that minimizes the error in the current iteration at the current linearization point

$$x^* = \check{x} + \Delta x^*. \quad (6)$$

As the measurements z and the poses x do not form a Euclidean space, it is advantageous to not subtract the expected and obtained measurement in (1) but to perform the operations in a non-Euclidean manifold space [27], [28]. This is especially helpful for constraints involving orientations.

In their seminal paper [1], Lu and Milios compute (5) by inverting the quadratic matrix H . This is reported to be the most computationally expensive operation as it scales cubic with the number of nodes. A lot of graph-based SLAM

research focuses on efficiently solving (5) using domain knowledge and sparse linear algebra methods. Gutmann and Konolige [29] propose a method that could incrementally build a map and required the expensive matrix inversions only after certain predetermined steps. Konolige [30] provided a computationally efficient algorithm with a complexity of $O(n)$ for single-loop closures and $O(n \log n)$ for multiple looped maps. He identified the sparse connectivity of the information matrix resulting from SLAM graphs and used conjugate gradient preconditioned with an incomplete Cholesky factor to reduce computational requirements. Folkesson and Christensen [2] formulate the least-squares problem in (2) as an energy-minimization problem. They also incorporate data association within the energy function, which implicitly performs a χ^2 test. They furthermore reduce the complexity and size of the graph by collapsing subgraphs into a single node, which they call a *star node*.

Dellaert and Kaess [31] explore the graph SLAM formulation as a factor graph using smoothing and mapping. They call their method \sqrt{SAM} as it uses matrix factorization methods, such as QR, LU, and Cholesky decomposition to solve (5). In addition to the offline approach, an efficient variant for incremental updates using Givens rotation is available [32].

Other authors minimize (2) using relaxation techniques, where parts of graphs are incrementally optimized [33]–[35]. Olson et al. [36] solve the least-squares problem using stochastic gradient descent. In stochastic methods, the error induced by each constraint is reduced, one at a time, by moving the nodes accordingly. Grisetti et al. [37] propose a reparametrization of the problem to improve convergence. Stochastic methods are typically more robust to bad initial estimates and can be run incrementally by tuning the learning rate [38], [39]. In addition, hierarchical and submapping approaches have shown to efficiently compute solutions by decomposing the optimization problem at different levels of granularity [16], [27], [40]–[44].

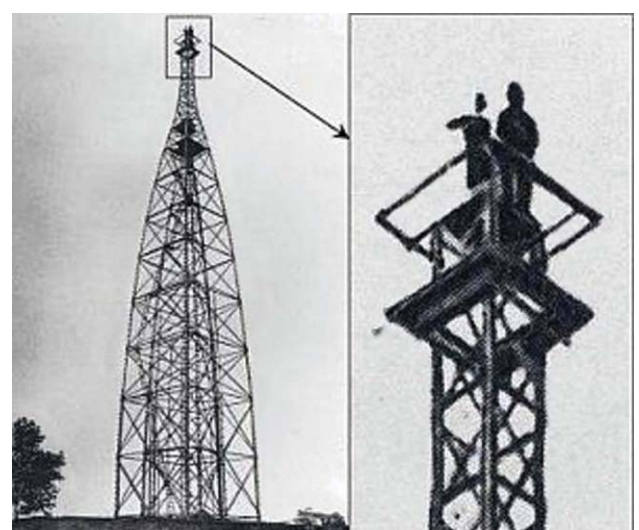


Figure 1. The observing towers called Bibly towers built for triangulating other towers. (Photos courtesy of [45].)

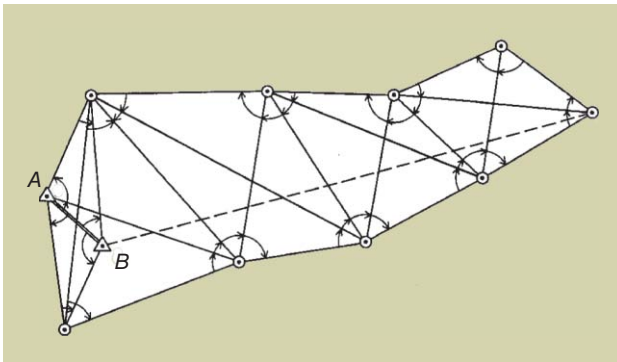


Figure 2. A simple triangle net. The distance between towers A and B is physically measured. The angular constraints to all other towers are measured, and the lengths of all other segments are computed with respect to the baseline AB with the measured angles. (Image courtesy of [46].)

Geodetic Mapping

Geodetics, also known as *geodesy*, is the science that studies the Earth at various global and local scales. It measures large-scale changes in the Earth's crustal movements, tidal waves, magnetic and gravitational fields, and so on. The aspects of geodesy, which are most interesting in the context of SLAM, are related to geodetic mapping.

The basic principle behind geodetic surveying is triangulation. Various observation towers, called Bibly towers, typically 20–30 m in height, are built in the line of sight of neighboring towers [46]. An example of a Bibly tower with surveyors on top is shown in Figure 1. Geodetic surveyors built a large interconnected mesh of observation towers by triangulating measurements between them. The resulting mesh of towers and constraints is commonly called a *triangle net*. A simple example of a triangle net is shown in Figure 2. Each line segment in Figure 2 is a constraint between two observation towers. Some of these constraints are directly measured, while others are computed using trigonometrical relationships.

The method of obtaining constraints between the observing towers has evolved over time. Initially, constraints were distance-only or angle-only measurements. The distance measurements were obtained using tapes and wires of Invar, which has a very low coefficient of thermal expansion. Later, more sophisticated instruments, such as parallax range finders, stadiometer, tellurometer, and electronic distance measuring instruments, were used. Angular measurements were obtained using theodolites. Measuring distance using tapes and wires is more cumbersome than computing angles with theodolites. Hence, only a few distance measurements called *baselines* are computed, and the other distance measurements are deduced based on angular measurements and trigonometrical relationships. In Figure 2, the towers A and B are the baseline, and only angular measurements to other towers are measured. The distances between all other towers are deduced using the measured baseline AB , angles, and trigonometrical relations.

Moreover, the measurement constraints used in geodetic surveys can be differentiated as absolute and relative mea-

surements. Absolute measurements involve directly measuring the position of a tower on the surface of the Earth. These include measuring latitudes by observing stars at precise times and then comparing them with the existing catalogs. Stars were also used as fixed landmarks for bearing-only measurements from different base towers at precisely the same time. Later, more sophisticated techniques, such as very long baseline interferometry (VLBI) and global positioning system (GPS) measurements, which lead to an improved measurement accuracy, were introduced. Angular measurements obtained with theodolites for large-scale geodetic mapping were abandoned after the introduction of VLBI, and the triangulation techniques were replaced by trilateration around 1960. In the United States, a high accuracy reference network was built using VLBI and GPS only [48] by 1990. The continuously operational reference station introduced in 1995 uses only GPS measurements and is regularly updated. The National Spatial Reference System of 2007 known as NAD83(NSRS2007) is the latest readjustment, containing only static GPS measurements [49].

Examples of large-scale triangle nets are shown in Figure 3. Figure 3(a) shows the geodetic triangle net used for mapping Central Europe in 1987, whereas Figure 3(b) shows the triangulation network in existence for mapping North America in 1983 (NAD 83). The thick lines in NAD 83 are long sections of triangulation nets comprising thousands of Bibly towers. The connections between multiple sections are small triangle networks called *junctions*.

The geodetic mapping community typically chose the Earth's center of gravity as the sensor origin. This eased the process of acquiring measurements as it is quick and easy to standardize the calibration technique. The primary form of triangulation was done using theodolites, all of which contain a level that allows aligning the instruments with respect to the center of Earth's gravity (E_{cg}). All other instruments used some form of a plumb line as a reference, which aligned them with E_{cg} . Choosing E_{cg} is also preferred when using satellites for acquiring measurements as they orbit the E_{cg} . The exact shape of the Earth is not a sphere but a geoid, which can be approximated as an ellipsoid. However, the center of this approximate ellipsoid does not coincide with E_{cg} . This is because the Earth's mass is not uniformly distributed. Hence, although choosing the sensor origin as E_{cg} is practically a good choice, it is mathematically inconvenient. It requires additional mathematical computations for mapping measurements to the center of the ellipsoid. This problem is commonly called *computing the deflection of the vertical*.

The geodetic mapping problem can be broken down into two major subproblems: 1) the adjustment of the vertical and 2) the adjustment of the net. The problem of adjustment of the net is finding the least-squares system of the planar triangulation net, whereas adjustment of the vertical involves finding parameters to wrap this mesh network on a geoid representing Earth [50].

Adjustment of the Net—Geodetic Back Ends

The problem of adjustment of the net is similar to the graph-based SLAM formulation. In the SLAM notation, the geodetic mesh network consists of various observation towers constrained by nonlinear measurements. These physical towers are similar to the unknown state vector $x = (x_1, \dots, x_n)^T$ in the SLAM problem. In SLAM, 2-D and 3-D robot headings (roll, pitch, and yaw) are estimated in addition to the cartesian coordinates (x, y, z) . For geodesy, the surveyors were mainly interested in the cartesian coordinates of the towers on the surface of the Earth. Angular components were used until the 1960s in geodesy before GPS and VLBI systems were available.

The task of the back-end optimizer in geodesy is to find the best possible configuration of the towers on the surface of the Earth to minimize the sum of errors from all constraints. All nonlinear constraints can be linearized using Taylor series expansion and stacked into a matrix [8]. The least-squares solution can be computed directly by solving the least-square system in (5). SLAM and geodetic problems inherently contain nonlinear equations constraining a set of positional nodes. The process of linearizing the constraints and solving the linearized system is repeated to improve the solution.

The biggest challenge faced by the geodetic community over centuries was limited computing power. Even with the

most efficient storage and sparse matrix techniques, there was no computer available that could solve the full system of equations as a single problem. For example, the NAD 83 mesh network, shown in Figure 3(b), requires solving 900,000 unknowns with 1.8 million equations [51]. A dense matrix of size $900,000 \times 900,000$ would require more than 3,000 GB just to store it. Even when using sparse matrix data structures, such as compressed sparse rows or columns, NAD 83 would still require roughly 30 GB of memory to store the matrix of normal equations (considering that only 0.5% of the matrix elements are nonzeros). In the following section, we explain some of the geodetic back-end optimizers used for mapping large continental networks, such as that of North America and Europe.

Helmert Blocking

When geodetics started to develop the large-scale triangulations in the mid-1800s, the only way of solving large geodetic networks was by dividing the problem so that multiple people could work on solving each subproblem. Helmert proposed the first method for solving the large optimization problem arising from the triangulation network in parallel. His strategy, which was proposed in 1880, is possibly the oldest technique to partition the set of equations into smaller problems [6], [52]. Although

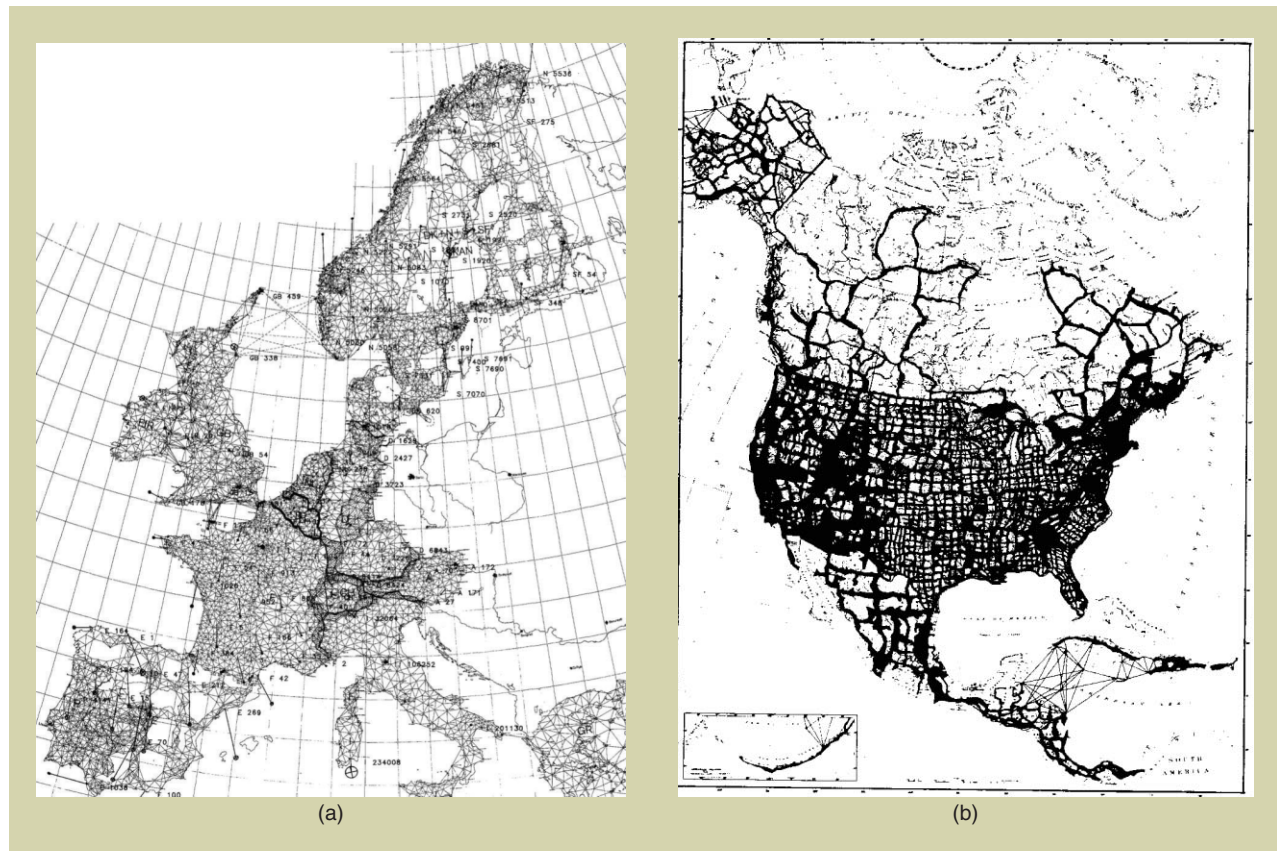


Figure 3. The triangulation networks spanning across Europe and North America: (a) the network of constraints used for the European Datum (ED) of 1987 (figure courtesy of [47]) and (b) the network of constraints existing in 1981 for mapping the North American continent (image courtesy of [5]).

Algorithm 1. Helmert blocking.

- 1) Given a partitioning scheme, establish the normal equations for each partial subnet separately.
- 2) Eliminate the unknowns for all nodes that do not have constraints with neighboring partial subnets.
- 3) Establish the main system after eliminating all the inner nodes containing only intrasubnet measurements.
- 4) Solve the main system of equations containing only separator nodes.
- 5) Solve for inner nodes given the value of separator nodes.

graph partitioning and submapping have been frequently used in robotics, to the best of our knowledge, Helmert's method has not been referenced in the robot mapping community—only Triggs et al. [53] mention it as an optimization procedure in their bundle adjustment survey.

Helmert observed that by partitioning the triangle net in a particular way, one can solve the overall system of equations in parallel. He outlined that the whole triangle net can be broken into multiple smaller subnets. All nodes that have constraints only within the same subnet are called *inner nodes* and can be eliminated. All separator nodes, i.e., those that connect multiple subnets, are then optimized. The previously eliminated inner nodes can be computed independently given the values of the separator nodes. Most importantly, the formed subnets can be solved in parallel.

There might still be more methods in geodetic mapping that are unknown outside their community but could inspire other fields.

Helmert's blocking method is outlined in Algorithm 1 and is explained more precisely as a mathematical algorithm by Wolf in [54]. Consider a simple triangle net shown in Figure 4. In Figure 4(a), each line segment is a constraint and the end of segments represents a physical observation tower. Helmert observed that if he divides the triangle net into two halves, for example, as shown in Figure 4(b), the top half of the towers will be independent of the bottom half given the values of the separators, as shown in Figure 4(c). Such a system can be solved using reduced normal equations [5], [54].

Let us represent the whole system of equations from the triangle net in Figure 4(a) as

$$Ax = b. \quad (7)$$

This equation can be subdivided into three parts in the following manner:

$$[A_s \ A_1 \ A_2] \begin{bmatrix} x_s \\ x_1 \\ x_2 \end{bmatrix} = b. \quad (8)$$

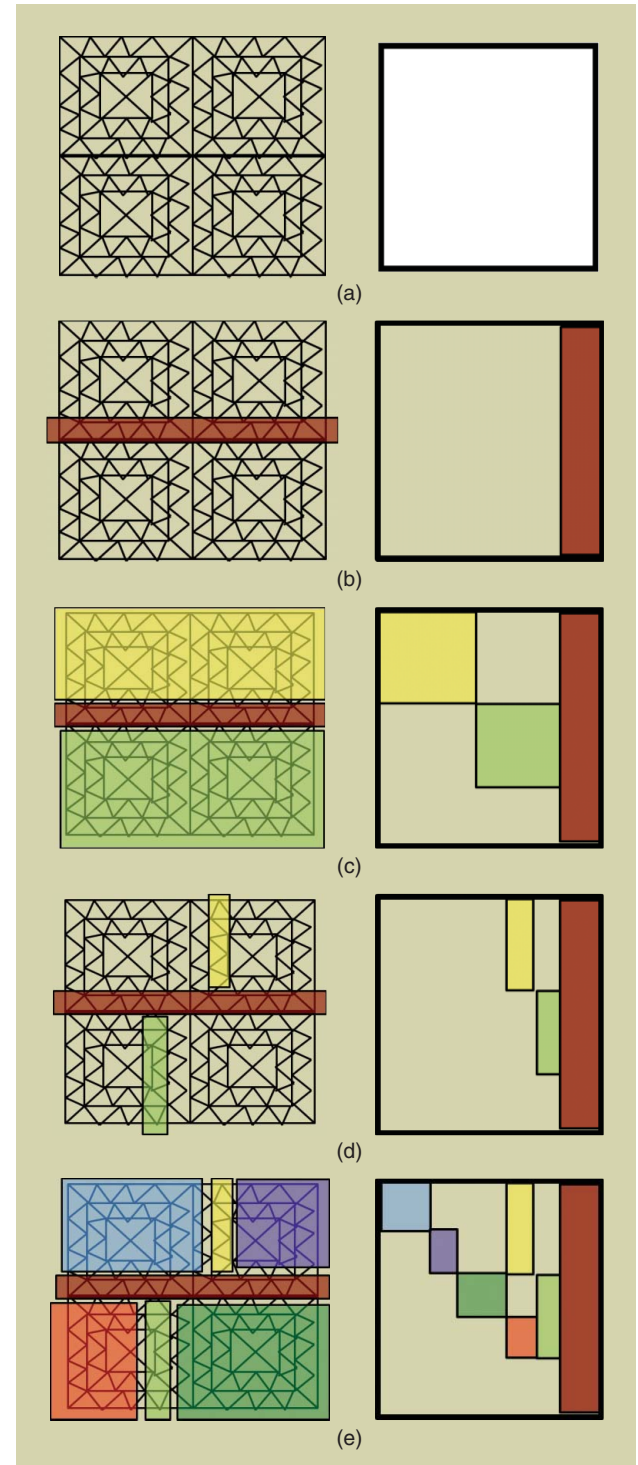


Figure 4. (a)–(e) The Helmert blocking in action. The left column shows a toy example of triangle net. The right column shows the corresponding stacked coefficient matrix for each net.

Here, A_s and x_s represent the coefficients and unknowns, respectively, arising from the central separator. A_1 and A_2 are coefficients of the top and bottom subnets. The coefficient matrix $[A_s \ A_1 \ A_2]$ in (8) is shown on the right-hand side of Figure 4(c). The corresponding system of normal equations is

$$\begin{bmatrix} N_s & N_1 & N_2 \\ N_1^T & N_{11} & 0 \\ N_2^T & 0 & N_{22} \end{bmatrix} \begin{bmatrix} x_s \\ x_1 \\ x_2 \end{bmatrix} = \begin{bmatrix} b_s \\ b_1 \\ b_2 \end{bmatrix}. \quad (9)$$

The towers in x_1 do not share any constraints with towers in x_2 , whereas x_1 and x_2 share constraints with x_s but not with each other. The key element in (9) is the block structure of N_{11} and N_{22} . The system of equation in (9) can be reduced such that

$$\bar{N}_s x_s = \bar{b}_s, \quad (10)$$

where \bar{N}_s is computed as

$$\begin{aligned} \bar{N}_s &= N_s - [N_1 \ N_2] \begin{bmatrix} N_{11}^{-1} & 0 \\ 0 & N_{22}^{-1} \end{bmatrix} [N_1^T \ N_2^T] \\ &= N_s - \sum_{i=1,2} N_i N_{ii}^{-1} N_i^T, \end{aligned} \quad (11)$$

and \bar{b}_s is computed as

$$\bar{b}_s = b_s - \sum_{i=1,2} N_i N_{ii}^{-1} b_i^T. \quad (12)$$

Here, \bar{N}_s is called the reduced normal equations. Once N_s has been solved, x_1 and x_2 can be computed by solving

$$N_{11} x_1 = b_1 - \bar{N}_s^T x_s \quad (13)$$

$$N_{22} x_2 = b_2 - \bar{N}_s^T x_s. \quad (14)$$

Moreover, Wolf [54] states that matrices should never be inverted for computing (10), (13), and (14). Instead, Cholesky decomposition or Doolittle-based LU decomposition should be employed. The steps outlined for computing the reduced normal forms in (11) and (12) represent the Schur complement. The inverse computation in this step is trivial if the subnets result in block diagonal matrices. If not, Schwarz [5] and Wolf [54] mention that each of the subnets can themselves be sparse and can be further subdivided, as shown in Figure 4(d). Reference [49, Part IV] also contains a detailed methodology for applying Helmert blocking for optimizing geodetic networks used for National Spatial Reference System of 2007.

The structure of the normal matrix shown in Figure 4(d) looks like the matrix shown in Figure 5. In the example explained in Figure 5, we have two levels of Helmert blocks. The number of levels can be arbitrary, and each subnet can have a different number of recursive subblocks. Elimination takes place in a bottom-up manner. Then, the solution at the highest level is used to recursively propagate back to smaller subnets. Helmert also outlines the strategy to select separators at each level. This is discussed later in the “Variable Ordering” section.

The Helmert blocking method was used for creating the NAD 83. Ten levels of Helmert blocks were created with a total of 161 first-level blocks. This is shown in Figure 6. The colored lines show the partitions of the graph at different levels. On average, each of these 161 subnets contained 1,000 nodes, but roughly 80% of these nodes contained only inter-

nal measurements, and can be eliminated [5]. Three nonlinear iterations of the whole system were performed, which took roughly four months each [5].

The Helmert blocking method is inherently multicore and parallel, but it still requires solving a large number of equations when solving for the reduced normal equation for a large separator set. The complexity of the exact method can be reduced if networks are built in sections, as shown in Figure 7(b). Whenever the triangular network was not built

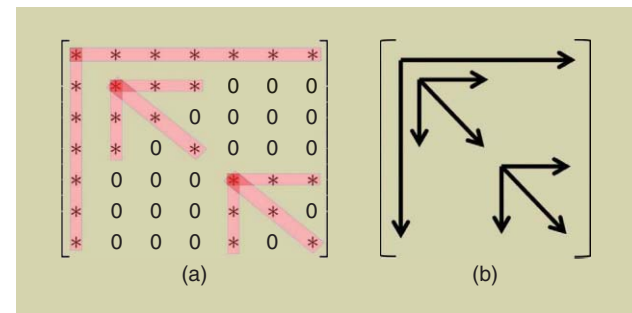


Figure 5. (a) and (b) The structure of the coefficient matrix arising from two levels of Helmert blocks. The arrows show nonzero cells.

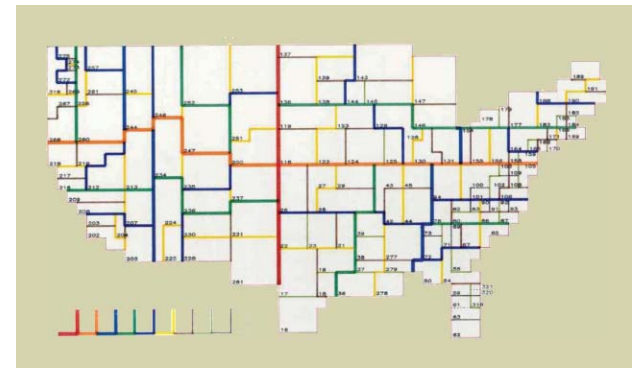


Figure 6. Helmert blocking applied to North America with ten levels. The legend in the bottom-left corner shows progressive levels of partitions. The first partition cuts the continent into east–west blocks, whereas the second cut partitions each half into north–south blocks. Hence, each geographical block is partitioned into four regions and this method is recursively performed on each subblock. (Image courtesy of [5].)

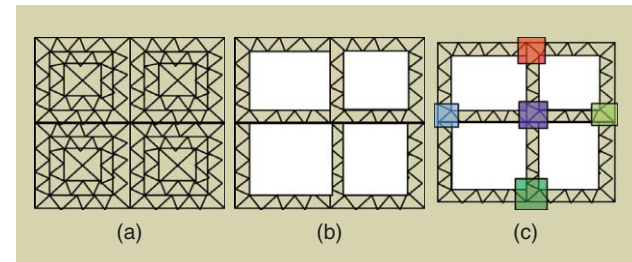


Figure 7. (a) The original triangle net and (b) the corresponding net after applying the polygon-filling method. This leads to a smaller and better tractable problem at the expense of reduced accuracy. Once the sparse solution is computed, the interior stations can be computed by fixing the sections. (c) Helmert blocking can be applied leading to the separator nodes illustrated by the colored squares.

using long sections, the net was approximated using polygon-filling methods, which are explained below.

Polygon Filling

Polygon-filling methods are used to convert a dense net into sections. An example for a dense network is shown in Figure 7(a) and the corresponding sparse mesh of sections in Figure 7(b). Inner regions in Figure 7(b) are completely removed from the initial optimization. Only the sections, as shown in Figure 7(b), are optimized. In a subsequent optimization, the structure of the grids is fixed and the interior dense nets are optimized. This is an approximation as the optimization of the sections does not contain any measurements from the interior nets. Any error in the sections is distributed over the interior shaded subnets [55].

SLAM researchers have often gone back to the graph theory and sparse linear algebra community for efficient algorithms.

are formed at the intersections of the sections rather than the long partitions in the original method. This difference can be observed by comparing Figures 7(c) and 4(e).

The polygon-filling method is also the preferred technique for incremental optimization. As triangulation networks evolve over time, large sections are built first and are subsequently triangulated densely—if and when required. This means that the outer sections are fixed and are never updated with measurements from the inner nodes. Thus, any error in the initial optimization of the outer section has to be distributed over the inner regions. Even when adding new sections from new surveys covering unmapped area, the ini-

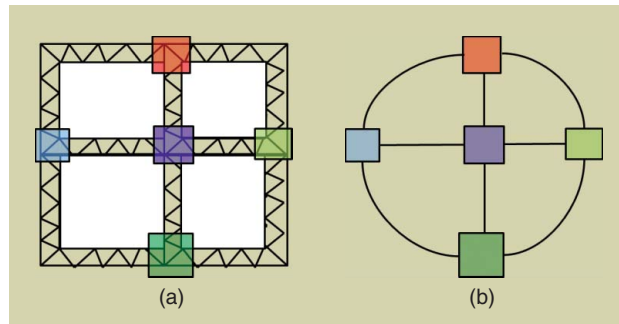


Figure 8. The Bowie approximate triangle net. The size of the separators is much smaller once the polygon-filling method is used. (a) The separators are shown in colored squares. (b) The Bowie method approximates this problem by abstracting the sections into a single constraint and all separator nodes as a single node.

tially obtained sections are often kept fixed. Although this procedure is an approximation, it allows for increasing the size of a triangulation net without having to start the optimization from scratch. Thus, it is an efficient incremental map building method.

The Bowie Method

The use of networks of sections and the polygon-filling method reduces the size of the optimization problem significantly, but it is still computationally demanding considering the resources of the early 1900s. Bowie approximated the above methods further to create the North American Datum in 1927. Bowie's main insight was that he can approximate the net comprising sections by collapsing intersections into a single node and the sections into a single virtual constraint. This is shown in Figure 8. This much smaller least-squares system is solved to recover the positions of the intersections, which can then be used to compute the sections independently.

The core steps of the Bowie method consist of separating the sets of unknowns into segments and junctions. The junctions act as a small set of separator nodes. The junction nodes are shown as colored squares in Figure 8. These are not a single node but a small subnet of towers, which separates the sections. A generic junction is shown in Figure 9. All nodes in one junction are optimized together using least-squares adjustment but ignore any interjunction measurements. After this optimization, the structure of the junction does not change, i.e., each node in a junction is fixed with respect to other nodes in that particular junction.

As a next step, new latitudinal and longitudinal constraints are created between junctions. This is done by

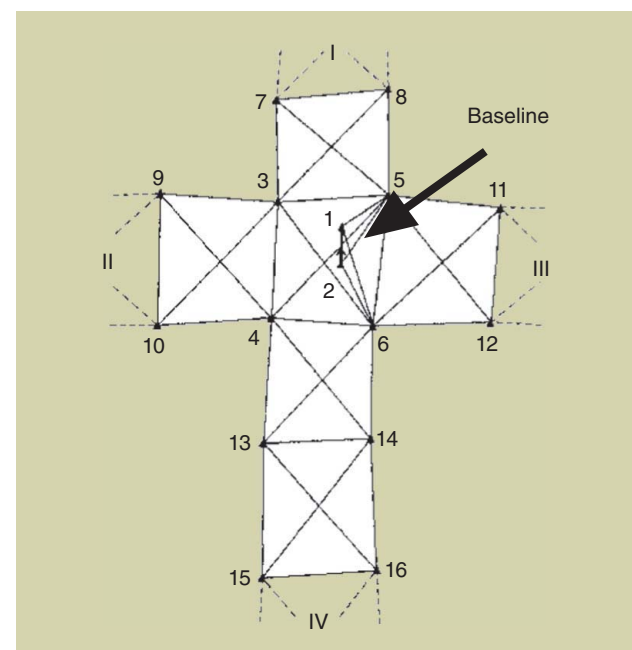


Figure 9. An example of a typical junction connecting segments in the four directions. The baseline and azimuth of stations 1 and 2 were measured directly. All other measurements were relative to other stations. (Image courtesy of [5].)

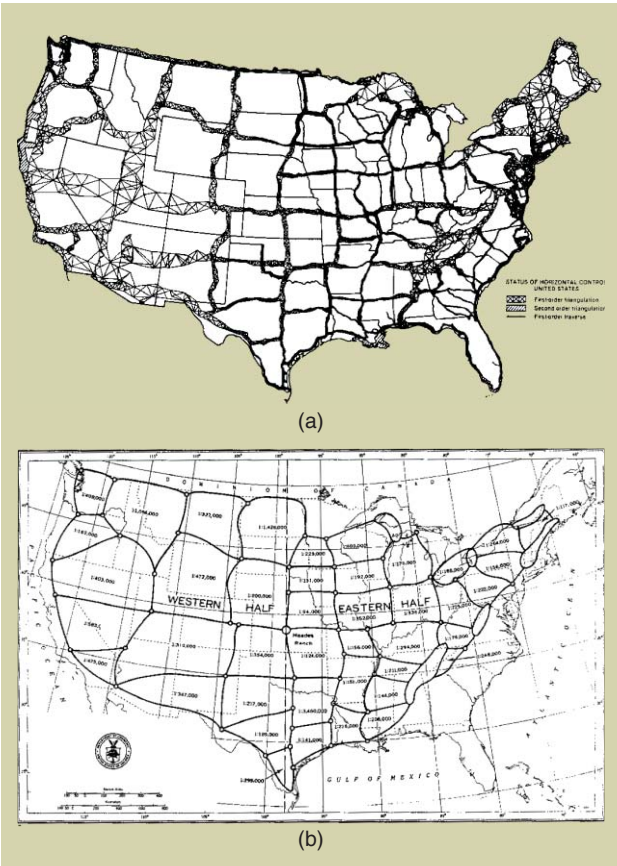


Figure 10. (a) The Bowie method as used for NAD 27 triangle net and (b) Bowie's approximation. Each small circle represents a junction, and the junctions are connected by sections. Given the values of the junctions, the segments are independent of the rest. The western half contains 26 junctions and 42 sections creating 16 loops. The eastern half contains 29 junctions and 55 sections forming 26 loops. All measurements were computed with respect to the Meades Ranch located in Kansas shown by the circle in the center of (b). The numbers inside the regions depict the error in a loop after the optimization is completed. (Images courtesy of [5].)

approximating each section with a single constraint. Each of such single constraints is a 2-D longitude and latitude constraint. As a result, each junction turns into a single node and each section into a single constraint. This leads to a much smaller but approximate problem, which is optimized using the full least-squares approach.

The previously described steps of the Bowie method are summarized in Algorithm 2 (see also [56]). The full least-squares problem is not solved by matrix inversion but by a variant of Gaussian elimination called *Doolittle decomposition* [57]. The Doolittle algorithm is an LU matrix decomposition method, which decomposes a matrix columnwise into a lower triangular and an upper triangular matrix. The solution can be computed using forward and backward substitution steps as with other matrix decomposition methods as well.

In essence, the Bowie method generates new virtual constraints from sections. He introduces a weight for each virtual measurement, which is chosen as the ratio of the length of the section with respect to the sum of all the section

Algorithm 2. The Bowie method.

- 1) Separate the triangle net into junctions and segments.
- 2) Optimize each junction separately.
- 3) Create new virtual equations between junctions treated as a single node.
- 4) Solve the abstract system of equations comprising of each junction as a single node and each section as a single constraint.
- 5) Update the resulting positions of stations in the segments using the new junction values.

lengths. Hence, these weights are proportional to the length of the sections so that the larger proportion of the error is distributed over long sections compared with shorter ones.

Another computational trick to lower the efforts is to use diagonal covariances for the 2-D virtual latitude/longitude constraints. This enables the separation of the system of equations for longitude and latitude. This yields two least-squares problems with half of the original size.

The partitioning of the triangular net into junctions and sections is done manually. Each junction has to contain at least one measured baseline and one measured azimuth direction. This is sometimes referred to as *astronomical stations*. Occasionally, the size of junctions was enlarged to include an azimuth measurement because azimuth measurement has not been taken at all towers. Figure 10 shows the original triangle net and Bowie's approximated net into segments and junctions used for NAD 27. In Figure 10, the small circles represent junctions and all lines connecting junctions are sections of triangle nets. These sections and junctions individually represent a subset of the constraints connecting stations.

In summary, the Bowie method is an approximation of Helmert blocking. The approximation uses single-level subnets and an approximate optimization of the junction nodes. The optimization of the highest level in Helmert blocking consists of junction nodes and is computed via reduced normal equations. In contrast to that, the Bowie method uses virtual constraints at the highest level. The main difference is that the system of equations created by the virtual constraints is much smaller and sparser and hence easier to optimize than the full set of reduced normals, as in the exact Helmert blocking method.

To the best of our knowledge, the Bowie method is the first implementation of a large-scale approximate least-squares system. It was effectively used in creating the NAD 27 as the triangulation nets were built in sections forming large loops. The Bowie method exploits this structure and also allows incremental optimization. New loops in the triangulation nets were not optimized as a whole; instead, they were integrated into the existing system by keeping the previous positions

The starting point of the Indian method is similar to the Bowie method.

fixed. This led to inaccuracies but was better tractable than optimizing the system as a whole.

Modified Bowie Method for Central European Triangulation

The approximation introduced by the Bowie method yielded suboptimal results for the ED of 1950 (ED 50) [55]. For example, the virtual latitudinal and longitudinal constraints are artificially generated and not directly measured constraints, but this fact is not fully considered in the optimization. Furthermore, cross correlations between latitudes and longitudes are ignored using diagonal covariances and the junctions are fixed as a whole. Another issue in the Bowie method results from the assumption that the size of sections is much longer than junctions, which was the case for NAD 27, but the triangulation nets in the ED 50 are denser. This results in the amplification of the errors introduced by the approximations [55].

The European geodetics thus proposed two modifications to the Bowie method to cope with the aforementioned problems for optimizing the ED 50 [55]. The first one addresses the virtual measurements. Line 3 of Algorithm 2 sets up as many equations as sections. Instead, one virtual equation for every loop was created, enforcing a zero error around the loop. The second modification addresses the way the linear system is solved efficiently. Instead of using the Doolittle method, they used the Boltz method, as explained below, which allowed for computing the matrix inversion in one shot.

Boltz Method

The Boltz method is an alternative to the Gaussian elimination with LU decomposition for solving large set of equations in one shot [58], [59]. An explanation of the Boltz method was provided by Wolf [57], which basically says that Boltz was tabulating matrices and their corresponding inverted solution. Boltz was able to simply look up the solutions for sub-problems from a table instead of recomputing the inverse.

The central question here is how to set up the linear system so that the matrix of the normal equations, which needs to be inverted, reappears during the calculations. In general, for this method to work infinitely many matrices would need to be tabulated. To keep the number of tabulated matrices tractable, Boltz proposed to divide the equations into two groups:

$$\begin{bmatrix} A & B \\ B^T & C \end{bmatrix} \begin{bmatrix} x \\ y \end{bmatrix} = \begin{bmatrix} v \\ w \end{bmatrix}. \quad (15)$$

Here, A , B , and C are coefficients of the normal matrix, and x and y are unknowns. Boltz proposed to cache A^{-1} and solve the reduced system of equation via

$$[C - [B^T A^{-1} B]]y = [w - B^T A^{-1} v]. \quad (16)$$

The key idea is to separate angle-only measurements from all others. Let x be the unknowns that arise from angle-only measurements, while y be the unknowns arise from all other measurements (see also [55]). The constraints in x are

simple given the triangular structure of the net: the sum of the angles in a triangle equals 180° and the sum of angles around a point must add up to 360° . Hence, the coefficients of the matrix A in (15) and (16) can be written so that it contains only ones, zeros, and negative ones. This, in combination with domain knowledge about the structure of the triangular nets, allows for efficiently caching A^{-1} . Boltz method is designed for triangle nets in which the structure repeats itself. This is often the case in geodetic mapping.

The lookup was done by humans, but we could not find details about the procedure for physically storing and retrieving the inverted matrices. One might even spot similarities between Boltz's proposal of caching matrix inversions and techniques like lifted probabilistic inference [60]. Caching can result in a substantial performance gain if majority of operations are done manually as was the case for the ED 50. Boltz's method was successfully used for eliminating up to 80×80 -sized matrices when creating ED 50 [55].

Note that reduction in (16) is the Schur compliment, but the motivation behind using the Boltz method is the fact that A^{-1} is tabulated and looking up the inverse is substantially faster than computing it (by hand). The geodetic researchers prior to 1950 mention that the Boltz method allowed solving least squares without biasing the solution toward any particular unknown. They mention that the Boltz method treated all unknowns equally unlike the Gaussian elimination, which caused the last variable to contain larger errors. From [61], "A method devised by Boltz for solving the normal equations occurring in the adjustment of a triangulation network; it allows a large set of equations to be solved in one straight operation by the method of least squares without biasing the solution towards any particular unknown. Initially, the normal equations were solved using the Gaussian method of successive elimination. This method, however, causes the last determined value to contain larger errors than the first determined value. Boltz's method treats all unknowns equally and is particularly suitable for solving large systems of equations."

The Indian Method of 1938

Bomford [62] proposed a different approach than the aforementioned methods for solving the triangulation net for the Indian subcontinent in 1938. He mentions that the Bowie method was infeasible for optimizing the network of towers in India, as the number of astronomical stations was too small and each junction in the Bowie method requires to have an astronomical station with independent latitude and longitude observations.

The starting point of the Indian method is similar to the Bowie method. Junctions and sections are created from the triangle nets. These junctions are points of intersection of sections, and do not require any astronomical constraints. This is shown in Figure 11(a). A spanning tree consisting of sections and junctions is chosen from the mesh network of the triangle nets. The initial spanning tree does not have errors as there are

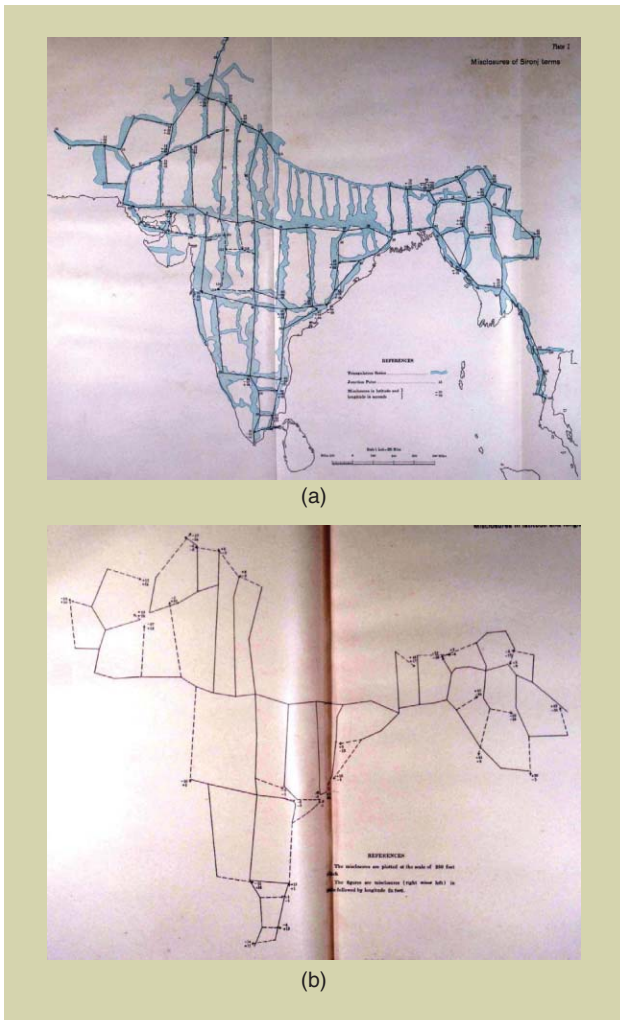


Figure 11. The dotted lines are sections, which complete loops. The point of intersection between a solid and a dotted line is a circuit point, which has a latitude and longitudinal error induced by the dotted line. (a) The Indian triangulation net on the map of the Indian subcontinent. The blue region shows the area covered by sections and the solid line is the represented single section. (b) The triangulation net with circuit errors at intersections. (Images from [62].)

no loops, and it is depicted by the solid lines in Figure 11(b). All other sections that are not part of the spanning tree will introduce a residual error (see dotted lines). Bomford refers to the points where multiple sections meet and have a residual error as circuits. These circuit points have a residual in latitude and longitude. A zoomed-in portion of the north-east part of the map is shown in Figure 12. Figure 12(a) shows the errors in latitude and longitude at each circuit point. Bomford proposed that the error in circuit points could be solved by distributing it around the loop. He had no automated system to distribute errors around the loop. He manually performed trial and error methods to reduce the total error induced in the circuit nodes. For example, he states that he first reduced the longitudinal error in the northwest regions, shown in Figure 12(a), by adjusting longitudinal values of the lower section. He incorporates the stiffness of sections, which he

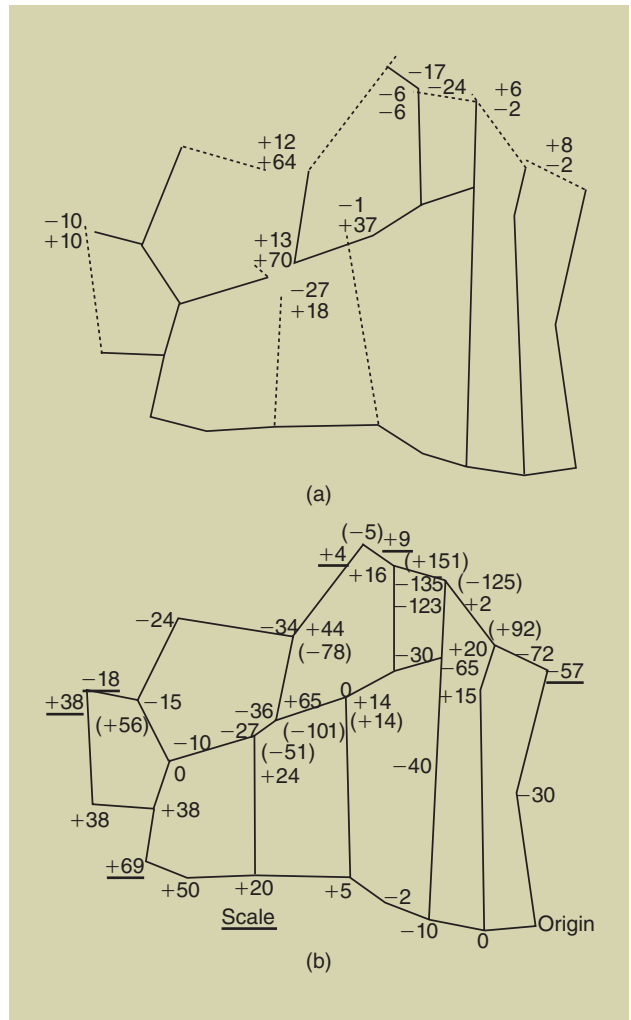


Figure 12. A zoomed-in view of the northeast section of the Indian subcontinent. It shows the initial and final configurations of the triangle net used in 1939 for surveying India. The solid lines represent the initial spanning tree. The dotted lines are the sections that induce circuit points and, thus, a residual error. (a) The mesh net with circuit errors on a zoomed-in section (each circuit point contains the latitudinal residual error) and (b) the resulting optimized net with the correction for each junction (each circuit point contains the longitudinal residual error). (Images courtesy of [62] and [63].)

approximated by the length and uncertainty of the sections [62]. This method does not appear to be as rigorous as the Bowie or Helmert methods, but still resulted in accurate maps of the Indian subcontinent.

Variable Ordering

In the “Helmert Blocking” section, we outlined the Helmert blocking method, but did not mention how the partitioning was performed. Helmert himself provided simple instructions for creating subnets and for partitioning the blocks, which is critical for his method. He first instructed to pick a latitude such that it partitions all the towers roughly into halves. Next, a longitude is chosen for each upper and lower half to partition the northern and southern regions into eastern and western partitions. Each obtained geographical rectangular block is recursively partitioned into four further blocks. This strategy is shown

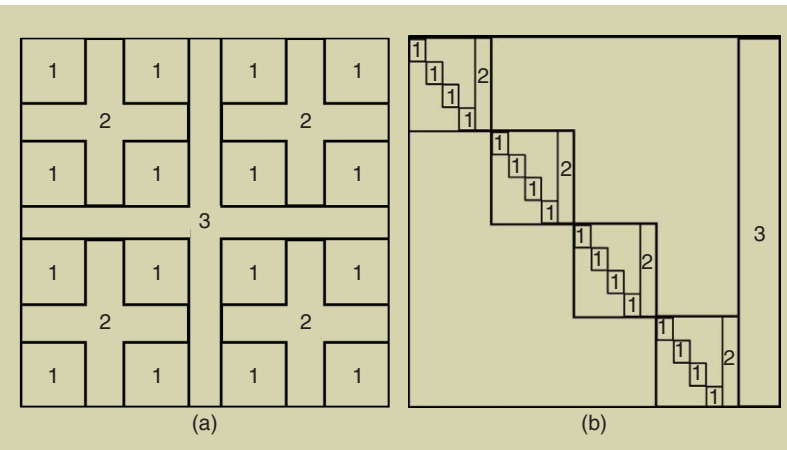


Figure 13. The nested dissection and the corresponding matrix arrangement. The four higher blocks with nodes numbered 1 and 2 are independent given the separator 3. All subblocks numbered 1 are independent given the subblock numbered 2. (a) A planar mesh partitioned according to nested dissection and (b) the corresponding matrix picture for this net.

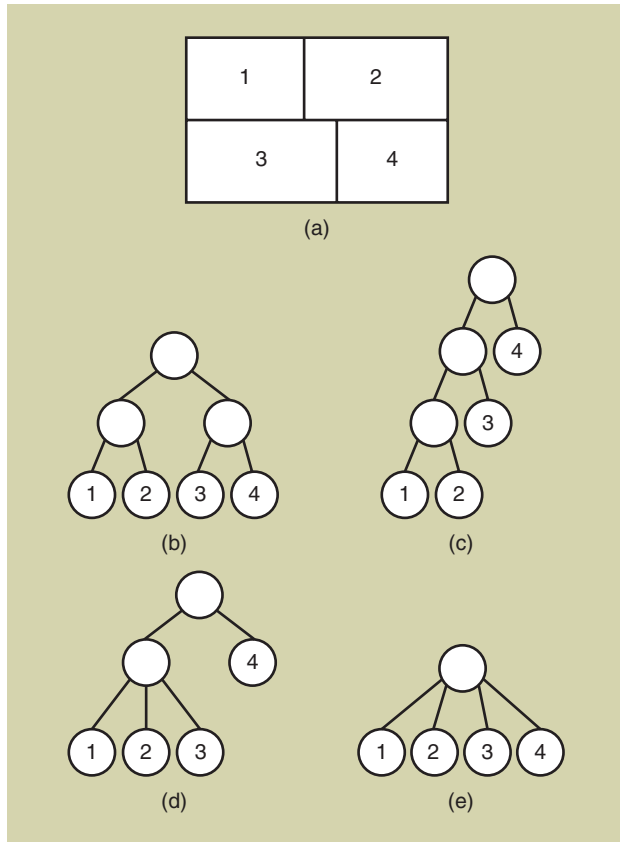


Figure 14. Possible different ways for joining four Helmert blocks according to [5]. (a) A rectangular area partitioned into four blocks, which can be joined in four ways (b) deep tree, (c), (d), and (e) broad tree.

In Figure 4(d) and (e). The proposed method is simple but effective, since the triangulation network is built roughly as a planar graph and the density of the net was approximately similar across different locations. Helmert's approach to partition the triangle nets also shares similarities to the nested dissection variable reordering strategies [64] used to efficiently factorize sparse

matrices. The use of variable reordering significantly improves the computation and memory requirements for matrix decomposition methods [65], [66].

The nested dissection variable reordering scheme was initially proposed for solving a system of equations for $n \times n$ grid problems arising from finite-element discretization of a mesh [64]. It partitions the graph with “+” shapes, as shown in Figure 13. Each resulting block is then recursively partitioned with a “+” shape. The number on each partition corresponds to the entry in the coefficient matrix. Helmert's proposal to divide a triangulation net recursively along latitudes and longitudes was used by Avila and Tomlin [67] for solving large least squares using the ILLIAC IV parallel processor for optimizing geodetic networks. Later,

Golub and Plemmons [68] used the Helmert blocking variable ordering strategy for solving a large system of equations using orthogonal decomposition techniques, such as QR decomposition for the system of equations arising from the geodetic network.

Given that Helmert's proposal and the nested dissection algorithm are so similar, researchers performed a study to understand the best way to create the separators and to join the blocks given a four-way partitioning for NAD 83 [5]. Figure 14 shows four ways of joining a block partitioned into four subblocks. The partitioning can be done using either Helmert's strategy or nested dissection. The key design choice is whether to use a deep tree or broad tree strategy, as shown in Figure 15. The deep tree strategy creates smaller and denser final blocks, while broad trees result in larger and sparser blocks. This can be observed from Figure 15(a) and (b) for a simple example. The large sparse matrix in the broad tree strategy implies further variable reordering to minimize the matrix fill-in. In the deep tree strategy, parallelism can be better exploited, but it requires more matrix allocations. In the simple example shown in Figure 15, seven matrices are allocated for the deep tree compared with five allocations for the broad tree strategy. Hence, the deep tree strategy was preferred for NAD 83 to enable more parallelism and because the created, dense subblocks do not require further reordering.

Removing Outliers for Geodetic Mapping

The task of traditional geodetic mapping involves hundreds of surveyors working in parallel to obtain measurements. This also results in many faulty constraints [5]. The typical sources of faulty constraints are human errors, errors in instruments, and sometimes errors when transferring entries from physical journals into the database management systems. For NAD 83, erroneous constraints are detected and removed through a block validation process.

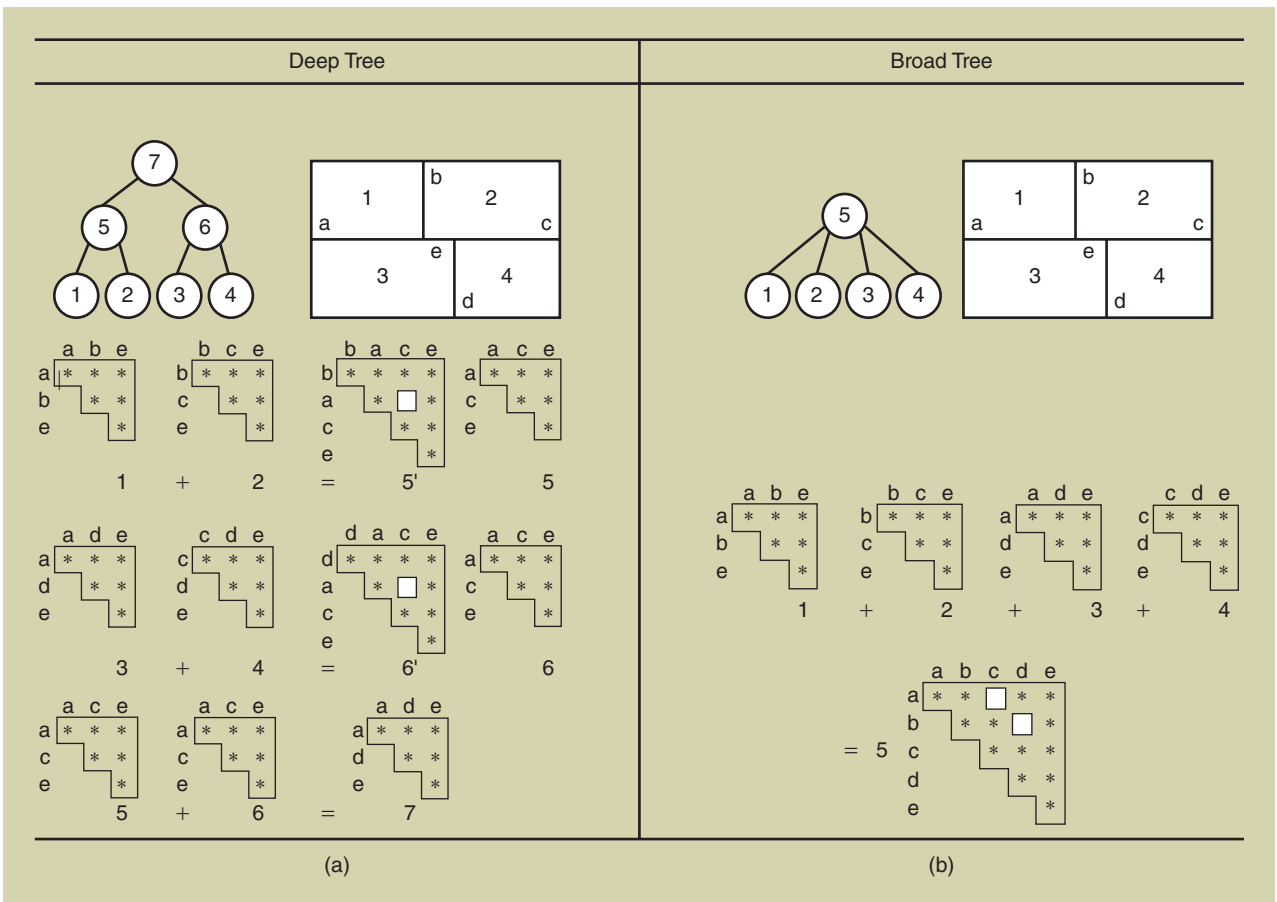


Figure 15. A comparison between (a) deep tree and (b) broad tree ordering according to [5]. The area is partitioned into four blocks labeled 1, 2, 3, and 4. Separator variables are represented by $a-e$. The variable set e are separators with constraints in all four blocks, a are variables with constraints only between blocks 1 and 3, b are variables constraining between blocks 1 and 2 only, and so on. In this example, the deep tree approach would merge two subgraphs at a time, while the broad tree approach merges four subgraphs at a time. In both methods, all low-level subgraphs labeled 1–4 are processed in parallel. The deep tree method requires two more matrix allocations compared to the broad tree approach, but the broad tree approach results in a larger matrix with zero blocks, which require additional variable reordering to reduce computation.

The block validation process validates constraints and towers in small geographical regions, one block at a time. The blocks are created by a geographical partitioning of stations, as shown in Figure 16. These also represent the lowest level of Helmert blocks.

The block validation process consists of two iterating steps: 1) by identifying underconstrained nodes and 2) by checking for outliers given small blocks of nodes. If any node in a block is underconstrained, either additional constraints are added from neighboring blocks or the node is removed from the block. This avoids any singularities within the least-squares solution. After this issue is resolved, the block is optimized and all constraints having a weighted residual error of greater than three ($\chi^2 > 3$) are evaluated. These are regarded as possible erroneous constraints. A constraint with a large residual error ($\chi^2 > 3$) is deleted if there is another constraint between the same nodes having a similar sensor modality but a smaller residual error. A constraint with high residual error is also deleted if there are additional constraints between other nodes capable of constraining the nodes under consideration. If no additional constraints are found, the standard deviation of the

possible outlier constrained is doubled until ($\chi^2 > 3$). In other words, the assumed sensor noise for this constraint is increased, which is a similar principle behind m-estimators in robust statistics [69], [70].

The whole process of optimizing a subblock and evaluating constraints with a large error is repeated until the block is free of outliers. For NAD 83, a total of 843 blocks were evaluated using block validation methods, as shown in Figure 16. Each block consisted of 300–500 nodes and required roughly one person month to validate [5]. This process for outlier detection was also used as recently as 2007 for NAD83 (NSRS2007), where seven trial solutions were carried out to account for outliers and singularities and handle weakly determined areas [49].

Relation to SLAM Back Ends

The use of sparse linear algebra and matrix decomposition methods has been introduced in robotics only recently [21], [22], [31], [71]. In contrast to that, the geodetic scholars were using LU, QR, and Cholesky decomposition for a long time—Cholesky decomposition was actually developed for geodetic mapping purposes. This section aims at

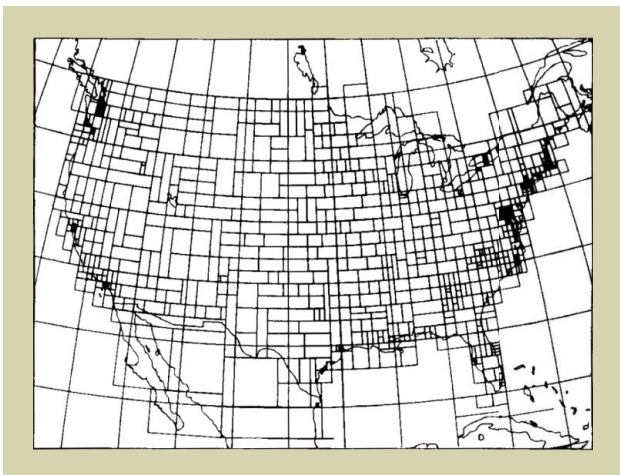


Figure 16. The boundaries of blocks of data used in the block validation process. (Image courtesy of [5].)

highlighting some of the similarities between the methods developed by both communities.

Hierarchical and Submap-Based SLAM Methods

Grisetti et al. [27] propose an efficient hierarchical multilevel method for optimizing pose graphs. The higher the level in the hierarchy, the smaller the pose graph. At each level, a subgraph from a lower level is represented by a single node on the higher level. The optimization is primarily carried out at the higher levels and only propagated down to the lower level if there is a significant update to the pose of a node. Each edge in the higher level is computed via a new deduced virtual measurement, which is created after a local optimization. The gain in speed by this method results from the fact that computationally expensive optimization is only performed when the pose of a node in the coarse representation gets affected more than a certain threshold (which we chose as 5 cm or 0.05°). There also exists an extension to general SLAM graphs and bundle adjustment problems [16].

The virtual measurements created by Grisetti et al. are similar in idea to those in the Bowie method explained in the “The Bowie Method” section. The Bowie method creates a two-level hierarchy instead of the multiple levels as in [27]. Both methods use a single node from a dense subgraph in the higher coarser level and add a virtual deduced measurement between the smaller new problem instances. A difference is that, given a geodetic network consisting of sections, each edge in the Bowie method represents a subgraph, whereas in the hierarchical approach of Grisetti et al., only nodes represent subgraphs. Furthermore, Grisetti et al. compute the uncertainty of a virtual constraint explicitly.

In addition, Ni et al. [42] and Ni and Dellaert [43] propose back ends, which divide the original problem into multiple smaller subproblems. These smaller problems are then optimized in parallel. The first approach [42] partitions the problem into a single level of submaps, while [43] partitions each map recursively multiple times. The speedup is mainly

due to caching the linearization result of each subgraph. In both methods, all nodes in a subgraph are expressed with respect to a single base node. This allows for efficiently reusing the linearization of the constraints within each subgraph. This insight results in a reduction of the total computation time. Boundary nodes and constraints connecting multiple subgraphs need to be recomputed at each iteration, while the results for nodes within a subgraph can be reused. The methods of Ni et al. would result in a batch solution if each nonlinear constraint within a subgraph is relinearized at every iteration, but they show experimentally that, by not doing so, a high speedup in optimization time is achieved at the expense of very small errors.

The submap methods proposed by Ni et al. show many similarities to Helmert’s approach of partitioning the triangle nets into subnets. The idea of anchoring submaps in [43] has a similar motivation as Bowie’s idea for anchoring junctions and moving them as a whole by shifting the anchor nodes and not reoptimizing each subgraph. Krauthausen et al. [72] prove that approximately planar SLAM graphs can be optimized in $O(n^{1.5})$ using the nested dissection reordering. The nested-dissection algorithm, which is at the heart of [43] and [72], is similar to Helmert’s strategy of recursively partitioning a planar triangulation net [68]. Furthermore, the out-of-core parallel Cholesky decomposition-based nonlinear solver for geodetic mapping proposed by Avila and Tomlin [67] uses Helmert blocking and is thus strongly connected to [43]. It should, however, be noted that the geodetic community was generating the partitioning manually with domain knowledge and that the triangle nets have a simpler and more planar structure than typical SLAM graphs.

Stochastic Methods

Olson et al. [36] propose a stochastic gradient descent for solving pose graphs with a bad initialization. They reparameterize the constraints from a global pose to a relative pose representation. In the global pose, all positional nodes are represented with global coordinates in the world frame, whereas, in the relative pose representation, each pose is represented with respect to its previous pose in the odometry chain. This allows the authors to distribute the errors of each constraint within the loop induced by it. Grisetti et al. [37], [73] improve this approach using a tree parameterization based on a spanning tree instead of the odometry chain. The basic idea of both approaches is to stochastically select a constraint and move nodes based on the parameterization to reduce the error induced by the constraint. A learning rate controls the step size and is gradually decreased to prevent oscillations. Both approaches also assume spherical covariances and intelligent data structures to efficiently distribute the errors. These methods are also capable of online and incremental approaches by increasing the learning rate for active areas [38], [39], [74].

A major intuition of using stochastic methods is equating error around a loop to zero. This is somewhat similar

to the motivation for the modified Bowie method, where one virtual equation is set up for each loop in the sparse mesh and the error around every loop is equated to zero. Examples of distributing errors around loops have also been explored in the “zero-sum property” of [15] and “trajectory bending” of [75].

The Indian method of 1938 [62] described in the “The Indian Method of 1938” section has a similar motivation to the stochastic methods described above. In the Indian method, an initial spanning tree is manually chosen, which is a similar initialization strategy than the one of Grisetti et al. The Indian method as a whole, however, is rather informal and distributes the errors manually in a trial-and-error fashion. In contrast to that, Olson et al. and Grisetti et al. minimize the error using stochastic gradient descent and provide a more formal treatment of the approach.

Robust Methods for Outlier Rejection

For quite a while, SLAM back ends suffered from data association failures that result in incorrect constraints between nodes in the graph. Recently, a set of different approaches was proposed that are robust even if a substantial number of constraints are outliers.

Latif et al. [13] propose Realizing, Reversing, Recovering (RRR), which is a robust SLAM back end, capable of rejecting false constraints. RRR first clusters mutually consistent and topological related constraints together. Each cluster is checked for introcluster consistency by comparing the residual of each constraint with a theoretical bound. Constraints that do not satisfy the bound are removed. This approach is similar to the block validation technique used for NAD 83. The individual blocks in block validation and the clusters in RRR conceptually represent similar subgraphs. The blocks are geographical partitions, but are actually a set of nodes and constraints similar to what clusters represent in RRR. Again, it should be noted that the triangular networks of the geodetic community have a simpler structure than SLAM graphs, and, thus, the verification step is easier to conduct.

The dynamic covariance scaling (DCS) approach by Agarwal et al. [14] is a robust back end that is able to reject outliers by scaling the covariance of the outlier constraint. DCS can be formulated as a generalization of switchable constraints [12], another state-of-the-art back end for robust operation in the presence of outliers. In DCS, the covariance matrix of constraints with large residuals is scaled such that the error stays within a certain bound. This is related to the “doubling of standard deviation of each constraint” strategy used in [5]. It is, however, not clear if and how the scaling in NAD 83 was modified between different iterations.

Linear SLAM

A good initial guess is critical for iterative nonlinear methods to converge to the correct solution. For providing a good initialization, Carlone et al. [15] propose a linear approximation for planar pose graphs. Their approach yields an approxi-

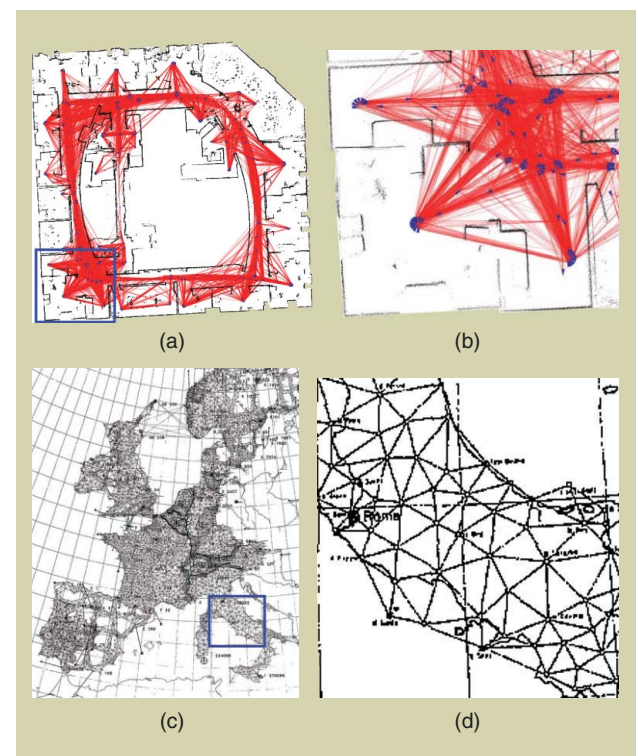


Figure 17. The intuitive illustration of planarity of geodetic triangle net compared to a SLAM graph: (a) The intel data set with 875 robot positions and 15,675 constraints and (b) a zoomed-in section. The robot positions are shown as blue triangles and constraints in red. The zoomed-in section of the bottom left portion intuitively shows the nonplanarity of a SLAM graph. (c) The triangle net for ED87 and (d) a zoomed-in section for Italy. The constraints covering Italy intuitively show that triangle nets used for geodesy were almost planar. (Images courtesy of [47].)

mate solution to the nonlinear problem without any initial guess and, thus, can be used as a high-quality initial guess for state-of-the-art back ends. Carlone et al. formulate the SLAM problem in terms of graph-embedding and suggest partitioning the system of equations into

$$A_2^T \rho = R(\theta) \Delta^l \quad (17)$$

$$A_2^T \theta = \delta. \quad (18)$$

Here, θ contains angular unknowns and ρ represents the positional unknowns. The terms A_1 and A_2 are their respective coefficient matrices, Δ^l and δ are the corresponding constraint residuals, and $R(\theta)$ is the stacked rotation matrix. Equation (18) is solved first, and the computed value of θ is used for solving (17). The authors provide a theoretical proof and real-world examples for the algorithm in [15].

Related to linear SLAM, Boltz was reordering the equations in (15) and eliminating angular unknowns first. His motivation was to cache matrix inversions for a faster human lookup, but geodetics used it not only for gains in speed but also because it “did not bias the solution toward any particular unknown like Gaussian elimination” [61]. In our geodetic

survey, we did not find any proof for this statement, but, as both approaches share similarities, we suspect that this statement is related to the properties of linear SLAM. The theoretical justification of [15] also holds in the case of Boltz's reordering of eliminating angular constraints first.

Dense Subblocks

Reference [5] describing NAD 83 offers several interesting aspects ranging from database management to memory and cache-friendly algorithms. During the project, engineers used punch card machines, which are rather inconvenient and cumbersome tools for solving large matrix problems compared with modern computers. A physical file management system and efficient card storage are reminiscent of sophisticated techniques used in modern software. We have decided to not discuss all topics in detail here, but, in essence, the NAD 83 engineers were arranging data similar to the block matrix representations. The punch cards describing the data comprising the station positions and constraints were also physically stored as low-level Helmert blocks. All punch cards corresponding to a single block were stored together for faster retrieval.

Such dense subblocks are central elements in some of the fastest SLAM back ends. Konolige et al. [10] describes a 2-D SLAM implementation, where the computation time is significantly reduced by storing each Jacobian as a 3×3 block matrix. Kummerle et al. [71] generalize the block storage and indexing strategy for 6×6 and other types of feature nodes. Finally, most modern graph-based SLAM implementations use the Cholesky decomposition algorithm from the suitesparse library by Davis [76]. The fastest supernodal Cholesky decomposition routine, CHOLMOD, also exploits dense subblocks [77].

Further Remarks

As an additional note, the Cholesky decomposition, which is commonly used in error minimization, was developed in the early 1900s by Cholesky for geodesy and map building while he was in the French Geodetic Section. The χ^2 distribution was also published by Helmert in [78]. This is further elaborated in [79], and the details with respect to Pearson's report can be found in [80, Sec. 7.3].

Discussion

Although there are similarities between the problems of both communities, it is also important to highlight the additional challenges that autonomous robots, which rely on working SLAM solutions, face compared with geodetic mapping. First, SLAM systems are completely autonomous, while geodetic mapping inherently involves humans at all levels of the process. It is difficult for automated front-end data-association methods to distinguish between visually similar but physically different places, and this is likely to occur, for example, in large manmade buildings. Perceptual aliasing creates false constraints, which often introduce errors in the localization and map building process.

Second, the quality of the initial guess is often different. The initial guess that is available for geodetic triangle networks is typically substantially better than the pose initializations of typical wheeled robots using odometry as well as flying or walking robots. A good initial guess substantially simplifies and even enables the use of polygon filling and other types of approximations.

Third, the geodetic triangle networks are almost planar, while most SLAM graphs are not. This can be intuitively observed from Figure 17. In addition, Eiffel-tower-type landmarks that connect all poses create highly nonplanar SLAM graphs [81]. Helmert's simple partitioning scheme of segmenting along latitudes and longitudes works for geodetic networks because the graphs are almost planar. Krauthausen et al. [72] prove that planar or approximately planar SLAM graphs can be optimized in $O(n^{1.5})$ by using the nested dissection reordering. Comparable results can be expected for Helmert's blocking strategy as both are rather similar [67]. The way most modern SLAM methods work, however, leads to a highly nonplanar graph with a high crossing number [82].

Conclusions

This article provides a survey of geodetic mapping methods and aims at providing a geodetic perspective on SLAM. We showed that both fields share similarities when it comes to the error minimization task: maps are large, computational resources are limited and incremental methods are required, nonlinear constraints require iterative procedures, and data associations are erroneous. There are, however, also differences: geodetic triangular nets have a simpler structure that can be exploited in the optimization, methods for robotics must be completely autonomous while the geodetic surveys always have humans in the loop, and often the geodetic community had a better initial configuration from the start.

Besides the elaborated similarities and differences between geodetic mapping and SLAM, we surveyed several core techniques developed by the geodetic community and related them to state-of-the-art SLAM methods. The central motivation for this article is to connect both fields and enable future synergies among them. While surveying the geodetic methods, we experienced strong respect toward the geodetic scholars. Their achievements, especially given their lack of computational resources, are outstanding.

SLAM researchers have often gone back to the graph theory and sparse linear algebra community for efficient algorithms. It is probably worth also looking into the geodetic mapping literature given that they addressed large-scale error minimization and developed highly innovative solutions to solve them. Several research activities by linear algebra researchers have been motivated by the large problem instances of geodetic mapping.

There might still be more methods in geodetic mapping that are unknown outside their community but could inspire other fields. Interested readers should begin with the excellent document by Schwarz [5] on the history of NAD 83.

Acknowledgments

We would like to thank Edwin Olson for introducing the work of Schwarz [5] to us and our librarian Susanne Hauser for locating some of the old geodetic journals and manuscripts. We would also like to thank Google Scholar for helping us find several of the discussed articles. Thanks are also due to Heiner Kuhlmann, Giorgio Grisetti, Steffen Gutmann, and Frank Dellaert as well as the reviewers for their valuable feedback. This work was partly supported by the European Commission under FP7-600890-R0VINA and ERG-AG-PE7- 267686-LifeNav and by the BMBF under contract number 13EZ1129B-iView.

References

- [1] F. Lu and E. Milios, "Globally consistent range scan alignment for environment mapping," *Auton. Robot.*, vol. 4, no. 4, pp. 333–349, 1997.
- [2] J. Folkesson and H. I. Christensen, "Graphical SLAM—A self-correcting map," in *Proc. IEEE Int. Conf. Robotics Automation*, 2004, pp. 383–390.
- [3] S. Thrun and M. Montemerlo, "The GraphSLAM algorithm with applications to large-scale mapping of urban structures," *Int. J. Robot. Res.*, vol. 25, nos. 5–6, pp. 403–429, 2006.
- [4] G. Grisetti, R. Kümmerle, C. Stachniss, and W. Burgard, "A tutorial on graph-based SLAM," *IEEE Intell. Transp. Syst. Mag.*, vol. 2, no. 4, pp. 31–43, 2010.
- [5] C. R. Schwarz, "North American Datum of 1983," in *Charting and Geodetic Services, National Ocean Service: For Sale by the National Geodetic Information Center*, NOAA, vol. 1. Rockville, MD: National Geodetic Survey, 1989.
- [6] F. Helmert, *Die Mathematischen Und Physikalischen Theorien Der Hoheren Geodasie-Einleitung*. Leipzig, Germany: B.G. Teubner, 1880.
- [7] P. Agarwal, W. Burgard, and C. Stachniss, "Helmert's and Bowie's geodetic mapping methods and their relationship to graph-based SLAM," in *Proc. IEEE Int. Conf. Robotics Automation*, 2014.
- [8] G. B. Kolata, "Geodesy: Dealing with an enormous computer task," *Science*, vol. 200, no. 4340, pp. 421–466, 1978.
- [9] H. Johannsson, M. Kaess, M. Fallon, and J. J. Leonard, "Temporally scalable visual SLAM using a reduced pose graph," in *Proc. IEEE Int. Conf. Robotics Automation*, 2013, pp. 54–61.
- [10] K. Konolige, G. Grisetti, R. Kümmerle, W. Burgard, B. Limketkai, and R. Vincent, "Efficient sparse pose adjustment for 2D mapping," in *Proc. IEEE/RSJ Int. Conf. Intelligent Robots Systems*, 2010, pp. 22–29.
- [11] E. Olson and P. Agarwal, "Inference on networks of mixtures for robust robot mapping," in *Proc. Robotics: Science Systems*, 2012, pp. 313–320.
- [12] N. Sünderhauf and P. Protzel, "Towards a robust back end for pose graph SLAM," in *Proc. IEEE Int. Conf. Robotics Automation*, 2012, pp. 1254–1261.
- [13] Y. Latif, C. C. Lerma, and J. Neira, "Robust loop closing over time," in *Proc. Robotics: Science Systems*, 2012, pp. 233–240.
- [14] P. Agarwal, G. D. Tipaldi, L. Spinello, C. Stachniss, and W. Burgard, "Robust map optimization using dynamic covariance scaling," in *Proc. IEEE Int. Conf. Robotics Automation*, 2013, pp. 62–69.
- [15] L. Carlone, R. Aragues, J. Castellanos, and B. Bona, "A linear approximation for graph-based simultaneous localization and mapping," in *Proc. Robotics: Science and Systems*, 2011, pp. 41–48.
- [16] G. Grisetti, R. Kummerle, and K. Ni, "Robust optimization of factor graphs by using condensed measurements," in *Proc. IEEE/RSJ Int. Conf. Intelligent Robots Systems*, 2012, pp. 581–588.
- [17] H. Wang, G. Hu, S. Huang, and G. Dissanayake, "On the structure of nonlinearities in pose graph SLAM," in *Proc. Robotics: Science Systems*, 2012, pp. 425–432.
- [18] L. Carlone, "A convergence analysis for pose graph optimization via Gauss-Newton methods," in *Proc. IEEE Int. Conf. Robotics Automation*, 2013, pp. 965–972.
- [19] G. Hu, K. Khosoussi, and S. Huang, "Towards a reliable SLAM back end," in *Proc. IEEE/RSJ Int. Conf. Intelligent Robots Systems*, 2013, pp. 37–43.
- [20] P. Agarwal, G. Grisetti, G. D. Tipaldi, L. Spinello, W. Burgard, and C. Stachniss, "Experimental analysis of dynamic covariance scaling for robust map optimization under bad initial estimates," in *Proc. IEEE Int. Conf. Robotics Automation*, 2014.
- [21] M. Kaess, A. Ranganathan, and F. Dellaert, "Fast incremental square root information smoothing," in *Proc. Int. Joint Conf. Artificial Intelligence*, 2007, pp. 2129–2134.
- [22] M. Kaess, H. Johannsson, R. Roberts, V. Ila, J. Leonard, and F. Dellaert, "iSAM2: Incremental smoothing and mapping using the Bayes tree," *Int. J. Robot. Res.*, vol. 31, no. 2, pp. 216–235, 2012.
- [23] F. Lu and E. Milios, "Robot pose estimation in unknown environments by matching 2D range scans," in *Proc. IEEE Computer Society Conf. Computer Vision Pattern Recognition*, 1994, pp. 935–938.
- [24] P. Biber and W. Straßer, "The normal distributions transform: A new approach to laser scan matching," in *Proc. IEEE/RSJ Int. Conf. Intelligent Robots Systems*, 2004, vol. 3, pp. 2743–2748.
- [25] E. Olson, "Real-time correlative scan matching," in *Proc. IEEE Int. Conf. Robotics Automation*, Kobe, Japan, June 2009, pp. 4387–4393.
- [26] G. D. Tipaldi, L. Spinello, and W. Burgard, "Geometrical FLIRT phrases for large scale place recognition in 2D range data," in *Proc. IEEE Int. Conf. Robotics Automation*, Karlsruhe, Germany, 2013.
- [27] G. Grisetti, R. Kümmerle, C. Stachniss, U. Frese, and C. Hertzberg, "Hierarchical optimization on manifolds for online 2D and 3D mapping," in *Proc. IEEE Int. Conf. Robotics Automation*, 2010, pp. 273–278.
- [28] C. Hertzberg, "A framework for sparse, non-linear least squares problems on manifolds," M.S. thesis, Dept. Comput. Sci., Univ. Bremen, Bremen, Germany, 2008.
- [29] J.-S. Gutmann and K. Konolige, "Incremental mapping of large cyclic environments," in *Proc. IEEE Int. Symp. Computational Intelligence*, 1999, pp. 318–325.
- [30] K. Konolige, "Large-scale map-making," in *Proc. Nat. Conf. Artificial Intelligence*, 2004, pp. 457–463.
- [31] F. Dellaert and M. Kaess, "Square root SAM: Simultaneous localization and mapping via square root information smoothing," *Int. J. Robot. Res.*, vol. 25, no. 12, pp. 1181–1203, 2006.
- [32] M. Kaess, A. Ranganathan, and F. Dellaert, "iSAM: Fast incremental smoothing and mapping with efficient data association," in *Proc. IEEE Int. Conf. Robotics Automation*, 2007, pp. 1670–1677.
- [33] A. Howard, M. J. Mataric, and G. Sukhatme, "Relaxation on a mesh: A formalism for generalized localization," in *Proc. IEEE/RSJ Int. Conf. Intelligent Robots Systems*, 2001, vol. 2, pp. 1055–1060.
- [34] T. Duckett, S. Marsland, and J. Shapiro, "Learning globally consistent maps by relaxation," in *Proc. IEEE Int. Conf. Robotics Automation*, San Francisco, CA, 2000, vol. 4, pp. 3841–3846.
- [35] U. Frese, P. Larsson, and T. Duckett, "A multilevel relaxation algorithm for simultaneous localization and mapping," *IEEE Trans. Robot.*, vol. 21, no. 2, pp. 196–207, Apr. 2005.
- [36] E. Olson, J. Leonard, and S. Teller, "Fast iterative optimization of pose graphs with poor initial estimates," in *Proc. IEEE Int. Conf. Robotics Automation*, 2006, pp. 2262–2269.
- [37] G. Grisetti, C. Stachniss, S. Grzonka, and W. Burgard, "A tree parameterization for efficiently computing maximum likelihood maps using gradient descent," in *Proc. Robotics: Science Systems*, 2007, pp. 65–72.
- [38] E. Olson, J. Leonard, and S. Teller, "Spatially-adaptive learning rates for online incremental SLAM," in *Proc. Robotics: Science Systems*, 2007.
- [39] G. Grisetti, D. L. Rizzi, C. Stachniss, E. Olson, and W. Burgard, "Online constraint network optimization for efficient maximum likelihood map learning," in *Proc. IEEE Int. Conf. Robotics Automation*, 2008, pp. 1880–1885.
- [40] M. Bosse, P. Newman, J. Leonard, and S. Teller, "Simultaneous localization and map building in large-scale cyclic environments using the Atlas framework," *Int. J. Robot. Res.*, vol. 23, no. 12, pp. 1113–1139, Dec. 2004.
- [41] C. Estrada, J. Neira, and J. Tardós, "Hierarchical SLAM: Real-time accurate mapping of large environments," *IEEE Trans. Robot.*, vol. 21, no. 4, pp. 588–596, 2005.
- [42] K. Ni, D. Steedly, and F. Dellaert, "Tectonic SAM: Exact; out-of-core; submap-based SLAM," in *Proc. IEEE Int. Conf. Robotics Automation*, 2007, pp. 1678–1685.
- [43] K. Ni and F. Dellaert, "Multi-Level submap based SLAM using nested dissection," in *Proc. IEEE/RSJ Int. Conf. Intelligent Robots Systems*, 2010, pp. 2558–2565.

- [44] L. Paz, J. Neira, and J. Tardós, "Divide and conquer: EKF SLAM in O(n)," *IEEE Trans. Robot.*, vol. 24, no. 5, pp. 1107–1120, 2008.
- [45] Natural Resources Canada. (2009). 100 years of geodetic surveys in Canada. [Online]. Available: http://www.geod.nrcan.gc.ca/timeline/timeline_e.php
- [46] R. K. Burkard. (1983). Geodesy for the layman. U.S. Dept. Commerce, Natl. Atmos. Administration, St. Louis, MO. [Online]. Available: http://www.ngs.noaa.gov/PUBS_LIB/HARN_CORS_COMP/eval_harn_to_cors.html
- [47] W. Ehrnsperger, "The ED87 adjustment," *J. Geodesy*, vol. 65, no. 1, pp. 28–43, 1991.
- [48] K. O. Milbert. An evaluation of the high accuracy reference network relative to the continuously operating reference stations. *National Geodetic Survey, National Ocean Service*, NOAA. [Online]. Available: http://www.ngs.noaa.gov/PUBS_LIB/HARN_CORS_COMP/eval_harn_to_cors.html
- [49] D. G. Pursell and M. Potterfield. (2008). NAD 83(NSRS2007) national readjustment final report. Natl. Ocean. Atmos. Administration, National Ocean Service. Silver Spring, MD. Tech. Rep. NOS NGS 60. [Online]. Available: http://www.ngs.noaa.gov/PUBS_LIB/NSRS2007/NOAATRNOSNGS60.pdf
- [50] H. Wolf, "Triangulation adjustment general discussion and new procedure," *Bull. Géodésique*, vol. 16, no. 1, pp. 87–104, 1950.
- [51] J. D. Bossler, "Geodesy solves 900,000 equations simultaneously," *Eos, Trans. Amer. Geophys. Union*, vol. 68, no. 23, pp. 569–569, 1987.
- [52] Aeronautical Chart and Information Center, *Preface and Part I: The Mathematical Theories*, St. Louis, MO, 1964.
- [53] B. Triggs, P. F. McLauchlan, R. I. Hartley, and A. W. Fitzgibbon, "Bundle adjustment modern synthesis," in *Vision Algorithms: Theory and Practice*. Berlin Heidelberg, Germany: Springer-Verlag, 2000, pp. 298–372.
- [54] H. Wolf, "The Helmert block method, its origin and development," in *Proc. 2nd Int. Symp. Problems Related to the Redefinition of North American Geodetic Networks*, 1978, pp. 319–326.
- [55] F. W. Hough, "The adjustment of the Central European triangulation network," *Bull. Géodésique*, vol. 7, no. 1, pp. 64–93, 1948.
- [56] O. S. Adams, *The Bowie Method of Triangulation Adjustment, as Applied to the First-Order Net in the Western Part of the United States*. Washington, D.C.: U.S. Govt. Print. Office, 1930.
- [57] H. Wolf, "Gaußscher algorithmus (Doolittle-Methode) und Boltzsches Entwicklungsvorfahren," *Bull. Géodésique*, vol. 26, no. 1, pp. 445–452, 1952.
- [58] H. Boltz, *Entwickelungs-Verfahren zum Ausgleichen Geodätischer Netze nach der Methode der kleinsten Quadrate*. Potsdam, Germany: Veröffentlichungen des Geodätischen Instituts Potsdam, 1923, no. 90.
- [59] H. Boltz, *Substitutions-Verfahren zum Ausgleichen grosser Dreiecksnetze in einem Guss nach der Methode der kleinsten Quadrate*. Potsdam, Germany: Veröffentlichungen des Geodätischen Instituts Potsdam, 1938, no. 108.
- [60] K. Kersting, "Lifted probabilistic inference," in *Proc. 20th European Conf. Artificial Intelligence*, 2012, pp. 33–38.
- [61] American Congress on Surveying, American Society for Photogrammetry and Remote Sensing, and American Society of Civil Engineers, *The Glossary of the Mapping Sciences*, American Society of Civil Engineers, Bethesda, MD, 1994.
- [62] G. Bomford, "The readjustment of the Indian triangulation," Professional Paper No. 28, Survey of India, Dehra Dun, 1939.
- [63] G. Bomford, *Geodesy*. London, United Kingdom: Oxford Univ. Press, 1952.
- [64] A. George, "Nested dissection of a regular finite element mesh," *SIAM J. Numer. Anal.*, vol. 10, no. 2, pp. 345–363, 1973.
- [65] T. A. Davis, *Direct Methods for Sparse Linear Systems*, vol. 2. Philadelphia, PA: Soc. Ind. Appl. Math., 2006.
- [66] P. Agarwal and E. Olson, "Variable reordering strategies for SLAM," in *Proc. IEEE/RSJ Int. Conf. Intelligent Robots Systems*, Oct. 2012, pp. 3844–3850.
- [67] J. Avila and J. Tomlin, "Solution of very large least squares problems by nested dissection on a parallel processor," in *Proc. 12th Symp. Interface*, 1979, pp. 9–14.
- [68] G. H. Golub and R. J. Plemmons, "Large-scale geodetic least-squares adjustment by dissection and orthogonal decomposition," *Linear Algebra Appl.*, vol. 34, pp. 3–28, Dec. 1980.
- [69] R. Hartley and A. Zisserman, *Multiple View Geometry in Computer Vision*, 2nd ed. Cambridge, U.K.: Cambridge Univ. Press, 2004.
- [70] Z. Zhang, "Parameter estimation techniques: A tutorial with application to conic fitting," *Image Vis. Comput. J.*, vol. 15, no. 1, pp. 59–76, 1997.
- [71] R. Kümmerle, G. Grisetti, H. Strasdat, K. Konolige, and W. Burgard, "G2o: A general framework for graph optimization," in *Proc. IEEE Int. Conf. Robotics Automation*, 2011, pp. 3607–3613.
- [72] P. Krauthausen, F. Dellaert, and A. Kipp, "Exploiting locality by nested dissection for square root smoothing and mapping," in *Proc. Robotics: Science Systems*, 2006, pp. 73–80.
- [73] G. Grisetti, C. Stachniss, and W. Burgard, "Nonlinear constraint network optimization for efficient map learning," *IEEE Trans. Intell. Transport. Syst.*, vol. 10, no. 3, pp. 428–439, 2009.
- [74] G. Grisetti, S. Grzonka, C. Stachniss, P. Pfaff, and W. Burgard, "Efficient estimation of accurate maximum likelihood maps in 3D," in *Proc. IEEE/RSJ Int. Conf. Intelligent Robots Systems*, 2007, pp. 3472–3478.
- [75] G. Dubbelman, P. Hansen, B. Browning, and M. B. Dias, "Orientation only loop-closing with closed-form trajectory bending," in *Proc. IEEE Int. Conf. Robotics Automation*, 2012, pp. 815–821.
- [76] T. Davis. (2006). SuiteSparse. [Online]. Available: <http://www.cise.ufl.edu/research/sparse/SuiteSparse/>
- [77] Y. Chen, T. A. Davis, W. W. Hager, and S. Rajamanickam, "Algorithm 887: CHOLMOD, supernodal sparse cholesky factorization and update/downdate," *ACM Trans. Math. Softw.*, vol. 35, no. 3, pp. 22:1–22:14, 2008.
- [78] F. Helmert, "Über die Wahrscheinlichkeit der Potenzsummen der Beobachtungsfehler und über einige damit im Zusammenhang stehende Fragen," *Zeitschrift für Mathematik und Physik*, vol. 21, pp. 192–218, 1876.
- [79] W. Kruskal, "Helmert's distribution," *Amer. Math. Monthly*, vol. 53, no. 8, pp. 435–438, 1946.
- [80] O. Sheynin, "Helmert's work in the theory of errors," *Arch. History Exact Sci.*, vol. 49, no. 1, pp. 73–104, 1995.
- [81] F. Dellaert, J. Carlson, V. Ila, K. Ni, and C. E. Thorpe, "Subgraph-preconditioned conjugate gradients for large scale SLAM," in *Proc. IEEE/RSJ Int. Conf. Intelligent Robots Systems*, 2010, pp. 2566–2571.
- [82] P. Hliněný and G. Salazar, "On the crossing number of almost planar graphs," in *Graph Drawing*. Berlin Heidelberg, Germany: Springer-Verlag, 2007, pp. 162–173.

Pratik Agarwal, University of Freiburg, Institute of Computer Science, 79110 Freiburg, Germany. E-mail: agarwal@informatik.unifreiburg.de.

Wolfram Burgard, University of Freiburg, Institute of Computer Science, 79110 Freiburg, Germany. E-mail: burgard@informatik.unifreiburg.de.

Cyrill Stachniss, University of Freiburg, Institute of Computer Science, 79110 Freiburg, Germany, and University of Bonn, Institute of Geodesy and GeoInformation, 53115 Bonn, Germany. E-mail: cyrill.stachniss@igg.unibonn.de.

Optical Tweezers

Autonomous Robots for the Manipulation of Biological Cells

By Ashis Gopal Banerjee,
Sagar Chowdhury, and
Satyandra K. Gupta

Optical tweezers (OTs) are a popular tool for manipulating biological objects, especially cells [1], [2]. Using a tightly focused laser beam, they exert sufficient forces to tweeze, i.e., hold (trap) and move, freely diffusing cells in the vicinity of the beam focus. The beam can be focused at any point in the workspace, which is typically a liquid-filled glass slide. The trapped cell can, thus, be translated and rotated (transported) in three dimensions by changing the beam focus position. OTs provide certain advantages over other cell-manipulation techniques. They are able to manipulate cells with a greater degree of precision as compared with microfluidic flow. Significant contact forces are not exerted on the cells, unlike in mechanical manipulation, thereby avoiding damages due to contact friction or surface chemistry. The cells are also easily released at the end of the manipulation by simply switching off the laser beam. Hence, OTs have been extensively used for mechanical characterization of cells by measuring their viscoelastic properties to distinguish between normal and diseased cells [3]. They have also been used for separating cells of different types [4] and investigating the response of cells to external stimuli [5]. However, manual or teleoperated control of the laser beam has limited their applicability for multicellular studies.

Over the past decade or so, researchers have started using OTs as an autonomous microrobot [6]–[11]. Like any conventional robot, an OT system comprises an actuator, sensor, and controller. While sensing is done by a video camera and the controller hardware that sets the laser beam intensity, the focal position and speed are standard, and actuation is performed using optical forces. The laser beam acts as the manipulator hand; it is focused using a high-numerical-aperture objective lens that functions as the end effector. A computer-generated hologram [12], which can be dynamically reconfigured in real time, is commonly used to split the beam into multiple components with complete control over the focal positions of the individual beams in three dimensions. Thus, each split beam functions as an

Digital Object Identifier 10.1109/MRA.2014.2332407
Date of publication: 20 August 2014

© ISTOCKPHOTO.COM/ANTISHOCK

1070-9932/14 ©2014 IEEE

SEPTEMBER 2014 • IEEE ROBOTICS & AUTOMATION MAGAZINE • 81

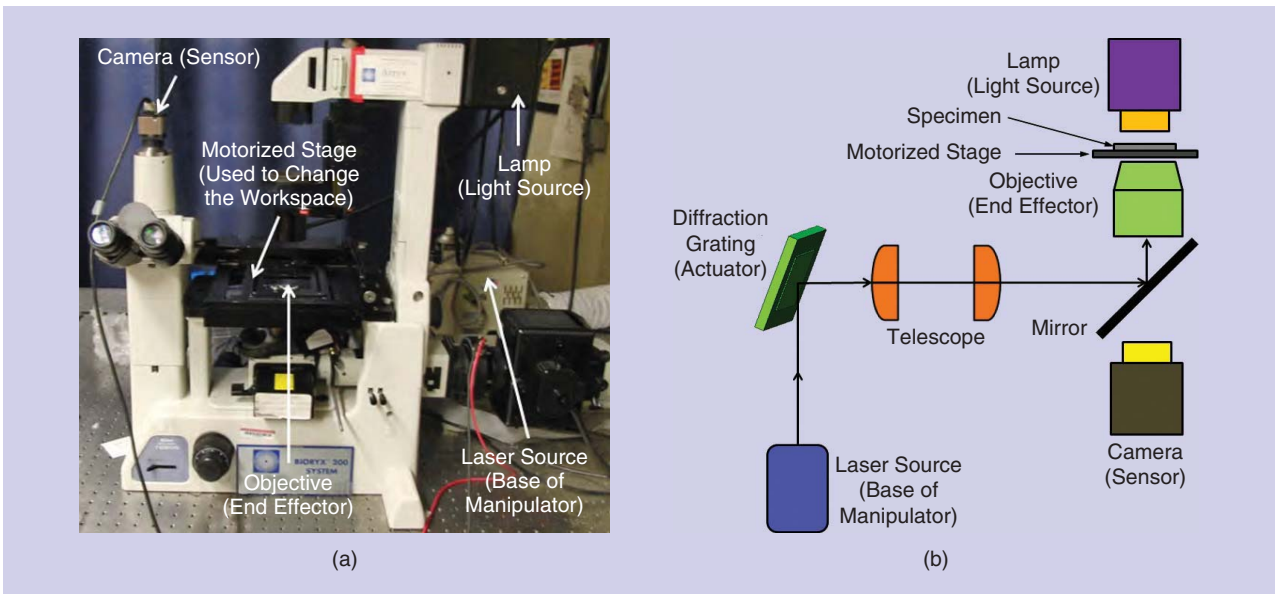


Figure 1. Holographic OTs can be used as a microrobot: (a) the hardware setup and (b) a schematic diagram.

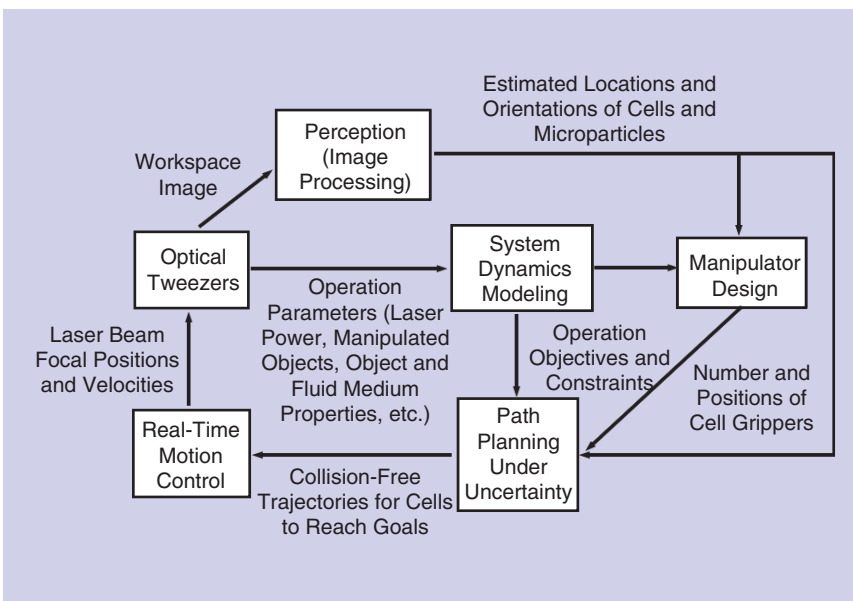


Figure 2. An autonomous robotic system for cell manipulation. Arrows denote the direction of information flow between the system components.

optical finger to grip the manipulated cell, with three independent degrees of freedom for every finger. This multiplexing capability enables deformation and concurrent transport of several cells. The number of manipulated cells is only restricted by the number of split beams that can be generated, which is generally around 100. A representative holographic OT setup that shows how OTs are used as a robotic system is shown in Figure 1.

Autonomous cell manipulation required significant developments in robotic perception, planning, control, and design. These developments were necessary to adapt the methods that were successful in macroscale robotics and address the challenges present in the current problem

domain. More specifically, the perception algorithms had to process both translucent (cells) and opaque (microparticles pushing the cells) objects of arbitrary shapes in the same workspace. The planning and control methods needed to incorporate trapping dynamics, viscous drag, and fluid motion as well as explicitly model the uncertainties in the control action executions and sensor measurements. The manipulator designs had to be reconfigured during ongoing operations to accommodate changing cell shapes. In addition, optimal actions and designs needed to be computed within a few milliseconds to prevent them from being rendered ineffective due to varying workspace conditions resulting from the random Brownian motion.

These challenges are shown in Figure 2 using a system component diagram. New strategies for autonomous cell manipulation have been developed [13], [14] recently that limit the exposure of the cells to laser light. Thus, these new strategies enable experiments with cells that are sensitive to laser exposure. Moreover, it has been shown that OTs are amenable to integration with other types of micromanipulation modes, such as microfluidic flow [15]. This integration is further expanding our capabilities to perform useful biological experiments, including cell sorting and cancer studies via regulated cellular signaling. The goal of this article is to inform the robotics community about the latest advances in automated optical

biomanipulation and foster new developments in the biomanipulation area by promoting the integration of OTs with other modalities.

Optical Tweezers

The advent of high-intensity lasers with intensities a million times that of sunlight on the Earth's surface made it possible to generate forces of the order of piconewtons to manipulate objects at the micrometer size scale. Ashkin et al. [16] at Bell Laboratories first demonstrated this capability, leading to the development of the OTs.

For both axial and transverse displacements of an object from the trap center (laser beam focus), the optical trapping forces can be well approximated as linear restoring spring forces [17] given by

$$F_{\text{trap}}(\Delta x) = \begin{cases} K_1 \Delta x, & 0 < \Delta x < x_0 \\ -K_2 \Delta x + c, & \Delta x > x_0. \end{cases} \quad (1)$$

Here, Δx is the displacement of the object center; K_1 and K_2 are trapping stiffness constants that are different for axial above the focal plane, axial below the focal plane, and transverse displacements; and x_0 and c are parameters that depend on the object properties and laser power. The overall equation of motion of a trapped object [18] in any dimension then becomes

$$m\ddot{x} = F_{\text{trap}}(\Delta x) - \gamma\dot{x} + \zeta\Gamma(t) + F_{\text{ext}}, \quad (2)$$

where $\gamma = 6\pi\eta R_o$ is the Stokes coefficient for a spherical object of radius R_o in a medium of viscosity η . The scaling factor $\zeta = \sqrt{2\gamma k_B T}$ is obtained by applying the fluctuation-dissipation theorem [19], where k_B is the Boltzmann constant, and T is the absolute temperature. Thus, $\gamma\dot{x}$ represents the viscous drag force, $\zeta\Gamma(t)$ models the thermal force arising from Brownian motion, and F_{ext} encodes the external forces due to collisions, gravity, and buoyancy. The stochastic form of $\Gamma(t)$ prevents a direct analytical solution of (2). However, $\zeta\Gamma(t)$ can be replaced by $\sqrt{(2\gamma k_B T)/(\delta t)} N(0, 1)$ to solve (2) numerically in discrete time. For low object-transport speeds (a few micrometers per second), the Reynolds number is small, and the inertial term on the left-hand side of (2) can be ignored. Consequently, OTs can robustly manipulate an object when the piconewton-magnitude trapping forces overcome drag and thermal forces either supported or opposed by other external forces.

Manipulation Using Direct Trapping

Direct trapping of cells is the simplest and most common optical manipulation strategy. Researchers at the City University of Hong Kong have successfully used a suite of autonomous planning and control methods in conjunction with cell-trap dynamics analysis to transport living yeast cells with as little as 10 mW of laser power. In particular,

they have adapted graph search-based planning algorithms, such as rapidly exploring random trees and A* or derived closed-loop controllers using synchronization and potential functions for the concurrent manipulation of multiple cells. Their experiments have shown that 1) cells can be transported while avoiding collisions with other cells in the workspace [20], 2) cells have limited possibilities of escaping from the optical traps [17], 3) multiple cells can be transported while maintaining a fixed pattern [9], and 4) cells can be arranged in stable array configurations while preserving a minimum distance among any two pairs of cells [21]. These are significant advances that offer a lot of promise for conducting robust and efficient multicell studies using OTs without manual intervention.

Researchers at the University of Maryland, in collaboration with biophysicists at Vanderbilt University, have

**The cells are pushed
indirectly by optically
trapped beads that
directly push a nontrapped
intermediate bead
positioned between the
optically trapped beads and
the target cell.**

where $\gamma = 6\pi\eta R_o$ is the Stokes coefficient for a spherical object of radius R_o in a medium of viscosity η . The scaling factor $\zeta = \sqrt{2\gamma k_B T}$ is obtained by applying the fluctuation-dissipation theorem [19], where k_B is the Boltzmann constant, and T is the absolute temperature. Thus, $\gamma\dot{x}$ represents the viscous drag force, $\zeta\Gamma(t)$ models the thermal force arising from Brownian motion, and F_{ext} encodes the external forces due to collisions, gravity, and buoyancy. The stochastic form of $\Gamma(t)$ prevents a direct analytical solution of (2). However, $\zeta\Gamma(t)$ can be replaced by $\sqrt{(2\gamma k_B T)/(\delta t)} N(0, 1)$ to solve (2) numerically in discrete time. For low object-transport speeds (a few micrometers per second), the Reynolds number is small, and the inertial term on the left-hand side of (2) can be ignored. Consequently, OTs can robustly manipulate an object when the piconewton-magnitude trapping forces overcome drag and thermal forces either supported or opposed by other external forces.

Direct trapping of cells is the simplest and most common optical manipulation strategy. Researchers at the City University of Hong Kong have successfully used a suite of autonomous planning and control methods in conjunction with cell-trap dynamics analysis to transport living yeast cells with as little as 10 mW of laser power. In particular,

they have adapted graph search-based planning algorithms, such as rapidly exploring random trees and A* or derived closed-loop controllers using synchronization and potential functions for the concurrent manipulation of multiple cells. Their experiments have shown that 1) cells can be transported while avoiding collisions with other cells in the workspace [20], 2) cells have limited possibilities of escaping from the optical traps [17], 3) multiple cells can be transported while maintaining a fixed pattern [9], and 4) cells can be arranged in stable array configurations while preserving a minimum distance among any two pairs of cells [21]. These are significant advances that offer a lot of promise for conducting robust and efficient multicell studies using OTs without manual intervention.

Researchers at the University of Maryland, in collaboration with biophysicists at Vanderbilt University, have

**The cells are pushed
indirectly by optically
trapped beads that
directly push a nontrapped
intermediate bead
positioned between the
optically trapped beads and
the target cell.**

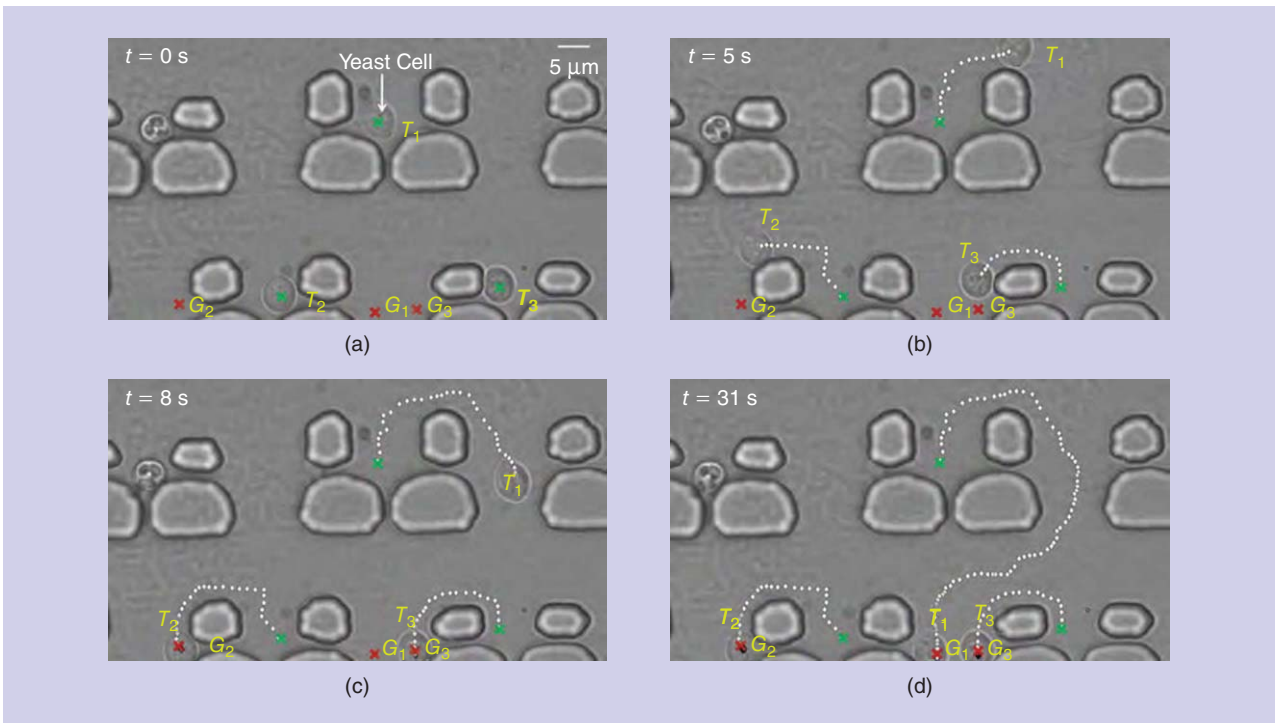


Figure 3. An autonomous transport of three yeast cells to their desired goals using direct optical trapping (the target cells are labeled as T_i , their initial locations are marked using green \times symbols, and their corresponding release locations are marked using red \times symbols and labeled as G_i , where i represents the index of the target cell). (a) Initial scene where three target cells are directly trapped by three laser beams. (b) Target cells are transported toward their respective goal locations, while avoiding obstacles in the workspace (trajectories of the laser beams are marked with white dots). (c) Target cells T_2 and T_3 reach their goal locations G_2 and G_3 , respectively. (d) Target cell T_1 reaches its desired goal location G_1 .

Manipulation Using Tool Attachment

The direct trapping of cells exposes them to high-intensity lasers, causing structural damages and adverse effects on physiological properties and processes [24]. To avoid direct laser exposure, cells are attached to inert microparticles with adhesives (see [25] for a review). The optically trapped microparticles, thus, act as attached end-effector tools to manipulate the cells indirectly.

Even though autonomy has not yet been used for this manipulation strategy, we discuss it to highlight the gradual development of more complex optical micromanipulator designs.

Researchers at National Taiwan University have

**Direct trapping of cells
is the simplest and
most common optical
manipulation strategy.**

demonstrated this manipulation strategy for rotation control of cells using irregularly shaped diamond microparticles of size 15–25 μm as the tool fingers [26]. Diamond is chosen as the finger material as it is stable under the influence of lasers and inert even in cell-culture solutions. The particles are mixed with 0.01% poly-L-lysine to provide strong adhesion. The cells undergo structural polarity due to the membrane protein distribution across the cell membrane that determines

their physiological functions. Therefore, rotating cells in a controlled manner is important to study their physiological behaviors. Moreover, controlled cell rotation allows easy access to cell organelles for microinjection and microdissection. Rotation control is achieved by changing the focal plane of the laser at the interface to generate angular momentum for the laser. Figure 4 shows full (360°) counterclockwise rotation of a mesophyll protoplast cell using 150 mW of laser power.

A gel-based microtool was developed by researchers at Nagoya University [7]. The tool fingers are made of hydrophilic photocross linkable resin. Spiropyran chromospheres, a type of photochromic polymer, is used for adhesion of the tool with the manipulated yeast cells. By adjusting the electrolyte concentration of the fluid solution after the tool is subjected to ultraviolet illumination, the adhesion can be either temporary or permanent. This setup is used to transport cells by pushing and pulling as well as measure cell pH levels by immobilizing the cells and coating the tool with bromothymol blue pH indicator. An alternative parallelizable tool fabrication process is reported in [27]. Polystyrene beads are used as the finger material. Dispersed-bead solutions are injected over silicon substrates that have been patterned into the desired tool shapes, resulting in an aggregation of the fingers due to surface tension. The aggregated fingers are then fused together by subjecting them to temperatures above the glass transition temperature. The

fused fingers can be detached from the patterns by ultrasound treatment, thereby providing the option of reconfiguring the tool shapes arbitrarily. This fabrication technique enables faster transport speed as compared with the previous photofabrication process.

Manipulation Using Reconfigurable Gripping

Since the attached end-effector tools provide one-to-one adhesion with cells, one tool finger is enough to manipulate a cell indirectly. However, the cells often cannot be easily released from the tools after manipulation, and that poses problems, especially for experiments where the cells need to be arranged in certain configurations and then allowed to exhibit natural behaviors for a long time. In such cases, an alternative manipulation strategy is to grip the cells using optically trapped inert microparticles that do not have any adhesive coatings. We refer to this strategy as *optical gripping*, and the formation of trapped beads to grip a cell as *end-effector gripper* or just *gripper*. The trapped beads themselves form the gripper fingers. This strategy can prevent about 90% of the laser power from being incident on the cells, thereby enhancing their viabilities significantly.

Researchers at the University of Maryland have been successful in bringing about autonomy for indirect manipulation of yeast cells using silica as the gripper finger material [13]. The sequence of operations during manipulation are as follows: 1) target gripper fingers are trapped and transported to the cell to form the gripper, 2) the cell is transported using the gripper to the desired goal location, 3) the gripper fingers are moved away from the cell to release the cell at the goal location, and 4) the manipulation is completed by removing the fingers by switching off the laser beams. Image processing is done using the Hough transform, and the spherical cells are easily differentiated from the beads since their radii are different. Successful manipulation then depends not only on finding collision-free paths (defined using waypoint sequences) for the cells using an A* planner but also on the coordinated transport of the gripper fingers to move the cells along the desired paths. Based on the current locations of the gripper fingers, an additional planner selects a sequence of atomic maneuvers, involving rotations, translations, and retaining trap positions, at a rate of 10 Hz to push the cells from their current waypoints to the next waypoints. Figure 5 shows a representative experiment to transport a cell using a three-finger gripper in a challenging workspace containing several obstacles.

Manipulation Using Indirect Pushing

Dictyostelium discoideum is used as a model organism to study collective cell migration [28] that is important in many biological processes from organ development to immune response to cancer metastasis. With the ability to move directionally in the presence of gradients of chemoattractants and relay signals to the neighboring cells, the migration of a large number of *D. discoideum* cells is seen as an important model of how cells operate collectively. While the migration is trig-

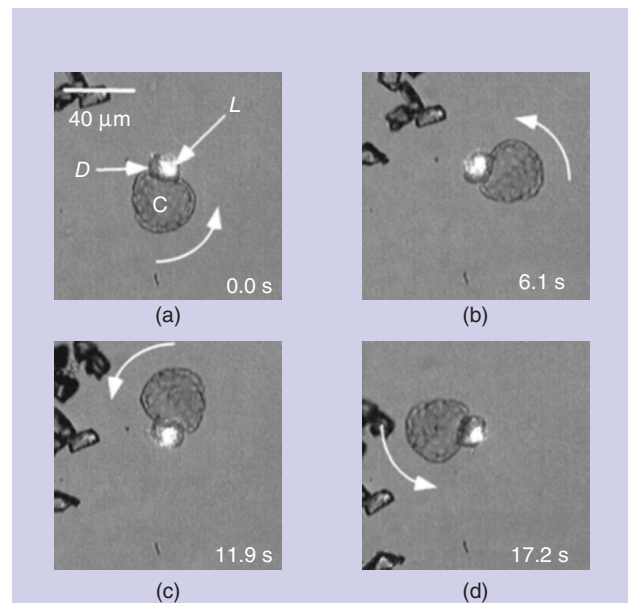


Figure 4. The rotation of a mesophyll protoplast using a laser-trapped diamond particle as an optical microtool: (a) a diamond particle denoted by *D* is tagged with a mesophyll protoplast cell and trapped by laser beam *L*, (b) the tool is moved along the periphery of the cell to induce rotation, (c) the cell rotates about the optical axis as the tool moves along its periphery, and (d) the cell is rotated by 360°. (Figure adapted with permission from [26].)

gered by the presence of chemoattractants, the cells do not move toward the chemoattractants individually. Instead, they first form chains with the surrounding cells and then approach the chemoattractants collectively. This behavior poses interesting questions: what is the underlying mechanism of this unique pattern of migration, and what is the influence of the surrounding cells in the migration of an individual cell? The traditional method of studying neighboring cells as a single group is not able to answer the questions. Instead, individual cells have to be perturbed from the chain systematically to arrange them in different configurations and investigate the resulting variations in the collective migration trajectories. The perturbations also need to be properly synchronized for the individual cells to exhibit the desired motility. These studies, therefore, require a strategy for the fast, reconfigurable, and precise manipulation of cells in parallel with complete control over individual cell manipulation.

Researchers at the University of Maryland have made some progress in this regard. They first polarize (create states of extended protrusions) the *D. discoideum* cells using a regular pulse of chemoattractant cyclic adenosine monophosphate. OTs are then used to arrange the cells in predefined configurations to observe the evolution of their migration behaviors. However, the cells are very sensitive to the laser beam. Even 10% of laser exposure that occurs during gripping affects their normal physiological activities. Hence, a different strategy has been developed, where the cells are pushed indirectly by optically trapped beads that directly

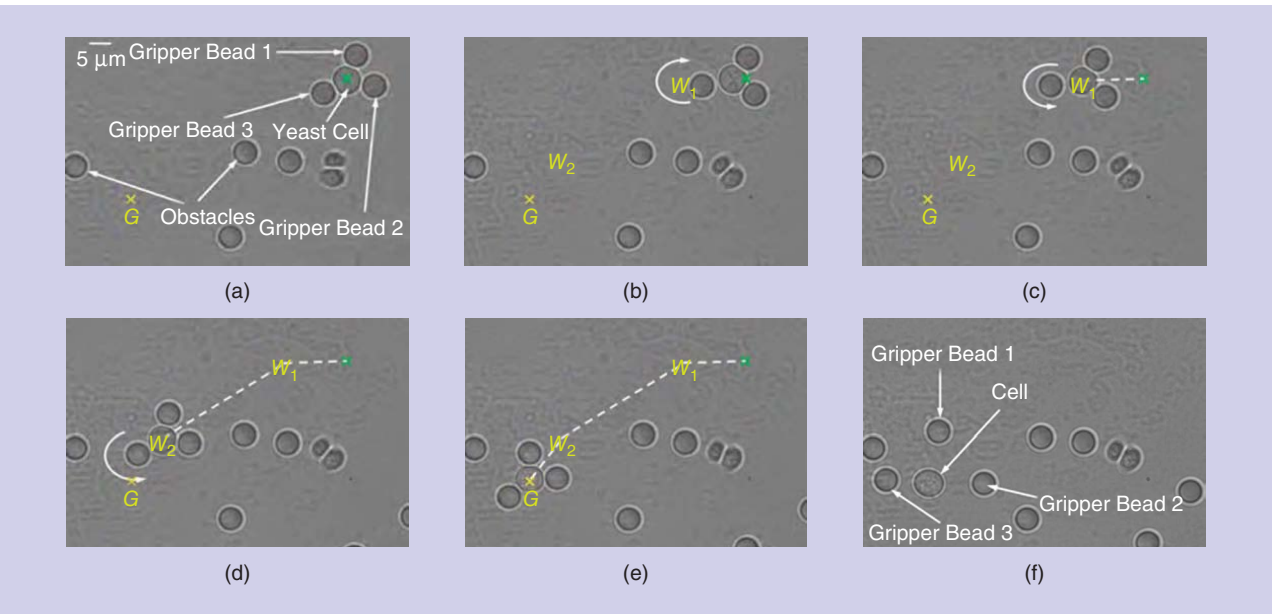


Figure 5. An indirect transport of a yeast cell using a three-finger optical gripper. (a) Initial scene where the cell is indirectly trapped by the gripper (initial and goal locations are marked by green and yellow \times signs, respectively). (b) The gripper rotates to align itself toward the waypoint W_1 . (c) The cell is transported to the waypoint W_1 . (d) The cell is transported to the waypoint W_2 through a sequence of rotation and linear motion. (e) The gripper reaches the final goal G with the use of rotation and linear motion, respectively. (f) The cell is released by moving the gripper fingers away from each other. (Figure adapted from [13].)

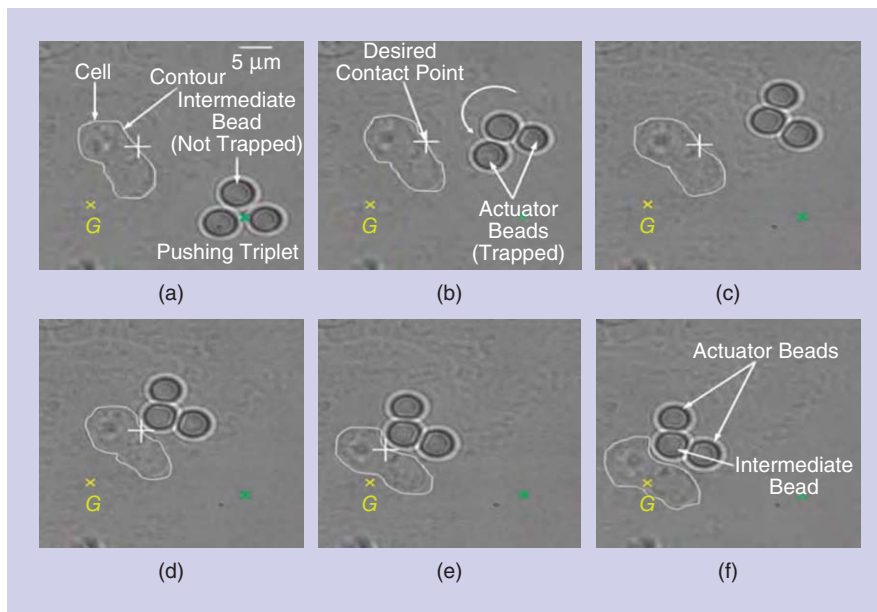


Figure 6. Pushing a dynamic *D. discoideum* cell with a formation (two actuator fingers are directly trapped by laser beams while the pushing finger is not directly trapped by any laser beam and is used to keep the cell away from the laser beam). (a) Initial scene where the pushing formation location is marked by a green \times sign and the desired goal location of the cell is marked by yellow \times sign and denoted by G . (b) The actuator fingers rotate about the optical axis to align the formation with the desired contact point denoted by white $+$ sign. (c) The pushing formation gets aligned with the desired contact point. (d) The pushing formation reaches the contact location. (e) The formation starts pushing the cell toward the goal G . (f) The cell reaches the goal G . (Figure adapted from [29].)

push a nontrapped intermediate bead positioned between the optically trapped beads and the target cell. The trapped beads, thus, function as actuator fingers and the intermediate

bead acts as a pushing finger. The overall strategy is referred to as indirect optical pushing and the collection of actuator and pushing fingers is called a pushing formation. The researchers have devised an autonomous approach [14], [29] that considers the inherent instabilities of the contact points between the pushing fingers and the cells. A series of operations are performed on the input images to identify the irregular shaped cells and the spherical finger objects. Spherical objects are extracted and separated from the images using the Hough transform. The resulting images are then processed with Canny edge detection, dilation, and flood filling successively to identify the cell boundaries. As in the case of reconfigurable gripping, an A^* planner with a modified cost function based on the pushing formation-cell ensemble dynamics is first used to compute the collision-free paths for the cells. Another A^* planner is then applied to compute the sequence of waypoints for transporting the pushing formations to the desired contact points on the cell boundaries. The movement from one waypoint to

Table 1. A comparison of the different cell manipulation strategies.

Characteristic	Strategy			
	Direct Trapping	Tool Attachment	Gripping	Indirect Pushing
Control complexity	Simple	Moderate; depends on number of fingers	Moderate; depends on number of fingers	Complex
Cell exposure to laser	Significant	Moderate	Moderate	Minimal
Cell release	Easy	Often not possible	Easy	Easy
Preparation time	Negligible	Long	Small	Small
Manipulation type	Translation and rotation	Translation, rotation, pulling, and pushing	Translation, rotation, and pushing	Translation, rotation, and pushing
Transport time (same laser power and finger material)	Least	More than direct trapping; slower for cells with changing shapes	More than direct trapping; varies with the number and size of fingers	More than gripping; faster for larger cells

the next is performed using the same set of maneuvers discussed in the “Manipulation Using Reconfigurable Gripping” section. Figure 6 shows the reorientation of a *D. discoideum* cell by a pushing formation composed of two actuator fingers using only 5.3 mW of laser power.

Conclusions

This article describes how OTs have evolved from a tool for single cell studies in the hands of biophysicists to powerful, precise, and flexible robots for autonomous manipulation of multiple cells. Table 1 presents a comparison of the different manipulation strategies. While the complexity of controlling the manipulation operations increases from direct trapping to tool attachment/gripping to indirect pushing, laser exposure to cells is reduced progressively. The damage due to such exposure can be completely eliminated for sensitive cells as opposed to occurrence rates of 67% and 33% for direct trapping and tool attachment or gripping, respectively [29]. Even though both tool attachment and gripping utilize fingers (optically trapped beads) to manipulate the cells, the presence of adhesive coatings on the tool fingers means that it is often not possible to release the cells after manipulation is over. Furthermore, it requires a longer preparation time of the order of several minutes (instead of a few seconds for the other strategies) and sometimes additional equipments and processes to fabricate the tools. However, this strategy enables pulling or stretching of the cells from two ends unlike any of the other strategies. Direct trapping, being the simplest strategy, provides the least transport time even though the cells may no longer be viable if the operations last for more than a few seconds. Indirect pushing requires the maximum transport time among the other three strategies particularly when rotation maneuvers are required. The actual times depend on laser power and the number and size of the fingers; they are of the orders of tens of seconds for transport operations shown in the figures. Importantly though, tool attachment works slowest for cells with changing shapes due to the adhesive bonding between the

fingers and cells making it difficult to remove and reposition the fingers at suitable contact points. On the other hand, indirect pushing works well for cells with changing shapes particularly for those with relatively large dimensions of more than 10 μm .

We have not yet, however, fully harnessed the potential of autonomous cell manipulation using optical robots. There are several important research directions, which include manipulating a large number of cells in three dimensions to investigate tissue-level behaviors, further leveraging the benefits of hybrid manipulation set-ups such as optofluidic and optoelectronic, optimizing the overall manipulator designs, and automating complete operations from selecting the target cells and beads to preserving the configurations of cell patterns for hours. Such

long-term automation of cellular systems would require further advances in various areas of microrobotics. Examples include the development of more scalable yet tightly coupled planning and control algorithms, synchronized control of optical traps and motorized workstage, integration of fluorescence or phase contrast microscopy to better estimate the irregular cell boundaries, additional optical imaging instrumentation to view the entire three-dimensional (3-D) workspace, and novel perception algorithms to reconstruct the 3-D workspace in real time.

An alternative manipulation strategy is to grip the cells using optically trapped inert microparticles that do not have any adhesive coatings.

Acknowledgments

This work was supported in part by the National Science Foundation (NSF) under grant CMMI-0835572 and grant CPS-0931508. The opinions expressed in this article are ours and do not necessarily reflect the opinions of the sponsors.

References

- [1] A. Ashkin, J. M. Dziedzic, and T. Yamane, "Optical trapping and manipulation of single cells using infrared-laser beams," *Nature*, vol. 330, pp. 769–771, Dec. 1987.
- [2] K. K. Ramser and D. Hanstorp, "Optical manipulation for single cell studies," *J. Biophotonics*, vol. 3, pp. 187–206, Apr. 2010.
- [3] J. P. Mills, L. Qie, M. Dao, C. T. Lim, and S. Suresh, "Nonlinear elastic and viscoelastic deformation of the human red blood cell with optical tweezers," *Mech. Chem. Biosyst.*, vol. 1, pp. 169–180, Sept. 2004.
- [4] K. Dholakia, W. M. Lee, L. Paterson, M. P. MacDonald, R. McDonald, I. Andreev, P. Mthunzi, C. T. A. Brown, R. F. Marchington, and A. C. Riches, "Optical separation of cells on potential energy landscapes: Enhancement with dielectric tagging," *IEEE J. Select. Topics Quantum Electron.*, vol. 13, pp. 1646–1654, Nov./Dec. 2007.
- [5] L. Y. Pozzo, A. Fontes, A. A. de Thomaz, B. S. Santos, P. M. A. Farias, D. C. Ayres, S. Giorgio, and C. L. Cesar, "Studying taxis in real time using optical tweezers: Applications for Leishmania amazonensis parasites," *Micron*, vol. 40, pp. 617–620, July/Aug. 2009.
- [6] F. Arai, C. Ng, H. Maruyama, A. Ichikawa, H. El-Shimy, and T. Fukuda, "On chip single-cell separation and immobilization using optical tweezers and thermosensitive hydrogel," *Lab Chip*, vol. 5, pp. 1399–1403, Dec. 2005.
- [7] H. Maruyama, T. Fukuda, and F. Arai, "Laser manipulation and optical adhesion control of functional gel-microtool for on-chip cell manipulation," in *Proc. IEEE/RSJ Int. Conf. Intelligent Robots Systems*, St. Louis, MO, 2009, pp. 1413–1418.
- [8] A. G. Banerjee, A. Pomerance, W. Losert, and S. K. Gupta, "Developing a stochastic dynamic programming framework for optical tweezer-based automated particle transport operations," *IEEE Trans. Autom. Sci. Eng.*, vol. 7, pp. 218–227, Apr. 2010.
- [9] S. Hu and D. Sun, "Automated transportation of biological cells with a robot-tweezer manipulation system," *Int. J. Robot. Res.*, vol. 30, pp. 1681–1694, Dec. 2011.
- [10] A. G. Banerjee, S. Chowdhury, W. Losert, and S. K. Gupta, "Real-time path planning for coordinated transport of multiple particles using optical tweezers," *IEEE Trans. Autom. Sci. Eng.*, vol. 9, pp. 669–678, Oct. 2012.
- [11] X. Li, C. C. Cheah, S. Hu, and D. Sun, "Dynamic trapping and manipulation of biological cells with optical tweezers," *Automatica*, vol. 49, pp. 1614–1625, June 2013.
- [12] J. E. Curtis, B. A. Koss, and D. G. Grier, "Dynamic holographic optical tweezers," *Opt. Commun.*, vol. 207, pp. 169–175, June 2002.
- [13] S. Chowdhury, A. Thakur, C. Wang, P. Svec, W. Losert, and S. K. Gupta, "Automated manipulation of biological cells using gripper formations controlled by optical tweezers," *IEEE Trans. Autom. Sci. Eng.*, vol. 11, pp. 338–347, Apr. 2014.
- [14] A. Thakur, S. Chowdhury, C. Wang, P. Svec, W. Losert, and S. K. Gupta, "Indirect pushing based automated micromanipulation of biological cells using optical tweezers," *Int. J. Robot. Res.*, vol. 33, pp. 1098–1111, 2014, doi: 10.1177/0278364914523690.
- [15] S. Chowdhury, P. Svec, C. Wang, K. Seale, J. P. Wikswo, W. Losert, and S. K. Gupta, "Automated cell transport in optical tweezers assisted microfluidic chamber," *IEEE Trans. Autom. Sci. Eng.*, vol. 10, pp. 980–989, Oct. 2013.
- [16] A. Ashkin, J. M. Dziedzic, J. E. Bjorkholm, and S. Chu, "Observation of a single-beam gradient force optical trap for dielectric particles," *Opt. Lett.*, vol. 11, pp. 288–290, May 1986.
- [17] Y. Wu, D. Sun, W. Huang, and N. Xi, "Dynamics analysis and motion planning for automated cell transportation with optical tweezers," *IEEE/ASME Trans. Mechatron.*, vol. 18, pp. 706–713, Apr. 2013.
- [18] A. G. Banerjee, A. Balijepalli, S. K. Gupta, and T. W. LeBrun, "Generating simplified trapping probability models from simulation of optical tweezers system," *J. Comput. Inf. Sci. Eng.*, vol. 9, p. 021003, June 2009.
- [19] P. Grassia, "Dissipation, fluctuations, and conservation laws," *Amer. J. Phys.*, vol. 69, pp. 113–119, Feb. 2001.
- [20] T. Ju, S. Liu, J. Yang, and D. Sun, "Rapidly exploring random tree algorithm-based path planning for robot-aided optical manipulation of biological cells," *IEEE Trans. Autom. Sci. Eng.*, vol. 11, pp. 649–657, July 2014.
- [21] C. Haoyao and D. Sun, "Moving groups of microparticles into array with a robot-tweezers manipulation system," *IEEE Trans. Robot.*, vol. 28, pp. 1069–1080, Oct. 2012.
- [22] K. T. Seale, S. L. Faley, J. Chamberlain, and J. P. Wikswo, Jr., "Macro to nano: A simple method for transporting cultured cells from milliliter scale to nanoliter scale," *Exp. Biol. Med.*, vol. 235, pp. 777–783, June 2010.
- [23] M. K. Driscoll, C. McCann, R. Kopace, T. Homan, J. T. Fourkas, C. Parent, and W. Losert, "Cell shape dynamics: From waves to migration," *PLoS Comput. Biol.*, vol. 8, p. e1002392, Mar. 2012.
- [24] T. Aabo, I. R. Perch-Nielsen, J. S. Dam, D. Z. Palima, H. Siegumfeldt, J. Glückstad, and N. Arneborg, "Effect of long- and short-term exposure to laser light at 1070 nm on growth of *Saccharomyces cerevisiae*," *J. Biomed. Opt.*, vol. 15, p. 041505, July/Aug. 2010.
- [25] A. G. Banerjee, S. Chowdhury, W. Losert, and S. K. Gupta, "Survey on indirect optical manipulation of cells, nucleic acids, and motor proteins," *J. Biomed. Opt.*, vol. 16, p. 051302, May 2011.
- [26] C.-K. Sun, Y.-C. Huang, P. C. Cheng, H.-C. Liu, and B.-L. Lin, "Cell manipulation by use of diamond microparticles as handles of optical tweezers," *J. Opt. Soc. Amer. B*, vol. 18, pp. 1483–1489, Oct. 2001.
- [27] H. Maruyama, R. Iitsuk, K. Onda, and F. Arai, "Massive parallel assembly of microbeads for fabrication of microtools having spherical structure and powerful laser manipulation," in *Proc. IEEE Int. Conf. Robotics Automation*, Anchorage, AK, 2010, pp. 482–487.
- [28] P. Friedl, Y. Hegerfeldt, and M. Tusch, "Collective cell migration in morphogenesis and cancer," *Int. J. Dev. Biol.*, vol. 48, pp. 441–449, July 2004.
- [29] S. Chowdhury, A. Thakur, C. Wang, P. Svec, W. Losert, and S. K. Gupta, "Automated indirect manipulation of irregular shaped cells with optical tweezers for studying collective cell migration," in *Proc. IEEE Int. Conf. Robot. Autom.*, Karlsruhe, Germany, 2013, pp. 2789–2894.

Ashis Gopal Banerjee, Complex Systems Engineering Laboratory, General Electric Global Research, Niskayuna, New York. E-mail: banerjee@ge.com.

Sagar Chowdhury, Department of Mechanical Engineering and The Institute for Systems Research, University of Maryland. E-mail: sagar353@umd.edu.

Satyandra K. Gupta, Department of Mechanical Engineering and The Institute for Systems Research, University of Maryland. E-mail: skgupta@umd.edu.

The Feel of MEMS Barometers

© COREL

Inexpensive and Easily Customized Tactile Array Sensors

By Yaroslav Tenzer, Leif P. Jentoft, and Robert D. Howe

This article presents a new approach to the construction of tactile array sensors based on barometric pressure sensor chips and standard printed circuit boards (PCBs). The chips include tightly integrated instrumentation amplifiers, analog-to-digital converters, pressure and temperature sensors, and control circuitry that provides excellent signal quality over standard digital bus interfaces. The resulting array electronics can be easily encapsulated with soft polymers to provide robust and compliant grasping surfaces for specific hand designs. The use of standard commercial off-the-shelf technologies means that only basic electrical and mechanical skills are required to build effective tactile sensors for new applications. The performance evaluation of prototype arrays demonstrates excellent linearity (typically <1%) and low noise (<0.01 N). External addressing circuitry allows multiple sensors to communicate on the same bus at more than 100 Hz per sensor element. Sensors can be mounted with as close as 3 × 5-mm spacing, and spatial impulse response tests show that linear solid-mechanics-based signal processing is feasible. This approach promises to make sensitive, robust, and inexpensive tactile sensing available for a wide range of robotics and human-interface applications.

Digital Object Identifier 10.1109/MRA.2014.2310152
Date of publication: 13 August 2014

Background

Tactile sensing is widely considered an essential capability for effective grasping and manipulation [1]–[3]. Parameters, such as the location of object contacts on the robot hand and contact pressure distribution, are believed to be essential for effective manipulation in unstructured environments. Yet despite decades of research and the availability of several commercial tactile array sensors, there has been little experimental progress in using tactile information to control grasping and manipulation.

There are many reasons for the lack of headway in this area, but a major factor is certainly the cost and complexity of integrating tactile sensing into robot hands. Hundreds of touch-sensing device designs have been published in the robotics literature, but building such sensors requires custom fabrication using nonstandard techniques [1]–[3]. Alternatively, commercial single-element pressure sensors can be configured as arrays. Inexpensive pressure sensors (e.g., Flexi-Force, Tekscan Inc., South Boston) often provide limited accuracy and significant hysteresis. In addition, the engineering effort required to integrate these sensors into arrays (including wiring, amplification, analog multiplexing, and analog-to-digital conversion) usually overwhelms the transducer cost. Commercial tactile array sensors avoid the need to master exotic fabrication technologies and integrate sensors into arrays, but they are typically costly and fragile and cover

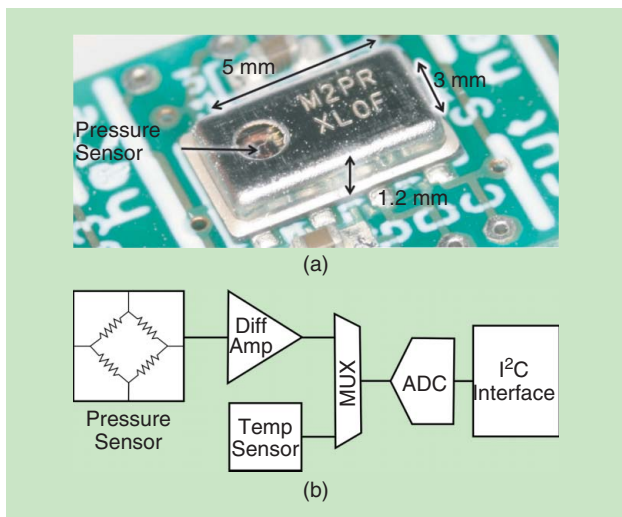


Figure 1. (a) The MPL115A2 sensor from Freescale Semiconductor, Inc. and (b) the block diagram of the device. (Photo courtesy of Yaroslav Tenzer.)

only a limited area of a hand [4]–[7]. Both custom-built and commercial sensors require considerable effort to mechanically integrate into the contact surfaces of a new robotic hand.

This article presents a new method for tactile array construction and integration that avoids many of the shortcomings of the current technologies. The approach takes advantage of the recently available miniature barometric sensor chips, which include a microelectromechanical systems (MEMS) pressure sensors, temperature sensors, instrumentation amplifiers, analog-to-digital converters, and standard bus interfaces, all for as little as US\$1 per sensor. These devices can be mounted on standard PCBs (rigid or flexible) using standard integrated circuit (IC) surface-mount techniques. The circuit boards can be mounted to robot fingers and easily overmolded with rubber to provide robust grasping surfaces. The resulting tactile array sensors have moderate spatial resolution (3–5 mm) and excellent sensitivity (< 0.01 N), linearity (<1%), and bandwidth (>100 Hz).

Technological Approach

Barometric Sensors

Barometric sensor chips were originally developed for consumer products, such as desktop weather stations and global positioning systems, where altimeters can improve vertical positioning accuracy [8]. As such, these sensors have a small footprint and low power consumption, and they are mass-produced at low cost. Several versions are available, all sharing the combination of a MEMS transducer with integrated signal conditioning and bus interface in a standard surface-mount IC package (e.g., [9] and [10]). In this article, we focus on the MPL115A2 sensor (Freescale Semiconductor, Inc., Austin, Texas). This device (Figure 1) has a miniature 5 × 3 × 1.2-mm package, uses the interintegrated-circuit (I²C) bus protocol [11], and was the least expensive alternative during 2013. These sensors have an air pressure range of 50–115 kPa with a

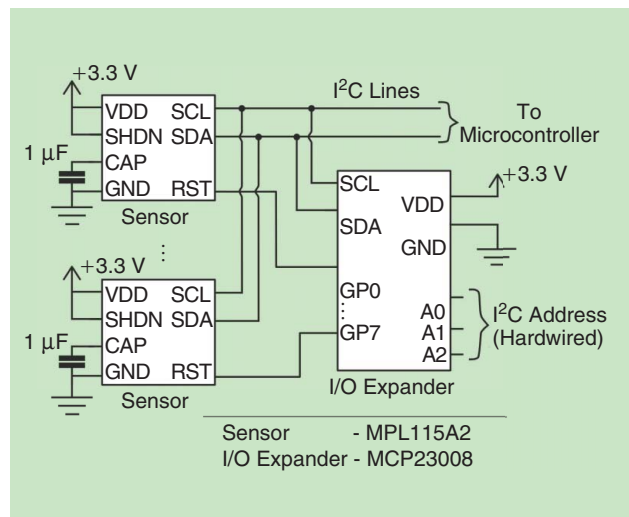


Figure 2. An example of the use of auxiliary circuits to enable connection of up to eight barometric sensors on the same I²C bus.

resolution of 0.15 kPa. This sensor also has a relatively large ventilation hole (1-mm diameter) directly above the pressure sensor. This is advantageous for rubber casting, as described in the following.

Circuitry Design

A number of steps are required to adapt the barometric sensors for tactile applications. First, circuitry and programming protocols are required to access multiple sensors over the I²C bus because all sensors are manufactured with the same preassigned I²C address. Chip select can be implemented through the reset (RST) pin, which disables the I²C interface when driven low [10]. This is preferable to applying and removing power because it avoids the power-up delay that would greatly limit sampling rates. In the circuit example in Figure 2, the RST pin of up to eight sensors are controlled by an input/output (I/O) expander (MCP23008, Microchip Technology Inc., Chandler, Arizona). Multiple I/O expanders can share the I²C bus with the sensors, so a total of only two communication wires and two power lines are required to communicate to an array of hundreds of sensors. Arrays with a large number of sensors would require the use of I/O expanders with larger addressing range and extra I/O pins (e.g., PCA9671, NXP Semiconductors, Eindhoven, The Netherlands).

The sensor array sampling speed was calculated based on the performance characteristics of the sensors, the I/O expander, and the bus communication speed; for the latter, we use the chip maximum of 400 kHz. The main performance bottleneck is the sensor data conversion time of 1.6 ms, which is the minimum interval between the start convert command and the data available in the internal registers. Two different algorithms were developed to scan an array of sensors. The first is a serial approach, where the controller sends the start-convert command to a sensor, waits for the conversion time interval, and then reads the data. The time to scan an array is

$$\left(\frac{C_b + S_b + R_b}{\text{bus speed}} + T_c \right) \cdot N,$$

where C_b is the number of bits required to command the I/O expander to select a single barometer chip, S_b is the number of bits required to command data conversion, R_b is the number of bits required to read the data, T_c is the conversion time of the sensors, and N is the number of sensors in the array. The second algorithm utilizes the waiting time to communicate the start-conversion command to the other sensors in the array, then returns to each sensor after the appropriate interval and reads the data. Using this double-loop method the array sampling time is

$$\left(\frac{2C_b + S_b + R_b}{\text{bus speed}} \right) \cdot N + T_c.$$

The performance of the algorithms is shown in Figure 3. The second algorithm is about three times as fast for the selected eight-sensor example in Figure 2 with a 400-kHz bus speed and about four times as fast for a 22-sensor array, which is currently under development for a robotic finger.

Rubber Casting

The second issue requiring special attention is the casting of the sensors in rubber. Rubber forms a robust and compliant contact surface for grasping and manipulation and serves to communicate surface contact pressure within the layer of rubber to the ventilation hole, and, thus, to the MEMS transducer. Encapsulation of the array can be readily accomplished

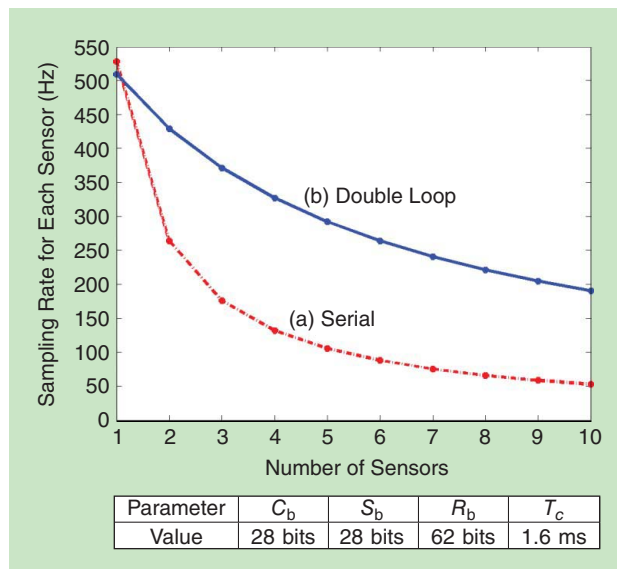


Figure 3. The theoretical sampling rates of an array with an I²C bus speed of 400 kHz. (a) The serial approach where, for each sensor, the system commands to start the conversion, waits until the data are available (1.6 ms), and then reads the data. (b) The double-loop (i.e., alternating start conversion and read sensor) approach utilizing the waiting time to communicate the start-conversion command to other sensors in the array. The table summarizes the coefficients for the circuit in Figure 2. The values include the start and stop bits required for I²C communication.

by suspending the circuit board with mounted sensors in a mold and pouring in liquid polymer, which then cures to form the elastomer contact surface. When molding is performed at atmospheric pressure, however, air is trapped within the sensor chip inside the ventilation hole. This results in low sensitivity because the surface pressure produces only small changes in the volume of the trapped air below the ventilation hole.

One solution is to remove the top of the sensor metal case so that the rubber directly encapsulates the MEMS pressure transducer. This improves sensitivity but requires nonstandard chip-handling techniques. We also found that this exposes fragile components, such as bond wires, that can break when large forces are applied to the rubber surface.

A more successful approach is vacuum degassing. The mold is placed in a vacuum chamber (e.g., a standard laboratory bell jar) immediately after the rubber is poured, and the air is removed with a vacuum pump. This removes the air from inside the sensors, allowing the rubber to enter the case through the ventilation hole. Postcasting dissection of a number of sensors showed that the rubber fills the sensor without damaging the internal structures (e.g., Figure 4).

In the supplementary multimedia materials for this article, we include an example implementation of a tactile array sensor created using this approach [12]. This sensor array has eight columns and five rows with 6-mm spacing. Onboard microcontrollers handle sensor addressing and I²C-to-universal serial bus (USB) conversion. The material includes schematics, PCB layout, and microprocessor firmware.

Performance Evaluation

To experimentally characterize the performance of the proposed tactile array, three sensors were soldered in a line at 5-mm spacing to a rigid PCB (Figure 5); this is the closest obtainable spacing for sensors mounted end to end in the longest dimension. Three PCBs were then cast in rubber with thicknesses of 4, 6, and 10 mm, which spans the typical range of rubber covering for robot fingers. The rubber was a two-part room temperature curing polyurethane elastomer (VytalFlex 20, Smooth-On, Inc., Easton, Pennsylvania). This

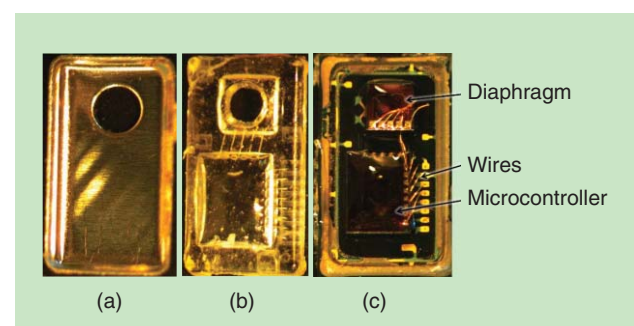


Figure 4. The postcasting dissection of a barometric sensor: (a) the sensor cover, (b) the rubber that clearly filled the air gaps inside the sensor, and (c) the PCB with the diaphragm and the microcontroller. (Photo courtesy of Yaroslav Tenzer.)

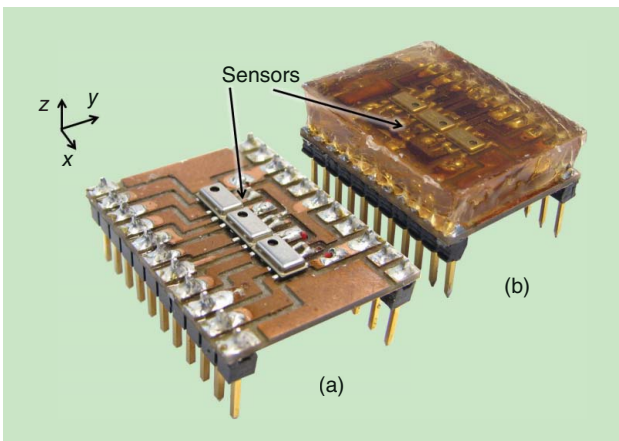


Figure 5. The sensors layout in the experimental setup (a) before casting and (b) in 6 mm of rubber. (Photo courtesy of Yaroslav Tenzer.)

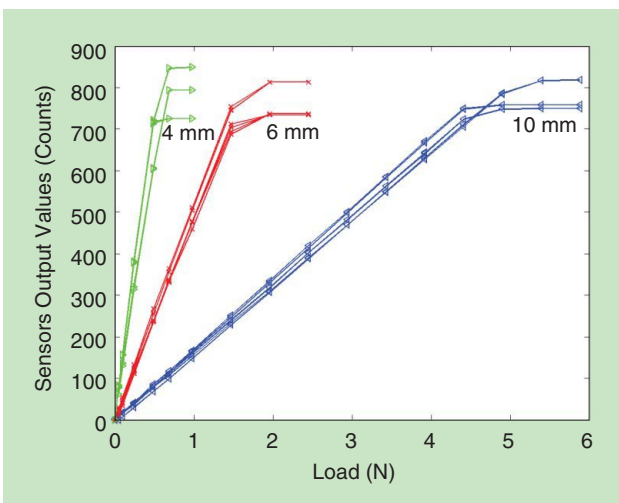


Figure 6. The sensor output values versus the applied surface load for rubbers of different thicknesses. The three lines per rubber thickness represent the offset corrected readings from the three sensors in each array. The symbols indicate the output from each sensor during the loading and unloading cycles. The manufacture calibration algorithm was used during the calculations, but the final result was not rounded or scaled for atmospheric pressure.

inexpensive rubber has low viscosity for mixing and pouring, is compliant but mechanically robust after curing, and is compatible with shape deposition manufacturing (SDM) prototyping techniques, which have proved useful for robot hand construction [13]. Its modulus of elasticity was experimentally confirmed to be 280 kPa.

Communication with the sensors was through a USB-to-I²C bridge interface (CY3240, Cypress Semiconductor Corporation, San Jose, California). The pressure values from the sensors were calibrated using algorithms provided by the sensor manufacturer, including gain and temperature correction [10]. The compensation algorithm was modified so that the final result was not rounded or scaled for atmospheric pressure.

The sensitivity of the resulting sensor arrays was evaluated by applying a load to the rubber directly above the ventilation

hole using a probe with a spherical tip with a diameter of 6 mm. The probe was attached to a triple beam balance with about 0.001-N resolution. The load was applied incrementally until the sensor output was saturated. Then the load was gradually removed to evaluate the hysteresis of the sensor. The typical interval between load changes was 30 s, and the total interval for loading and unloading of each sensor was approximately 10 min. The process was repeated for each sensor in each array for the three rubber thicknesses.

The temporal response was evaluated by preloading the sensors to 50% of the saturation load through a probe with a spherical tip with a diameter of 6 mm and then quickly removing the load in less than 10 ms. Pressure readings were sampled at 125 Hz.

Noise and temperature drift were evaluated by recording outputs of both pressure and temperature at 30 Hz for 1,000 s at ambient temperatures between 20 and 26 °C, which bounds the duration of most simple grasping and manipulation tasks at around room temperature. All three sensors in each of the three arrays were sampled with no applied load. The spatial response of the sensors was measured in terms of the impulse response. A constant force was applied sequentially along the line of sensors while the output was recorded for each sensor. To avoid the need for precise alignment, we used a line load oriented perpendicular to the line of sensors, i.e., a narrow metal probe with negligible width in the *x* direction (along the line of sensors, as shown in Figure 5) but wider than the rubber pad in the perpendicular *y* direction.

Results and Discussion

The sensitivity measurements show excellent linearity and no visible hysteresis (Figure 6). For each rubber thickness, the three lines represent the readings from the three sensors in the array. The plot shows one symbol for loading and one for unloading at every value for the applied load for each of the nine sensors; these symbols are typically so close that they are visually indistinguishable. The results show a highly linear behavior for most of the measurement range, where the coefficient of determination was $r^2 > 0.99$ for all sensors, and the maximum deviation from linearity was 2.2% for 4 mm, 1.3% for 6 mm, and 0.4% for 10 mm of rubber. The average variability in sensitivity for test arrays was 4.4%, and the maximum observed was 11.5% for 4 mm of rubber. One cause of the observed variation may be due to the limited manual alignment accuracy between the sensor port and probe.

Subsurface stress at the sensor depth was calculated using the Hertz theory for a spherical indenter [14], [15]. The saturation stress for a sensor at 4-mm depth was found to be $\sigma_z = -24,050$ Pa. The theoretically predicted curve for loads, which results in the saturation stress for a known sensor depth, and the experimentally evaluated values are shown in Figure 7. These results show close agreement, indicating that the methods from solid mechanics could be useful for the design of sensing devices.

The useful pressure measurement range appears to be larger than stated in the data sheet: the mean of the outputs at the saturation is 775.3 counts, corresponding to a calibrated air pressure of 149.2 kPa, well above the maximum of data sheet 115 kPa. The effects of regularly exceeding the specified maximum are not clear; our prototypes have shown no degradation in performance under thousands of loading cycles and under repeated loads above ten times saturation.

The sensor output in step tests showed a fast response and no hysteresis. The experiments have shown that the full step response invariably occurs within two samples or 16 ms. The negligible hysteresis level is expected for a system with force (or pressure) input and output. If the input was specified as a position step, hysteresis would likely have been evident in the sensor output, but the behavior under force loads seems most germane to robotic manipulation applications, where forces must be controlled for grasping and manipulation. In any case, the hysteretic properties depend on the properties of the elastomer used for encapsulation and could be limited if needed through the careful choice of materials.

The sensor output variation with ambient temperature is highly linear ($r^2 > 0.99$ for all sensors) over the range of 20–26 °C. The manufacturer provides a temperature compensation algorithm using the onboard temperature sensor for use in the air [10], but it is not accurate for sensors cast in rubber, probably due to the differences in the thermal expansion coefficients. The observed linearity suggests that a simple linear compensation scheme is adequate, although high accuracy may require the determination of the specific calibration coefficient for each sensor.

The signal noise was recorded from all nine unloaded sensors in the three arrays at 100 Hz for 60 s. The overall average root-mean-square noise was 1.27 counts with a standard deviation of 0.1 counts. This corresponds to an applied load of 0.0077, 0.0026, and 0.00092 N for rubbers of 10, 6, and

4 mm, respectively, where the sensitivity was calculated using the measured ratios from Figure 6. These noise levels are small with respect to the measurement range of the sensor, and simple filtering can further reduce the effects of the noise; for example, we were able to detect reliably a 1-g load on the 6-mm array with a 10-Hz bandwidth.

Power spectrum analysis suggests that the noise is homogeneously distributed across frequencies. We observed variations in the noise level as a function of the capacitor value (Figure 2) with higher capacitance reducing noise, which may have an impact on the response time. The results reported here used the recommended capacitor value of 1 μF [10].

The spatial impulse response from an array of sensors for different rubber thicknesses is presented in Figure 8. The results show that as rubber thickness increases, the strain distribution spreads laterally, but the sensor loses sensitivity. Some variation in the output values and curve amplitude between the sensor readings can be observed, and these also may be attributed to the alignment accuracy of the setup. The impulse response from a single sensor was compared with the theoretically predicted curve for the subsurface vertical normal stain distribution at the sensor depth [15]. The rubber thickness for the theoretical curve was adjusted with respect to the thickness of the sensor (i.e., 1.2 mm), and the sensor values were offset corrected while the theoretical curve magnitude (but not the spatial dimension) was scaled to the data. The calculated and experimental curves show close agreement, indicating that methods from solid mechanics [15] may be useful for the

These sensors have a small footprint and low power consumption, and they are mass-produced at low cost.

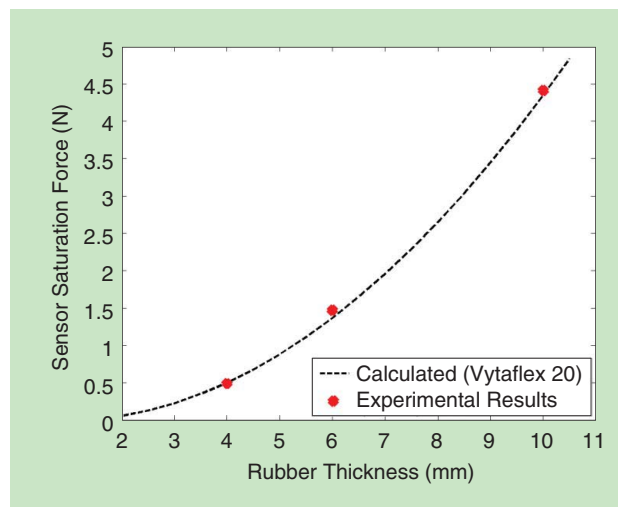


Figure 7. The sensor saturation force for rubber thicknesses of 4, 6, and 10 mm and the theoretically predicted curve [14]–[16]. The coefficient for 4 mm was fit, and results for 6 and 10 mm closely match predictions.

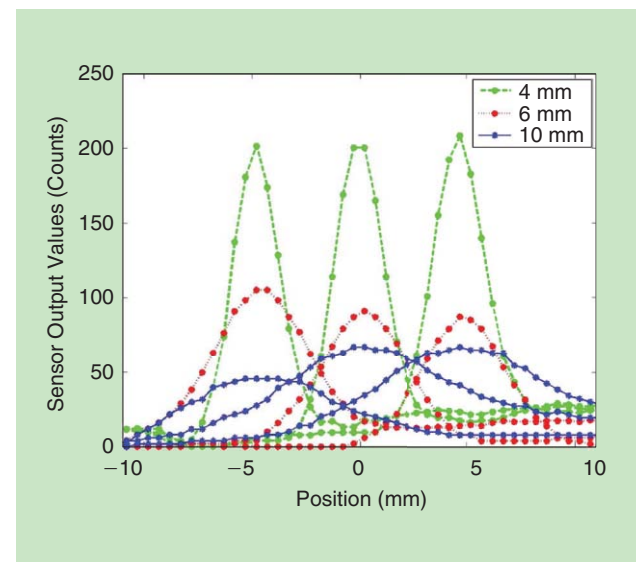


Figure 8. A spatial response to a scanned normal impulse for three sensors in each array with different rubber thicknesses.

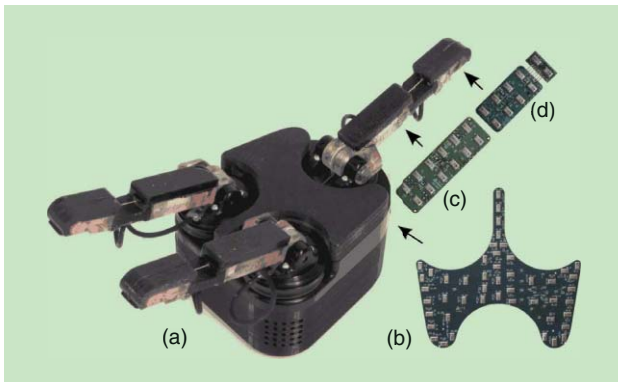


Figure 9. The tactile boards developed for the i-HY hand. (a) The hand. (b) The palm board. (c) The board for the proximal link. (d) The board for the distal link. There are total of 108 sensors used in this design. (Photo courtesy of the authors.)

analysis and interpretation of the sensor signals. A small discrepancy between the theoretical prediction (based on an infinite half-space model) and the data at the edges of the bell-shaped curve was observed. For example, for a sensor in 6 mm of rubber, the discrepancies could be seen at the distance of 5 mm onward from the peak. This may be due to the irregular structures within the rubber, i.e., the rigid sensor package mounted on the PCB and the location of the MEMS sensor beneath the ventilation hole.

A Brief Introduction to Applications

The developed technology is easily adaptable and, therefore, can be used in a variety of applications. The aim of this section is to provide a few illustrative examples.

Robotic Hands

Tactile sensing for robotic hands is especially demanding because of the ongoing innovation in the design of robotic hands. An iterative approach requires adjustments to the sensor layout. The technology presented in this article is compatible with the standard manufacturing processes, making the integration into prototypes very convenient. For example, the i-HY [17] shown in Figure 9 has two PCB boards per finger and a dedicated board for the palm. This design features 108 sensors in 6 mm of rubber. Interestingly, the rubber cast

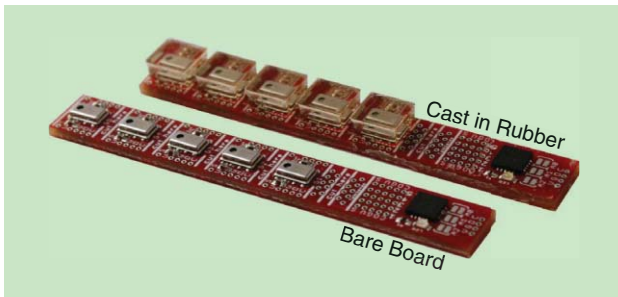


Figure 10. The five sensors arranged on a strip along the chip-select microcontroller. The strip is using the I²C protocol to communicate, and up to eight strips can be placed on the same data lines (from [12]).

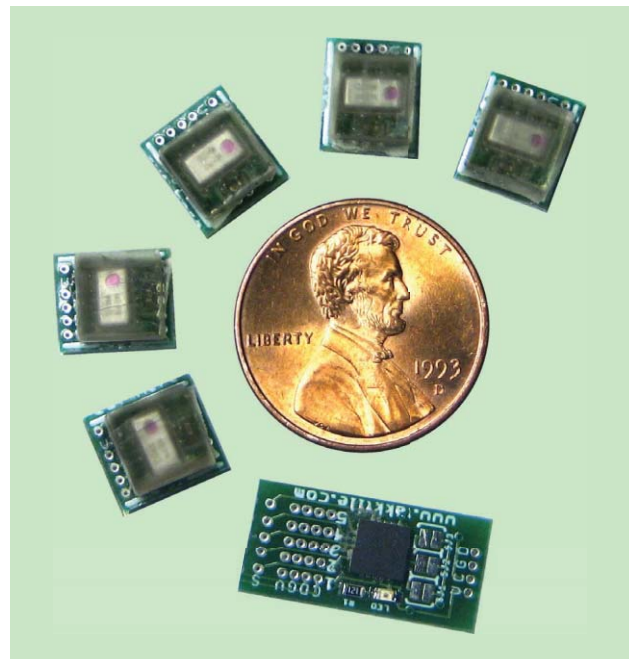


Figure 11. The separated sensors of a cast strip and the chip-select microcontroller next to a penny. The sensors can be wired back to the microcontroller through the dedicated vias.

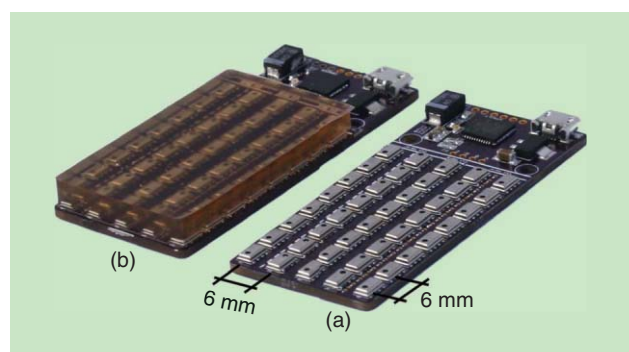


Figure 12. An array of 40 sensors (a) before casting and (b) cast in 6 mm of rubber. The spacing between the sensors is 6 mm. The array communicates with a computer through a USB and can be sampled at 50 Hz. (Photo courtesy of Yaroslav Tenzer.)

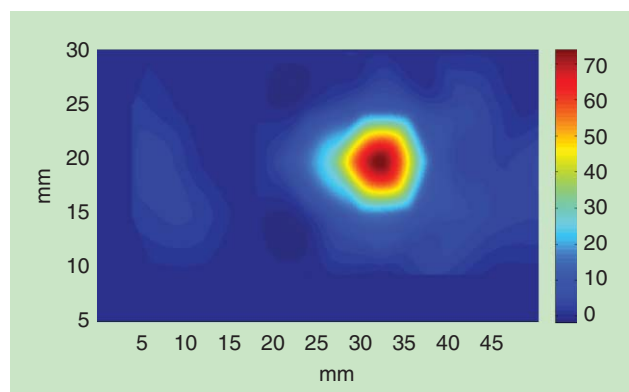


Figure 13. The sensor response in counts when a tennis ball is placed on the array in Figure 12. Cubic interpolation was applied to the sensor data. (Photo courtesy of Yaroslav Tenzer.)

makes the design waterproof. The sensors are sampled by dedicated onboard microcontrollers at 100 Hz through the serial peripheral interface protocol.

Customizable Arrays

The sensing technology has also been featured in the form of customizable sensor arrays [12]. The aim of this design is to allow researchers to become familiar and experiment with the technology without the need to understand electronics or manufacturing and, as such, lowers the barrier for adaption. A strip with five sensors spaced at 8 mm is shown in Figure 10. The strip where the sensors have been separated is shown in Figure 11. The separated sensors can be positioned as desired for the application and easily wired to the microcontroller (see [12] for more details).

Another customizable design was featured in the form of a five-by-eight sensor array (see Figure 12). The spacing between the sensors is 6 mm, and it can be cut to size for desired shape. The communication with the array can be carried out through the I²C protocol or dedicated USB interface. The sampling speed of an array is 50 Hz. The sensor reading from an array when a tennis ball is placed on the surface is shown in Figure 13.

Conclusions

This article presents a new approach to the construction of tactile arrays based on barometric pressure sensor chips and standard PCBs. The chips include tightly integrated instrumentation amplifiers, analog-to-digital converters, temperature sensors, and control circuitry that provides excellent signal quality over standard digital bus interfaces. The resulting electronic array can be easily encapsulated in soft polymers to adapt the sensors to specific robot hand designs.

The performance evaluation of the prototype arrays demonstrated excellent linearity (<1% typical) and low noise levels (<0.01 N). The external addressing circuitry allows multiple sensors to communicate on the same bus at over 100 Hz per sensor element. Sensors can be mounted as close as 3 × 5 mm spacing, and spatial impulse response tests show that solid-mechanics-based signal processing approaches are feasible [15]. The sensors also have temperature-sensing capabilities, which can be useful for the development of thermal sensing systems [18], although the elastomer overlayer may limit the response speed.

The use of standard commercial off-the-shelf technologies means that only basic electrical and mechanical skills are required to build effective tactile sensors, and costs are low despite the high performance of the resulting sensor system. The sensor arrays circuits can be embedded in rubber using custom three-dimensional-printed molds to integrate the sensors into robot finger structures with a robust and compliant grasping surface. This approach can enable progress in understanding the role of tactile information in robotic grasping and manipulation, as well as research in diverse fields, such as biomechanics and human-machine interfaces, where contact location and pressure distribution information can be valuable.

Acknowledgment

We would like to acknowledge seminal discussions with Gill Pratt. This work was supported by the National Science Foundation under award IIS-0905180 and by the Defense Advanced Research Projects Agency under contract W91CRB-10-C-0141.

References

- [1] R. S. Dahiya, G. Metta, M. Valle, and G. Sandini, "Tactile sensing—From humans to humanoids," *IEEE Trans. Robot.*, vol. 26, no. 1, pp. 1–20, 2010.
- [2] M. R. Cutkosky, R. D. Howe, and W. R. Provancher, "Force and tactile sensing," in *Springer Handbook of Robotics*, B. Siciliano and O. Khatib, Eds. Heidelberg, Berlin: Springer, 2008, ch. 19.1, p. 1611.
- [3] M. H. Lee and H. R. Nicholls, "Tactile sensing for mechatronics: A state of the art survey," *Mechatronics*, vol. 9, no. 1, pp. 1–31, 1999.
- [4] Pressure Profile Systems, Inc. (2012, Nov.). [Online]. Available: <http://www.pressureprofile.com/>
- [5] Tekscan Inc. (2012, Nov.). Tactile pressure measurement, pressure mapping systems, force sensors and measurement systems. Tekscan is the leading pressure mapping manufacturer. [Online]. Available: <http://www.tekscan.com/>
- [6] Syntouch—The BioTac. (2012, Nov.). [Online]. Available: <http://www.syn-touchllc.com/>
- [7] Weiss Robotics—Tactile sensors. (2012, Nov.). [Online]. Available: <http://www.weiss-robotics.de/en/english/technology/tactilesensors.html>
- [8] G. Lammel and J. Patzel. (2009, July 1). Pressure sensors provide indoor competency for navigation. *Small Times* [Online]. pp. 1–4. Available: <http://electroiq.com/blog/2009/07/pressure-sensors-provide-indoor-competency-for-navigation/>
- [9] Bosh Sensortec. (2009, Oct.). BMP085 digital pressure sensor. Datasheet. [Online]. Available: <http://media.digikey.com/pdf/Data%20Sheets/Bosch/BMP085.pdf>
- [10] Semiconductor Freescale. (2010). MPL115A2 Miniature I²C Digital Barometer. Datasheet. [Online]. Available: http://cache.freescale.com/files/sensors/doc/data_sheet/MPL115A2.pdf
- [11] UM10204 I²C-Bus Specification and User Manual. NXP Semiconductors, User Manual, Eindhoven, The Netherlands, vol. 4, Feb. 2012.
- [12] (2012, Nov.). TakkTile project. [Online]. Available: <http://www.takktile.com>
- [13] A. M. Dollar and R. D. Howe, "A robust compliant grasper via shape deposition manufacturing," *IEEE/ASME Trans. Mechatron.*, vol. 11, no. 2, pp. 154–161, 2006.
- [14] R. R. G. Budynas and J. K. Nisbett, *Shigley's Mechanical Engineering Design* (Series in Mechanical Engineering), 9 ed. New York: McGraw-Hill Education, 2011.
- [15] R. S. Fearing and J. M. Hollerbach, "Basic solid mechanics for tactile sensing," *Int. J. Robot. Res.*, vol. 4, no. 3, pp. 266–275, 1984.
- [16] G. Vásárhelyi, B. Fodor, and T. Roska. (2007, Oct.). Tactile sensing-processing: Interface-cover geometry and the inverse-elastic problem. *Sens. Actuators A: Phys.* [Online]. 140(1), pp. 8–18. Available: <http://dx.doi.org/10.1016/j.sna.2007.05.028>
- [17] L. U. Odhner, L. P. Jentoft, M. R. Claffee, N. Corson, Y. Tenzer, R. R. Ma, M. Buehler, R. Kohout, R. D. Howe, and A. M. Dollar. (2013, Jan.). A compliant, underactuated hand for robust manipulation. [Online]. Available: <http://arxiv.org/abs/1301.4394>
- [18] H. R. Nicholls and M. H. Lee. (1989, June). A survey of robot tactile sensing technology. *Int. J. Robot. Res.* [Online]. 8(3), pp. 3–30. Available: <http://ijr.sagepub.com/content/8/3/3.abstract>

Yaroslav Tenzer, Harvard University and TakkTile LLC, Cambridge, Massachusetts, USA. E-mail: ytенzer@seas.harvard.edu.

Leif P. Jentoft, Harvard University and TakkTile LLC, Cambridge, Massachusetts, USA. E-mail: lјentoft@seas.harvard.edu.

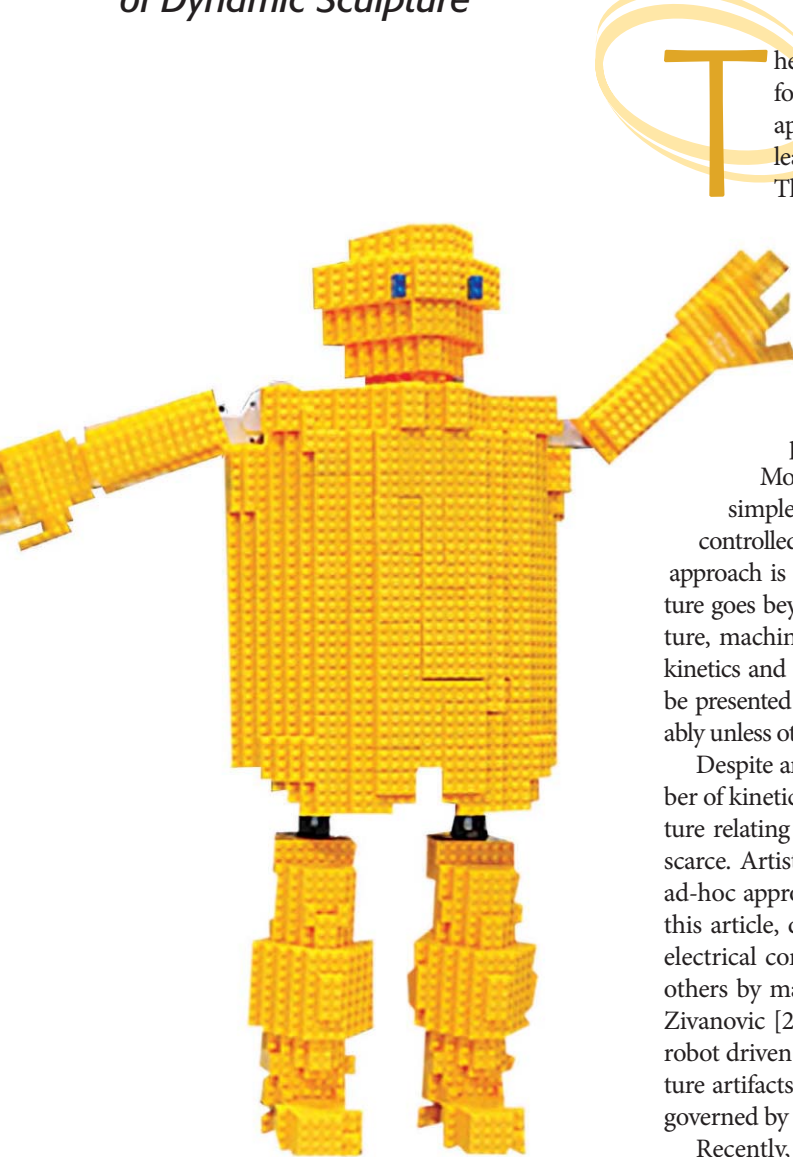
Robert D. Howe, Harvard University, Cambridge, Massachusetts, USA. E-mail: howe@seas.harvard.edu.



Robotic Dynamic Sculpture

Architecture, Modeling, and Implementation of Dynamic Sculpture

By Tan Zhang, Kirk Backstrom, Richard E. Prince, Changli Liu, Zhiqin Qian, Dan Zhang, and Wenjun Zhang



Digital Object Identifier 10.1109/MRA.2014.2312842
Date of publication: 20 August 2014

The well-developed and well-known robotic technology used for product adaptability and versatility has the potential to be applied to sculptures or three-dimensional (3-D) artifacts, leading to a new class of sculptures called *dynamic sculpture*. The promise of dynamic sculpture is to enable the sculpture to exhibit controlled motion. This article introduces the architecture, modeling, and implementation of dynamic sculpture.

Dynamic Sculpture and Its Related Works

Unlike traditional static arts, kinetic arts create artifacts that exhibit motion. It is well known that movement is a powerful means to express semantics and change emotion.

Movements in contemporary kinetic arts are, however, relatively simple and passively or naturally controlled. Although naturally controlled kinetic sculptures do change emotion, the natural control approach is restricted in creating a variety of motions. Dynamic sculpture goes beyond the nature-driven kinetic sculpture. In dynamic sculpture, machine-driven systems are introduced. The difference between kinetics and dynamics is not really relevant to the dynamic sculpture to be presented in this article. Thus, these two terms are used interchangeably unless otherwise stated explicitly.

Despite an increase in production in the past few decades, the number of kinetic sculptures produced remains relatively small. In the literature relating to sculpture, research into dynamic sculpture is relatively scarce. Artists who designed dynamic sculpture artifacts are based on ad-hoc approaches and techniques. Prince [1], one of the coauthors of this article, designed some dynamic sculptures using mechanical and electrical components, some of which are controlled by humans and others by machines, to perform some repeating periodic movements. Zivanovic [2] presented a robotic art work, *Senster*, which is a welded robot driven by two or more hydraulic actuators. These dynamic sculpture artifacts were created with pure artistic instinct, although they are governed by the basic mechanical laws.

Recently, engineering researchers have designed several dynamic sculptures using the theory of automatic control. Raine and Gooch [3] analyzed the dynamics and explored the design laws for maintaining the static and dynamic similarity when the original sculptures are scaled up. Based on a classical theory and a finite-element method, they

succeeded in identifying the scaling rules that enable a quick evaluation of the design implications in scaling up dynamic flexible sculptures, such as the Len Lye works—see Raine et al. [4]. Furthermore, Gooch and Raine [5] discovered that different scaling rules have different effects. Giesbrecht et al. [6] designed the leg of a well-known kinetic sculpture, a wind beast [7], using the theory of mechanism design and genetic algorithms. A prototype of a small wind beast, comprising both mechanical and electrical components, was built based on the dynamic force analysis. The foregoing works did apply some engineering and design principles and techniques. However, there is a lack of a general framework upon which dynamic sculptures can be developed more systematically while not losing artistic flavors.

In this article, we present a new paradigm of creating a dynamic sculpture along with its technology for the realization of the dynamic sculpture based on the new paradigm. The new paradigm for dynamic sculpture is to view a dynamic sculpture as consisting of a backbone and flesh. The backbone follows the architecture of robots, and the flesh is any object that can be attached onto the backbone. To implement this concept of a dynamic sculpture, a modular system made of plastic materials is used, known as a *modular plastic module (MPM)*, for which any block modular system can be employed. An example of an MPM is the LEGO block. Note that the LEGO system follows the so-called sectional interface [8], so its modularity is of the highest degree. This feature makes the LEGO system a good candidate to implement the new paradigm; in particular, both the backbone and flesh can be constructed using the LEGO system. Figure 1 shows several modules of the LEGO MPM system; as such, a dynamic sculpture in essence becomes an MPM system. In this article, we present a technique to analyze the characteristics of motion of the MPM system, which is the first step to designing the dynamic sculpture. The use of the MPM has an additional benefit, as it virtually provides a new avenue to construct a sculpture. On a historical note, the foregoing paradigm for dynamic sculpture first appeared in [9]. The work presented in this article is a significant extension of that work.

A fundamental requirement for such a technique is systematization using a computer program to generate the model and code automatically. This code generation is typically performed by having a computer code for a general analysis procedure based on the availability of a particular formalism, such as the finite-element method shown in [10] and [11], and requiring a user to provide a description of the system to be analyzed through an input file to the code [11]. In the literature relating to robotics, the development of such a technique may be called *automatic kinematic and dynamic analysis* [11].

The MPM system is different from the conventional modular robots or machines in the sense that the latter mostly has serial and parallel structures and there is no rigid joint or connector among the modules. Note that the rigid joint connects two modules with no relative motion, and its concept was perhaps first proposed in [12]. Despite these differences, the

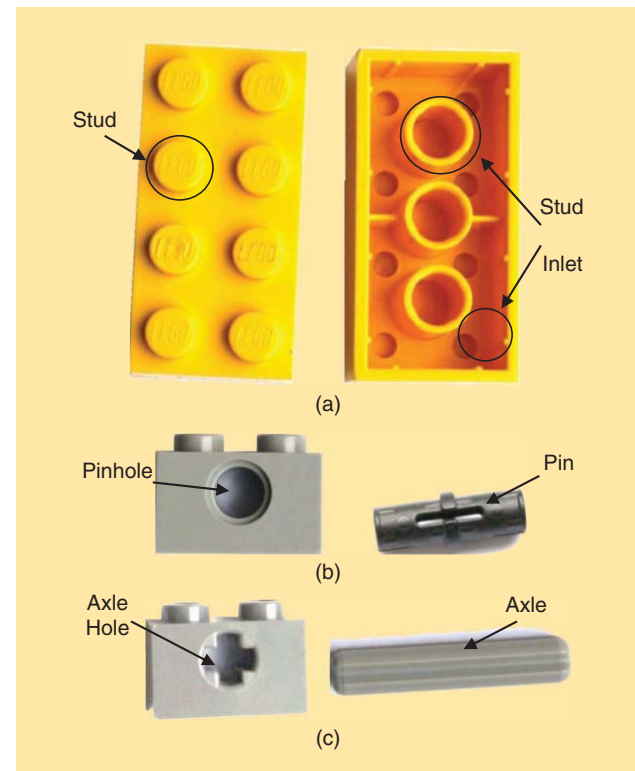


Figure 1. The interfaces in MPM systems [9]. (a) The stud-stud inlet interface between two link modules, which forms fixed connections. (b) The pinhole-pin interface between a link module and a rotary joint module. (c) The axle hole-axle interface between a link module and a prismatic joint module.

existing work on the motion analysis of modular robots is useful to this article and is reviewed in the following.

There has been considerable interest in the automatic modeling of modular robot configurations [13]–[21]. Note that the complexity of developing a system for the computer generation of the kinematic and dynamic equations depends on the generality of the modular robot configuration. Chen and Yang [16], [17] and Chen et al. [18] considered a relatively more general modular robot architecture, and they addressed the issue of the automatic kinematic and dynamic modeling for modular robot configurations based on their architecture using the product-of-exponentials method. Benhabib et al. [19] proposed methods to generate kinematic Denavit–Hartenberg (D–H) parameters from the configuration-space representation of robots. Bi et al. [20] and Bi [21] proposed a more general architecture of modular robots and an approach to determine the kinematics and dynamics of the modular robots based on the D–H architecture of kinematic representation of the links and the kinematic pairs.

In our technique, the D–H architecture is used, and, therefore, two challenges in our case are 1) a computational representation of the MPM systems and 2) an algorithm to convert this computational representation to the D–H representation. This article will address these two challenges. Finally, this article will present both virtual and physical dynamic sculptures made using the MPM system.

MPM Architecture

Architecture is an abstract description of the entities of a system and the relationships between these entities [22]. Specifically, the entities are characterized by a set of properties, including the elements and functions, and the relationships include the relationship between the elements and the mapping from elements to functions. The main problem in defining architecture is to define the entities by classification. Here, entity classification means that the elements are classified based on the functionality, which is further represented by the interfaces. An interface is the point of contact between parts, which has a form and function [23]. Therefore, each element should be classified according to the category of its interface from the viewpoints of both the form and the function.

MPM objects are fundamental parts that have independent functions. Each object has an interface. Take the LEGO system as an example. There are three major types of interfaces: 1) stud–stud inlet; 2) pinhole–pin; and 3) axle hole–axle, as shown in Figure 1. The stud–stud inlet interface type forms fixed connections between two modules. The pinhole–pin interface and the axle hole–axle interface form kinematic pairs to generate relative rotary and linear motions between two modules, respectively. Note that there could be another type of kinematic pair that combines rotary and linear kinematic pairs. For example, the axle–pinhole interface permits the axle to rotate and slide in the pinhole. Therefore, we can reduce the number of interfaces to two types: one type that forms fixed connections and the other type that allows relative motion. According to the classification of the functions of the interfaces, the LEGO elements and assemblies can be classified into two categories: 1) joint modules and 2) link modules. Link modules are the modules with stud–stud inlet interfaces. A set of link modules connected with their stud–stud inlet interfaces is called a *link*. To avoid confusion, the link modules are called *basic MPM modules*. Joint modules include pin-shaped modules and axle-shaped modules. With the assembly of links and joint modules, a mechanism or robot is produced. The mechanism makes up the backbone of a dynamic sculpture. Note that the flesh is a set of MPM objects that are assembled onto the backbone through the stud–stud inlet interface.

The architecture of the MPM systems is summarized as follows:

- 1) MPM systems have a modular architecture, with the interface between any two modules being identical.
- 2) MPM systems have links and joints.
- 3) A link is formed by basic MPM modules through the stud–stud inlet interface. All of the stud–stud interfaces are identical; see 1).
- 4) The joint is formed by connecting the basic MPM modules or links through the pinhole–pin or axle hole–axle interface. All of the pinhole–pin and axle hole–axle interfaces are identical; see 1).

MPM-Based Architecture for Dynamic Sculpture

The system architecture determines the system configuration because the architecture specifies the properties of components.

The configuration is a property of the system, which describes what and how components are distributed in space [24]. To make systems more adaptive, the number of configuration variants is expected to be as high as possible. The representation of the configuration becomes the first step. In this article, a configuration is presented to describe the kinematic connections among modules with the information of both types of connections and of modules. Note that the information of the module's spatial occupation is further derived from the configuration representation, and, in that sense, the representation indeed gives the information of configuration. We use three matrices to represent the configuration of the MPM system, including the types of modules (type matrix M_t), the adjacency of modules (adjacency matrix M_c), and the position of ports that participate in connection (port matrix M_p)

$$M_t = [t_1 \dots t_i \dots t_n],$$

where t_i denotes the type of module I (Figure 1).

$$M_c = \begin{bmatrix} c_{11} & \cdots & c_{1n} \\ \vdots & c_{ij} & \vdots \\ 0 & \cdots & c_{nn} \end{bmatrix},$$

where c_{ij} denotes the adjacency of two modules; 1: two objects are adjacent and 0: two components are not adjacent

$$M_p = \begin{bmatrix} p_{11} & \cdots & p_{112} \\ \vdots & p_{ik} & \ddots & \vdots \\ p_{m1} & \cdots & p_{m12} \end{bmatrix},$$

where M_p denotes the connection port information between adjacent or connected modules or connection objects (i.e., $c_{ij} = 1$ in M_c). Suppose that there are m connections in an assembly; i.e., in the M_c matrix, the total number of 1 elements is m . Each row in M_p , therefore, represents the detailed information of how two modules or objects are connected. Furthermore, note that for whatever type of connection, generally, the information of two ports from each module of the two in connection is sufficient. If the type of connection is revolute or sliding, the information of one port is sufficient, whereas, for the fixed type of connection, the information of any two ports on a module is sufficient. Therefore, each row in M_p has 12 elements and represents the detailed information of the ports of two connected modules. The first six elements represent two ports of one module, and the latter six elements represent two ports of the other module. In each of the six elements, the first three are for one port and the second three are for the other port. In the three elements for each port, the first element represents the face, and the remaining two elements represent the row and column number of a port.

In summary, the complete information of a particular configuration of a dynamic sculpture is determined by the three matrices: M_t , M_c , and M_p .

Kinematic Modeling

Kinematic modeling is a process to generate the D–H parameter for a particular configuration variant of the MPM system

(i.e., dynamic sculpture), which is represented by the three matrices, M_t , M_c , and M_p . This generation is completed by an algorithm operating on the three matrices, which has two steps in particular:

- 1) Generate the D-H architecture from the MPM system architecture. Note that the D-H architecture denotes the description of a robot with the D-H parameters that describe the kinematic geometry of the link or mechanism based on the D-H architecture.
- 2) Generate the kinematic model and dynamic model from the D-H architecture, i.e., generate the D-H parameters for the kinematics and the D-H parameters and information of mass, mass distribution and moment, and product of inertia for the dynamics. Furthermore, these parameters are obtained in a recursive way when all of the joints are labeled from the first to the last joint.

To determine the D-H architecture, the kinematic configuration (i.e., links, joint modules, and the connections between all modules) should be identified from the three matrices previously discussed. A procedure to identify the configuration used the following two steps:

- 1) Read matrix M_t to determine the joint and link modules as well as the virtual joint (VJ), which is composed of two link modules and one interface that allows for either relative rotation or translation between the two link modules (Figure 2). The sense of virtual is such that the physical entity that fulfills the joining of two link modules does not affect the kinematics or the dynamics of the two concerned link modules.
- 2) Read the adjacency matrix, M_c , to determine all adjacent connections between any two modules. Then, use the VJ to determine the basic MPM modules and, thus, the links.

The D-H architecture, along with its parameters, is explained with the help of Figure 2, which shows an example robot that contains three joint modules and two link modules. Each joint module has one degree of freedom in the robot. The D-H architecture includes the local coordinate system on each link module, i.e., $\{X_i, Y_i, Z_i\}$ for link i . The local coordinate system or frame is denoted by F_i . $F_i = \{O_{i+1,1}, X_i, Y_i, Z_i\}$ (Figure 2). $O_{i+1,1}$ is the intersecting points between X_i and Z_i . The position and orientation of F_i are relative to a reference coordinate system. This reference coordinate system is denoted as $\{F_{i,0}\}$. $F_{i,0} = \{O_{i,0}, X_{i,0}, Y_{i,0}, Z_{i,0}\}$. Furthermore, in the MPM system, $\{F_{i,0}\}$ is a local coordinate system that is attached to the port on VJ_{2i} (Figure 2). The representation of $\{X_i, Y_i, Z_i\}$ is described in the following sections.

Determination of Z_i

Z_i is assigned to the motion axis of joint body $i + 1$, as shown in Figure 2. Z_i can be expressed by

$${}_{i,0}Z_i = -\frac{P_i}{VJ_{2i}}T \cdot \frac{VJ_{2(i+1)}}{VJ_{2(i+1)}}T \cdot \frac{VJ_{2(i+1)}}{P_{i+1}}T \cdot {}_{i+1,0}Z_i, \quad (1)$$

where ${}_{i+1,0}Z_i$ is the description of Z_i with respect to joint module $i + 1$ and n_mT expresses the description of m with respect to n . For example, $\frac{P_i}{VJ_{2i}}T$ is the description of VJ_2 with respect to port P_i on VJ_2 through which joint i is connected. n_mT can be determined with the following formulation.

As shown in Figure 3, two link modules are connected, with port 1 on module 1 and port 2 on module 2 participating in the connection. The position of the module is obtained from the connection between the ports, i.e.,

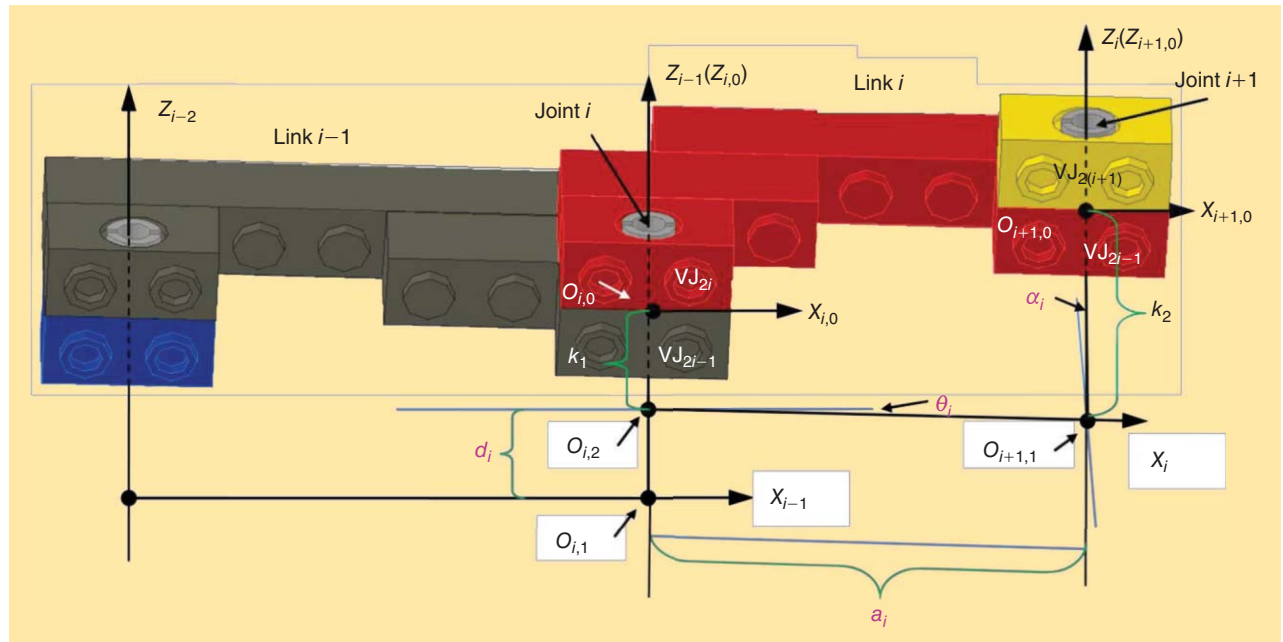


Figure 2. The architecture for the D-H parameters [9]. a_i : the length of the common normal between Z_{i-1} and Z_i ; α_i : the angle between Z_{i-1} and Z_i measured about X_i ; d_i : the distance from X_{i-1} to X_i measured along Z_{i-1} ; and θ_i : the angle between X_{i-1} and X_i measured about Z_{i-1} .

$$\begin{cases} {}^1_2 T {}^2 P_2 = {}^1 P_1 \\ {}^1_2 R {}^2 \hat{U}_2 = -{}^1 \hat{U}_1, \end{cases} \quad (2)$$

where ${}^1 P_1$ and ${}^1 \hat{U}_1$ are the position and orientation of port 1 with respect to the coordinate system of module 1. ${}_2 R$ is the rotation matrix of module 2 with respect to module 1.

Determination of X_i

X_i is perpendicular to both Z_{i-1} and Z_i , and its direction follows the right-hand rule from Z_{i-1} to Z_i . X_i can be expressed by

$$X_i = O_{i+1,1} - O_{i,2}, \quad (3)$$

where $O_{i,2}$ and $O_{i+1,1}$ are the intersecting points between X_i and Z_{i-1} and between X_i and Z_i , respectively; they are determined by two scales, k_1 and k_2 , which are computed by the following equations:

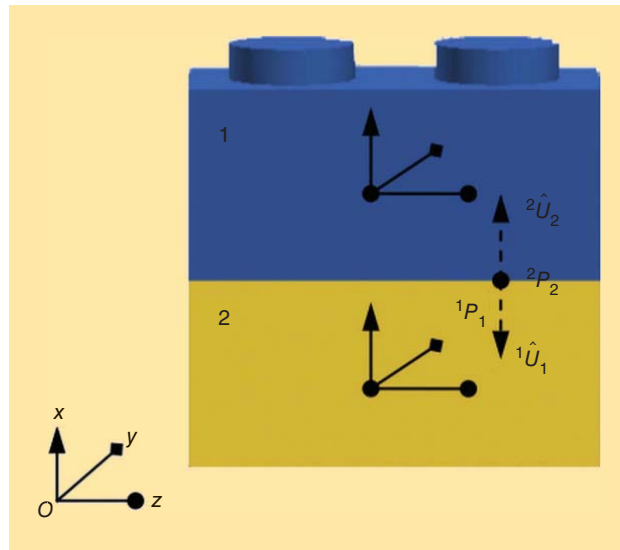


Figure 3. A link with two link modules [9].

$$\begin{cases} O_{i,2} = O_{i,0} + k_1 \cdot Z_{i-1} \\ O_{i+1,1} = O_{i+1,0} + k_2 \cdot Z_i \end{cases}. \quad (4)$$

Because X_i is perpendicular to both Z_{i-1} and Z_i , we obtain the following:

$$\begin{cases} (O_{i,2} - O_{i+1,1}) \cdot Z_{i-1} = 0 \\ (O_{i,2} - O_{i+1,1}) \cdot Z_i = 0 \end{cases}. \quad (5)$$

From (4) and (5), k_1 and k_2 can be obtained. Thus, X_i is determined. The D-H parameters are calculated by

$$\begin{cases} a_i = |O_{i+1,1} - O_{i,0} O_{i,2}| \\ \alpha_i = \cos^{-1}(Z_{i-1} \cdot Z_i) \\ d_i = (O_{i,2} - O_{i,1}) \cdot Z_{i-1} \\ \phi_i = \cos^{-1}(X_{i-1} \cdot X_i) \end{cases}. \quad (6)$$

Dynamic Modeling

Dynamic modeling refers to determining the mass, the mass center, and the moment of inertia of the links on the top of the kinematic model. Note that a link here has three contributions to its total mass: two VJs and the MPM modules between the two VJs (Figure 2).

Mass of Link i

The mass of link i is the sum of the mass of each basic MPM module in the link

$$m_i = m_{i,1} + m_{i,2} + \dots + m_{i,n}, \quad (7)$$

where m_i is the total mass of link i and $m_{i,j}$ is the mass of each module in the link, and, in particular,

$$\begin{aligned} j &= 1: \text{half VJ } i \text{ (left);} \\ j &= 2 \sim n-1: \text{link modules (middle);} \\ j &= n: \text{half VJ } i+1 \text{ (right).} \end{aligned}$$

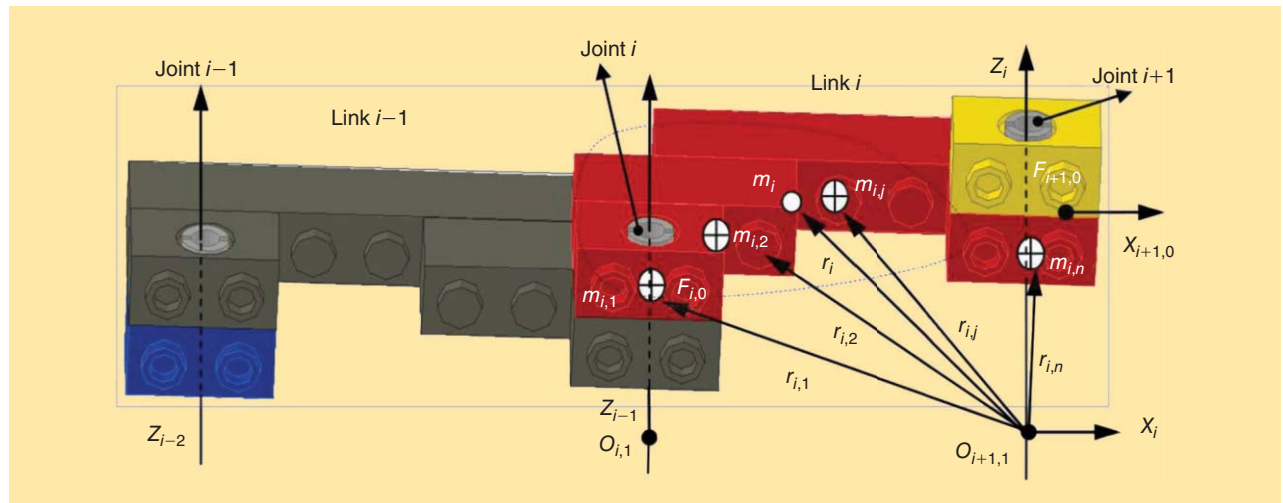


Figure 4. The dynamic parametric conversion.

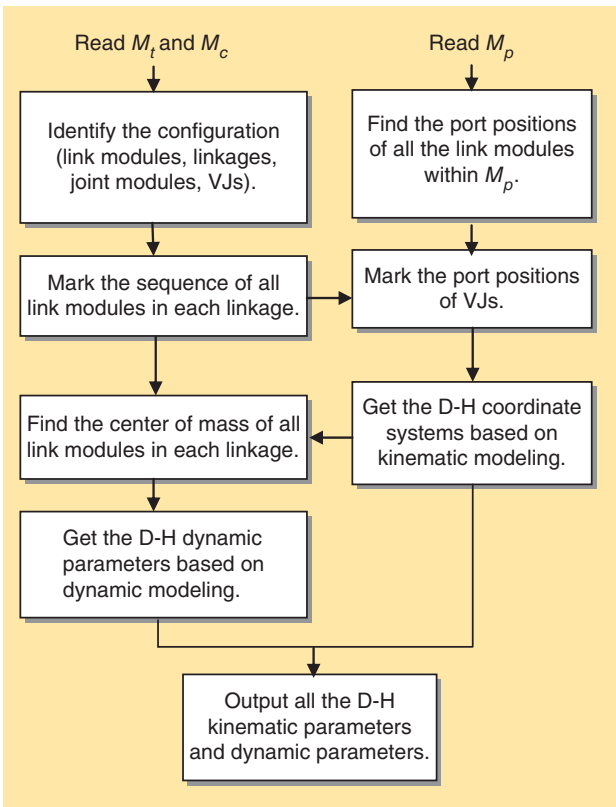


Figure 5. The procedure of the automated kinematic and dynamic model [9].

Center of Mass of Link *i*

Link *i* is assembled with *n* modules, so the coordinate \mathbf{r}_i of the center of mass of link *i* is

$$\mathbf{r}_i = \frac{(m_{i,1}\mathbf{r}_{i,1} + m_{i,2}\mathbf{r}_{i,2} + \dots + m_{i,n}\mathbf{r}_{i,n})}{(m_{i,1} + m_{i,2} + \dots + m_{i,n})}, \quad (8)$$

where \mathbf{r}_i is the center of mass of link *i* and $\mathbf{r}_{i,j}$ is the center of mass of each module in link *i*.

Note that the center of mass of each basic MPM module (i.e., \mathbf{r}_i and $\mathbf{r}_{i,j}$) should refer to a reference coordinate system that is the coordinate system of link *i*, denoted by $F_i = \{\mathbf{O}_{i+1,1}, X_i, Y_i, Z_i\}$ (Figure 4). Note that this coordinate system was determined in the kinematic modeling discussed in the “Moment of Inertia of Link *i*” section.

Moment of Inertia of Link *i*

We ignore the product of inertia of the link and only develop the representation of the moment of inertia. Note that the moment of inertia must be with respect to a local coordinate system that takes the center of mass as its origin and is further parallel to $F_i = \{\mathbf{O}_{i+1,1}, X_i, Y_i, Z_i\}$, as previously discussed.

The following describes the equation to compute the moments of inertia of all modules in link *i*. For details, see [21].

$$\begin{aligned} \bar{I}_{x_{i,0}x_{i,0},1} &= I_{x_{i,0}x_{i,0},1} + m_{i,1}((Y_{i,0} \cdot (\mathbf{r}_i - \mathbf{r}_{i,1}))^2 + (Z_{i,0} \cdot (\mathbf{r}_i - \mathbf{r}_{i,1}))^2), \\ \bar{I}_{y_{i,0}y_{i,0},1} &= I_{y_{i,0}y_{i,0},1} + m_{i,1}((X_{i,0} \cdot (\mathbf{r}_i - \mathbf{r}_{i,1}))^2 + (Z_{i,0} \cdot (\mathbf{r}_i - \mathbf{r}_{i,1}))^2), \\ \bar{I}_{z_{i,0}z_{i,0},1} &= I_{z_{i,0}z_{i,0},1} + m_{i,1}((X_{i,0} \cdot (\mathbf{r}_i - \mathbf{r}_{i,1}))^2 + (Y_{i,0} \cdot (\mathbf{r}_i - \mathbf{r}_{i,1}))^2), \end{aligned} \quad (9)$$

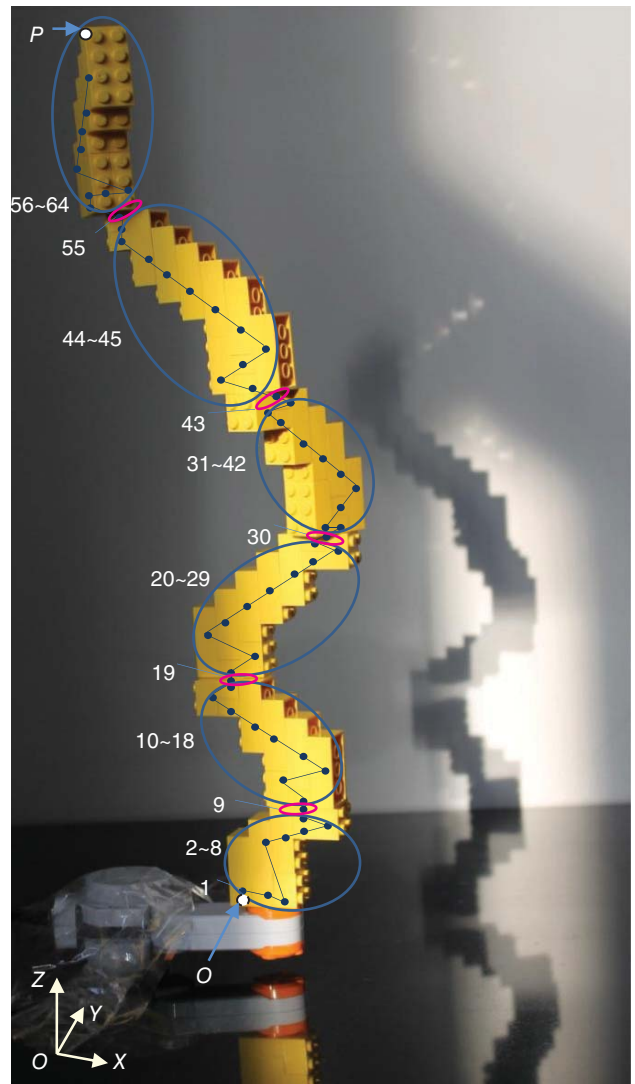


Figure 6. An MPM system built with LEGO modules. The backbone is marked with the curves, where dark (blue circle) curves denote links and light (pink circle) curves denote joints. Each link module is marked with a dot and is named sequentially.

where \bar{I}_{j_1,j_2,j_3} represents the principal inertial moment of the mass component j_3 at the mass center of link *i* with respect to the inertial axes j_1 and j_2 ; I_{j_1,j_2,j_3} represents the principal inertial moment of the mass component j_3 at its mass center with respect to the inertial axes j_1 and j_2 .

The moments of inertia of the other modules in link *i* can also be obtained through a similar procedure. Therefore, the moments of inertia of link *i* are described by

$$\bar{I}_{x_ix_i} = \sum_{j=1}^{j=n} I_{xx,j}, \quad \bar{I}_{yiy_i} = \sum_{j=1}^{j=n} I_{yy,j}, \quad \bar{I}_{ziz_i} = \sum_{j=1}^{j=n} I_{zz,j}, \quad (10)$$

where $\sum_{j=1}^{j=n} \bar{I}_{xx,j}$ represents the moments of inertia of link *i* at its mass center with respect to the principal axes.

A procedure is used to generate the kinematic and dynamic models for MPM systems automatically, as shown

in Figure 5. The program was implemented in the MATLAB environment. The inputs to this program are the representation of the configuration and the information of the MPM. The outputs are the D-H kinematic and dynamic parameters.

A Case Study

This section illustrates how to apply the kinematic model to a physical dynamic sculpture. The dynamic sculpture was built with 64 LEGO modules, including 59 link modules and five rotary joint modules, as shown in Figure 6. The configuration matrices of this MPM system as well as the pseudocode of the kinematic model can be found in [9]. Based on both the configuration matrices and the kinematic model, the joint modules, links, and VJs are identified, as shown in Table 1. Compared with the assembly of the MPM system in Figure 6, we can observe that the result in Table 1 is correct. Five kinematic states are captured to validate the kinematic model. The D-H parameters of each state are obtained based on both the configuration matrices and the kinematic model, as shown in Table 2.

To validate the result in Table 2, we compare the description of point P (the vertex of module 64) with respect to the coordinate system with origin O (the vertex of module 1). The theoretical result is obtained based on the D-H parameters in Table 2. We measured the result manually. The comparison results are shown in Figure 7, from which we can observe that there is a good match between the

Table 1. Identification of the joints and links.

Links	Link Modules	Joints	VJ 1	VJ 2
0	1 ~ 8	—	—	—
1	10 ~ 18	9	8	10
2	20 ~ 29	19	18	20
3	31 ~ 42	30	29	31
4	44 ~ 54	43	42	44
5	56 ~ 64	55	54	56

Note: VJ 1 and VJ 2 denote the first link module and the last link module in one link, respectively.

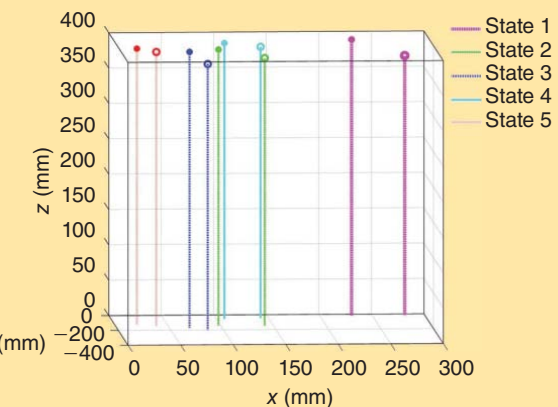


Figure 7. A comparison of the theoretical results and the measured results for point P with respect to the coordinate system of module 1 (Figure 6). Point P is on module 64. The origin of the coordinate system of module 1 is located at point O . Five states of point P are compared. The theoretical and measured results are denoted by * and o, respectively.

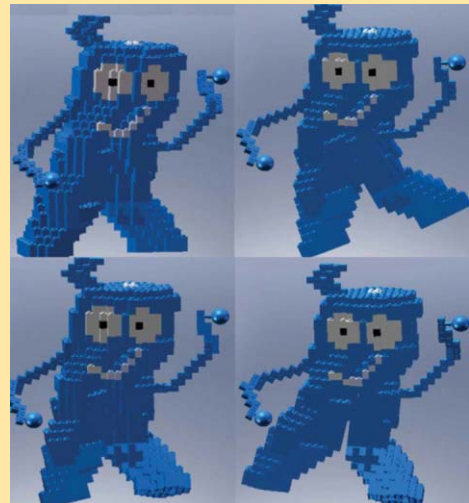


Figure 8. The four states of the dynamic sculpture *Haibao*, the Shanghai 2010 Expo Mascot, created in Solidworks [9]. The sculpture can move all of the limbs as in a dance. Each lower limb has three joints, and each upper limb has two joints.

Table 2. D-H parameters of the modular configurations.

Joint	a_{ji} (mm)	d_{ji} (mm)	α_{ji} (rad)	θ_{1i} (rad)	θ_{2i} (rad)	θ_{3i} (rad)	θ_{4i} (rad)	θ_{5i} (rad)
1	0.0	0.0	0.0	0.000000	0.000000	-1.570796	0.000000	-1.570796
2	28.8	54.6	0.0	0.000000	0.000000	1.570796	1.570796	1.570796
3	38.4	62.4	0.0	0.000000	-1.570796	-1.570796	-1.570796	-1.570796
4	48.0	78.0	0.0	0.000000	0.000000	0.000000	-1.570796	-1.570796
5	48.0	78.0	0.0	0.000000	0.000000	0.000000	0.000000	1.570796

Note: θ_i of configuration j is denoted as θ_{ji} ; $j = 1, 2, 3, 4, 5$.



Figure 9. The two states of the dynamic sculpture *Dance with the Wind*. The sculpture was created in Solidworks using five joint modules. The sculpture behaves in an exciting manner.

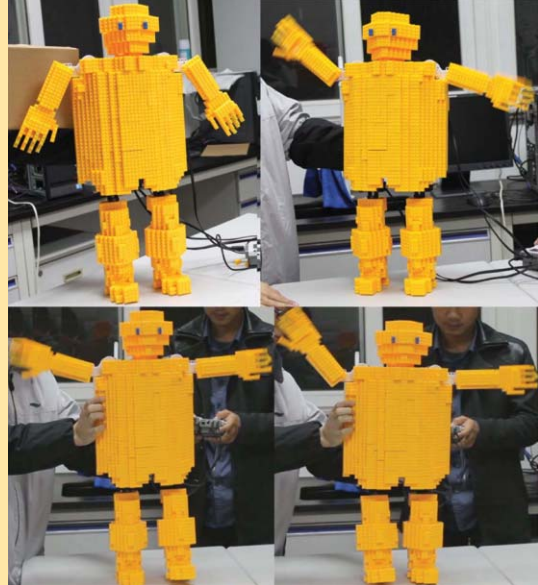


Figure 11. The four states of a *Haibao*-like dynamic sculpture built with LEGO-like modules. The sculpture can walk and wave its hands. Each limb has one NXT LEGO motor.

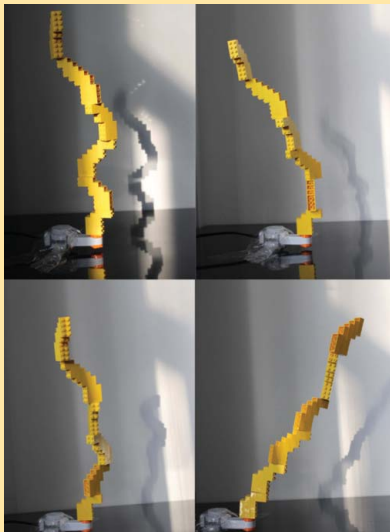


Figure 10. The four states of a physical MPM system built using LEGO modules. The sculpture has six rotary joints. Actuated by the NXT LEGO motor at the bottom, the entire system moves in a number of ways.

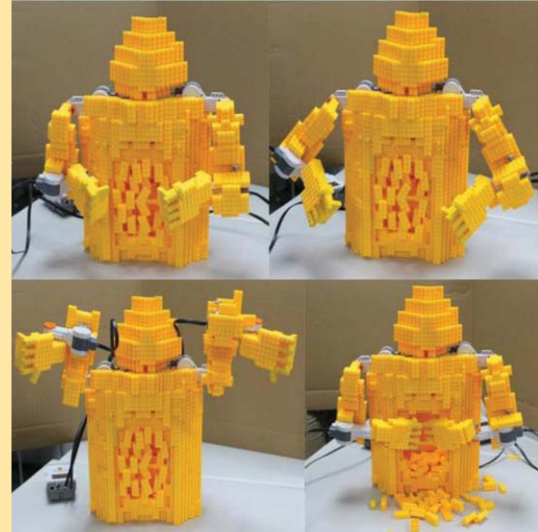


Figure 12. The four states of the *Yellow*-like dynamic sculpture built with LEGO-like modules, i.e., a torso of a man tearing open his chest with his arms, with many LEGO bricks falling out. Each arm has two NXT LEGO motors.

results from the kinematic model and the results from the physical system. Note that a discrepancy remains between the theoretical and the measured results. This discrepancy is due to the lack of stiffness of the LEGO material; as a result, the connections between the modules generate errors. In the measurement, we only consider the kinematic properties of LEGO modules without considering the mass. However, the agreement is reasonable, which validates our algorithm for kinematic modeling and analysis.

Examples

In this section, several dynamic sculpture prototypes are described. Figures 8 and 9 show the dynamic sculptures *Haibao* and *Dance with the Wind*, both of which were created in Solidworks. *Dance with the Wind* was inspired by a metal dynamic sculpture designed in [25]. Three physical prototypes were built with LEGO modules, as shown in Figures 10–12. Figure 12 shows a dynamic sculpture that is inspired by a static LEGO sculpture named *Yellow*, which

was created in [26]. The sculptures shown in Figures 8, 9, 11, and 12 are composed of thousands of LEGO modules.

Conclusions

In this article, we proposed a new paradigm of dynamic sculpture. The proposed approach involves assembling a dynamic sculpture using MPMs and using a robot as the backbone. Three issues were addressed: 1) the architecture for a dynamic sculpture based on the MPM principle, which is composed of link modules and joint modules; 2) a general representation of the dynamic sculpture configuration, which can be used to identify the link and joint module in the model; and 3) automated kinematic and dynamic modeling in which the configuration is determined automatically. In addition, the automated kinematic model was validated with a physical MPM system built with LEGO modules.

References

- [1] R. E. Prince. (2000). Advanced hyper-viewing angle [Online]. Available: <http://ahva.ubc.ca/reprince/gallery2.htm>
- [2] A. Zivanovic, "The development of a cybernetic sculptor: Edward Ihnatowicz and the senster," in *Proc. Creativity Cognition Conf.*, London, Apr. 12–15, 2005, pp. 586–591.
- [3] J. K. Raine and S. D. Gooch, "Dynamic analysis and engineering design of flexible kinetic sculptures," *IPENZ Trans.*, vol. 25, no. 1, pp. 29–42, 1998.
- [4] J. K. Raine, J. J. Harrington, E. A. Webb, and Z. A. Meredith, "Expanding Universe: Design study for scaling up a kinetic sculpture," *J. Eng. Design*, vol. 7, no. 4, pp. 397–410, 1996.
- [5] S. D. Gooch and J. K. Raine, "The dynamics and limits on the scaling of a flexible kinetic sculpture," *Proc. Inst. Mech. Eng., Part C: J. Mech. Eng. Sci.*, vol. 214, no. 4, pp. 537–548, Apr. 1, 2000.
- [6] D. Giesbrecht, C. Wu, and N. Sepehri, "Design and optimization of an eight-bar legged walking mechanism imitating a kinetic sculpture," *Trans. Canadian Soc. Mech. Eng.*, vol. 36, no. 4, pp. 343–355, 2012.
- [7] T. Jansen, *The Great Pretender*. Rotterdam, The Netherlands: 010 Publishers, 2007.
- [8] K. Ulrich, "The role of product architecture in the manufacturing firm," *Res. Policy*, vol. 24, no. 3, pp. 419–440, 1995.
- [9] T. Zhang, "Modular robot based dynamic sculpture," M.S. thesis, School Mech. Eng., East China Univ. Science and Technol., Shanghai, China, 2010.
- [10] K. van der Werff, "Kinematic and dynamic analysis of mechanisms: A finite element approach," Ph.D. dissertation, TU-Delft, Delft Univ. Technol., The Netherlands, 1977.
- [11] W. J. Zhang and K. van der Werff, "Automatic communication from a neutral object model of mechanisms to mechanism analysis program system based on a finite element approach," *Finite Elements Analysis Design*, vol. 28, no. 3, pp. 209–240, 1997.
- [12] W. J. Zhang, K. van der Werff, and C. A. van Lutterveld, "A generic mechanism model for use in a CIM environment for the development of mechanized production machines," *Annals CIRP*, vol. 42, no. 1, pp. 135–138, 1993.
- [13] R. Hooper and D. Tesar, "Computer-aided configuration of modular robotics systems," *J. Comput. Control Eng.*, vol. 5, pp. 137–142, June 1994.
- [14] J. Han, W. K. Chung, Y. Youm, and S. H. Kim, "Task based design of modular robot manipulator using efficient genetic algorithm," in *Proc. 1997 IEEE Int. Conf. Robotics Automation*, Albuquerque, New Mexico, Apr. 20–25, 1997, pp. 507–512.
- [15] C. J. J. Paredis, "An agent-based approach to the design of rapidly deployable fault tolerant manipulators," Ph.D. dissertation, Dept. Elect. and Comput. Eng., Carnegie Mellon Univ., Pittsburgh, PA, 1996.
- [16] G. Yang and I.-M. Chen, "Automatic generation of dynamics for modular reconfigurable robots," in *Proc. 1997 IEEE Int. Conf. Robotics Automation*, Albuquerque, New Mexico, Apr. 20–25, 1997, pp. 2288–2293.
- [17] I.-M. Chen and G. Yang, "Kinematic calibration of modular reconfigurable robots using product-of-exponentials formula," *J. Robot Syst.*, vol. 14, no. 11, pp. 807–821, 1997.
- [18] G. Yang, I.-M. Chen, W. K. Lim, and S. H. Yeo, "Kinematic design of modular reconfigurable in-parallel robots," *Auton. Robots*, vol. 10, no. 1, pp. 83–89, 2001.
- [19] B. Benhabib, G. Zak, and G. Lipton, "A generalized kinematic modeling method for modular robots," *J. Robot. Syst.*, vol. 6, no. 5, pp. 545–571, 1989.
- [20] Z. M. Bi, W. J. Zhang, I.-M. Chen, and S. Lang, "Automated generation of the D-H parameters for configuration design of modular manipulators," *Robot. Comput.-Integrated Manuf.*, vol. 23, no. 5, pp. 553–562, 2006.
- [21] Z. M. Bi, "On adaptive robot systems for manufacturing applications," Ph.D. dissertation, Dept. Mech. Eng., Univ. Saskatchewan, Saskatoon, Canada, 2002.
- [22] E. Crawley, O. D. Weck, S. Eppinger, C. Magee, J. Moses, W. Seering, J. Schindall, D. Wallace, and D. Whitney, "Engineering systems monograph," Massachusetts Inst. Technol., Cambridge, MA, Tech. Rep., 2004.
- [23] E. Crawley, *Lecture Notes for System Architecture, Engineering Systems Division*. Cambridge, MA: Massachusetts Institute Technol., 2007.
- [24] N. P. Suh, *Axiomatic Design: Advances and Applications*. New York: Oxford Univ. Press, 2001.
- [25] Youtube. (2000). Dance with the wind. [Online]. Available: www.youtube.com/watch?v=KDtvdl3-hD
- [26] N. Sawaya. (2003). Yellow. [Online]. Available: <http://brickartist.com/gallery/yellow/?ref=all>

Tan Zhang, Complex and Intelligent Systems Research Center, East China University of Science and Technology, China and Advanced Engineering Design Laboratory, University of Saskatchewan, Canada. E-mail: tan.zhang@usask.ca.

Kirk Backstrom, Advanced Engineering Design Laboratory, University of Saskatchewan, Canada. E-mail: kirk.backstrom@usask.ca.

Richard E. Prince, Department of Art History, Visual Art, and Theory, University of British Columbia, Canada. E-mail: richard.prince@ubc.ca.

Changli Liu, Complex and Intelligent Systems Research Center, East China University of Science and Technology, China. E-mail: clliu@ecust.edu.cn.

Zhiqin Qian, Complex and Intelligent Systems Research Center, East China University of Science and Technology, China. E-mail: qianzhiqin@ecust.edu.cn.

Dan Zhang, Complex and Intelligent Systems Research Center, East China University of Science and Technology, China, and Robotics and Automation Laboratory, University of Ontario Institute of Technology, Canada. E-mail: dan.zhang@uoit.ca.

Wenjun Zhang, Advanced Engineering Design Laboratory, University of Saskatchewan, Canada. E-mail: chris.zhang@usask.ca.

The CUIK Suite

Analyzing the Motion of Closed-Chain Multibody Systems

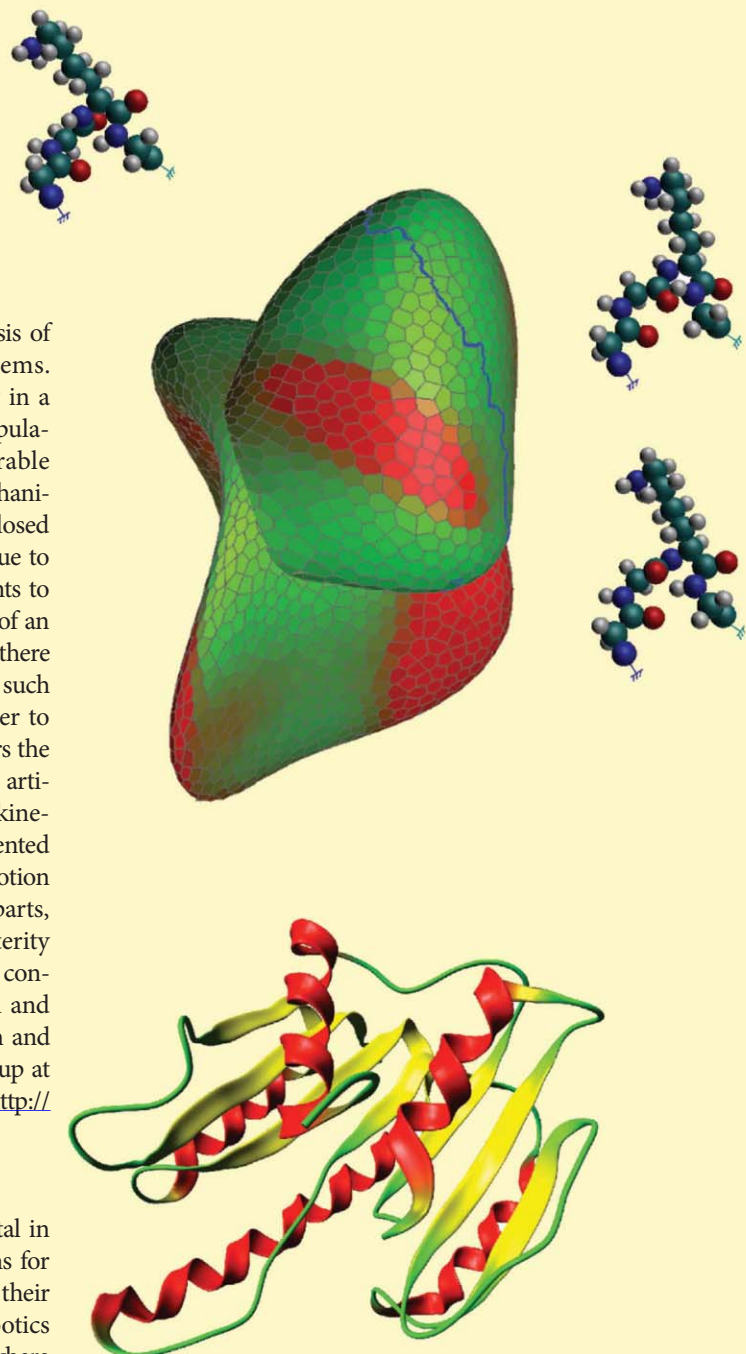
By Josep M. Porta, Lluís Ros, Oriol Bohigas, Montserrat Manubens, Carlos Rosales, and Léonard Jaillet



Many situations in robotics require the analysis of the motions of complex multibody systems. These are sets of articulated bodies arising in a variety of devices, including parallel manipulators, multifingered hands, or reconfigurable mechanisms, but they appear in other domains too as mechanical models of molecular compounds or nanostructures. Closed kinematic chains arise frequently in such systems, either due to their morphology or due to geometric or contact constraints to fulfill during operation, giving rise to configuration spaces of an intricate structure. Despite appearing very often in practice, there is a lack of general software tools to analyze and represent such configuration spaces. Existing packages are oriented either to open-chain systems or to specific robot types, which hinders the analysis and development of innovative manipulators. This article describes the CUIK suite, a software toolbox for the kinematic analysis of general multibody systems. The implemented tools can isolate the valid configurations, determine the motion range of the whole multibody system or of some of its parts, detect singular configurations leading to control or dexterity issues, or find collision- and singularity-free paths between configurations. The toolbox has applications in robot design and programming and is the result of several years of research and development within the Kinematics and Robot Design group at IRI, Barcelona. It is available under GPLv3 license from <http://www.iri.upc.edu/cuik>.

Motivation and Outlook

The notion of configuration space (C-space) is fundamental in robotics. It allows the design of motion analysis algorithms for broadly defined classes of robots without worrying about their particular geometry or multibody structure. In most robotics courses, this notion is introduced for open-chain robots, where the C-space has an explicit global parameterization. In this way, C-spaces are readily understood and algorithms operating on



Digital Object Identifier 10.1109/MRA.2013.2287462
Date of publication: 10 September 2014

them can be easily defined. In real problems, however, C-spaces can have a more complex structure. On a welding robot, for instance, the set of valid configurations reduces to those where the end-effector is in contact with the surface to be welded. This constraint implicitly defines a nonparametric C-space whose analysis is not trivial in general.

To deal with larger dimensional spaces, the CUIK suite implements randomized path planning algorithms.

Similar problems arise in structural biology, when analyzing the feasible motions of a molecule, or in computer-aided design, when assembling parts using spatial constraints. The CUIK suite provides effective tools aimed at analyzing the C-spaces arising in such a broad range of applications, a point not properly addressed in the related packages available so far.

In all of the considered problems, the valid configurations are implicitly defined by a system of kinematic equations encoding the assembly, task, or contact constraints

intervening in the problem, and the goal is to analyze the motion capabilities by finding the solutions of such a system. In an extreme case, the valid configurations are isolated points. This is what happens, for example, when solving position analysis problems on parallel or serial manipulators, where one wishes to compute the feasible configurations for given values of the input or output coordinates. Historically, the preferred approach to tackle these problems has been variable elimination: the initial equations are reduced to a resultant univariate polynomial, which is solved using well-established methods. The approach is sound, but it may introduce extraneous roots, and the size and degree of the resultant polynomial rapidly grow with the number of bodies and the complexity of their connection pattern. General elimination packages can be used [8], but they rapidly explode in complexity even on small problems, which explains why no general software for motion analysis has been built using them. The CUIK suite circumvents these issues by adopting an opposite approach. Instead of reducing the initial system of equations to a resultant polynomial, we formulate it as a larger system including only linear and quadratic equations. This particular formulation is then exploited to implement a branch-and-prune

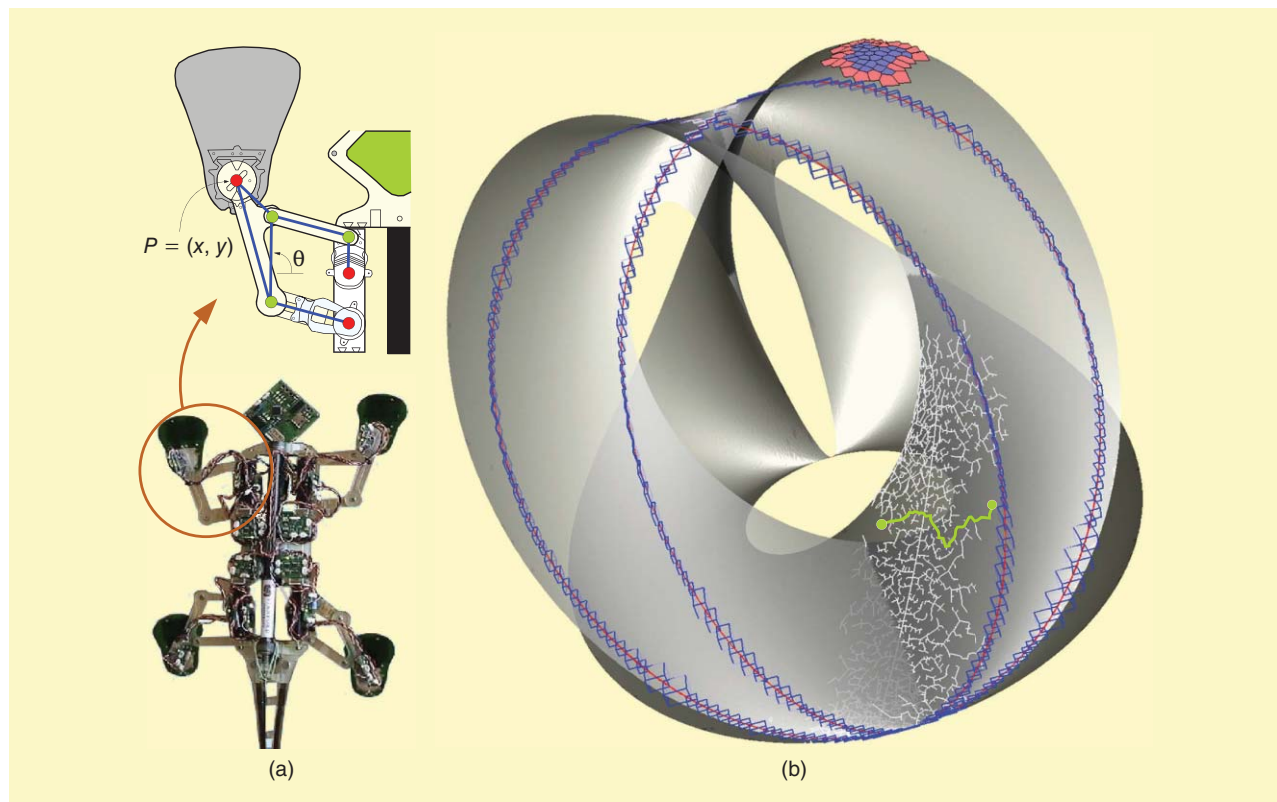


Figure 1. The results of the CUIK suite tools on the Stickybot III robot from the Stanford Biomimetics and Dexterous Manipulation Lab (<http://bdml.stanford.edu>). (a) Each leg has a five-bar mechanism (with actuated joints in red), (b) whose C-space is shown projected to the (x, y) coordinates of point P and angle θ . The suite allows a comprehensive analysis of the motions of systems of this kind. It can compute the C-space (the translucent gray surface), incrementally produce atlases to solve optimization or path-planning problems (the red and blue mesh at the top), obtain multiresolution approximations of singularity loci (the blue boxes and the refined red curve), or generate probabilistic road maps to connect configurations (the white tree, with a path highlighted in green). The projection of this surface to the (x, y) plane produces the reachable workspace of point P .

method able to compute the whole solution set. The method departs from an initial box bounding this set and effectively prunes unfeasible portions of the box until all solution points are isolated at the desired accuracy. Software toolboxes, such as ALIAS [16], Bertini [1], and PHC [28], have been successfully applied to kinematics, but they implement general methods for solving systems of algebraic equations. In contrast, the CUIK suite sacrifices generality to gain simplicity and efficiency in the implementation. Opposite to [1] and [28], moreover, it directly isolates the real roots instead of the complex ones, which is beneficial in practice.

While many approaches can only identify the solutions when they are isolated points, the branch-and-prune methods in the CUIK suite can also approximate positive-dimensional solutions. This can be used to compute the whole C-space or some of its subsets, providing global information on the motion capabilities of a manipulator. In particular, by adequately defining the equations passed to the solver, the CUIK suite can isolate the workspace boundaries and any of the singularity sets typically defined [7], becoming the first general tool able to do so, to the best of our knowledge.

Branch-and-prune methods are complete in the sense that they obtain all configurations, irrespective of whether they form one or several connected components. In many problems, however, it may be sufficient to explore only those configurations that are path connected to a given point. To this end, the CUIK suite implements higher dimensional continuation tools to trace arbitrary manifolds [10]. While

branch-and-prune methods proceed by discarding nonvalid configurations, continuation techniques march from a given point in all directions identifying new feasible configurations. Local charts of the C-space are constructed and coordinated along the way, defining a global atlas that is suitable to determine feasible motion ranges, optimal configurations, or paths between configurations. Packages to compute the latter exist, but they are oriented to open-chain robots [9], [15], [26], [27] or to specific classes of closed-chain devices [14]. The CUIK suite complements these packages by providing the new methods to deal with the general closed-chain case. For

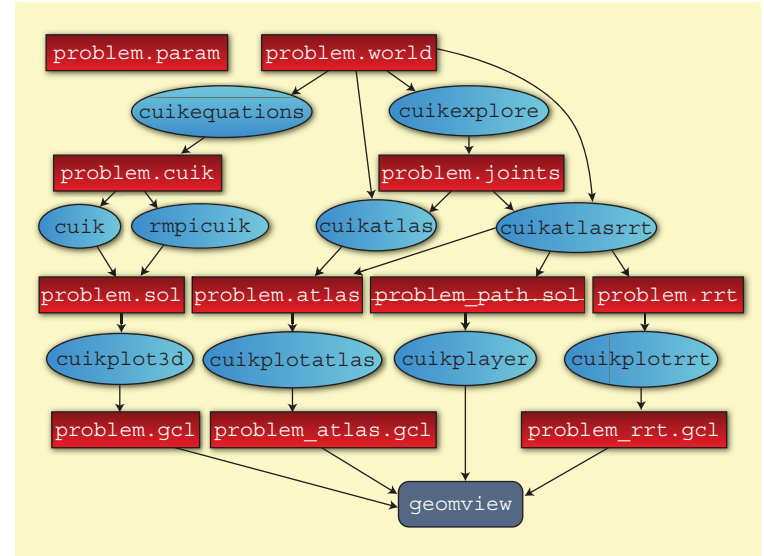


Figure 2. A representative set of the commands implemented in the CUIK suite (ellipses) and their input/output files (rectangles). The parameters file `problem.param` is used by all the commands. The suite implements many other tools not shown here for simplicity. Note: `geomview` is an external visualization program.

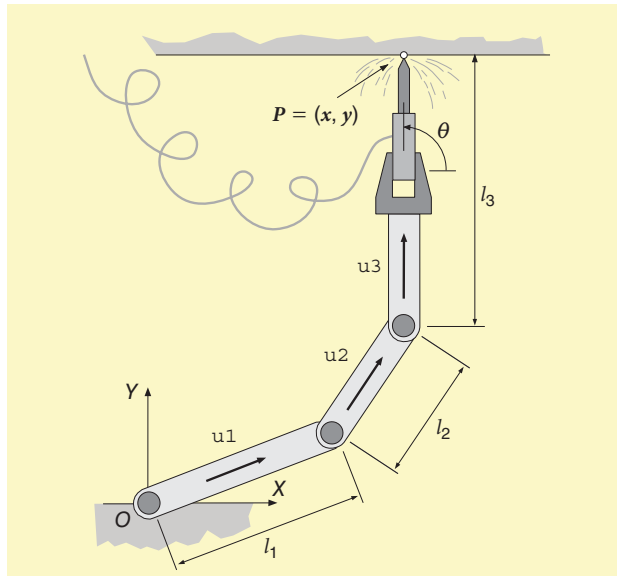


Figure 3. A planar arm welding on a beam. The goal is to weld on a particular point P with orientation θ .

```

[constants]
l1 := 1
l2 := 1
l3 := 1.3
x := 0.25
y := 2.05
theta := pi/2
[system vars]
u1_x: [-1,1]
u1_y: [-1,1]
u2_x: [-1,1]
u2_y: [-1,1]
u3_x: [-1,1]
u3_y: [-1,1]
[system eqs]
u1_x^2+u1_y^2=1;
u2_x^2+u2_y^2=1;
u3_x=cos(theta);
u3_y=sin(theta);
l1*u1_x+l2*u2_x+l3*u3_x=x;
l1*u1_y+l2*u2_y+l3*u3_y=y;

```

Example 1. The `welding.cuik` file encoding the problem in Figure 3.

```
[constants]
l1:= 1
l2:= 1
l3:= 1.3
x:= 0.25
y:= 0.75
theta:= pi/2

[links]
environment: body "beam.off" blue
link1: body "link1.off" gray
link2: body "link2.off" gray
link3: body "link3.off" gray
body "gripper.off" black

[joints]
revolute: ground (0,0,0) (0,0,1)
link1 (0,0,0) (0,0,1)
revolute: link1 (l1,0,0) (l1,0,1)
link2 (0,0,0) (0,0,1)
revolute: link2 (l2,0,0) (l2,0,1)
link3 (0,0,0) (0,0,1)
fix: environment
link3
Tx(x)*Ty(y)*Rz(theta)
```

Example 2. The weldingOD.world file from which a system of equations equivalent to that in Example 1 can be automatically generated.

C-spaces of moderate dimension, the suite provides strategies to connect start and goal configurations through low-cost, collision- or singularity-free paths. To deal with larger dimensional spaces, the suite implements randomized versions of such tools based on the construction of rapidly exploring random trees (RRTs) spanning the C-space.

The branch-and-prune methods of the CUIK suite can approximate zero- or positive-dimensional C-spaces.

associated line commands, illustrating them on a simple tutorial example. A representative set of commands and their input/output files are shown in Figure 2. The documentation available online describes all the examples and functionalities in thorough detail.

Branch-and-Prune Methods

A basic example shows how the CUIK suite can address position analysis problems. Consider the planar manipulator in Figure 3, which has three links of lengths l_1 , l_2 , and l_3 and three revolute (3-RRR) joints. The goal is to compute the arm configurations, allowing it to weld at the indicated point $P = (x, y)$, with orientation θ . Example 1 shows the equations expressing this inverse kinematics problem in the

implements randomized versions of such tools based on the construction of rapidly exploring random trees (RRTs) spanning the C-space.

Figure 1 shows the main outputs of the CUIK suite on a particular example. In the rest of this article, we describe the methods used to produce such outputs and the



Figure 4. Some of the robots modeled in the CUIK suite: (a) the Schunk anthropomorphic hand, (b) the Barret hand-arm system, (c) the YouBot two-arm mobile platform, and (d) the PR2 service robot.

suite. Observe that the arm configurations are represented using three normalized vectors, $(u1_x, u1_y)$, $(u2_x, u2_y)$, and $(u3_x, u3_y)$, encoding the orientation of each link relative to the x -axis of the global frame. The position of the end-effector is given by the last two linear equations, and the $[-1, 1]$ ranges for the variables

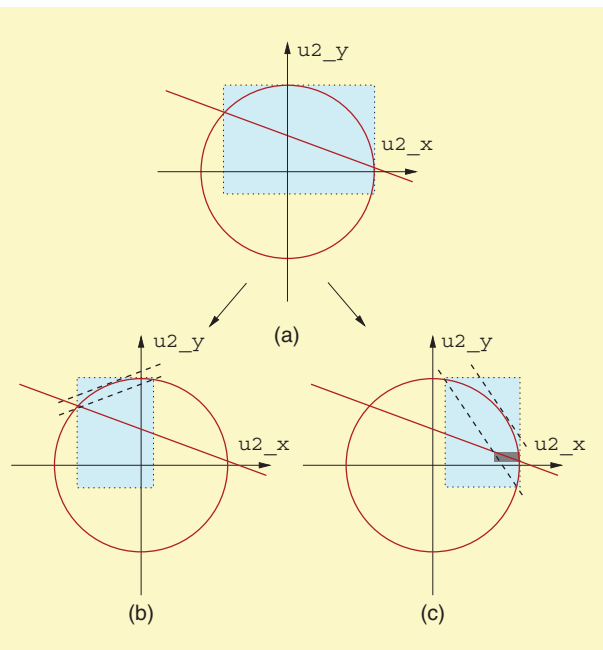


Figure 5. The bisection of (a) the blue box in the plot produces (b) and (c) the child boxes. By considering the linear equation and the relaxed version of the circle equation, we can accurately bound the solution points for the problem in Figure 3.

define a six-dimensional box bounding the location of all the possible solutions of the problem.

To facilitate the generation of the cuik files, the suite allows the definition of problems in a high-level form. By executing

```
> cuikequations welding0D.world
```

a set of equations equivalent to that in Example 1 is obtained from the world file shown in Example 2. This file describes the links and joints of the multibody system. A link definition includes the name of the link and its geometric shape, and a joint is given by its type, the two links connected, and the position of the joint in the local frame of each link. Figure 4 shows some of the robots modeled with world files in the CUIK suite. These predefined world files can be used as a starting point to easily define new problems.

By means of trivial manipulations, the equations in Example 1 can be simplified into the following system of equations:

$$\begin{aligned} 0.5*u2_x + 1.5*u2_y &= 0.625, \\ u2_x^2 + u2_y^2 &= 1, \end{aligned}$$

and the search box can be limited to the ranges $[-0.75, 1]$ and $[-0.25, 1]$ in $u2_x$ and $u2_y$, respectively. The graph of these equations and the new search box are represented in Figure 5(a) using the solid and dotted lines, respectively. As shown, the solution points lie in the intersection of a line and a circle in the space of $u2_x$ and $u2_y$. To identify such points, the box is first bisected along the $u2_x$ axis, obtaining

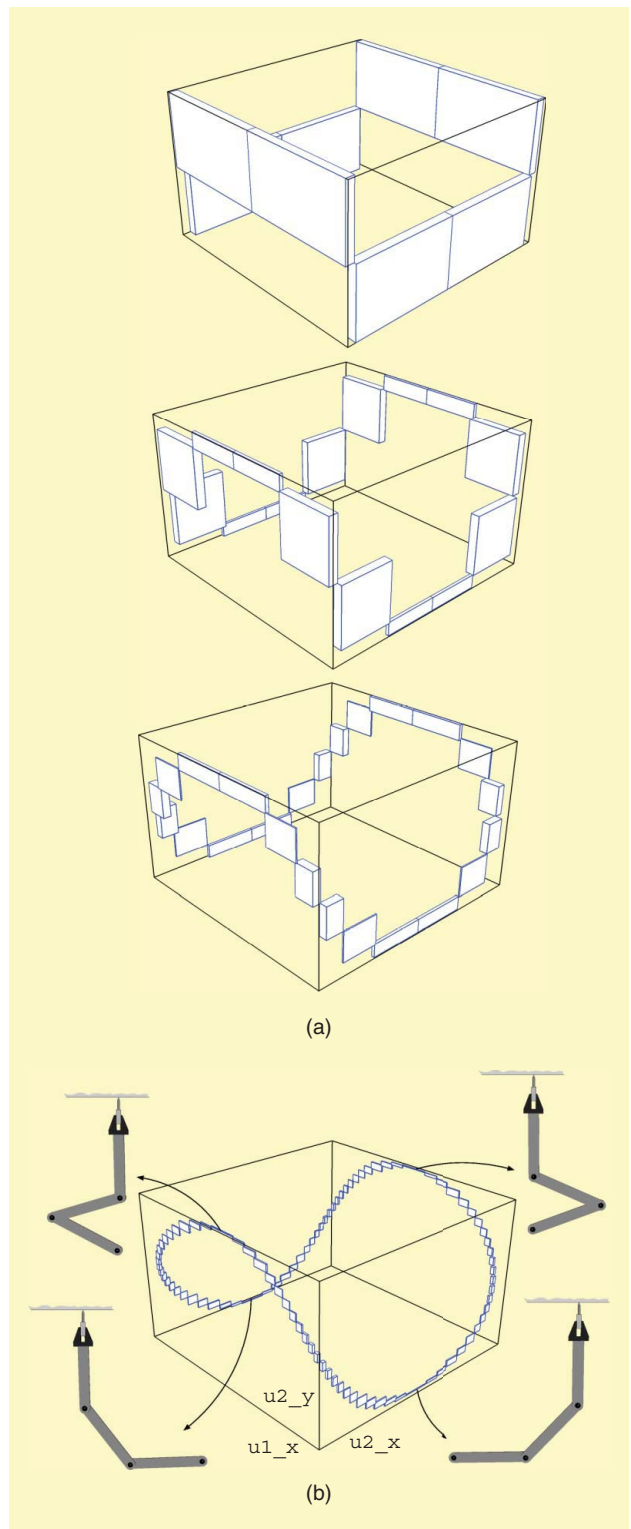


Figure 6. (a) The progress of the branch-and-prune method when computing the C-space of the robot arm in Figure 3, when the end-effector is set to contact the lower line of the beam with a fixed orientation. (b) The arm configurations for some of the solution boxes.

the two blue boxes Figure 5(b) and (c). The circular arc inside each blue box is then approximated by half-planes (shown as dashed lines in the figure). These half-planes are used in

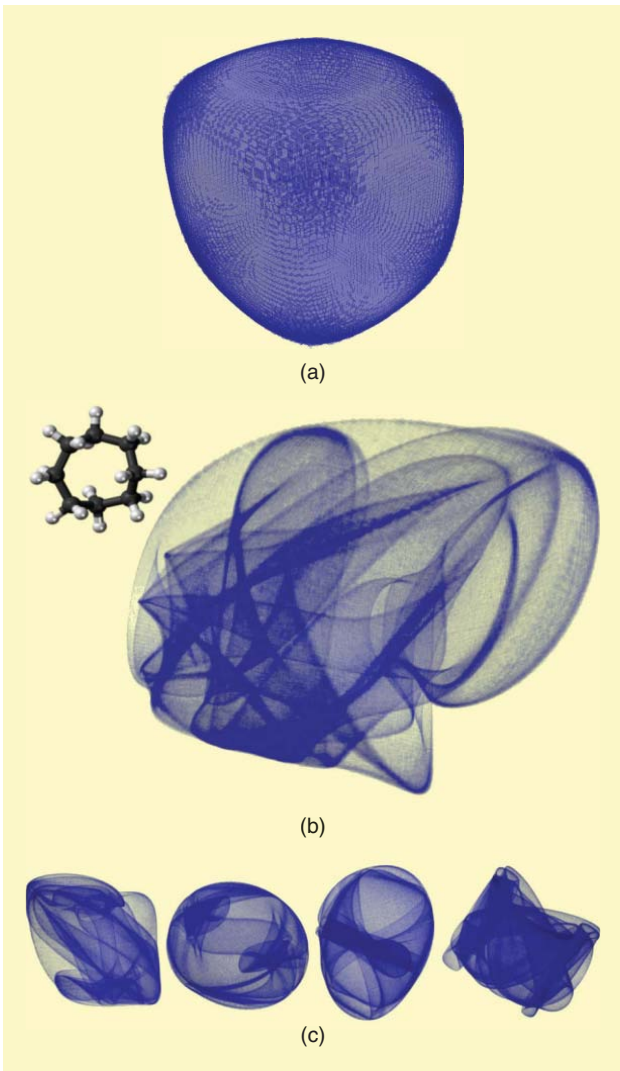


Figure 7. (a) A box approximation of the 2-D C-space of the welding task when the tool can contact the lower part of the beam with any orientation. The approximation contains $\sim 15,000$ boxes, which are here rendered with translucent material. (b) The cyclooctane molecule, a ring of eight carbon atoms pairwise connected through rotatable covalent bonds, and a box approximation of its 2-D C-space with $\sim 300,000$ boxes projected on three of the problem variables. (c) Different shapes are obtained by projecting the boxes on alternative triplets of variables.

conjunction with the linear equation to derive a tiny box around the solution in Figure 5(b) and a larger dark gray box bounding the solution in Figure 5(c). This pruning operation is implemented using linear programming, and it is repeated for each box until no further significant reduction is possible. In the end, if the largest side of the box is below a given threshold, it is considered a solution box. Otherwise, it is bisected and the process is recursively applied to the newly created subboxes. The following command:

```
> cuik welding0D.cuik
```

automates this process. It reads the cuik file, simplifies the equations when possible, and applies the pruning and

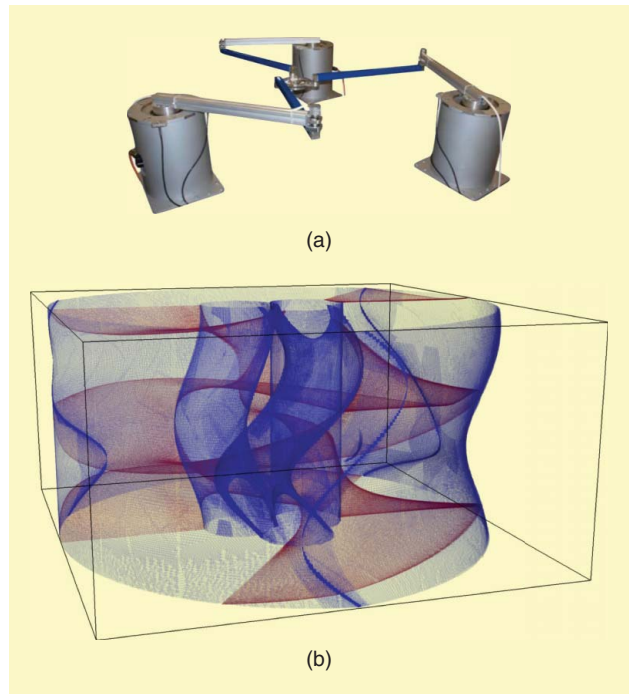


Figure 8. (a) A 3-RRR manipulator from the University of Hannover (photo courtesy of Jens Kotlarski <http://www.imes.uni-hannover.de>). (b) Typical singularity loci computed for such kind of manipulators [6].

bisection operations until all solution points are isolated at the desired accuracy. The problem in Figure 3 is simple, but the method is also successful on complex problems involving general 6R robots and Stewart platforms [21] or in mechanisms with more than 12 kinematic loops [20]. To have an idea, elimination or resultant methods are finding their limit in mechanisms of substantially less complexity [23].

The cuik command can also be used to isolate C-spaces of positive dimension. For instance, if the robot in Figure 3 has to weld along a line in the lower part of the beam while keeping the tool orientation fixed, then the problem exhibits a one-dimensional manifold of solutions. Figure 6 shows several stages of the branch-and-prune method in this case [Figure 6(a)] and the final box approximation returned as output [Figure 6(b)]. The plots are obtained and visualized by executing

```
> cuik welding1D.cuik
> cuikplot3d welding1D.sol 1 3 4
  welding1D.gcl
> geomview welding1D.gcl
```

which projects the solution boxes to the subspace of the $u1_x$, $u2_x$, and $u2_y$ coordinates. These are the variables appearing in the first, third, and fourth positions of the *welding1D.cuik* file describing the problem. The insets in Figure 6(b) show the arm configurations corresponding to some of the boxes.

If the welding task is further relaxed and the tool can contact the beam with any orientation, the problem exhibits a

two-dimensional (2-D) C-space. Such a space can be interactively explored using the following command:

```
> cuikexplore welding2D.world
```

and it can again be approximated using the `cuik` command, producing the results in Figure 7(a). The box approximation includes ~15,000 boxes that are computed in just 45 s on a standard desktop computer. To solve more difficult problems in a reasonable amount of time, the CUIK suite implements a parallel version of the solver, which can be invoked through the `rmpicuik` command. With this tool, the branch-and-prune solver can be executed in large computer grids, where a “master” CPU manages the exploration tree and a number of “slave” CPUs apply the pruning operations to the assigned boxes. Using this tool on a cluster with 160 CPUs, it took a few minutes to isolate 2-D C-spaces like the one in Figure 7(b). This process would require costly computations using single-CPU machines or alternative approaches [22].

C-spaces of robotic systems typically exhibit singularity subsets. These are loci of configurations where problematic losses of control or dexterity arise [6], [7]. They also reveal the boundaries of the task and joint workspaces and all motion barriers that may be encountered in their interior [4]. The ability to compute these loci is thus essential, not only to anticipate possible problems during robot operation but also to provide valuable information to the robot designer. The CUIK suite can be employed to isolate all singular configurations of a manipulator by appropriately formulating their equations and passing them to the solver [2], [7]. For example, Figure 8 shows typical forward and inverse singularity loci obtained by the suite tools on a 3-RRR manipulator, shown projected to the pose coordinates of the end effector, x , y , and θ . The blue surface corresponds to the inverse singularities, which delimit the boundary of the (x, y, θ) workspace. The red surface corresponds to the forward singularities, which indicate the configurations in which velocity control issues arise [6].

Continuation Methods

Continuation methods generate atlases of the C-space regions that are connected to a given point. To see how such atlases can be constructed, let us assume that $F(\mathbf{x}) = \mathbf{0}$ is any system of equations encoding the kinematic constraints of the multi-body system, whose solution set constitutes the C-space C under consideration. Also, let \mathbf{x}_i be an initial configuration satisfying $F(\mathbf{x}_i) = \mathbf{0}$. The points in \mathcal{T}_i , the tangent space of C at \mathbf{x}_i , can be parameterized by

$$\mathbf{x}' = \mathbf{x}_i + \Phi_i \mathbf{u}, \quad (1)$$

where Φ_i is a matrix providing an orthonormal basis of \mathcal{T}_i , and \mathbf{u} is a parameter vector with the same dimension as C . By choosing a value for \mathbf{u} in (1), we obtain a point $\mathbf{x}' \in \mathcal{T}_i$, which can be projected to \mathbf{x}_j , the point in C lying in the normal line through \mathbf{x}'_i by solving the system

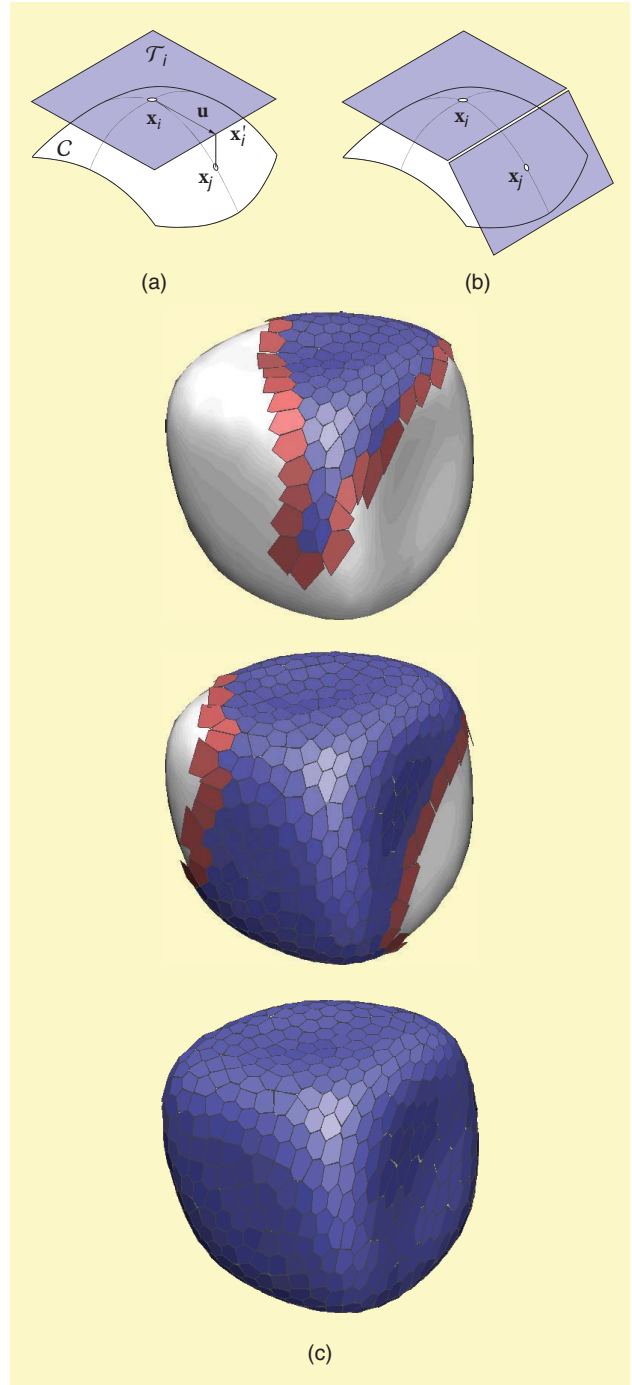


Figure 9. (a) A chart is used to obtain new configurations by projecting points from the tangent space. (b) When a new chart is defined, the chart domains are mutually coordinated to keep track of the explored area. (c) Progress of the atlas construction method on the C-space of the robot arm in Figure 3, assuming that the welding tool can contact the lower part of the beam with any orientation. This C-space is shown projected on three of the problem variables. Red polygons represent the charts to be extended in subsequent iterations.

$$\begin{cases} F(\mathbf{x}_j) = \mathbf{0}, \\ \Phi_i^\top (\mathbf{x}_j - \mathbf{x}'_i) = \mathbf{0}, \end{cases} \quad (2)$$

as shown in Figure 9(a). The new configuration \mathbf{x}_j can be used to define a new chart that can be coordinated with the

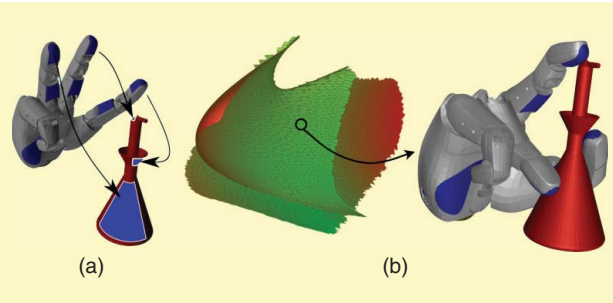


Figure 10. An optimization problem in the context of grasp synthesis. (a) The configuration of the hand-object system must satisfy a number of contact constraints. An initial feasible grasp is computed using the branch-and-prune methods [25] and is used as the initial configuration from which to construct an atlas of the relevant C-space subset [24]. (b) The chart centers of this atlas can be evaluated according to a performance criterion in order to select the optimal grasp. The red and green colors in the atlas correspond to low- and high-quality grasps, respectively.

previous chart [Figure 9(b)], and the process can be iterated until the component of C reachable from \mathbf{x}_i gets fully covered [Figure 9(c)]. Every time a new chart is defined, the CUIK suite checks for the presence of bifurcations of C and propagates the atlas construction through such bifurcations so as not to leave areas unexplored. The command

```
> cuikatlas welding2D
```

takes the `world` file describing the robot welding problem when the robot can contact the lower part of the beam with any orientation and a `joints` file providing the initial configuration. As output, it returns an `atlas` file including the charts, which can be visualized using

```
> cuikplotatlas welding2D 0 9 18
> geomview welding2D_atlas.gcl
```

where the indices 0, 9, and 18 indicate the three coordinates on which to represent the atlas. The results of these commands are shown in Figure 9(c). In this case, the atlas

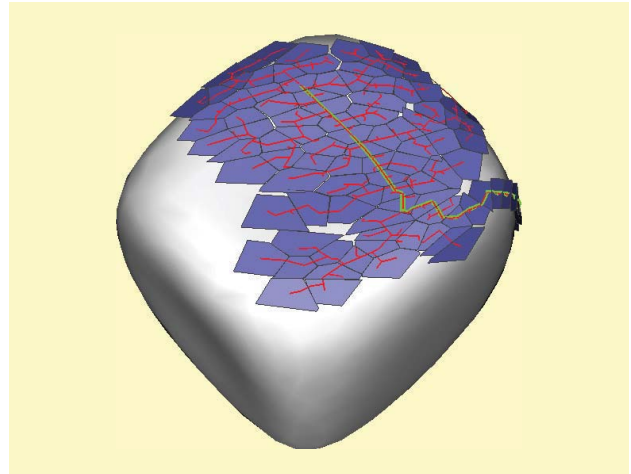


Figure 12. An RRT and a partial atlas solving a path-planning query over the C-space manifold of the welding robot when the tool can contact the lower part of the beam with any orientation. In this problem, the robot has to avoid colliding with the beam. The path over the RRT solving the planning query is shown in green.

construction takes 0.1 s on a standard desktop computer, while the isolation of the same space using branch-and-prune techniques requires ~45 s. Such a remarkable speedup comes at the expense of neglecting other connected components but allows for the tackling of difficult optimization problems involving large multibody systems (Figure 10).

To solve path-planning problems, the CUIK suite exploits the fact that an atlas implicitly defines a road map of the C-space, whose nodes and edges are, respectively, the chart centers and collision-free transitions between neighboring charts. The collisions to avoid can be specified in the `world` files. The road map can be readily used to resolve multiple planning queries between different configurations. However, for cases where only one query needs to be resolved, it is better to employ the `cuikatlasAstar` tool, which constructs only those charts leading to the shortest path between the given configurations. With this tool, singularity-free path planners for general closed-chain [3] and cable-driven manipulators [5] have been developed, solving problems for which no alternative satisfactory solution had been given to date (Figure 11). Trading off optimality for efficiency, the `cuikatlasGBF` tool

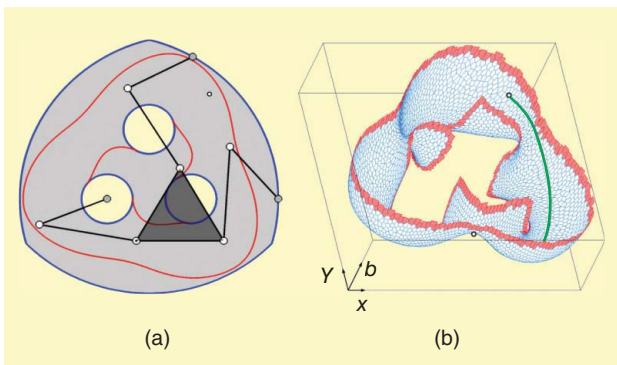


Figure 11. (a) A singularity-free path-planning problem on a 3-RRR manipulator [3], the gray area is the constant-orientation workspace of the manipulator, and the red curves correspond to the forward singularity locus to be avoided during the move. (b) The solution path computed by the CUIK suite, in green, projected on the three variables relevant to the problem. The red charts correspond to configurations that are almost singular.

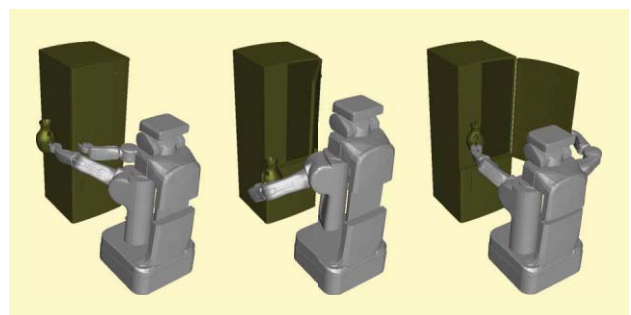


Figure 13. The different stages of the execution of a path allowing the arm to put a pitcher in a fridge that is initially closed.

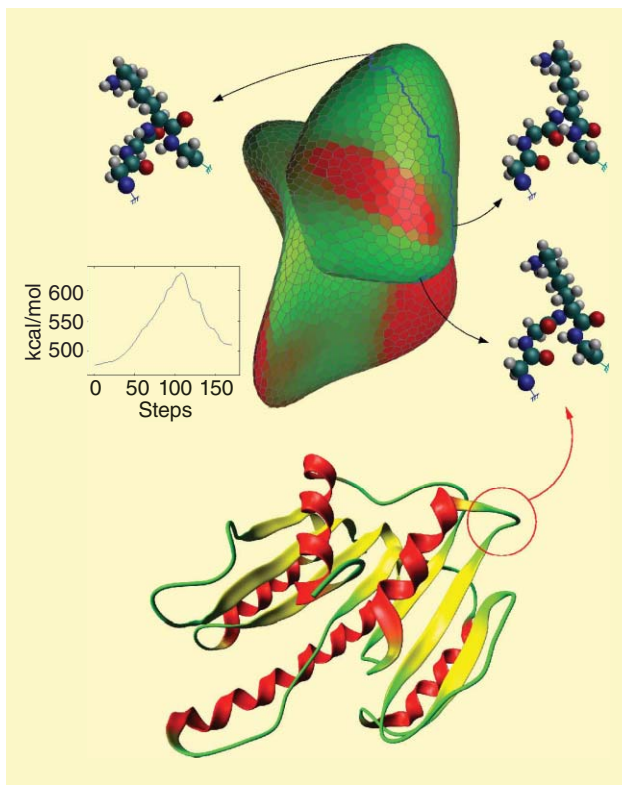


Figure 14. A low-cost path (in blue) computed in the conformational space of a loop of the FTSJ protein of *Escherichia coli* (in the ribbon diagram in the bottom). The cost is the potential energy of each conformation. Inset: the initial conformation, the transition state (i.e., the conformation with the highest potential energy along the path), and the final conformation. Only the atoms in the loop are shown in such conformations. The plot shows the energy profile along the transition path.

provides a path planner that implements a greedy best first strategy to connect the query configurations [19].

Both the cuikatlasAstar and the cuikatlasGBF tools can be inefficient in cluttered environments, and they do not scale gracefully to higher dimensions. To avoid these weaknesses, the CUIK suite includes the cuikatlasrrt tool, which implements a sampling method where a partial atlas is used to extend an RRT, which in turn is exploited to decide expansion directions for the atlas [13]. For instance, after specifying the start and goal configurations in the joints file, the sequence of commands

```
> cuikatlasrrt welding2D
> cuikplotatlas welding2D 0 9 18
> cuikplotrrt welding2D 0 9 18
> geomview welding2D_rrt.gcl
welding2D_atlas.gcl
```

produces an RRT and an atlas like those shown in Figure 12. The motion of the robot along the path solving the planning problem can be visualized executing

```
> cuikplayer welding2D welding2D_path
```

Using this technique, it is possible to solve problems in pretty high dimensions. Figure 13, for example, shows three snapshots of the path computed by this method in a manipulation problem involving a PR2 robot. The robot has to carry a pitcher without tilting it and put it in a fridge that is initially closed. The two arms are open-chain robots, but their configurations are restricted by task and contact constraints, respectively, which make the planning problem rather difficult. The C-space is eight-dimensional, but it takes less than 3s to determine the solution path.

Paths generated with RRT-like algorithms might be costly or unnecessarily long. To address these issues, the CUIK suite includes procedures to generate near-optimal paths when there is a cost function related to the C-space. If the cost is defined for each configuration, one can use the cuikatlasrrt tool, which implements an extended version of the T-RRT algorithm in [11]. For instance, Figure 14 shows a low-cost path computed with this method in the case of a short loop of the FTSJ protein of *Escherichia coli*, where the cost function is the potential energy of each protein conformation [18]. If the cost is the length of the path, the cuikatlasrrtstar tool can be used instead, which is an adaptation of the RRT* asymptotically optimal path planner to the case of implicitly defined C-spaces [12].

To solve more difficult problems in reasonable times, the CUIK suite implements a parallel version of the solver.

Conclusions

This article described the CUIK suite, a comprehensive set of tools to analyze C-spaces implicitly defined by systems of kinematic constraints. We provided a brief account of the underlying techniques and the commands used to invoke them. Since problems involving kinematic constraints are ubiquitous in robotics, the suite may potentially be used in contexts beyond those described in this article, including mobile robot localization and mapping [17], motion analysis and synthesis of robot formations, tensegrity and deployable structures, or programmable surfaces, to name a few.

In the future, we plan to extend the suite to also accommodate the dynamics of the multibody systems to facilitate a direct interfacing with robots operating under inertia effects. However, the suite is an open-source package under continuous development, and hence, we invite the community to use it and help us to improve it by sending feedback and suggestions on new functionalities to include.

Acknowledgments

The branch-and-prune methods in the CUIK suite have evolved from years of collaboration with Federico Thomas, whose guidance and inspiring comments have certainly

shaped the final result. The authors would like to thank Michael E. Henderson for introducing them to the higher dimensional continuation methods and Dimiter Zlatanov for his feedback and support on the analysis and interpretation of mechanism singularities.

This work was partially supported by the Spanish Ministry of Economy and Competitiveness under projects DPI2010-18449 and DPI2011-13208-E, by CSIC project 201250E026, by a Juan de la Cierva fellowship supporting Montserrat Manubens, and by a CSIC JAE-Doc fellowship partially funded by the ESF supporting Léonard Jaillet.

References

- [1] D. J. Bates, J. D. Hauenstein, A. J. Sommese, and C. W. Wampler. (2014). The Bertini software. [Online]. Available: <http://www3.nd.edu/~sommese/bertini>
- [2] O. Bohigas. (2013). Numerical computation and avoidance of manipulator singularities. Ph.D. dissertation, Institut de Robòtica i Informàtica Industrial, Universitat Politècnica de Catalunya, Barcelona, Catalonia. [Online]. Available: <http://goo.gl/wlR0i>
- [3] O. Bohigas, M. E. Henderson, L. Ros, M. Manubens, and J. M. Porta, "Planning singularity-free paths on closed-chain manipulators," *IEEE Trans. Robot.*, vol. 29, no. 4, pp. 888–898, 2013.
- [4] O. Bohigas, M. Manubens, and L. Ros, "A complete method for workspace boundary determination on general structure manipulators," *IEEE Trans. Robot.*, vol. 28, no. 5, pp. 993–1006, 2012.
- [5] O. Bohigas, M. Manubens, and L. Ros, "Navigating the wrench-feasible C-space of cable-driven hexapods," in *Proc. Int. Conf. Cable-Driven Parallel Robots*, 2012, pp. 53–68.
- [6] O. Bohigas, M. Manubens, and L. Ros, "Singularities of non-redundant manipulators: A short account and a method for their computation in the planar case," *Mech. Mach. Theory*, vol. 68, pp. 1–17, Oct. 2013.
- [7] O. Bohigas, D. Zlatanov, L. Ros, M. Manubens, and J. M. Porta, "A general method for the numerical computation of manipulator singularity sets," *IEEE Trans. Robot.*, vol. 30, no. 2, pp. 340–351, 2014.
- [8] D. Cox, J. Little, and D. O'Shea, *An Introduction to Computational Algebraic Geometry and Commutative Algebra*. 3rd ed. New York: Springer-Verlag, 2007.
- [9] I. A. Sucan, M. Moll, and L. E. Kavraki, "The open motion planning library," *IEEE Robot. Automat. Mag.*, vol. 19, no. 4, pp. 72–82, 2012.
- [10] M. E. Henderson, "Multiple parameter continuation: Computing implicitly defined k-manifolds," *Int. J. Bifurcation Chaos*, vol. 12, no. 3, pp. 451–476, 2002.
- [11] L. Jaillet, J. Cortés, and T. Siméon, "Sampling-based path planning on configuration-space costmaps," *IEEE Trans. Robot.*, vol. 26, no. 4, pp. 635–646, 2010.
- [12] L. Jaillet and J. M. Porta, "Efficient asymptotically-optimal path planning on manifolds," *Robot. Auton. Syst.*, vol. 61, no. 8, pp. 797–807, 2013.
- [13] L. Jaillet and J. M. Porta, "Path planning under kinematic constraints by rapidly exploring manifolds," *IEEE Trans. Robot.*, vol. 29, no. 1, pp. 105–117, 2013.
- [14] LAAS-CNRS. (2014, Feb.). Move 3D. [Online]. Available: <http://www.openrobots.org/wiki/move3d>
- [15] S. LaValle. (2014, Feb.). The motion strategy library. [Online]. Available: <http://msl.cs.uiuc.edu/msl>
- [16] J.-P. Merlet. (2014, Feb.). Alias software. [Online]. Available: <ftp://ftp-sop.inria.fr/coprin/ALIAS>
- [17] J. M. Porta, "CuikSLAM: A kinematic-based approach to SLAM," in *Proc. IEEE Int. Conf. Robotics Automation*, 2005, pp. 2425–2431.
- [18] J. M. Porta and L. Jaillet, "Exploring the energy landscapes of flexible molecular loops using higher-dimensional continuation," *J. Comput. Chem.*, vol. 34, no. 3, pp. 234–244, 2013.
- [19] J. M. Porta, L. Jaillet, and O. Bohigas, "Randomized path planning on manifolds based on higher-dimensional continuation," *Int. J. Robot. Res.*, vol. 31, no. 2, pp. 201–215, 2012.
- [20] J. M. Porta, L. Ros, T. Creemers, and F. Thomas, "Box approximations of planar linkage configuration spaces," *ASME J. Mech. Des.*, vol. 127, no. 4, pp. 397–405, 2007.
- [21] J. M. Porta, L. Ros, and F. Thomas, "A linear relaxation technique for the position analysis of multiloop linkages," *IEEE Trans. Robot.*, vol. 25, no. 2, pp. 225–239, 2009.
- [22] J. M. Porta, L. Ros, F. Thomas, F. Corcho, J. Cantó, and J.-J. Pérez, "Complete maps of molecular-loop conformational spaces," *J. Comput. Chem.*, vol. 29, no. 1, pp. 144–155, 2008.
- [23] N. Rojas and F. Thomas, "Closed-form solution to the position analysis of Watt-Baranov trusses using the bilateration method," *ASME J. Mech. Robot.*, vol. 3, no. 3, p. 031001, 2011.
- [24] C. Rosales, J. M. Porta, and L. Ros, "Grasp optimization under specific contact constraints," *IEEE Trans. Robot.*, vol. 29, no. 3, pp. 746–757, 2013.
- [25] C. Rosales, L. Ros, J. M. Porta, and R. Suárez, "Synthesizing grasp configurations with specified contact regions," *Int. J. Robot. Res.*, vol. 30, no. 4, pp. 431–443, 2011.
- [26] M. Saha. (2014, Feb.). The motion planning kit. [Online]. Available: <http://ai.stanford.edu/~mitul/mpk>
- [27] N. Vahrenkamp. (2014, Feb.). Simox. [Online]. Available: <http://simox.sourceforge.net>
- [28] J. Verschelde. (2014, Feb.). The PHC software. [Online]. Available: <http://homepages.math.uic.edu/~jan/PHCpack/phcpack.html>

Josep M. Porta, Institut de Robòtica i Informàtica Industrial, CSIC-UPC, Barcelona, Spain. E-mail: porta@iri.upc.edu.

Lluís Ros, Institut de Robòtica i Informàtica Industrial, CSIC-UPC, Barcelona, Spain. E-mail: lros@iri.upc.edu.

Oriol Bohigas, Institut de Robòtica i Informàtica Industrial, CSIC-UPC, Barcelona, Spain. E-mail: obohigas@iri.upc.edu.

Montserrat Manubens, Institut de Robòtica i Informàtica Industrial, CSIC-UPC, Barcelona, Spain. E-mail: mmanuben@iri.upc.edu.

Carlos Rosales, Institut de Robòtica i Informàtica Industrial, CSIC-UPC, Barcelona, Spain. E-mail: crosales@iri.upc.edu.

Léonard Jaillet, NANO-D, INRIA Rhône-Alpes, Grenoble, France. E-mail: leonard.jaillet@inria.fr.

Vary Slow Motion



IMAGE LICENSED BY INGRAM PUBLISHING

Effect of Task Forces on Movement Variability and Implications for a Novel Skill Augmentation Mechanism

By Ozkan Celik and Marcia K. O'Malley

This article presents the results of a human subject experiment aimed at answering the question, “can increased muscle force variability in low force levels explain increased variability or intermittency of slow movements?” To address this research question, we conducted an experiment with eight subjects, which involved the completion of slow elbow flexion movements at two target speed levels and under five resistive torque fields implemented via an elbow exoskeleton. The results of this experiment demonstrated that increasing levels of resistive torques decreased movement speed variability only until a certain torque level. This observation indicates that a motor-unit pool-based muscle force generation variability, which is known to increase at low force levels, can indeed underlie increased variability in slow movements. Our results imply that resistive torques may be used to significantly decrease movement speed variability, opening up new possibilities for novel assistive devices for motor skill augmentation.

Digital Object Identifier 10.1109/MRA.2013.2275696
Date of publication: 6 August 2014

Variability in Slow Movements

In their seminal research, Flash and Hogan [1] proposed the minimum jerk theory (MJT) to explain planning in unconstrained reaching movements. With the MJT, the central nervous system (CNS) chooses the trajectory that minimizes the squared jerk (time derivative of acceleration) among many infinite possible trajectories, leading to an optimally smooth trajectory. The minimum jerk velocity profile is smooth, symmetric, and bell shaped and accurately predicts the velocity profiles observed in unconstrained reaching experiments [1]. A summary of the observations, implications, and assumptions of MJT, as well as those of two other computational motor control theories discussed subsequently in this section, is provided in Table 1.

Flash and Hogan anticipated that MJT would not hold for movements that reached the limits of the neuromuscular system, such as very fast movements. A lower limit for the speed below which the observation of unimodal smooth velocity profiles would break, however, was not initially anticipated. Doeringer and Hogan [2] showed that movements lose their smoothness and become increasingly intermittent with decreasing movement speed as demonstrated by distinct peaks in the velocity profile. Although many studies interpreted the intermittency to be caused by corrective actions [3], [4], which is correct under certain circumstances, Doeringer and Hogan showed that the submovements persisted under no visual feedback, indicating that not all submovements can be attributed to corrective actions. They concluded that increased movement intermittency in slow movements is a very robust characteristic of the human motor control system: people cannot avoid moving intermittently during slow movements [5]. It is also important to note that similar highly intermittent behavior

is observed in the movements of stroke patients, and smoothness of movement is used as a reliable and objective measure of motor function recovery [6]–[9].

Doeringer and Hogan [2] proposed two potential sources of movement intermittency: neuromuscular noise and submovements-based central planning. However, they did not arrive at a final conclusion about the source of intermittency, and a satisfactory explanation for the origins of intermittency has remained elusive.

An alternative theory of movement planning and control, the minimum variance theory (MVT) proposed by Harris and Wolpert [10], has been remarkably successful in predicting the well-known and experimentally well-documented Fitts' law [11], bell-shaped velocity profiles of arm reaching movements, saccadic eye movements, and even the two-thirds power law [12]. MVT proposes that principles for minimizing the effects of the noise present in biological processes and mechanisms underlie movement planning rather than cost functions (such as jerk), which are difficult to be sensed or integrated by CNS. MVT relies on the assumption of a linear relationship between the standard deviation (SD) of the control signals and their mean levels, an assumption known as *signal-dependent noise (SDN)*. According to this assumption, during the planning of a rapid goal-directed movement, moving as fast as possible should be avoided, otherwise the end-point error will be very large due to the large control signals involved in the movement. Therefore, it places a tradeoff between movement duration and end-point variability.

Todorov and Jordan [13] proposed the optimal feedback control model (OFCM) to overcome the shortcomings of MVT. Specifically, Todorov [14] pointed out that despite the success of MVT in providing a unified explanation for numerous seemingly unrelated experimental observations in motor control, it is limited to open-loop control scenarios

Table 1. Computational motor control theories for reaching movements.

Theory	Implications and Observations	Underlying Assumptions
MJT proposed by Flash and Hogan [1]	The smooth, symmetric, and bell-shaped minimum jerk velocity profile accurately predicts the velocity profiles observed in unconstrained reaching experiments.	For reaching movements, the central nervous system chooses the trajectory that minimizes the squared endpoint jerk among infinitely many possible trajectories.
MVT proposed by Harris and Wolpert [10]	Principles for minimizing the effects of the noise present in biological mechanisms underlie movement planning rather than cost functions (such as jerk), which are difficult to be sensed by the CNS. MVT successfully predicts Fitts' law, bell-shaped velocity profiles of arm reaching movements, saccadic eye movements, and even the two-thirds power law.	MVT relies on the assumption of a linear relationship between the SD of the control signals and their mean levels, an assumption known as <i>SDN</i> .
OFCM proposed by Todorov and Jordan [13]	MVT is limited to open-loop control scenarios and, hence, only rapid goal-directed movements with no disturbances. Tasks in daily life are slow enough to allow feedback and involve various disturbances. OFCM takes into account noise in both control and sensing and provides a variable structure feedback controller that changes its parameters during the movement based on disturbances or feedback.	The noise in motor commands is still assumed to comply with <i>SDN</i> .

and, hence, rapid goal-directed movements with no disturbances. However, tasks in daily life are often slow to allow enough time for feedback to be incorporated and involve various disturbances. OFCM considers noise in both control and sensing (or state estimation) and provides a variable structure feedback controller that is allowed to change its parameters during the movement, based on disturbances or feedback. The noise in motor commands is still assumed to comply with SDN. Unlike MJT and MVT, where motor planning and execution are considered to be two separate processes, in the OFCM, they take place simultaneously [15].

It is important to highlight that both MVT and OFCM rely on one essential assumption: SDN. With the SDN assumption, movements involving smaller control signals will always result in less variability. In fact, Jordan and Wolpert state that “longer movements can always be made smoother than short movements,” [16] which is in contradiction with Doeringer and Hogan’s experimental results. Therefore, MVT and OFCM fall short of providing an explanation for intermittency in slow movements and are concerned with only rapid movements.

Although speed-accuracy tradeoff [11] and planning and execution of rapid goal-directed movements have garnered significant research interest [1], [10], [13], [17], [18], far fewer studies have reported results on the lower end of the movement speed spectrum. Not only do very interesting observations exist for slow movements but an explanation of these observations is highly relevant to motor function recovery and motor skill learning, where movements are typically slow at the initiation of therapy or learning and movement speed increases through practice, exercise, or therapy. Understanding the mechanisms behind movement intermittency in slow movements can help: 1) establish objective, accurate, and biologically plausible measures of motor function recovery for stroke and spinal cord injury rehabilitation and 2) develop novel motor skill augmentation methods or devices that can reduce movement variability in critical or high-precision tasks that normally require a significant amount of motor skill training.

Newell et al. [19] provided experimental evidence that movements slower than 15 cm/s became less accurate and more variable in terms of movement timing. They provided insight into the origins of this increased variability by showing that even movements with a duration as short as 100 ms demonstrated increased variability and, therefore, cannot be attributed solely to a feedback mechanism. Rather, they pointed out that the source of this variability should be sought in actuation. Although the main variability measure in this study was time and not speed, the results in [19] are considered to be relevant to and indicative of the same type of variability observed in movement speed.

In this article, we propose to explore the origins of the intermittency problem from a movement variability point of view. We define movement intermittency as within-trial variability rather than trial-to-trial variability, which is a common type of variability measure used for rapid goal-directed

movements [10]. This point of view provides a framework to study movement intermittency as a special case of movement variability observed in slow movements.

In our earlier work [20], we showed that intermittency of various joints along the arm during a multijoint tracking task increased in the distal direction along the arm. Considering that muscle size decreases in the distal direction along the arm, this result is in agreement with the results of Hamilton et al. [21], which showed that larger muscles are capable of producing force with less variability than small muscles. Hamilton et al. complemented their results with a motor unit pool-based isometric neuromuscular model and suggested that a similar mechanism due to the number of active motor units may be responsible for the significant increase in muscle force variability at low force levels. More precisely, this range of low force levels corresponds to 20–30% of the maximum voluntary contraction force [22]. We propose that this range may as well be the range of forces involved in slow movements.

This article reports the results of a human subject experiment that aimed to evaluate whether increased muscle force variability in low force levels can explain increased variability or intermittency in slow movements.

Methods

Participants

A total of eight subjects (four male and four female) participated in the experiment. The mean age was 25.5 years (SD 3.1), ranging from 21 to 29. One subject was left-handed. All subjects had normal or corrected-to-normal vision, none had any movement disorders affecting their upper extremities, and all provided their informed consent for the experimental protocol approved by the Rice University Institutional Review Board.

Experimental Setup

Subjects were seated at a 17-in liquid crystal display computer screen, and their right arms were attached to an elbow exoskeleton device via foam padding and pressure cuffs, which provided a comfortable and tight fit, as shown in Figure 1. The exoskeleton allowed elbow flexion and extension movements in the horizontal plane and was capable of applying controlled torques on the elbow. The device used a Platinum ServoDisc U9D-E pancake motor from Kollmorgen Motion Technologies with a E3-2048-500-H optical encoder from US Digital with 2048×4 counts/rev resolution in quadrature mode. The output torque and position sensing resolution were further improved via a 1:11.25 ratio cable drive mechanism, leading to a maximum torque capability of 5.48 Nm and 0.0039° position reading resolution at the elbow joint. The inherent friction of the device was predominantly of cumbic nature and was canceled via a motion-based friction cancellation algorithm [23]. It was verified that the movements of the exoskeleton were essentially frictionless after friction cancellation. A platform allowed the height of the exoskeleton to be properly adjusted for each subject so as to have the right arm

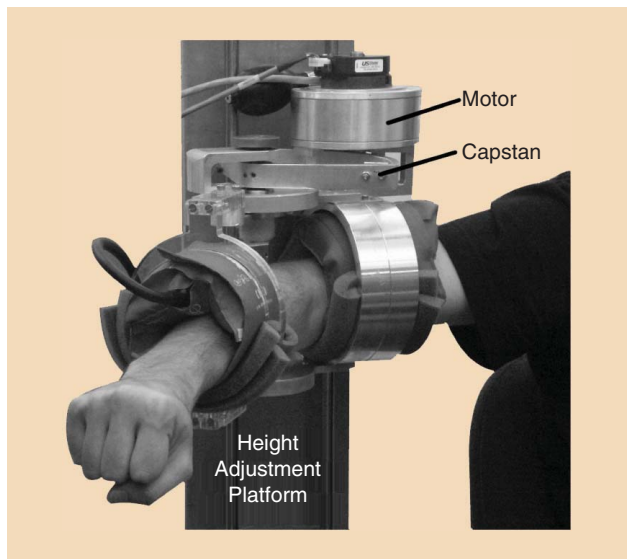


Figure 1. The elbow exoskeleton. The subject's right arm was attached to the device via foam padding and pressure cuffs to provide a comfortable and tight fit. The height of the device was adjusted for each subject so as to have his or her arm moving in the horizontal plane at shoulder level throughout the experiments.

moving in the horizontal plane at shoulder level throughout the experiments. An emergency stop button placed within easy reach of the subject's left hand and hard stops at the fully extended and at approximately 100° flexed positions of the elbow constituted the safety precautions. Also the maximum elbow torque that the device could apply was limited to 3 Nm in the software. MATLAB and SIMULINK by Mathworks Inc. and QUARC by Quanser Inc. were used for the real-time control software and experiment interface. The feedback control loop ran at 1 kHz, and the data capture rate was 100 Hz.

Experimental Protocol

The subjects were asked to always look at the screen and not at their arms and to make a fist with their right hands and keep it in this consistent posture throughout the experiment. On the screen, the subjects could see a time plot of their elbow movement speed (°/s) and three numerical indicators. The plot was not updated in real time but rather generated after every 4-s-long trial, displaying the speed profile of the last trial. This configuration ensured that visual feedback during the trials did not lead to corrective actions. At the end of each trial, the first indicator displayed the mean speed of subjects' movement during the trial. Two additional numerical indicators displayed the current trial number and time in seconds (a chronometer with ms precision) during the trial, as depicted in Figure 2.

The task assigned to the subjects was to complete constant speed elbow flexion movements against free or constant resistive torque fields generated by the exoskeleton so as to match a target constant speed profile. There were two target speed levels (5 and 10°/s) and five resistive torque levels (0–2 Nm, with 0.5-Nm increments). All subjects completed all ten speed and torque level combinations, following

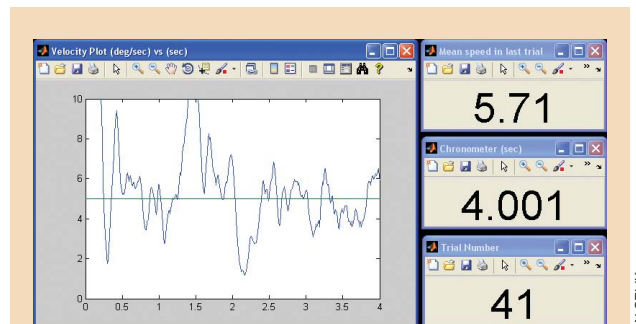


Figure 2. The computer interface for the experiment. At the end of every 4-s-long trial, the speed profile of the subject during the last trial was displayed together with the target speed level. The first indicator displayed the mean speed of the subject's movement for the last trial. Two additional numerical indicators displayed the current trial number and time in seconds (a chronometer with ms precision) during the trial.

OZKAN CELIK

a full factorial design. One experiment session took around 45 min, and all subjects completed the experiment in two sessions with different target speed levels on two consecutive days. The presentation order of speed and an increasing or a decreasing order for resistive torque levels within a speed level were counterbalanced and randomized among subjects. For example, 5°/s target speed on the first session (or day) with an increasing order for torque levels and 10°/s target speed on the second session (or day) with a decreasing order for torque levels constituted one specific presentation order. A total of eight possible combinations for the presentation order of speed and torque levels were randomly assigned to the eight subjects.

Each session consisted of five blocks, with each block involving a specific resistive torque level. In each block, subjects completed 40 trials in around 6 min, and subjects were required to have a 2-min rest between blocks to avoid fatigue. Each trial started with the subject's initiation of movement from a fully extended elbow position (the chronometer started counting to indicate the start of the trial, as subjects passed through 1° of flexion). No feedback was available to the subjects during their movement, except proprioception. After the 4-s trial ended, the subjects observed their speed profile time plot in the trial, superimposed with the target speed level as a horizontal line on the computer screen (see Figure 2). The ordinate of the plot was adjusted so that the target speed level always appeared vertically centered. When subjects moved back to the initial fully extended posture, the trial number counter was incremented indicating that they can initiate the next trial when they felt ready.

The experimental task did not involve precision tracking [24] or compensating for unstable dynamic interactions [25], the most common scenarios where cocontraction would be expected, allowing us to neglect existence and confounding effects of cocontraction. When the subjects arrived for their first session, they were given written instructions about the experiment. The instructions explained the experimental setup, protocol, and interface. The primary goal was defined

as always making a constant speed flexion movement to match the target constant speed level as closely as possible. The subjects were instructed to always check the mean speed indicator after every trial and adjust their speed in the following trials accordingly. As a secondary goal, they were also instructed to observe the speed profile plots to not only match the mean speed but also to keep their speed constant throughout the trial and avoid increasing or decreasing trends in this plot. The instructions asked them to avoid slowing down or stopping toward the end of the trial but rather to keep a constant speed until the trial ended. After the subjects read the written instructions, example speed profile plots depicting successful and unsuccessful trials (in terms of satisfying target speed levels) were shown to them and explained by the experimenter.

At the beginning of each session, the subjects were allowed to practice as many trials as they wanted until they were convinced that they were able to successfully and consistently complete the constant speed movement task. Only the last 20 trials out of 40 for each block was included in data analysis. Also, the last 3 s of each 4-s trial was used in the analyses to avoid the sudden jerks that occasionally occurred at movement initiation and during movements near the joint limits. Note that the experiment's focus was on the sustained constant speed movements rather than the initiation of the movements.

Analysis of Movement Speed Variability

In the literature, various measures are used to quantify movement intermittency or variability. Usually, a number of significant peaks in the speed profile quantifies movement intermittency [6], [7], [20]. Movement variability measures, on the other hand, are most commonly defined as end-point error or variability [8], [10], quantifying only trial-to-trial variability [14]. In contrast, within-trial variability measures are commonly used for force variability, such as SD of force, and most importantly a normalized version of SD, coefficient of variation (CV) of force. CV facilitates comparing the results of different studies [22] and is defined as SD of force normalized by the mean level of force.

Although trial-to-trial variability measures are well suited to discrete movement tasks, such as reaching, a within-trial variability measure is much better suited to continuous movement tasks, such as maintaining a constant speed during movement. Hence, we use the CV of speed (CV_{speed}) as the measure of movement variability in this article. For each trial in the experimental protocol described in the previous section, CV_{speed} during the last 3 s of the trial quantified the speed variability. The speed was obtained from encoder readings via Euler's forward difference method and was bidirectionally filtered offline (for zero-phase shift) with a second-order low-pass Butterworth filter with 20-Hz cutoff frequency.

Statistical Analysis

We used a repeated measures analysis of variance (ANOVA) with no between-subjects factors and with subject, trial, speed, and torque within-subjects factors. CV_{speed} constituted

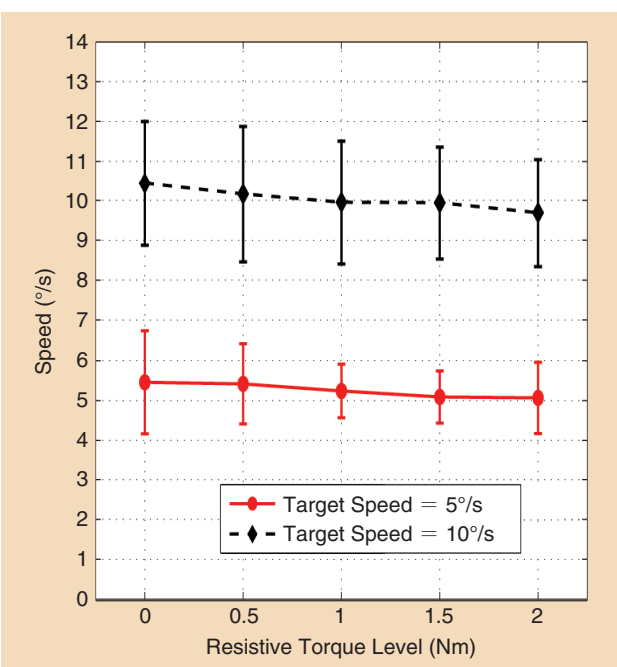


Figure 3. The subjects were successful in matching the target speed level on average. The error bars denote the SD of speed.

the dependent measure. The trial had 20 levels, speed had two levels (5 and 10 °/s), and torque level had five levels (0–2 Nm with 0.5-Nm increments). The subject (eight levels) is treated as a random factor. Out of 1,600 total observations, three data points were not included in the statistical analysis. In these three trials, the subject mistakenly thought that the trial did not initiate properly and quit moving at before the midpoint of the trial. We used the Kenward-Rogers adjusted degrees of freedom method to account for Type I error risk. The alpha level was set at 0.05 for all significance tests. Since the trial did not lead to any significant results when included as a factor main or interaction effects, we report only the main and interaction effects of speed and torque on CV_{speed} . Tukey-Kramer's post hoc analysis test was used for pairwise comparisons of the main and interaction effects of torque. We used Statistical Analysis System (SAS) software by SAS Institute Inc. for conducting the statistical analyses. We used a MIXED procedure (PROC MIXED) design (due to both random and fixed effects), with the trial treated as a repeated measure and with a compound symmetry structure for the covariance matrix. This design allows for the incorporation of all available observations, excluding only missing individual observations, without having to drop a group or condition of data points [26], [27], and therefore provides higher statistical power for data sets with missing data points.

Results

Figure 3 shows the mean speed values achieved by the subjects in the experiment with error bars depicting the SD of speed. The subjects were able to perform the constant speed flexion task reasonably well but with high variability, which is an expected observation for slow movements. Increasing resistive

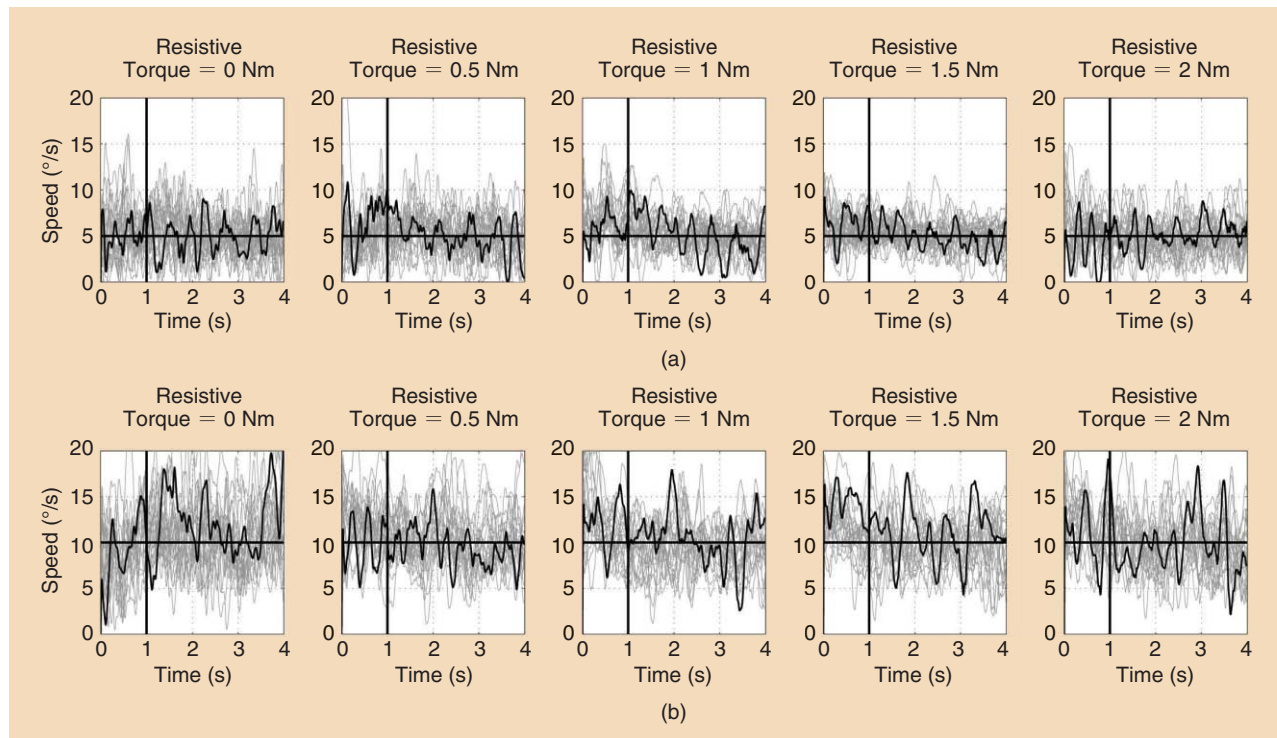


Figure 4. The representative speed profiles achieved by subject 5 under all torque and speed condition combinations. The last 20 of 40 trials are plotted in gray, with the final trial in black. The horizontal lines correspond to the target speed levels, and the vertical lines mark the range (1–4 s) for which the measure CV_{speed} was calculated. (a) Target speed = 5°/s. (b) Target speed = 10°/s.

torque levels led to a weak and insignificant decreasing speed trend. It can be observed that variability generally decreases as the resistive torque level increases. The variability is lower for the target speed level of 5°/s, but this is simply due to the effect of scaling. A fair comparison of the variability of speed for different levels of mean speed necessitates the use of the CV_{speed} measure that normalizes the SD of speed by mean speed.

Figure 4 shows the raw speed profile data from a representative subject (Subject 5)

Our experimental results indicate potential novel methods of human skill augmentation in delicate or critical tasks such as surgery.

The results of the ANOVA indicate a significant main effect of speed [$F(1,1390) = 465.4, p < 0.05$] and a significant main effect of torque [$F(4,1390) = 42.53, p < 0.05$] on CV_{speed} . The interaction effect of torque by speed is also significant [$F(4,1390) = 5.57, p < 0.05$]. The results of the post hoc Tukey-Kramer test for pairwise comparison of torque are

summarized in the bar plot in Figure 5. The error bars indicate standard errors. This plot indicates that CV_{speed} is significantly higher for the no resistive torque condition in comparison with all other torque levels ($p < 0.05$). Although there is initially a decreasing trend for CV_{speed} with increasing resistive torque levels, after 1.5 Nm the trend reverses direction and CV_{speed} starts to increase. CV_{speed} for $T_r = 2$ Nm is significantly higher than it is for $T_r = 1.5$ Nm.

Figure 6 summarizes the results of pairwise comparison tests for interaction effects of resistive torque level by speed on speed variability in an interaction plot format. Although the CV_{speed} versus torque level curves under two different target speed level conditions mostly follow a parallel trend, the overall interaction effect is significant because of the nonparallel sub-trends, such as those observed between $T_r = 1$ Nm and $T_r = 1.5$ Nm.

Discussion

The significant main effect of speed on movement speed variability is in agreement with findings using movement intermittency [2], [20] or timing [19] as the measure of variability in the literature. This possibly indicates a single mechanism of variability behind all, as we have proposed in the “Variability in Slow Movements” section.

The nonmonotonic relationship between speed variability and resistive torques observed in Figures 5 and 6 is a novel finding. These experimental results indicate that increased muscle force variability in low force levels can indeed explain increased variability or intermittency in slow movements.

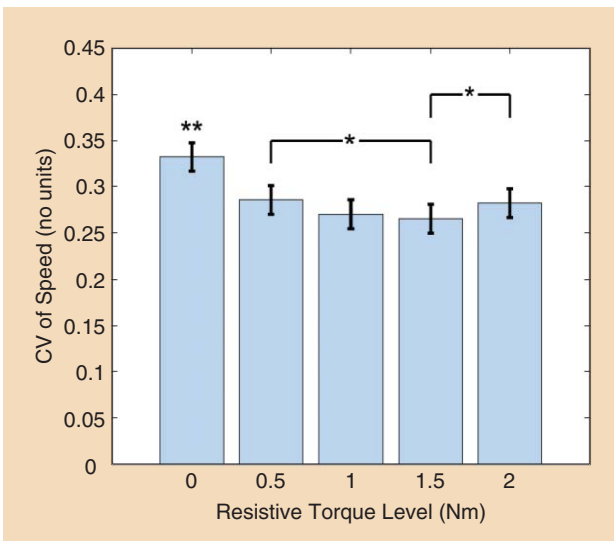


Figure 5. The main effect of resistive torque level on speed variability is significant. The mean and standard error values are displayed. A pairwise comparison of effect of torque levels indicates that, when speed level is not taken into consideration, CV_{speed} is significantly higher for the no resistive torque condition in comparison with all other torque levels (denoted by **, $p < 0.05$). Additional pairwise significant differences are denoted by * ($p < 0.05$). Although initially there is a decreasing trend for CV_{speed} with increasing resistive torque levels, after 1.5 Nm, the trend reverses direction and CV_{speed} starts to increase. In fact, CV_{speed} for $T_r = 2$ Nm is significantly higher than it is for $T_r = 1.5$ Nm. See the “Discussion” section for details about these results.

Increasing resistive torque levels increase the force requirement of the task and, hence, may push the muscle forces out of the low force range with increased force variability [21], [22]. However, the speed variability increases after a certain torque level. This might be due to entering the region where SDN takes hold, with force SD linearly increasing with mean force.

From a dynamics point of view, one can question whether the effect of increasing resistive torques is equivalent to applying increased dry friction and whether decreased variability can be attributed to increased friction. Although resistive torques and dry friction are indeed functionally equivalent, the nonmonotonic nature of the relationship helps dismiss this alternative explanation for decreased variability.

Our experimental results indicate potential novel methods of human skill augmentation in delicate or critical tasks such as surgery. Existing technologies such as surgical robots [28] allow for the filtering of tremors in a surgeon’s movement within a master-slave teleoperation framework. However, the unilateral nature of the existing teleoperation structures for surgical robots causes a deterioration in dexterity due to the loss of haptic feedback [28]. Skill augmentation algorithms based on resistive torques or forces that will be implemented on the master side can enhance surgeons’ ability to generate less variable forces and provide better control over slow and critical tasks. Such an algorithm can be implemented with much lower cost and fewer potential safety hazards compared with bidirectional teleoperation algorithms, although it would not improve the dexterity of the surgeon as much. However, it

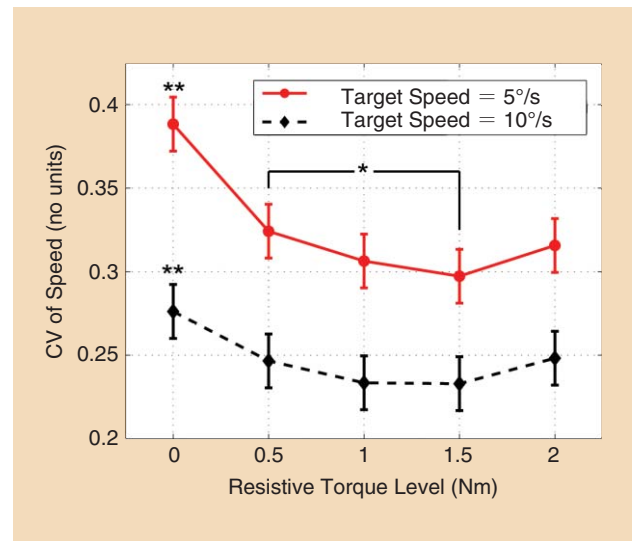


Figure 6. The interaction effect of resistive torque level by speed level on speed variability is significant. The mean and standard error values are displayed. A pairwise comparison of the effect of torque levels indicates that, when different speed level results are grouped and analyzed separately, CV_{speed} is significantly higher for the no resistive torque condition in comparison with all other torque levels (denoted by **, $p < 0.05$) in the same speed level. The only other significant difference is between $T_r = 0.5$ Nm and $T_r = 1.5$ Nm (denoted by *, $p < 0.05$). See the “Discussion” section for details about these results.

can potentially provide a midpoint solution. In fact, recent research has focused on increasing surgeon dexterity in robotic surgery via safe midpoint solutions without resorting to bidirectional teleoperation algorithms [29].

Similarly, resistive torques may be used in facilitating or accelerating the learning of a new motor skill. Studies in this area concluded that, although task performance can be enhanced during training with various assistance methods, it does not translate to faster or better learning in general [30], [32]. Based on our results, although it may seem counterintuitive, it might be possible to design resistive forces that would make the task easier for a trainee and potentially lead to faster and more complete learning in comparison with virtual practice without any augmented forces. In fact, research in rehabilitation of motor-impaired patients provided evidence for such counterintuitive methods to improve rehabilitation outcomes [33]. Our results here might provide one potential explanation for the mechanisms behind these counterintuitive results.

We show that resistive forces can reduce kinematic variability possibly via moving the task forces into a more

**Tasks in daily life are often
slow to allow enough
time for feedback to be
incorporated and involve
various disturbances.**

favorable region in terms of variability. However, the amount of resistive forces must be adjusted carefully or it might increase rather than decrease variability.

Conclusion

Our results imply that resistive torques may be used to significantly decrease movement speed variability. The relationship between resistive torque levels and speed variability, however, is not monotonic. These results support our hypothesis that the force requirements of the movement are responsible for the observed movement variability in the slow movement range through muscle force generation variability. Our findings also point to the potential for using this mechanism to augment motor skills in slow but delicate tasks that require consistency and precision via controlled delivery of resistive forces and torques by use of assistive exoskeleton or force-feedback devices.

Acknowledgment

This project was supported in part by National Science Foundation Grant IIS-0812569.

References

- [1] T. Flash and N. Hogan, "The coordination of arm movements: An experimentally confirmed mathematical model," *J. Neurosci.*, vol. 5, no. 7, pp. 1688–1703, 1985.
- [2] J. A. Doeringer and N. Hogan, "Intermittency in preplanned elbow movements persists in the absence of visual feedback," *J. Neurophysiol.*, vol. 80, no. 4, pp. 1787–1799, 1998.
- [3] S. Pasalar, A. V. Roitman, and T. J. Ebner, "Effects of speeds and force fields on submovements during circular manual tracking in humans," *Exp. Brain Res.*, vol. 163, no. 2, pp. 214–225, 2005.
- [4] T. Milner and M. Ijaz, "The effect of accuracy constraints on three-dimensional movement kinematics," *Neuroscience*, vol. 35, no. 2, pp. 365–374, 1990.
- [5] J. A. Doeringer, "An investigation into the discrete nature of human arm movements," Ph.D. dissertation, Dept. Mech. Eng., Massachusetts Inst. Technol., Cambridge, MA, 1999.
- [6] L. E. Kahn, M. L. Zygmanski, W. Z. Rymer, and D. J. Reinkensmeyer, "Effect of robot-assisted and unassisted exercise on functional reaching in chronic hemiparesis," in *Proc. IEEE Int. Conf. Engineering Medicine Biology Society*, 2001, vol. 2, pp. 1344–1347.
- [7] B. Rohrer, S. Fasoli, H. I. Krebs, R. Hughes, B. Volpe, W. R. Frontera, J. Stein, and N. Hogan, "Movement smoothness changes during stroke recovery," *J. Neurosci.*, vol. 22, no. 18, pp. 8297–8304, 2002.
- [8] J. J. Daly, N. Hogan, E. M. Perepezko, H. I. Krebs, J. M. Rogers, K. S. Goyal, M. E. Dohring, E. Fredrickson, J. Nethery, and R. L. Ruff, "Response to upper-limb robotics and functional neuromuscular stimulation following stroke," *J. Rehabil. Res. Develop.*, vol. 42, no. 6, pp. 723–736, 2005.
- [9] O. Celik, M. K. O'Malley, C. Boake, H. S. Levin, N. Yozbatiran, and T. A. Reistetter, "Normalized movement quality measures for therapeutic robots strongly correlate with clinical motor impairment measures," *IEEE Trans. Neural Syst. Rehabil. Eng.*, vol. 18, no. 4, pp. 433–444, 2010.
- [10] C. M. Harris and D. M. Wolpert, "Signal-dependent noise determines motor planning," *Nature*, vol. 394, no. 6695, pp. 780–784, 1998.
- [11] P. M. Fitts and J. R. Peterson, "Information capacity of discrete motor responses," *J. Exp. Psychol.*, vol. 67, no. 2, pp. 103–112, 1964.
- [12] F. Lacquaniti, C. Terzuolo, and P. Viviani, "The law relating the kinematic and figural aspects of drawing movements," *Acta Psychol.*, vol. 54, nos. 1–3, pp. 115–130, 1983.
- [13] E. Todorov and M. I. Jordan, "Optimal feedback control as a theory of motor coordination," *Nature Neurosci.*, vol. 5, no. 11, pp. 1226–1235, 2002.
- [14] E. Todorov, "Optimality principles in sensorimotor control," *Nature Neurosci.*, vol. 7, no. 9, pp. 907–915, 2004.
- [15] F. Campos and J. M. F. Calado, "Approaches to human arm movement control—A review," *Annu. Rev. Control*, vol. 33, no. 1, pp. 69–77, 2009.
- [16] M. I. Jordan and D. M. Wolpert, "Computational motor control," in *Cognitive Neurosciences*, M. S. Gazzaniga, Ed. Cambridge, MA: MIT Press, 1999, pp. 601–620.
- [17] Y. Uno, M. Kawato, and R. Suzuki, "Formation and control of optimal trajectory in human multijoint arm movement," *Biol. Cybern.*, vol. 61, no. 2, pp. 89–101, 1989.
- [18] K. E. Novak, L. E. Miller, and J. C. Houk, "Kinematic properties of rapid hand movements in a knob turning task," *Exp. Brain Res.*, vol. 132, no. 4, pp. 419–433, 2000.
- [19] K. M. Newell, L. E. Hoshizaki, and M. J. Carlton, "Movement time and velocity as determinants of movement timing accuracy," *J. Motor Behav.*, vol. 11, no. 1, pp. 49–58, 1979.
- [20] O. Celik, Q. Gu, Z. Deng, and M. K. O'Malley, "Intermittency of slow arm movements increases in distal direction," in *Proc. IEEE/RSJ Int. Conf. Intelligent Robots Systems*, St Louis, MO, 2009, pp. 4499–4504.
- [21] A. F. C. Hamilton, K. E. Jones, and D. M. Wolpert, "The scaling of motor noise with muscle strength and motor unit number in humans," *Exp. Brain Res.*, vol. 157, no. 4, pp. 417–430, 2004.
- [22] K. E. Jones, A. F. C. Hamilton, and D. M. Wolpert, "Sources of signal-dependent noise during isometric force production," *J. Neurophysiol.*, vol. 88, no. 3, pp. 1533–1544, 2002.
- [23] N. L. Bernstein, D. A. Lawrence, and L. Y. Pao, "Friction modeling and compensation for haptic interfaces," in *Proc. First Joint Eurohaptics Conf. Symp. Haptic Interfaces Virtual Environment Teleoperator Systems*, IEEE Computer Society, 2005, pp. 290–295.
- [24] L. P. J. Selen, J. H. van Dieën, and P. J. Beek, "Impedance modulation and feedback corrections in tracking targets of variable size and frequency," *J. Neurophysiol.*, vol. 96, no. 5, pp. 2750–2759, 2006.
- [25] L. P. J. Selen, D. W. Franklin, and D. M. Wolpert, "Impedance control reduces instability that arises from motor noise," *J. Neurosci.*, vol. 29, no. 40, pp. 12606–12616, 2009.
- [26] E. B. Moser, "Repeated measures modeling with PROC MIXED," in *Proc. 29th SAS Users Group Int. Conf.*, 2004, pp. 1–19.
- [27] W. G. Hopkins. (2000). A new view of statistics [Online]. Available: <http://www.sportsci.org/resource/stats/>
- [28] A. M. Okamura, "Methods for haptic feedback in teleoperated robot-assisted surgery," *Ind. Robot: Int. J.*, vol. 31, no. 6, pp. 499–508, 2004.
- [29] K. J. Kuchenbecker, J. Gewirtz, W. McMahan, D. Standish, P. Martin, J. Bohren, P. J. Mendoza, and D. I. Lee, "VerroTouch: High-frequency acceleration feedback for telerobotic surgery," in *Proc. Int. Conf. Haptics: Generating Perceiving Tangible Sensations*, 2010, pp. 189–196.
- [30] Y. Li, V. Patoglu, and M. K. O'Malley, "Negative efficacy of fixed gain error reducing shared control for training in virtual environments," *ACM Trans. Appl. Perception*, vol. 6, no. 1, pp. 1–21, 2009.
- [31] Y. Li, J. C. Huegel, V. Patoglu, and M. K. O'Malley, "Progressive shared control for training in virtual environments," in *Proc. IEEE World Haptics Conf.*, 2009, pp. 332–337.
- [32] J. C. Huegel and M. K. O'Malley, "Progressive haptic and visual guidance for training in a virtual dynamic task," in *Proc. IEEE Haptics Symp.*, 2010, pp. 343–350.
- [33] J. L. Patton, M. E. Stoykov, M. Kovac, and F. A. Mussa-Ivaldi, "Evaluation of robotic training forces that either enhance or reduce error in chronic hemiparetic stroke survivors," *Exp. Brain Res.*, vol. 168, no. 3, pp. 368–383, 2006.

Ozkan Celik, Department of Mechanical Engineering, Colorado School of Mines, Golden, CO 80401. E-mail: ocelik@mines.edu.

Marcia K. O'Malley, Department of Mechanical Engineering, Rice University, Houston, TX 77005. E-mail: omalley@rice.edu.

Patient-Tailored Assistance

A New Concept of Assistive Robotic Device That Adapts to Individual Users

By Ricardo Morales, Francisco J. Badesa, Nicolas Garcia-Aracil, Carlos Perez-Vidal, Jose M. Sabater, Eugenia Papaleo, Antonino Salerno, Loredana Zollo, and Eugenio Guglielmelli



IMAGE LICENSED BY INGRAM PUBLISHING

This article presents the development of a new concept for an assistive robotic device that can help people as needed, considering their residual physical and cognitive abilities, and, at the same time, increase their cognitive and physical abilities in activities of daily living (ADLs), such as drinking, cooking, eating, personal hygiene, and grooming.

According to the United Nations, life expectancy will continue to rise all over the world. In the more developed regions, the population aged 60 or older is increasing at the fastest pace ever (growing at 2.4% annually) and is expected to increase by more than 50% over the next four decades, rising from 274 million in 2011 to 418 million in 2050 [1].

Among age-related pathologies, cerebral vascular accidents, also known as strokes, are the leading cause of permanent disability in the industrialized nations. More than 536,000 Europeans and 780,000 North Americans have a

stroke each year; more than 50% survive, but they are often severely impaired [2]. People who have had a stroke can be classified, according to their stage, as acute, subacute, or chronic patients. Although most of the recovery process after a stroke takes place in the first three months, recovery might continue over a longer period of time in patients who have not reached their full potential recovery.

During the last few decades, a great variety of assistive robotic devices have been developed using different approaches: from robots with a fixed base, attached or not to a wheelchair (e.g., the iARM manufactured by Exact Dynamics and previously known as MANUS [3]), to mobile autonomous systems (e.g., three generations of Care-O-bot from Fraunhofer IPA [4]). In this article, a new concept of assistive robotic device is presented; it is a seven-degrees-of-freedom (7-DOF) assistive robot arm that, provided with a multimodal human–robot interface (HRI), is able to 1) measure the user's physiological and biomechanical state, 2) adapt the robot's behavior accordingly, 3) enable the execution of assisted three-dimensional (3-D) ADL tasks, and 4)

Digital Object Identifier 10.1109/MRA.2014.2304051
Date of publication: 10 September 2014

enhance the level of user involvement by means of two communication channels (i.e., speech recognition and audio-visual feedback). In addition, the use of a lightweight modular robot designed for safe physical human–robot interaction is proposed to investigate the feasibility of its application to a real scenario of interaction with human subjects.

The assistive robotic device proposed in this article offers one important feature: it can be adapted to each user's individual characteristics, and it can be used for assistive tasks as well as for rehabilitation purposes. This is an example of the integration of robotic systems into medicine and health, as reported in [6]: physical human–robot interfaces, automated understanding of human behavior, automated understanding of emotional and physiological state, long-term adaptation to the user's changing needs, context-appropriate guidance, and safe robot behavior. Most of these capabilities can only be achieved by giving the user an active role in the task accomplishment and placing him or her in the control loop, as currently made also in the development of novel assistive and rehabilitation robotic systems [7]. In 2003, the major benefit of performance-based control based on kinetic and kinematic indicators was shown with respect to standard sensorimotor therapy with constant control gains [8].

The main components of this assistive robotic device, as shown in Figure 1, are: 1) a multimodal HRI, including speech recognition and audio-visual feedback, a physiological monitoring system, and a biomechanical monitoring system and 2) an anthropomorphic robot arm in tight physical contact with the user. The visual feedback as well as the level of robot assistance can be adapted to the user's global state by measuring his or her performance through

the physiological and biomechanical monitoring systems, thus enabling a user-tailored level of assistance.

Multimodal Human–Machine Interface

A human–machine interface can be called multimodal if it is able to fuse and interpret the information provided by different sensory and communication channels [9]. The first multimodal human–machine interface was proposed in 1980 within the field of human–computer interaction in Richard Bolt's "put that there" applications [10]. The multimodal human–machine interface proposed in this article integrates a twofold communication channel (speech recognition and audio-visual feedback) and different sensors for monitoring user state [physiological sensors, inertial measurement units (IMUs), and robot position and force sensors] (Figure 1), which allow the robot control to be adapted to the behavior and emotional state of the user.

Speech Recognition

Speech is the main means of communication among humans. It is fast and efficient; nevertheless, it is barely used in the interaction with machines. To implement an automatic speech recognition module, the IBM ViaVoice software development kit (SDK) and, in particular, the ActiveX controls embedded in the SDK were used. This approach was chosen since incorporating ActiveX controls into the system was fairly easy. ActiveX controls allow for the implementation of several functions, including recognizing dictations, recognizing commands given by the user, and recognizing the user from a list. In particular, to implement the voice command recognition, the ViaVoice Phrases Control ActiveX was used; this control is recommended to carry out command recognition in cases in

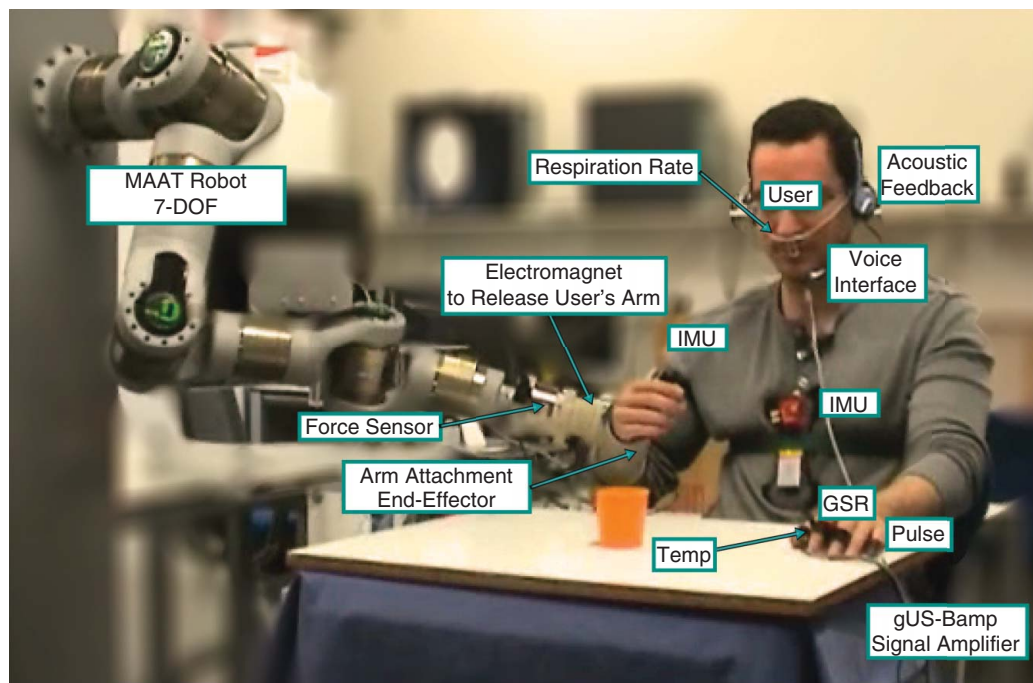


Figure 1. A multimodal assistive robotic platform: 7-DOF MAAT robot, force sensor, equipment for monitoring physiological signals (sensors and signal amplifier), voice interface, acoustic feedback, mechanical human–robot interface based on an electromagnetic system, and IMUs.

which the vocabulary may remain limited. The steps followed in the configuration of the ActiveX control were: 1) addition of the ViaVoice Phrases Control object, 2) definition of the variable, 3) definition of the events, and 4) definition of the event management. Then, two functions were implemented: 1) `SpeechRecognized()` for the identification of the spoken command and the execution of the program code related to it and 2) `textitSpeechRejected()`, which produces an error message that asks to the user to repeat the command when it is not recognized. In the developed application, 20 commands can be recognized.

Acoustic and Visual Feedback

To improve the interaction between the user and the system, a virtual voice was added to the system; the voice provides encouraging words and sounds, which motivate the user during the task execution and congratulates or consoles on task completion.

The ViaVoice SDK, used for the speech recognition module, also offers the possibility of generating a virtual voice through the virtual voices control object. The following steps describe how to add and configure this control: 1) add the virtual voices control object into the system, 2) define the variable, and 3) define the speech management. This last step was carried out through two functions: 1) the `SetSpeakText()` function, which saves in the created variable the words that the system has to utter and 2) the `Speak()` function, which is in charge of speaking the words stored in the variable.

The visual feedback was implemented to show the user the accuracy of his or her movement. In particular, the upper-limb kinematic reconstruction (see the “Upper-Limb Kinematic Reconstruction” section), performed by fusing the information

provided by two IMUs and robot position sensors, was implemented for showing, in a 3-D virtual environment, the user's upper extremity movement together with the correct position of the arm (Figure 2); both models were updated in real time.

Upper-Limb Kinematic Reconstruction

To reconstruct the upper-limb kinematics, a novel approach resorting to inverse kinematics algorithms to solve arm redundancy was used. It is grounded on a robust and reliable analytical procedure for inverse kinematics, which was conceived for redundant manipulators [11] and uses robot position sensors and two IMUs located on the subject's arm to determine the constraint concerning elbow trajectories and, thus, solves arm redundancy. In particular, the proposed upper-limb motion reconstruction algorithm allows for computation of the upper-limb joint angles starting from hand pose data (provided by the robot position sensors and an IMU placed on the subject's hand) and upper arm radial acceleration measurements (provided by an IMU sensor placed on the user's arm) (Figure 3).

The employed Razor 9-DOF IMU consists of 3-D accelerometers, 3-D magnetometers, and 3-D gyroscopes and uses an embedded microcontroller to real-time fuse sensory information and compute the device 3-D orientation. Razor data were wirelessly sent to the computer and processed in real time through the reconstruction algorithm implemented in MATLAB/Simulink (The Mathworks, Natick, Massachusetts), using a Bluetooth modem that worked as a serial transmit (TX) and receive (RX) pipe.

The upper-limb kinematic chain was studied according to the Denavit-Hartenberg (D-H) convention and the kinematic model proposed in [12]. The upper-limb kinematic chain is characterized by the following parameters [Figure 3(a)]:

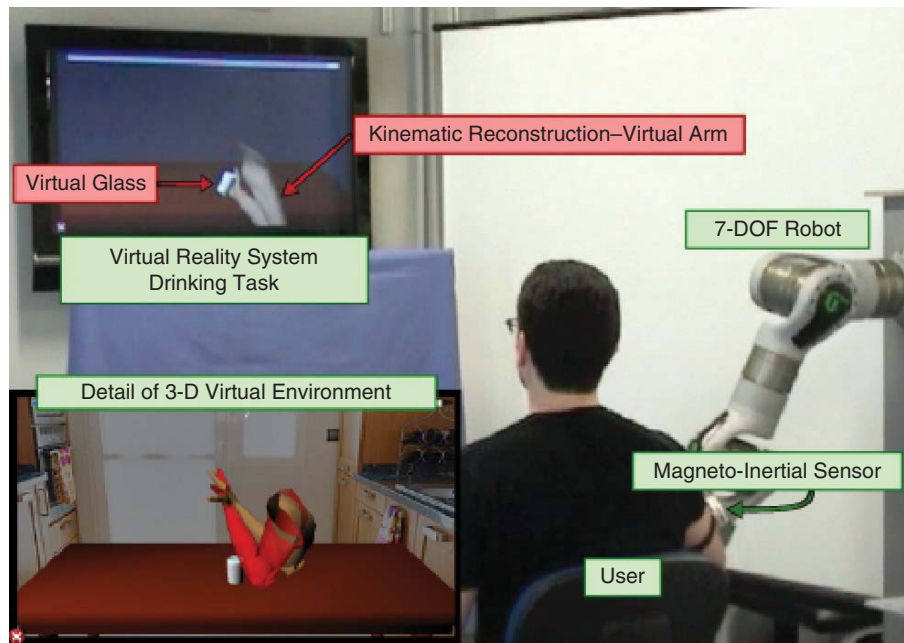


Figure 2. An experimental setup with a detail of the 3-D virtual environment. The correct position of the user's arm is colored red jointly with the current user position to show to the user the correctness of his/her movement.

upper-arm link (l_u), forearm link (l_f), a 3-DOF (q_1, q_2, q_3) shoulder joint, a 1-DOF (q_4) elbow joint, a 3-DOF (q_5, q_6, q_7) wrist joint (Figure 3). By assigning upper-limb frames, according to D-H convention, a homogeneous transformation matrix, $T_7^0(\bar{q})$, was obtained as a product of the matrices $T_3^0(q_1, q_2, q_3)$, $T_4^3(q_4)\text{Trans}(\bar{z}_4, l_f)$, and $T_7^4(q_5, q_6, q_7)$, related to the shoulder, elbow, and wrist, respectively [12]. The kinematic model was validated by means of an optoelectronic motion analysis system, as explained in [13].

A simple physical interpretation of the arm redundancy is based on the observation that, with fixed shoulder and hand positions, the elbow is still free to swivel about a circular arc that has a normal vector pointing in the direction of the line connecting shoulder and hand [14]; this type of elbow motion is called *self-motion* and was exploited to solve the arm redundancy in the applied inverse kinematics. A new variable, α , accounting for the self-motion, was added to the task space,

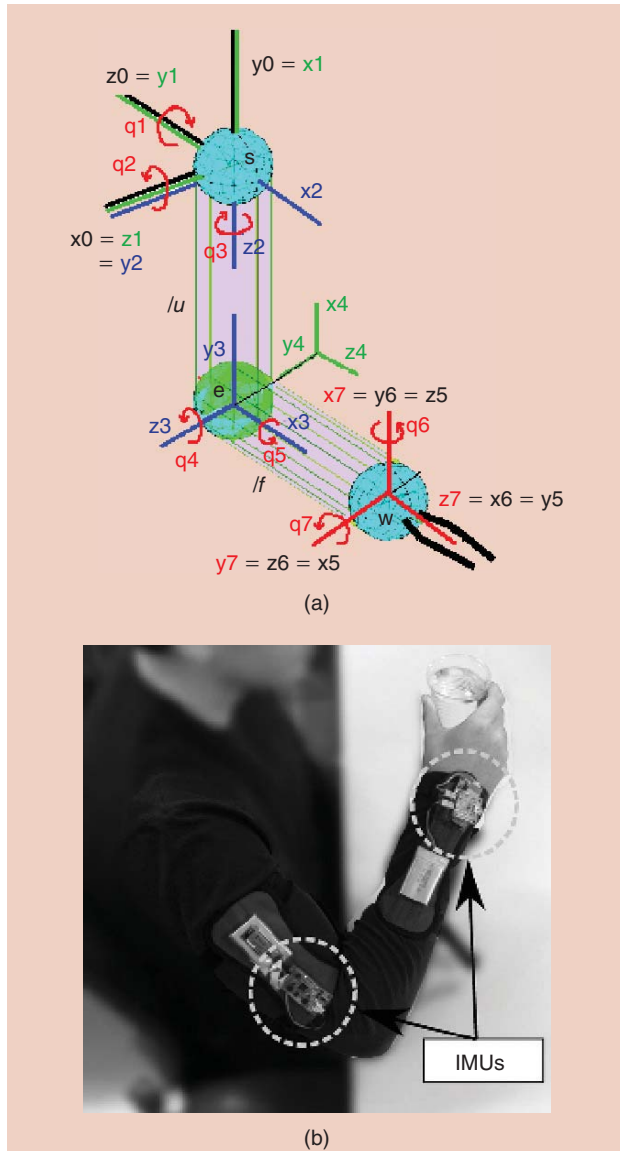


Figure 3. (a) The upper-limb kinematic chain, frames, and joint coordinate systems. (b) The placement of the IMU sensors.

thus yielding a (7×1) vector in the task space and a square (7×7) Augmented Jacobian matrix, J_A . Therefore, the applied inverse kinematics algorithm is given by

$$\dot{\bar{q}} = J_A^{-1}(\bar{q}) \left\{ \begin{bmatrix} \bar{v}_d \\ \dot{\alpha} \end{bmatrix} + K * e\bar{r} \right\} \text{ with } J_A = \begin{bmatrix} J_g \\ J_\alpha \end{bmatrix}, \quad (1)$$

where α represents the angle between an optionally chosen reference plane \hat{V} , and the plane, K , containing the shoulder \bar{s} , elbow \bar{e} , and wrist \bar{w} joints is a gain matrix, while \bar{v}_d and J_g represent the desired hand velocity and the arm geometric Jacobian, respectively.

The Jacobian vector J_α , related to the new variable, was computed as in [11] (Figure 4)

$$J_\alpha(\bar{q}) = \frac{(\hat{w} \times \hat{p})^T}{\|\bar{p}\|} E + \left[\frac{\hat{V}^T \bar{w}}{\|\bar{l}\|} (\hat{w} \times \hat{l})^T - \frac{\hat{w}^T \bar{e}}{\|\bar{w}\| \|\bar{p}\|} (\hat{w} \times \hat{p})^T \right] W. \quad (2)$$

Being $\bar{p} = \bar{e} - \bar{d}$ (the minimum distance between line \overline{sw} and point \bar{e}), with $\bar{d} = \hat{w}(\hat{w}^T \bar{e})$ (the projection vector of \bar{e} onto \bar{w}) and $\bar{l} = (\bar{w} \times \hat{V}) \times \bar{w}$ (the vector lying on the reference plane and orthogonal to \bar{w}), E and W are the Jacobian matrices of the human arm that relate joint velocities to \bar{e} and \bar{w} , respectively. On the other hand, α was determined as

$$\alpha = \arctan(\hat{w}^T(\hat{V} \times \bar{p}), \hat{V}^T \bar{p}). \quad (3)$$

The application of the inverse kinematics procedure in (1) requires the determination of the elbow trajectories; in particular, they are needed for defining α and J_α . The method that was applied for reconstructing the elbow motion resorts to the technique proposed in [12]; the gravitational radial acceleration of the upper arm was combined with hand pose data to estimate the Cartesian coordinates of the elbow joint.

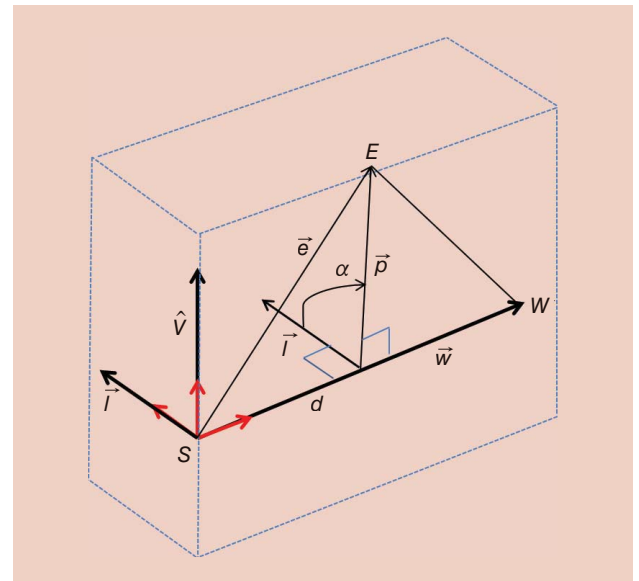


Figure 4. The upper-limb vectors and projections used for determining α and $J_\alpha(\bar{q})$.

One recent work by some of the authors [13] presents the validation of the joint reconstruction method through a comparative analysis with the joint angles measured by an optoelectronic motion capturing system. The mean error committed in joint reconstruction is 8.3×10^{-3} rad (with a standard deviation of 1.8×10^{-3} rad).

Physiological Signals

Psychophysiology is the branch of psychology that is concerned with the physiological bases of psychological processes. The most common measures of psychophysiology used in human–robot interaction studies include:

- 1) *The cardiovascular system*: heart rate variability, respiratory sinus arrhythmia, cardiac output, interbeat interval, and blood pressure.
- 2) *Electrodermal activity*: skin conductance and galvanic skin response (GSR).
- 3) *The respiratory system*: breaths per minute and respiration volume.
- 4) *The muscular system*: electromyography.
- 5) *Brain activity*: electroencephalography and brain imaging methods [15].

Pulse, GSR, skin temperature, and respiration rate (breaths per minute) were used to monitor the emotional state of the user during the execution of a drinking task assisted by the robotic device. Pulse, GSR, and skin temperature sensors were placed on the fingers of the user's left hand. The user's pulse was measured using a plethysmographic pulse sensor placed on the distal phalanx of the thumb, GSR was recorded using two electrodes placed on the medial phalanxes of the second and third finger, and skin temperature was measured using a thermistor located on the palmar surface of the distal phalanx of the fifth finger. The user's respiration rate was computed by employing a thermistor placed beneath the nose; its larger part covered the mouth, while its smaller part was slightly bent so that it could not enter the nose. All signals were sampled at 256 Hz, using the g.US-Bamp USB Bio-signal Amplifier, from g.tec Medical Engineering GmbH, and they were processed through the MATLAB/Simulink software.

To remove the noise and artifacts from the acquired physiological signals, they were preprocessed; then, aiming to determinate user's emotional state, different features were extracted from the acquired signals.

Force Sensor

To measure the interaction forces and torques between the user and the robotic arm, a force/torque sensor (from ATI Industrial Automation) was added at the end-effector. Furthermore, an electromagnetic system was employed to attach the user's arm and rapidly release it from the robotic arm in case of an emergency.

Robotic Arm

The design of the robotic arm was chosen by evaluating the ADLs that the system must perform and the corresponding model of the human arm reachable workspace (ARW) [16]. The human ARW that was used includes three rigid links: 1) the shoulder link (which represents the clavicle and the scapula), 2) the upper arm link (which represents the humerus), and 3) the forearm link (which represents the radius and the ulna). The model describes the Cartesian coordinates of the wrist (considered the reference point) that correspond to the end-effector coordinates.

Because of the anatomical properties of the arm, bones, and muscles, the lower and upper limits of the arm joint angles are strictly related. Referring to the upper-limb kinematic chain [Figure 3(a)], shoulder flexion-extension (q_2) limits can be defined as linear functions of the shoulder adduction/abduction (q_1), while the limits of the shoulder intra-/extrarotation can be stated as functions of both shoulder abduction-adduction (q_1) and flexion-extension (q_2). The limits of the other joint angles are considered constant and independent. Anthropometric data, such as the limits of the joint angles and lengths of the shoulder, upper arm, and forearm links, were derived from [16]. Finally, the human ARW was computed considering all of the joint angles (from the lower to the upper limit).

To analyze the workspace needed for six typical ADLs: eating with a spoon, combing one's hair, picking up or hanging up an object, drinking water from a glass, and washing one's face/brushing one's teeth, the arm kinematics of the tested healthy subjects were reconstructed during the execution of ADL tasks. The experiments were conducted at the Bioengineering Institute of UMH in a room in which no external stimuli could disturb the subject. Each subject performed three repetitions of each ADL task. The ADL tasks were carried out in either a standing or sitting position, depending on

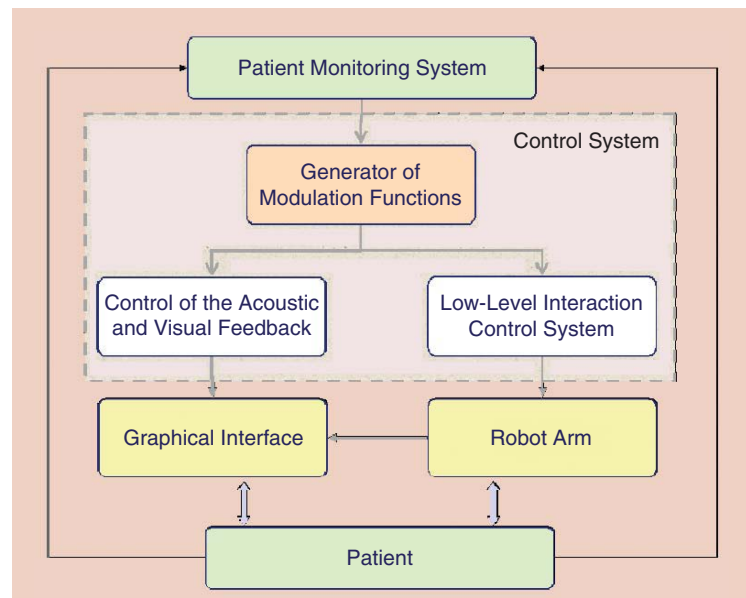


Figure 5. The block scheme of the overall system—the control system is reported in the dotted block, and its component modules are specified.

the nature of the ADL. In this way, the wrist trajectories for each ADL task and the corresponding subworkspaces within the human ARW were defined; they were used to define the workspace of the assistive/rehabilitation robot.

The implemented 7-DOF robotic arm was realized using PRL modules manufactured by Schunk and self-made links. To define the robot forward kinematic function, local coordinate frames were assigned according to D-H convention. The forward and inverse kinematics modules were implemented using the MATLAB/Simulink software; in particular, to avoid the problem of high joint speed in the neighborhood of singular configurations, a damped least-squares inverse of the Jacobian matrix was used: $J^* = J^T (J J^T + k^2 I)^{-1}$.

Finally, to overcome the problems deriving from the proximity to the joint limits, an algorithm for avoiding joint limits was implemented. The algorithm exploits the redundancy of the manipulator and the robot null space to keep the robot out of the joint limits. The problem is solved as a local optimization of an objective function, which is the distance of each joint from its mechanical limit. The objective function $\omega(q)$ can be computed from the following:

$$\omega(q) = \frac{1}{n} \sum_{i=1}^n \left(\frac{q_i - \bar{q}_i}{q_{iM} - q_{im}} \right)^2, \quad (4)$$

where q_{iM} and q_{im} denote the maximum and minimum limits, respectively, and \bar{q} denotes the middle value of each joint range.

The joint velocity vector \dot{q}_0 can be defined as

$$\dot{q}_0 = k_0 \left(\frac{\delta \omega(q)}{\delta q} \right), \quad (5)$$

where $\omega(q)$ is a scalar objective function of the joint variables and $(\delta \omega(q) / \delta q)^T$ is the gradient of $\omega(q)$.

Using this function, it is possible to compute the velocity joint vector to minimize the objective function. Finally, the projection of \dot{q}_0 over null space is computed to modify the manipulator pose without altering its task space configuration

$$\dot{q} = J^\dagger(q) \dot{x} + (I - J^\dagger(q) J(q)) \dot{q}_0. \quad (6)$$

Control System

The core concept of the implemented control system is to update the robot force control and the acoustic and visual feedback according to the information extracted from 1) user kinematic data, 2) user dynamic data (provided by the force/torque sensor), and 3) user physiological data. In particular, kinematic and dynamic data are used to assess the patient's biomechanical state through a set of purposely defined indicators. They can assess the patient's motion accuracy, direction, smoothness, interjoint coordination, and forces exerted by the patient during the interaction with the robotic device. The details can be found in [17]. An analogous work is being carried out for physiological data with the ultimate goal of extracting a set of performance indexes that can globally describe the user's behavior and physiological state. These indexes will serve as feedback to control the submodules that will be able to adapt the robot control gains and update the

acoustic and visual feedback system in accordance with the user's global state. Therefore, the overall control system will include three different modules: 1) a module for generating modulation functions for the interaction control and the acoustic and visual feedback system, 2) the control for the acoustic and visual feedback, and 3) the low-level interaction control system (Figure 5).

The module for generating modulation functions for the interaction control and the acoustic and visual feedback system was partially implemented: it is a multiple-input, multiple-output, nonlinear, time varying, and nondeterministic system based on a fuzzy logic system, which is divided into two hierarchical levels: the first estimates the user's emotional state starting from the acquired physiological signals, and the second determines the modulation functions using the information about the user's behavior and physiological status [18].

Experimental Results

Many experiments were carried out to show the performance of the upper-limb kinematic reconstruction algorithm, to evaluate the correlations between user's physiological signals and emotional state during the execution of an ADL task assisted by a robotic device, and to show the performance of the control system modulating the task complexity according to the estimation of the user's emotional state. Some of the results are reported in the following sections.

Kinematic Reconstruction Algorithm

The method for reconstructing the upper-limb kinematics was applied and evaluated during the execution of a drinking task. Figure 6(a) shows the overlapped hand Cartesian path in the 3-D space obtained from the reconstructed joint angles, through arm forward kinematics (dotted red line), and provided by the robot (blue line). The corresponding seven joint angles of the human arm are shown in Figure 6(b).

The reconstructed kinematics was used jointly with the recorded interaction forces to compute six performance indicators, accounting for the kinematic and dynamic features of patient motion. These features are: aiming angle α for evaluating user motion direction, mean arrest period ratio (MAPR) for measuring the level of smoothness, the correlation coefficient between shoulder flexion-extension and elbow flexion-extension degrees ($q_{corr1,4}$), the correlation coefficient between shoulder abduction-adduction and elbow flexion-extension degrees ($q_{corr2,4}$) for evaluating the level of interjoint coordination, useful mean force (UMF), and useful peak force (UPF) for measuring the user's capability to correctly address the applied force. The details of their definition and use can be found in [17]. The global patient biomechanical state was computed as the normalized weighted sum of these performance indicators. The weights were experimentally retrieved. Table 1 reports the values of performance indicators, the weighted sums, and the level of control for one representative volunteer subject who executed the drinking task. The subject was asked to exhibit two behaviors: 1) healthy behavior and 2) simulated poststroke behavior. Performance indicators assumed greater values in the case of healthy motion than in

the case of simulated poststroke behavior. Correspondingly, the robot control parameters were not updated, and the implemented behavior was unassisted (i.e., control level 1, as explained in the “Performance of the Control System” section). On the other hand, the simulated poststroke behavior (globally producing lower values of the performance indicators) determined an update of robot control parameters depending on the specific value. The corresponding robot control was changed to be assistive in an adaptive way (i.e., control level 2).

Physiological Responses

To know what features may be correlated with the user’s emotional state, a specific experiment was designed. The goal of this experiment was to answer the following questions: 1) Are there significant correlations between the acquired physiological signals and the user’s emotional state during an ADL task assisted by a robotic device? 2) What signal processing and feature extraction techniques can be used? and 3) Can the identification of the user’s emotional state be performed in real time?

The experiment consisted of carrying out a drinking task with the arm attached to the robot. To simulate different motor deficits, three tasks were designed varying the gains of the robot force control: in task 1, a high gain was used; in task 2, a very low gain was applied; and in task 3, negative gains were applied along two axes to simulate a lack of coordination. The experiment protocol was inspired by [19]. A specific visual feedback was implemented for this experiment; it was used to show the user:

- 1) the beginning and the end of each task
- 2) the number of completed drinking tasks
- 3) the time needed to complete the last drinking task
- 4) the time remaining for the task fulfillment.

At the end of each task, the robot brought the user arm to the initial position, and the user could not begin a new task until the start command prompted on the screen.

Before starting the experiment, the subjects were informed of the purpose and the procedure and signed the informed consent form. An adaptation period of few minutes was given to each subject to reach the baseline values of the acquired signals. The subject then remained in a relaxed state for 5 min; during this phase, the baseline values were registered. Successively, he or she had 5 min to perform the three tasks; at the end of each task, a computer version of the Self-Assessment Manikin [20] measured the subject’s emotional responses. Finally, the subject waited for 5 min before starting a new task.

Before the study began, ethical approval was requested and obtained from the Medical Ethics Committee

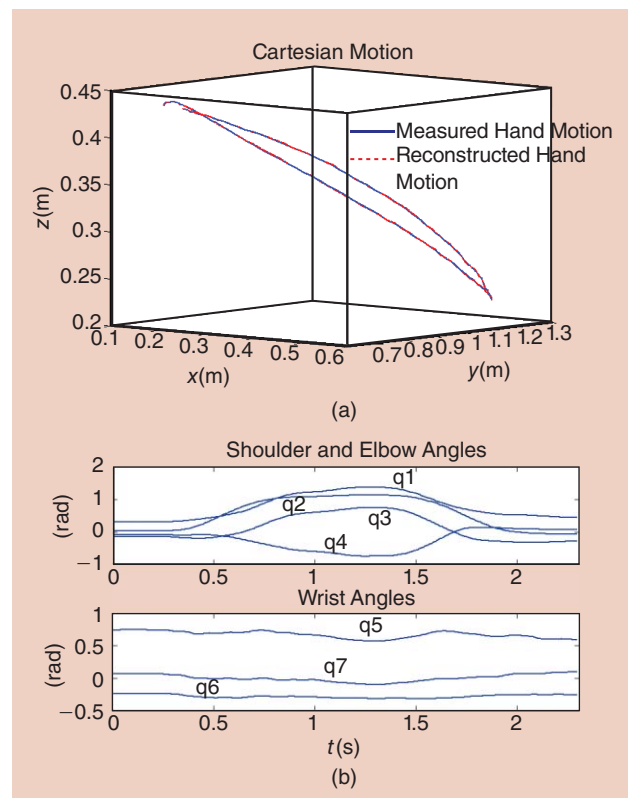


Figure 6. (a) A 3-D hand motion obtained from the reconstructed joint angles by applying the arm forward kinematics (dotted red line) and provided by robot position sensors (blue line). (b) The corresponding upper-limb joint angles.

of the Universidad Miguel Hernandez (UMH) of Elche (Spain). Ten healthy subjects (eight males and two females), students and staff members of the Bioengineering Institute of UMH, took part in the experiment; they were aged 20–41 (mean age 26 years and standard deviation 6.6 years).

Figure 7 shows a detail of the GSR signal acquired on a tested subject, where the beginning and the end movements of the

Table 1. Performance indicators and corresponding control level for one representative subject executing the drinking task in healthy and simulated poststroke conditions [17].

Subject 2 (Healthy)								
Trial No.	α	MAPR	$q_{corr1,4}$	$q_{corr2,4}$	UMF	UPF	Weighted Sum	Level
1	0.92	0.86	0.78	0.95	0.93	0.97	0.98	1
2	0.85	0.81	0.76	0.98	0.82	0.75	0.94	1
3	0.88	0.78	0.69	0.99	0.95	0.94	0.97	1
4	0.86	0.75	0.91	0.99	0.84	0.96	0.98	1

Subject 2 (Simulated Poststroke Behavior)								
Trial No.	α	MAPR	$q_{corr1,4}$	$q_{corr2,4}$	UMF	UPF	Weighted Sum	Level
1	0.34	0.57	0.54	0.65	0.60	0.78	0.56	2
2	0.27	0.71	0.61	0.52	0.47	0.35	0.46	2
3	0.52	0.16	0.52	0.63	0.43	0.30	0.51	2
4	0.29	0.76	0.01	0.51	0.54	0.79	0.47	2

drinking task are indicated, respectively, with white and black vertical lines; the different colors indicate the task execution phase (pink), the test phase (green), and the rest phase (blue).

A statistical data analysis was performed to investigate the possible and meaningful correlations between the acquired

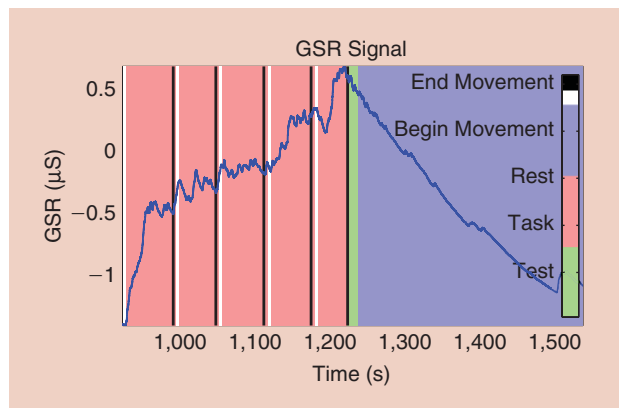


Figure 7. The GSR signal of one subject during the execution of the task 2 (pink), the rest phase (blue), and test phase (green). Beginning and end of the movement are indicated with white and black vertical lines, respectively.

Table 2. Differences of the physiological signals between the three different tasks and the rest phases. All the physiological signals are relative to their baseline values. The physiological signals are measured in pulse rate (beats per minute), respiration rate (breaths per minute), temperature (°C), and skin conductance level (SCL) (µS).

	Task 1				ANOVA	
	Task-Rest1		Rest2-Task			
	Mean	Standard Deviation	Mean	Standard Deviation		
Pulse rate	7.10	4.99	-4.54	4.48	0.002	
Respiration rate	-2.62	4.06	-2.72	2.45	0.01	
Temperature	-0.28	0.35	0.08	0.58	0.018	
SCL	0.85	0.64	-0.11	0.42	0.006	
Task 2						
	Task-Rest1		Rest2-Task		ANOVA	
	Mean	Standard Deviation	Mean	Standard Deviation		
	4.59	5.88	-4.80	6.21		
Pulse rate	4.59	5.88	-4.80	6.21	0.001	
Respiration rate	2.13	3.43	-0.80	2.66	0.128	
Temperature	-0.14	0.20	0.21	0.40	< 0.001	
SCL	0.53	0.52	-0.04	0.44	< 0.001	
Task 3						
	Task-Rest1		Rest2-Task		ANOVA	
	Mean	Standard Deviation	Mean	Standard Deviation		
	6.16	5.26	-7.54	6.38		
Pulse rate	6.16	5.26	-7.54	6.38	0.027	
Respiration rate	-0.83	2.91	-1.11	4.20	0.019	
Temperature	-0.35	0.39	0.69	1.05	< 0.001	
SCL	0.58	1.03	0	0.97	0.003	

physiological signals and the user's emotional state. Table 2 shows the results of the statistical significance analysis performed using the one-way analysis of variance (ANOVA). The differences were considered significant for $p < 0.05$. Furthermore, the Kolmogorov-Smirnov test was used to test if the data had a normal distribution, while Levene's test was used to evaluate the homogeneity of the variance. The results indicate that all of the physiological parameters, except for respiration rate, show a significant difference ($p < 0.05$) between the resting phase and the task execution phase for all three tasks (see Table 2).

Figure 8 shows the physiological signals of one subject acquired during the experiment. In all of the physiological signals, the task and the rest phases are clearly differentiated, while comparing the execution phases of the three tasks, it is only possible to see evident differences between tasks 1–2 and tasks 1–3, in particular, in GSR, skin temperature, and pulse rate.

To evaluate the possible use of all of the analyzed signals in a future assistive application, a new experiment was designed. The experiment consisted of four phases of 5 min: 1) relaxed state, 2) execution of an assistive task (the robot performed a drinking task following a defined trajectory), 3) execution of a resistive task (robot force control with low gain), and 4) rest

phase. In Figure 9, the physiological signals acquired during this kind of experiment are reported. A significant change can be seen between the assistive and the resistive tasks in the GSR, the respiration rate, and the pulse rate. Variations in skin temperature depend on the tested subject.

Performance of the Control System

The experimental trials were carried out with the purpose of reaching a challenging and motivating but feasible task difficulty (based on subject performance) during the drinking task execution with the multimodal assistive robot. Two levels of experimental trials were designed, which are based on the variation of the gain of the force control algorithm:

- Level 1: high gain—the user can easily move the robot—low physical effort
- Level 2: very low gain—the user can hardly move the robot—high physical effort.

The control level was determined depending on the subject's biomechanical and physiological state.

For the biomechanical state, performance indicators were calculated and subject state was evaluated as a weighted sum of the computed indicators (as explained in the “Kinematic Reconstruction Algorithm” section). Hence, the control level was selected as follows: if the value of the weighted sum fell in the interval [0.75, 1], Level 1 was applied (interval [0.75, 1] was experimentally retrieved by means of tests on healthy behavior); otherwise, Level 2 was used. The control levels for a representative subject during the experimental drinking trials are reported in Table 1, together with the values of the indicators and the weighted sum.

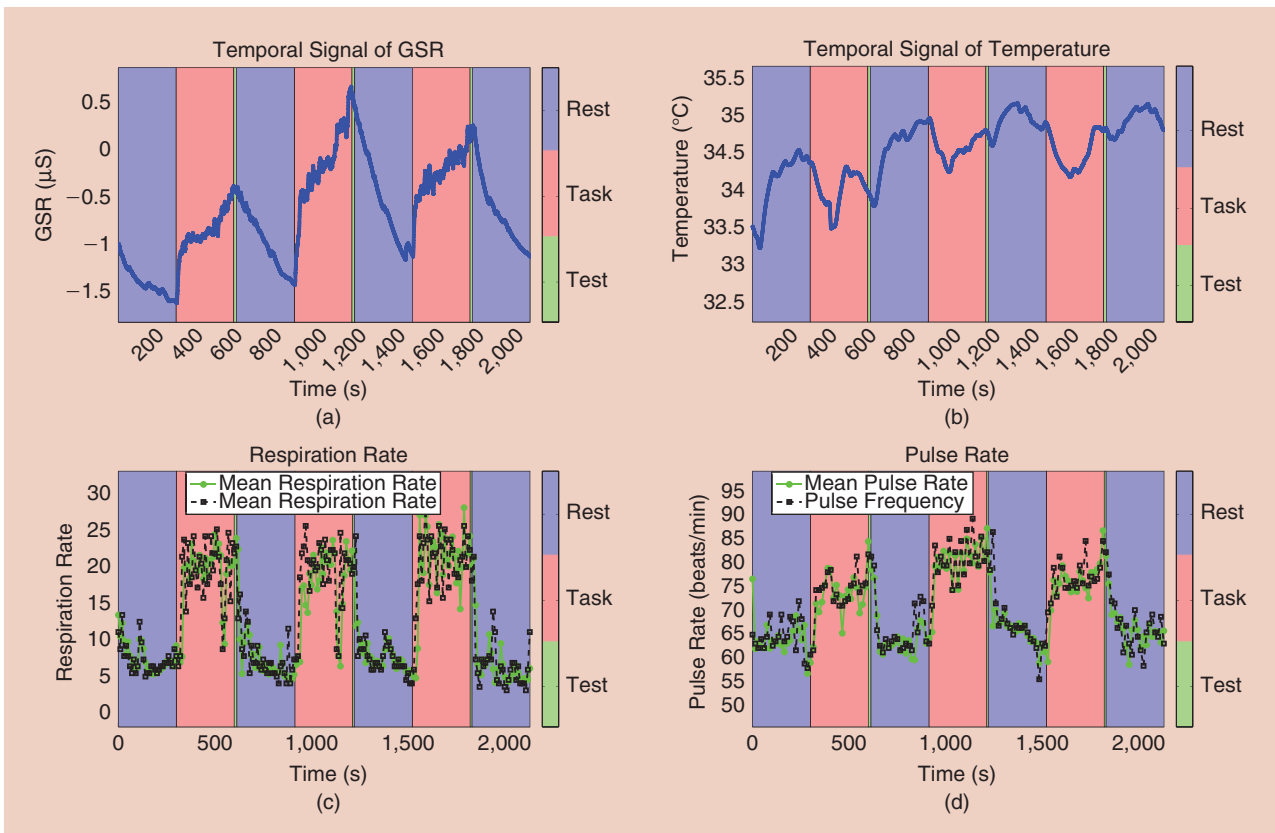


Figure 8. Variations of the physiological signals according to the fulfillment of different phases: test phase, task execution phase, and rest phase. (a) GSR. (b) Skin temperature. (c) Mean respiration rate. (d) Mean pulse rate.

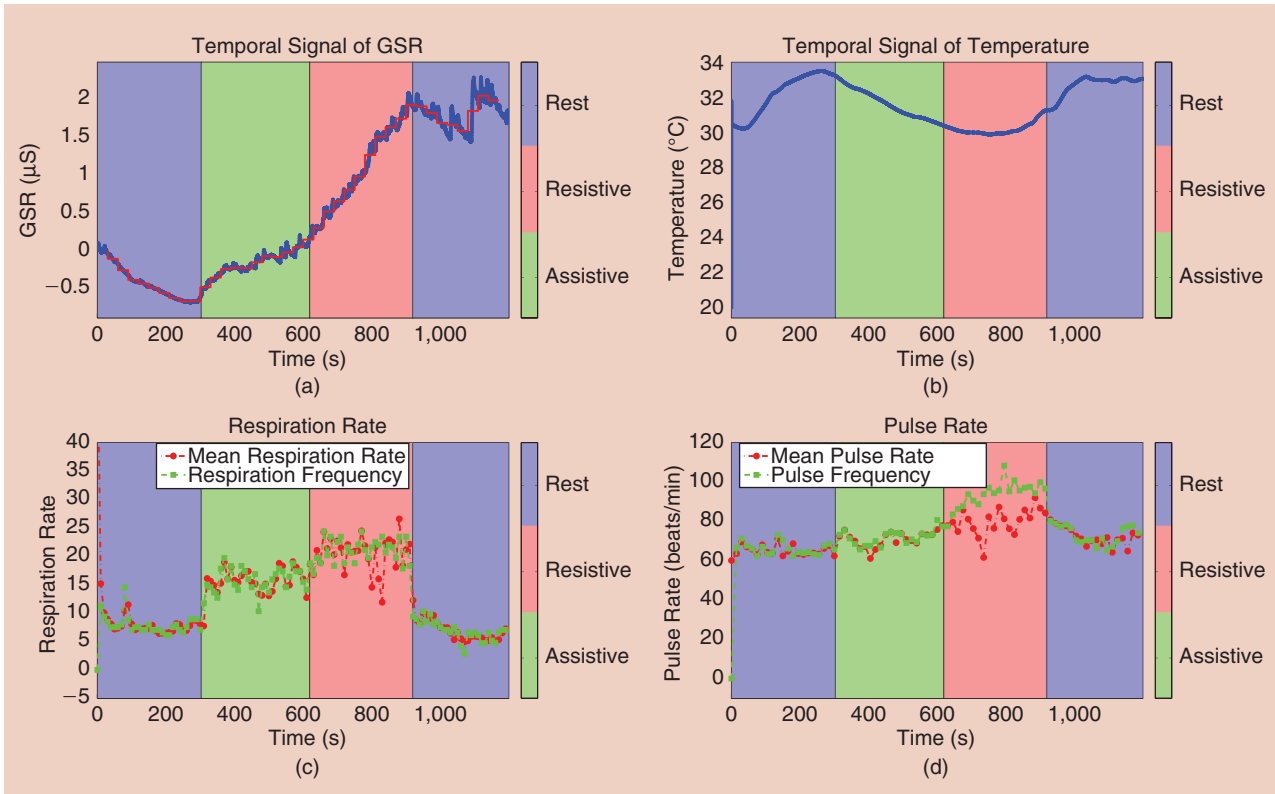


Figure 9. The variations of the physiological signals according to the fulfillment of different tasks: assistive task (Level 1 of the force control), resistive task (Level 2 of the force control), and rest phase. (a) GSR. (b) Skin temperature. (c) Mean respiration rate. (d) Mean pulse rate.

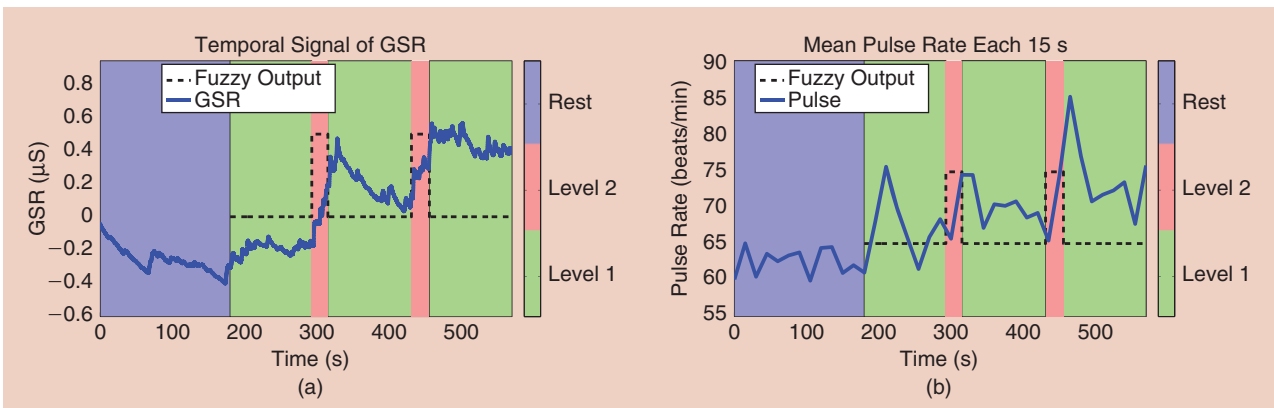


Figure 10. The variation of the force control level on the basis of the output of the fuzzy logic system. (a) GSR and fuzzy logic system output. (b) Pulse and fuzzy logic system output.

Figure 10 shows, for one of the tested subjects, the GSR and mean pulse rate signal changes together with the fuzzy logic system output in the case in which the force control gain was varied, during the drinking task execution, from Level 1 (green) to Level 2 (pink); the resting phase (blue) is also shown. In addition, the output of the fuzzy logic system, which estimates the user's arousal and valence, is depicted with a dotted black line; it was used to change the robot's control level and was computed every 30 s. Note that the pulse signal, which is shown in Figure 10(b), has fluctuations because of the way of computing it—the signal is computed as the mean of the pulse signal every 15 s.

The reported tests intend to provide evidence of the feasibility of the proposed new concept of assistive device. Nevertheless, the number of successes in achieving the tasks over the total number of trials also provides preliminary results on the efficacy of the proposed overall system. Performance measurements during the drinking task, such as the number of successful drinking tasks during the experiments and the time to properly perform the task, in ten healthy subjects are shown in Table 3. The results show that the mean value of successful drinking tasks decreases with the level of assistance provided by the robotic device (from task 1 to task 3); on the contrary, the mean value of the time taken to properly finish the task increases with it.

The performance of the overall control system is difficult to measure since the final goal of the system is to adapt the level of

task difficulty to the subject's biomechanical and emotional state. However, the experiments carried out with ten healthy subjects showed that the system is able to adapt to the subject's state by changing the control level four or five times during the experiments. For a more in-depth evaluation of the performance of such an assistive device, experimental trials with patients are needed. This requires long periods of experimentation (around three months) with the objective of involving clinical units and measuring patients' outcomes with the clinical scales in addition to the biomechanical and emotional evaluation performed here.

Conclusions

This article presents a new concept of multimodal assistive robotic system with three main key features: 1) it is able to provide assistance as needed by implementing a user-tailored approach that accounts for and adapts to subjects' residual physical and cognitive abilities, 2) it can augment users' physical and cognitive abilities in performing daily living activities, such as drinking, cooking, eating, personal hygiene, and grooming, and 3) it provides an increased level of safety in the interaction because of the specific arm design and the number of sensors monitoring the user's state. The proposed assistive device is composed of a 7-DOF modular robot arm conceived for safe human–robot interaction, a multimodal HRI for physiological and biomechanical monitoring of the user, two communication channels for speech recognition and audio-visual feedback, and the overall control system. It is able to manage all of the acquired sensory information and provide the robot with the commands needed for patient-tailored assistance.

Ten healthy subjects were tested for evaluating, on the one hand, the reliability of the multimodal human–machine interface and, on the other hand, the feasibility of overall system. The results confirm that it is possible to exploit users' physiological data to estimate their emotional state and performance data to estimate their biomechanical state during the execution of ADL tasks assisted by a robotic device. In addition, the combination of GSR and pulse rate is a reliable method for estimating the user's physical and cognitive workload, while skin temperature and respiration rate could be used depending on the subject.

Table 3. Performance measurements during the drinking task for ten healthy subjects. The number of successful drinking tasks during 5 min and the time to properly perform the task is reported.

	Drinking Tasks (Number)		Time (s)	
	Mean	Standard Deviation	Mean	Standard Deviation
Task 1	14.43	4.04	15.43	6.38
Task 2	7.71	2.29	36.15	4.20
Task 3	8.00	2.00	25.75	1.05

A reliable reconstruction of the user's kinematic data can be obtained through the presented method for upper-limb kinematic computation; it shows good results in the determination of all of the arm's DOFs during the executions of ADL tasks assisted by the robotic device. In addition, it will be enhanced with the integration of modules for the real-time computation of kinematic indexes that can describe the overall subject performance.

Furthermore, the possibility of modulating the task complexity by estimating the user's biomechanical and emotional state has been shown. In particular, the use of adaptive algorithms based on intelligent machine learning could be the basis for future rehabilitation devices that automatically update their assistance to the specific needs the user. The proposed approach, based on a fuzzy logic system, provided encouraging results; nevertheless, it needs a further extensive evaluation as well as a comparative analysis with other techniques based on neural networks to prove the effectiveness of the proposed assistive system.

Acknowledgments

This work was partly supported by the European Commission (FP7-ECHORD MAAT experiment), by the Spanish Government through the project "Interpretation of the Human Intention and Performance Through Biomedical Signals and Analysis of Kinematic and Dynamic Motion" (DPI2011-29660-C04-04), and by the Italian project PRIN 2010 HANDBOT—biomechatronic hand prostheses endowed with bioinspired tactile perception, bidirectional neural interfaces, and distributed sensorimotor control.

References

- [1] United Nations, "World population prospects: The 2010 revision," Tech. Rep. ST/ESA/SER.A/313, 2011.
- [2] A. D. Carlo, "Human and economic burden of stroke," *Age Ageing*, vol. 38, no. 1, pp. 4–5, 2009.
- [3] A. Timmermans, H. Seelen, R. Willmann, and H. Kingma. (2009, Jan.). Technology-assisted training of arm-hand skills in stroke: Concepts on reacquisition of motor control and therapist guidelines for rehabilitation technology design. *J. Neuroengineering Rehabilitation* [Online]. 6(1), article 1. Available: <http://ukpmc.ac.uk/abstract/MED/19154570>
- [4] H. H. Kwee, "Integrated control of manus manipulator and wheelchair enhanced by environmental docking," *Robotica*, vol. 16, no. 5, pp. 491–498, 1998.
- [5] B. Graf, U. Reiser, M. Hagele, K. Mauz, and P. Klein, "Robotic home assistant Care-o-Bot 3—Product vision and innovation platform," in *Proc. IEEE Workshop Advanced Robotics Social Impacts*, Nov. 2009, pp. 139–144.
- [6] A. Okamura, M. J. Matarić, and H. I. Christensen, "Medical and healthcare robotics," *IEEE Robot. Autom. Mag.*, vol. 17, no. 3, pp. 27–37, 2010.
- [7] D. Novak, M. Mihelj, J. Zihrl, A. Olensek, and M. Munih, "Psychophysiological measurements in a biocooperative feedback loop for upper extremity rehabilitation," *IEEE Trans. Neural Syst. Rehab. Eng.*, vol. 19, no. 4, pp. 400–410, Aug. 2011.
- [8] H. Krebs, J. Palazzolo, L. Dipietro, M. Ferraro, J. Krol, K. Rannekleiv, B. Volpe, and N. Hogan, "Rehabilitation robotics: Performance-based progressive robot-assisted therapy," *Auton. Robot.*, vol. 15, no. 1, pp. 7–20, 2003.
- [9] B. Dumas, D. Lalanne, and S. L. Oviatt, "Multimodal interfaces: A survey of principles, models and frameworks," in *Human Machine Interaction*, (Lecture Notes in Computer Science Series, vol. 5440), D. Lalanne and J. Kohlas, Eds. Berlin Heidelberg, Germany: Springer, 2009, pp. 3–26.
- [10] R. A. Bolt, "Put-that-there! Voice and gesture at the graphics interface," Presented at the 7th Annu. Conf. Computer Graphics and Interactive Techniques, ser. SIGGRAPH '80. [Online]. Available: <http://doi.acm.org/10.1145/800250.807503>
- [11] K. Kreutz-Delgado, M. Long, and H. Seraji, "Kinematic analysis of 7 DOF anthropomorphic arms," in *Proc. IEEE Int. Conf. Robotics Automation*, 1990, vol. 2, pp. 824–830.
- [12] M. Matjaz, "Human arm kinematics for robot based rehabilitation," *Robotica*, vol. 24, no. 3, pp. 377–383, 2006.
- [13] E. Papaleo, L. Zollo, S. Sterzi, and G. Guglielmelli, "An inverse kinematics algorithm for upper-limb joint reconstruction during roboaided motor therapy," in *Proc. IEEE Int. Conf. Biomedical Robotics Biomechatronics*, Rome, Italy, 24–27 June, 2012.
- [14] D. Tolani, A. Goswami, and N. Badler, "Real-time inverse kinematics techniques for anthropomorphic limbs," *Graphical Models*, vol. 62, no. 5, pp. 353–388, 2000.
- [15] C. Bethel, K. Salomon, R. Murphy, and J. Burke, "Survey of psychophysiology measurements applied to human-robot interaction," in *Proc. 16th IEEE Int. Symp. Robot Human Interactive Communication*, 2007, pp. 732–737.
- [16] J. Lenarcic and A. Umek, "Simple model of human arm reachable workspace," *IEEE Trans. Systems, Man, Cybernetics*, vol. 24, no. 8, pp. 1239–1246, Aug. 1994.
- [17] E. Papaleo, L. Zollo, L. Spedaliere, and G. Guglielmelli, "Patient-tailored adaptive robotic system for upper-limb rehabilitation," in *Proc. IEEE Int. Conf. Robotics Automation*, 2013, pp. 3860–3865.
- [18] M. Mihelj, D. Novak, and M. Munih, "Emotion-aware system for upper extremity rehabilitation," in *Proc. Virtual Rehabilitation Int. Conf.*, June 29–July 2, 2009, pp. 160–165.
- [19] D. Novak, M. Mihelj, and M. Munih, "Psychophysiological responses to different levels of cognitive and physical workload in haptic interaction," *Robotica*, vol. 29, no. 3, pp. 367–374, 2011.
- [20] M. M. Bradley and P. J. Lang, "Measuring emotion: The self-assessment manikin and the semantic differential," *J. Behav. Ther. Exp. Psychiatry*, vol. 25, no. 1, pp. 49–59, Mar. 1994.

Ricardo Morales, Miguel Hernandez University, Alicante, Spain. E-mail: rmorales@umh.es.

Franciso J. Badesa, Miguel Hernandez University, Alicante, Spain. E-mail: fbadesa@umh.es.

Nicolas Garcia-Aracil, Universidad Miguel Hernandez de Elche, Alicante, Spain. E-mail: nicolas.garcia@umh.es.

Carlos Perez-Vidal, Universidad Miguel Hernandez de Elche, Alicante, Spain. E-mail: carlos.perez@umh.es.

Jose M. Sabater, Universidad Miguel Hernandez de Elche, Alicante, Spain. E-mail: j.sabater@umh.es.

Eugenio Papaleo, Università Campus Bio-Medico di Roma, Rome, Italy. E-mail: e.papaleo@unicampus.it.

Antonino Salerno, ASML Netherlands BV, Veldhoven, The Netherlands. E-mail: antonino.salerno@unicampus.it; antonino.salerno84@gmail.com.

Loredana Zollo, Università Campus Bio-Medico, Rome, Italy. E-mail: l.zollo@unicampus.it.

Eugenio Guglielmelli, Università Campus Bio-Medico, Rome, Italy. E-mail: e.guglielmelli@unicampus.it; rameic@ieee.org.



The Safety of Domestic Robots

A Survey of Various Safety-Related Publications

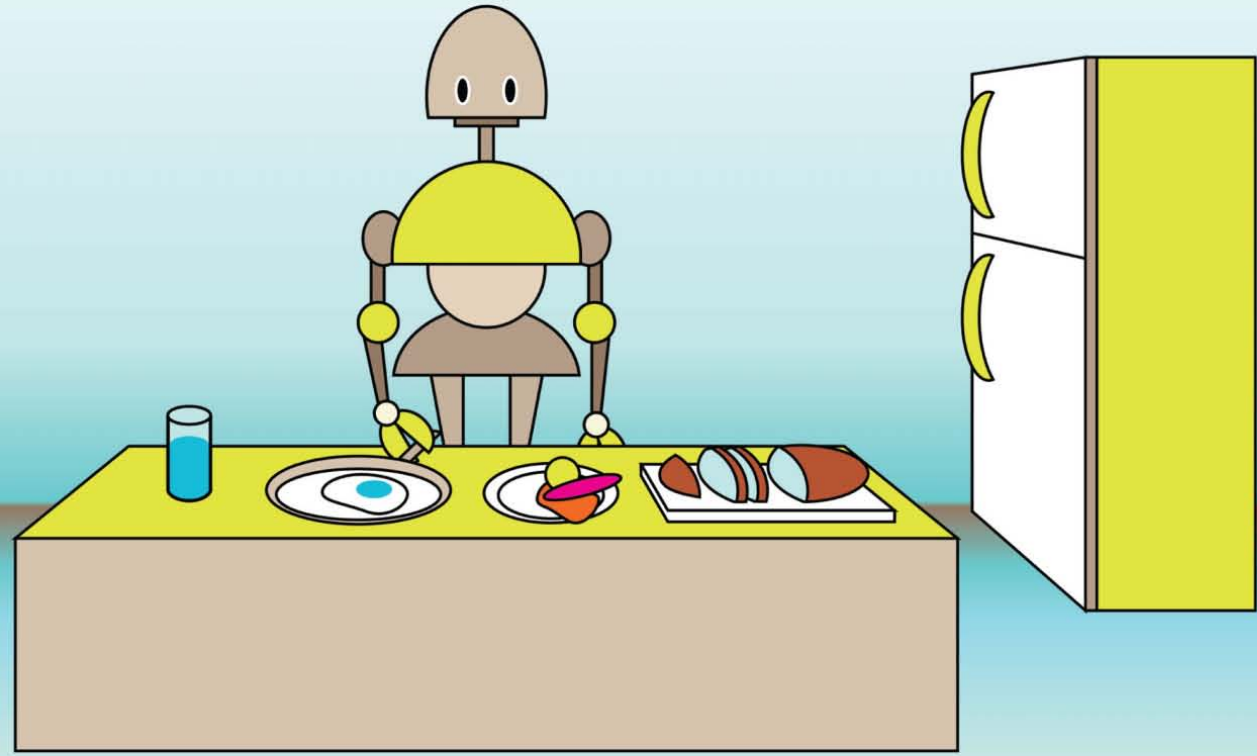
By Tadele Shiferaw Tadele, Theo J.A. de Vries, and Stefano Stramigioli

Different branches of technology are striving to come up with new advancements that will enhance civilization and ultimately improve the quality of life. In the robotics community, strides have been made to bring the use of personal robots in office and home environments on the horizon. Safety is one of the critical issues that must be guaranteed for the successful acceptance, deployment, and utilization of domestic robots. Unlike the barrier-based operational safety guarantee that is widely used in industrial robotics, safety in domestic robotics deals with a number of issues, such as intrinsic safety, collision avoidance, human detection, and advanced control techniques. In the last decade, a number of researchers have

presented their works that highlighted the issue of safety in a specific part of the complete domestic robotics system. This article presents a general survey of various safety-related publications that focus on safety criteria and metrics, mechanical design and actuation, and controller design.

Safety in Domestic Robots

Recent advances in robotics have led to the growth of robotic application domains, such as medical [1]–[3], military, rescue [4]–[6], personal care [7]–[10], and entertainment [11]. Out of these categories, a personal-care robot is defined as a service robot with the purpose of either aiding or performing actions that contribute toward the improvement of the quality of life of



Digital Object Identifier 10.1109/MRA.2014.2310151
Date of publication: 20 August 2014

IMAGE LICENSED BY INGRAM PUBLISHING

an individual [12]. A domestic robot is a personal-care robot with or without manipulators that operates in home environments and is often mobile. This cohabitation of domestic robots and humans in the same environment raised the issue of safety among standardization bodies [12], [13], research communities [14]–[17], and robot manufacturers [18]–[21].

As an attribute of dependability, safety is one of the fundamental issues that should be assured for flourishing the use of domestic robots in the future [22], [23]. In general, safety in domestic robotics is a broad topic that demands ensuring safety to the robot itself, to the environment, and to the human user, with the latter considered the most important requirement. In a robotic system where human interaction is involved with a certain risk, it is important to design robots carefully, considering the famous Murphy's law: "If something can go wrong, it will." The standard safety requirement used in robotics includes a three-step safety guideline: 1) risk assessment, 2) risk elimination and reduction, and 3) validation methods [12], [13], [24].

The primary risk assessment step identifies a list of tasks, environmental conditions, and potential hazards that should be considered during system design. Different techniques of performing risk assessment to identify and methodically analyze faults in robotic systems are presented in [25] and [26] as well as in International Organization for Standardization (ISO) 12100 standard [27]. The following risk identification and reduction step, by itself, is an iterative three-step process that includes safe design to avoid or minimize possible risks, a protection mechanism for risks, which cannot be avoided by design, and, finally, a warning to the user in case both design and protection failed. The final validation step establishes methods that are used to verify whether the desired safety requirements are satisfied by the developed system.

Even if all three steps are equally important to design robots that can be used in human environments, most of the safety-related works in domestic robotics over the past decade focused on risk elimination and validation steps in a selected part of the total robotic system. Therefore, this survey leaves out works related to risk assessment and, instead, covers publications that include risk elimination and validation steps of the standard robotic safety requirement in domestic robotics. For a complex domestic robot that consists of different mechanical, sensing, actuation, control system, perception, and motion planning subsystems (Figure 1), analyzing the overall safety can be done using the concept of functional safety [28], [29]. This systematic approach allows for a safety evaluation of domestic robots based on the standardized functional safety of each subsystem as well as the interactions that exist between them. Typical functional safety standards that can be used for safety analysis are ISO 13849: *Safety of Machinery: Safety Related Parts of Control System* and IEC 61508: *Functional Safety of Electrical/Electronic/Programmable Electronic Safety-Related Systems* [28].

Safety Criteria and Metrics

Domestic robots require meaningful criteria and metrics to analyze safety and define injury levels of potential hazardous conditions. Safety criteria define desired design requirements,

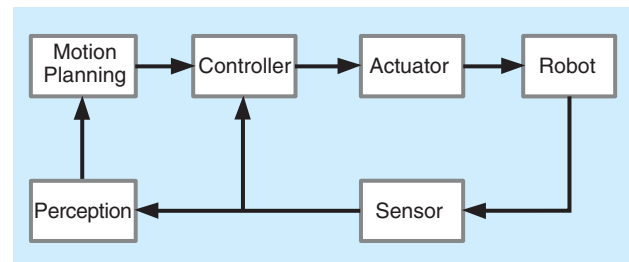


Figure 1. A typical robotic system.

while the quantitative safety metrics, defined based on the criteria, are essential for providing insightful safety improvement ideas, comparing successful system implementations, and assisting system accreditation. Safety metrics are, in general, used to identify what injury a robot might cause [30]. The safety criteria are mostly part of an international standard that is deemed acceptable by the manufacturing industry as well as the research community.

A standard framework used when dealing with safety in robotics is a risk- or injury-based safety requirement, which requires a system-level analysis of safety. The ISO uses this approach to release a set of safety requirements for robots, such as ISO 10218-1: *Safety Requirements for Robots in Manufacturing Industry* [31]. These standards are updated when needed, and, in the case of ISO 10218-1, a revised standard was released that deals with the emerging requirement in industrial robotics to share a workspace with humans [31]. An ISO committee has also addressed the issue of safety in personal robots and released an advanced draft of their work ISO 13482: *Safety Requirements: Non-Medical Personal Care Robot* [32].

There are a number of hazards and risks that are included in the safety standard for domestic robots, but contact-based injuries can be divided into two types: 1) quasistatic clamping and 2) dynamical loading. Different subclasses of the injuries exist, depending on the constraint on a human, the singularity state of the robot, and the sharpness of the contact area [33]. The dynamic loading collision between a robot and a human can be either a blunt impact or a sharp edge contact in which possible injuries range from soft-tissue contusions and bruises to more serious bodily harm. Collision analysis and modeling for the investigation of injury measurement was presented in [34], while [35] discussed the details of soft-tissue injuries, such as penetrations and stabs using experimental tests. There is no universally accepted safety metric that measures these injuries, but a number of approaches have been presented. The common safety metrics used to measure collision and clamping risks in domestic robotics can be categorized into different groups based on the parameters they use: acceleration based, force based, energy/power based, or other parameter based.

Acceleration Based

The most widely used safety metric in domestic robotics for injuries due to collision is the acceleration-based head injury criteria (HIC) [36]. The metric is derived from human biomechanics data given in the Wayne state tolerance curve [37] and is used in biomechanics studies and accident researches

in different fields, such as the automotive industry. It is a measure of the head acceleration for an impact that lasts for a certain duration and is given mathematically as [38]

$$\text{HIC}_{\Delta t} = \Delta t \left[\frac{1}{\Delta t} \int_0^{\Delta t} a(\tau) d\tau \right]^{2.5}, \quad (1)$$

where $a(\tau)$ is the head acceleration normalized with respect to gravity, g , and Δt is the measurement duration, which is often taken as 15 ms to investigate head concussion injuries [38].

HIC has been used in robotics as a severity indicator for potential injury due to blunt impact to the human head. Such collisions typically exhibit a high-frequency behavior above the controller bandwidth and, thus, are mainly influenced by the link dynamics and, for stiff robots, also by the motor dynamics. HIC-based safety requirements are used in [39] to identify dynamic constraints on a robot, and then the constraint information obtained to define a performance metric that allows for a better tradeoff between performance and safety is used. The effect of different robot parameters on HIC is analyzed and experimentally verified in [33]. This insightful work included the experimental results with different robots to conclude that a robot of any arbitrary mass cannot severely hurt a human head if measured according to HIC because of the low operating speed. Haddadin et al. [40] applied a number of safety criteria while investigating the safety of a manipulator at a standard crash-test facility. They conducted a meticulous safety analysis of the manipulator based on human biomechanics and were able to present quantitative experimental results using different safety metrics for the head, neck, and chest areas. For unconstrained blunt impact, they used HIC as a metric for severe head injury. While reviewing different topics in physical human–robot interaction, [23] noted the need for a new type of safety index in robotics other than HIC because the type of injury and operation speed in robotics is different from that of the automotive industry, where HIC is a standardized metric during crash tests.

Other metrics whose results are interpreted based on HIC were also reported in the literature. A metric based on HIC known as the *manipulator safety index (MSI)*, which is a function of the effective inertia of the manipulator, is proposed in [41]. After identifying effective inertia as the main factor in manipulator safety, this index analyzes the effective inertia of different manipulators under constant impact velocity and interface stiffness to compare their safety. This metric was used to validate the safety of a manipulator after design modifications in [42] and [43]. Three danger indexes whose results were interpreted based on HIC is developed and investigated in [44]. The work investigates force-, distance-, and acceleration-related danger indexes on a model to give a quantitative measure of the severity and likelihood of injury. The authors proposed a danger index that is a linear combination of the above qualities and considers the speed, effective mass, stiffness, and impact force.

Force Based

The other category of safety metrics for contact injuries is the force-based criteria, which considers that excessive force is the

cause of potential injuries and, thus, should be limited. Covering detailed analysis on force-based criteria, Ikuta et al. [45] used the minimum impact force that can cause injury as a factor to define a unitless danger index to quantify safety strategies. The danger index α of a robot is defined as

$$\alpha = \frac{F}{F_c}, \quad (2)$$

where F_c is the minimum critical force that can cause injury to a human and F is the possible impact force of the robot. Quantifying safety using this extendable metric was used to achieve safer design and an improved control strategy. In the mechanical design aspect, the index was used to relate safety and design modifications, such as low mass, soft covering, joint compliance, and surface friction or a combination of them.

Three safety requirements that are essential in human–robot interaction are proposed in [46]: 1) human–robot coexistence, 2) understandable and predictable motion by the robot, and 3) no injuries to the user. The author then defined a safety metric called the *impact potential* based on the maximum impact force that a multiple-degrees-of-freedom (DOF) robotic manipulator might exert during collision. For a set of possible impact surfaces on the robot P , the impact potential is given as

$$\pi = \sup_{p \in P} \pi_p, \quad (3)$$

where π_p is worst case impact forces at contact point p on the surface of the robot.

Due to the low HIC values observed even for heavier robots as a result of low collision velocity, [47] proposed to use minimum forces that cause damage to different body parts as a safety metric. Since different body parts have different tolerance limits, the limit for neck injuries was chosen as a working criterion as it has the lowest value. A force-based safety criterion was used in [48] to investigate the safety of a pneumatic muscle-actuated 2-DOF manipulator because HIC, according to the authors, does not provide an absolute measure of danger. While analyzing the safety of a manipulator with respect to injuries at different parts of the body, [40] used maximum bending torque as neck injury metrics and verified safety for quasistatic constrained impact at different body parts using the maximum contact force as a metric, whose allowed tolerance for different body parts is known.

Energy/Power Based

Different empirical fits were suggested for the Wayne state data other than HIC approximations, and one of them proposes reducing the power in (1) to two [49]. According to this approximation, the equation then becomes

$$f = \frac{1}{\Delta t} \left[\int_0^{\Delta t} a(\tau) d\tau \right]^2 \quad (4)$$

$$f = \frac{\Delta V^2}{\Delta t}, \quad (5)$$

where ΔV is the change in velocity of the head.

According to (5), possible injury to a human is proportional to the rate of kinetic energy transferred to the body during impact. Based on this observation, Newman et al. introduced a power-based safety metric called head impact power (HIP) from the experimental investigations. By evaluating concussion injury due to an impact on a human head, the proposed HIP risk curve relates the probability of having a concussion injury with the amount of power transferred during a collision. The rate of energy transfer was also suggested as a viscous criterion safety metric for constrained organs injury [50]. According to the viscous safety criterion, injury to human organs is proportional to the product of the compression and the rate of compression.

Uncontrolled extra energy was also suggested as a cause of accidents in robots [51], and various experimental tests on the dynamic responses of human biomechanics during impact were performed to define energy-based safety metrics that can be used in robotics. Energy limits that cause failure of the cranial bone in adult and infant subjects are identified in [52] and [53], respectively. The energy that causes a human skull fracture per volume of the skull was given as $\varepsilon_{\text{adult}} = 290 \text{ kJ/m}^3$ and $\varepsilon_{\text{infant}} = 160 \text{ kJ/m}^3$ for an adult and a six-month-old infant, respectively. The amount of energy that can cause fracturing of the neck bones and spinal injuries was determined in [54]. Accordingly, the amount of energy that can damage the spinal cord of an adult human was averaged at $E_{\text{neck}} = 35 \text{ J}$. It is apparent that, since the aforementioned energy-based tolerance values are obtained from severe fracture injuries, they cannot be directly used as acceptable safety threshold limits for domestic robots.

Other Parameter Based

Other safety metrics proposed for use in domestic robotics are based on factors such as pain tolerance, maximum stress, and energy density limit. The human pain tolerance limit for clamping or sudden collisions was used as a metric for safe robot design in [55]. The pain tolerance limit of a human for different parts of the body was used to identify the admissible force during normal operations, and a soft covering of the robot was designed based on this value. A strong correlation between the pain felt by a human and the impact energy density was indicated from the experimental investigation on the collision of a robotic manipulator with a human [56].

Skin injury to a human is the focus of [57], which provides a safety metric that evaluates the safety of a robot design based on its cover shape and material covering. Using Hertzian contact models to represent the impact, the proposed safety norm identifies safe design choices by evaluating the maximum stress on the skin that will occur during impact of a point on the robotic cover against a human body. Focusing on soft-tissue injuries, [58] also developed a Hertz contact theory-based collision model between a covered robot and a human head to analyze laceration and contusion injuries. Then, using tensile stress and energy density limits of the skin as a safety criteria, the authors proposed allowable elastic modulus and thickness for a robot covering. Soft-tissue injuries that might result from

sharp edge contacts between robot-operated tools and a human user were assessed using medical classifications in [59]. Instead of using a safety metric to define the injury level observed, this experimental study defined a risk curve that directly relates the observed injury with the mass, velocity, and geometry parameters of the operating robot.

Mechanical Design and Actuation

The variations in use cases and performance requirements between domestic and industrial robots understandably lead to different designs. Robots designed for industrial purposes have a high stiffness to achieve the main performance requirement, which is accuracy, and consist of heavier links to handle heavy loads [60]. Domestic robots are mostly designed with use cases that include performing humanlike activities in unstructured environments and, hence, have distinct mechanical design requirements [7], [61], [62].

Safety in mechanical design and actuation deals with the crucial issue of ensuring inherent safety, i.e., safety even in the unlikely case of loss of the entire control system. To achieve inherent safety, robotic arms mounted on domestic robots are designed to be lightweight and compliant so as to mitigate any possible injury that may arise in case of an uncontrolled collision with human. The presence of compliant behavior in the manipulator might result in unwanted oscillations during motion and compromise system performance. Hence, advanced controllers should be used to compensate the performance degradation in flexible robots [63] and enable an acceptable tradeoff between safety and performance [39]. The most widely used performance metric in the mechanical design of robotic manipulators is the payload-to-weight ratio, which is defined as the ratio of maximum payload that the robot can manipulate to its stand-alone weight. Mechanical designs in domestic robot manipulators are aimed at achieving a higher payload-to-weight ratio while being able to perform the tasks defined in their use cases [42], [62].

The main safety-based design rationale behind the lightweight links in domestic robotics is reducing the impact force by lowering the kinetic energy of the link. Compliance between the actuator and the end-effector is essential to decouple the actuator inertia and the link inertia so that only the inertia of the lightweight link is felt during uncontrolled impact. The dynamic relationship between the desired decoupling behavior, the maximum impact force, and the mechanical properties of flexible manipulators was recently investigated in [64]. Reference [33] indicated that even a moderate compliance achieved using harmonic drives was able to yield the required decoupling, and further lowering of the compliance reduces the impact torque at the joint, thereby protecting the robot itself during collision. The compliance can be implemented as either active compliance using control [62], [65], [66], passive compliance by inserting elastic elements at the joint actuation [67], or a combination of both in one manipulator, as used in [68]. Although active compliant manipulators offer satisfactory performance for nominal operation, current investigations in compliant actuation are trying to exploit the

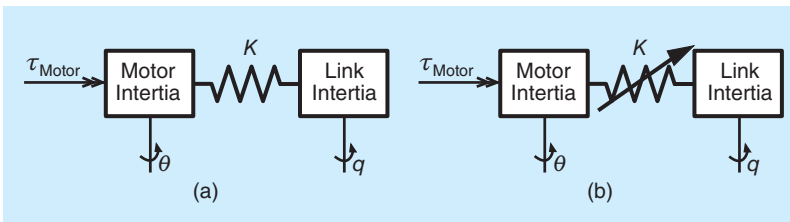


Figure 2. The schematics of (a) SEA and (b) VIA.

wide range of compliance and faster dynamic response rate offered by passive compliance [67], [69].

The first approach to have a compliant robot, called *series elastic actuation* (SEA), was done by inserting a passive compliant element between the joint and the actuator's gear train [70]. The authors presented a force-controlled actuation with less danger to the environment and less reflected actuator inertia during impact [Figure 2(a)]. A modified SEA actuation approach, variable impedance actuation (VIA), allows for tuning of the compliance in the transmission for improved performance and collision safety [34], [39], [71]. This mechanism allows for adapting the mechanical impedance depending on the tasks to yield a wide range of manipulation capabilities by the robot [Figure 2(b)]. Various VIA designs have been proposed in the literature, which differ in their range of motion and stiffness [72]–[75]. Although the potential inherent safety of SEA and VIA comply with the prioritized risk reduction of mechanical design over control system, as proposed in ISO 12100, the energy stored in the compliant element of VIA can lead to increased link speed and compromise safety, as shown in [76]. It should also be noted that the VIA design also incorporates damping of the compliant joints to avoid unnecessary vibrations during operation.

One of the earliest generations of manipulators designed for human interaction is the DLR lightweight robot with moderate joint compliance and suitable sensing and control capability [62] [Figure 3(a)]. The manipulator was planned to perform human-arm-like activities and mimicked the kinematics and sensing capability of a human arm. The manipulator has an active compliance, made possible by a joint torque control, and was able to have a payload-to-weight ratio of $\sim 1:2$. New generations of the DLR lightweight robot included an advanced control system [78] and achieved a payload-to-weight ratio of 1:1, while safety for interaction is evaluated using HIC [77]. A new DLR hand arm system was also developed with the aim of matching its human equivalent in size, performance, and weight [79]. The design uses a number of variable stiffness actuation designs and exploits the energy-storing capability of compliant joints to perform highly dynamic tasks.

Another actuation scheme designed to fit in the human-friendly robotics category is distributed macromini actuation (DM2). This novel actuation mechanism introduces two parallel actuators that handle the high- and low-frequency torque requirements [80]. In the first prototype that uses this mechanism, the low-frequency task manipulation torque actuation

was handled by a larger electrical actuator at the base of the arm, while high-frequency disturbance rejection actions were performed by low-inertia motors at the joints. Compliance is provided using low reduction cable transmissions for the high-frequency actuation and SEA for the low-frequency actuation. A follow-up study by the research group introduced the Stanford Human Safety Robot, S2 ρ , with the same

distributed actuation concept but replaced the heavy electrical actuators with pneumatic muscles to have a hybrid actuation arm [42]. The authors reported an improved payload-to-weight ratio and control bandwidth while evaluating the safety requirements using the MSI. Further iterations of the S2 ρ were indicated to have an improved control, responsiveness, and range of motion [43].

Another mechanical design relevant for the safety of a robot is a passive gravity compensation, as shown in [81]. The mechanism that is common in machine design uses geometrical analysis and springs to balance the gravitational energy with strain energy. Previously, passive gravity compensation was made possible using a counter mass that annuls the effect of gravity on the target manipulator. The spring-based system has an advantage over the counter mass in that it avoids the addition of inertia, which is unnecessary in domestic robotics. An extended arm actuation mechanism that uses passive gravity compensation is presented in [7]. Together with a backdrivable transmission, this design enhances safety and reduces the torque requirement at the joint actuators.

Although most of the discussion in this section focused on manipulators that can be used on autonomous domestic robots, the idea similarly applies to the mechanical design of other robot parts, such as the trunk or mobile base. Aiming to emulate the natural reaction of a human's waist to collision, [82] designed a passive viscoelastic trunk with a passive movable base. Other mechanical design issues addressed with regard to safety include using a backdrivable transmission [83], eliminating pinch points by covering dangerous areas of the robot, analyzing the flexibility of nonrigid links [23], adding force limiting devices [84], and placing a compliant cushion covering [55].

Controller Design

When it comes to controlling the robot to execute a planned motion and accomplish a task, most of the industrial robots use position controllers. This is because most of the robots perform simple position-focused tasks, such as spot welding, spray painting, or pick-and-place operations, in a well-known operating environment [85]. In tasks that demand contact with an object during operations, industrial robots adopt force control techniques to regulate the amount of force applied by the robot during the interaction [86]. Later, based on operational force and position constraints imposed on a manipulator, a hybrid position/force controller was introduced that uses position control on some DOF and force control for others [87]–[89]. In general, the pure position controller exhibits an

infinite stiffness characteristic working in a zero-stiffness environment, while the pure force controller exhibits a zero-stiffness characteristic working in a stiff environment.

For domestic robots that often operate in unstructured environments with humans, pure position control is incomplete because, if there is contact with an obstacle, the robot is not expected to go through the obstacle. Similarly, a pure force control is also inadequate as contactless tasks and motions are difficult to implement. An alternative control technique essential in domestic robotics is the interaction control scheme, which deals with regulating the dynamic behavior of the manipulator as it is interacting with the environment [90]. The core idea behind interaction control is that manipulation is done through energy exchange, and, during the energetic interaction, the robot and the environment influence each other in a bidirectional signal exchange. Thus, by adjusting the dynamics of the robot, how it interacts with the environment during operation can be controlled.

One of the most widely used interaction control schemes is impedance control presented in [91]. Most of the operating environments of the robot, such as mass to be moved or rigid obstacles in work space, can be described as admittances that accept force inputs and output velocity during interaction. Hence, for possible interactions in such an environment, the manipulator should exhibit an impedance characteristic, which can be regulated via impedance control. Consider a simplified 1-DOF robotic manipulator modeled as a mass m at position x , which is to be moved to a desired position x_d . A simple physical controller that can achieve this is a spring connected between the desired virtual point and the mass (Figure 4). To avoid continuous oscillation of the resulting mass-spring system and stabilize at the equilibrium point, a damper should be added to the system. The resulting controller is an impedance controller that can shape the dynamic behavior of the system.

The controller resembles a conventional proportional-derivative controller and introduces a desirable compliance to the system. A number of impedance controller designs have addressed issues such as robustness [92], [93], adding adaptive control techniques [94], [95], extension with a learning approach [96], dynamics of a flexible robot [78], [97], and dexterous manipulation [77], [98], [99].

Another crucial requirement in controller design for domestic robots is ensuring asymptotic stability even in the presence of apparent uncertainties about the properties of the operating environment [77]. To address this issue, several authors have applied passivity theory to design controllers commonly known as *passivity-based controllers* [78], [100], [101]. Passive systems are a class of dynamic systems whose total energy is less than or equal to the sum of its initial energy and any external energy supplied to it during interaction. Hence, passivity-based controller design ensures a bounded energy content, and the system achieves equilibrium at its minimum energy state. Any energetic interconnection of two passive systems will not affect the passivity of the combined system. As a result, an interconnection of a passivity-based controller, a passive manipulator, and a typical unstructured

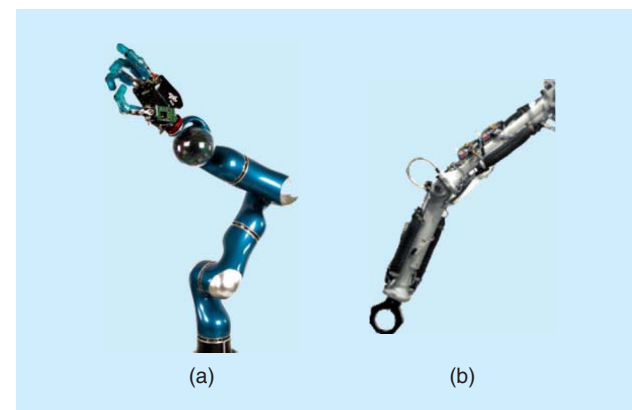


Figure 3. (a) The DLR lightweight robot arm and hand [77] and (b) the Stanford Safety Robot [42].

operating environment that is often passive results in an overall passive system whose Lyapunov stability is always guaranteed. Passive controller designs for domestic robot manipulators have often been addressed together with interaction control in a unified scheme to achieve a compliant, asymptotically stable, and robust manipulator [78], [102], [103].

Safety-aware control schemes that incorporate safety metrics in a controller design are also proposed in the literature. Focusing on collision risks to a human user, these controllers utilize a given safety metric to detect possible unsafe situations and use the controller to ensure that the acceptable safety levels defined in the metrics are achieved to avoid possible injuries. Using impact potential as a safety metric, [46] proposes an impact potential controller for a multiple-DOF manipulator. In this hierarchical controller design approach, the resulting safety status of a high-level motion controller torque output is evaluated according to the metric by a protective layer controller and clipped to an acceptable level in case of a possible unsafe condition. Using energy levels that cause failure of the cranial and spinal bones as a safety criterion, [104] proposes an energy regulation control that modifies the desired trajectory of the controller to limit the overall energy of a manipulator. After analyzing soft-tissue injuries and their relation with robot parameters, [59] proposes a velocity shaping scheme, which ensures that possible sharp contact with a multiple-DOF rigid robot will not result in unacceptable injury to a human user.

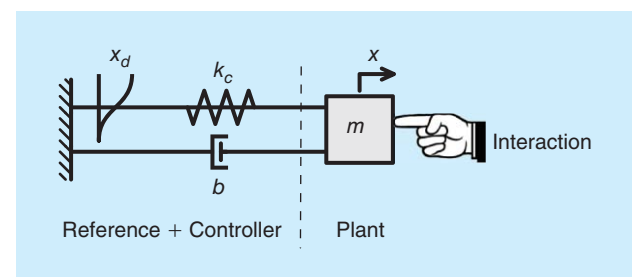


Figure 4. Impedance-controlled system.

Controller design can also increase postcollision safety by including a collision detection and reaction strategy. Using model-based analysis, [105] defines an energy-based collision detection signal using a disturbance observer and identified a number of reaction strategies to both stiff and compliant robots.

Conclusions

The previous sections presented different safety metrics and safety-related issues in mechanical design, actuation, and controller design of domestic robots. Although mechanical and controller subsystems are treated separately in this article, it is important to note that safety also depends on the interaction between the components making up the complete robot. For example, a failure in the sensory unit is a risk not only in the sensing aspect, but it also has consequences in the motion planning or control. Such propagation of risks is essential and must be detailed in the risk assessment level of the safety analysis.

Continuous improvements in risk elimination or reduction designs are not possible without suitable safety metrics that can be used for validation. These metrics are needed not only for collision but also for other feasible risks in domestic robotics. A number of collision-focused safety metrics for domestic robots were discussed in this article, and an experimental comparison of these metrics that follows a standardized testing procedure is essential to defining a universally acceptable safety metric for collision risks in domestic robotics. A groundwork study toward a standardized safety evaluation of domestic robots for collision risks was performed at a crash-test facility in [106] and [107].

Lightweight and compliant manipulators are the mechanical designs of choice in domestic robotics. Ongoing research on mechanical design and actuation to achieve better-performing domestic robots should ensure that safety requirements are not violated as well. Control systems should also keep up with mechanical design and actuation advancements to guarantee stability and provide acceptable manipulation capability.

References

- [1] J. E. Speich and J. Rosen, "Medical robotics," in *Encyclopedia of Biomaterials and Biomedical Engineering*, G. Wnek and G. Bowlin, Eds. New York: Marcel Dekker, 2004, pp. 983–993.
- [2] S. Najarian, M. Fallahnezhad, and E. Afshari, "Advances in medical robotic systems with specific applications in surgery—A review," *J. Med. Eng. Technol.*, vol. 35, no. 1, pp. 19–33, 2011.
- [3] R. Taylor, A. Menciassi, G. Fichtinger, and P. Dario, "Medical robotics and systems," in *Springer Handbook of Robotics*, B. Siciliano and O. Khatib, Eds. Berlin Heidelberg, Germany: Springer-Verlag, 2008, pp. 1199–1222.
- [4] S. Tadokoro, F. Matsuno, H. Asama, M. Onosato, K. Osuka, T. Doi, H. Nakanishi, I. Noda, K. Suzumori, T. Takamori, T. Tsubouchi, Y. Yokokohji, and M. Murata, "An overview of the DDT project," in *Rescue Robotics*, S. Tadokoro, Ed. New York: Springer-Verlag, 2009, pp. 17–31.
- [5] A. Birk and S. Carpin, "Rescue robotics—A crucial milestone on the road to autonomous systems," *Adv. Robot. J.*, vol. 20, no. 5, pp. 595–695, 2006.
- [6] R. Murphy, J. Kravitz, S. Stover, and R. Shoureshi, "Mobile robots in mine rescue and recovery," *IEEE Robot. Automat. Mag.*, vol. 16, pp. 91–103, June 2009.
- [7] K. Wyrobek, E. Berger, H. van der Loos, and J. Salisbury, "Towards a personal robotics development platform: Rationale and design of an intrinsically safe personal robot," in *Proc. IEEE Int. Conf. Robotics Automation*, May 2008, pp. 2165–2170.
- [8] J. Bohren, R. B. Rusu, E. G. Jones, E. Marder-Eppstein, C. Pantofaru, M. Wise, L. Mosenlechner, W. Meeussen, and S. Holzer, "Towards autonomous robotic butlers: Lessons learned with the PR2," in *Proc. IEEE Int. Conf. Robotics Automation*, Shanghai, China, May 2011, pp. 5568–5575.
- [9] M. Hans, B. Graf, and R. Schraft, "Robotic home assistant Care-O-Bot: Past-present-future," in *Proc. Conf. IEEE Int. Workshop Robot Human Interactive Communication*, 2002, pp. 380–385.
- [10] H. Iwata and S. Sugano, "Design of human symbiotic robot TWENDY-ONE," in *Proc. IEEE Int. Conf. Robotics Automation*, May 2009, pp. 580–586.
- [11] T. Ishida, Y. Kuroki, and J. Yamaguchi, "Mechanical system of a small biped entertainment robot," in *Proc. IEEE/RSJ Int. Conf. Intelligent Robots Systems*, Oct. 2003, vol. 2, pp. 1129–1134.
- [12] C. Harper and G. Virk, "Towards the development of international safety standards for human robot interaction," *Int. J. Social Robot.*, vol. 2, no. 3, pp. 229–234, 2010.
- [13] Y. Yamada and Y. Ota, "Novel activity on international safety standardization for personal care robots," in *Proc. ICCAS-SICE*, Aug. 2009, pp. 1882–1883.
- [14] PHRIENDS. (2011, July). Physical human-robot interaction: Dependability and safety. [Online]. Available: <http://www.phriends.eu/>
- [15] ROSETTA. (2011, July). Robot control for skilled execution of tasks in natural interaction with humans; based on autonomy, cumulative knowledge and learning. [Online]. Available: <http://www.fp7rosetta.org/>
- [16] SAPHARI. (2012, Aug.). Safe and autonomous physical human-aware robot interaction. [Online]. Available: <http://www.saphari.eu/>
- [17] NEDO. (2011, Oct.). Nedo safety verification technology project. [Online]. Available: <http://www.nedo.go.jp>
- [18] KUKA. (2011, July). Kuka safe robot. [Online]. Available: <http://www.kuka-robotics.com>
- [19] ABB. (2009, July). Safemove—Next generation in robot safety. [Online]. Available: <http://www.abb.com>
- [20] Baxter. (2013, July). Rethink robotics. [Online]. Available: <http://www.rethinkrobotics.com/products/baxter/>
- [21] Mekabot. (2011, July). Human-safe robot. [Online]. Available: <http://mekabot.com/>
- [22] R. Alami, A. Albu-Schäffer, A. Bicchi, R. Bischoff, R. Chatila, A. D. Luca, A. D. Santis, G. Giralt, J. Guiochet, G. Hirzinger, F. Ingrand, V. Lippiello, R. Matrone, D. Powell, S. Sen, B. Siciliano, G. Tonietti, and L. Villani, "Safe and dependable physical human-robot interaction in anthropic domains: State of the art and challenges," in *Proc. IROS Workshop on pHRI—Physical Human-Robot Interaction in Anthropic Domains*, A. Bicchi and A. D. Luca, Eds. Beijing, China: IEEE, Oct. 2006.
- [23] A. D. Santis, B. Siciliano, A. D. Luca, and A. Bicchi, "An atlas of physical human-robot interaction," *Mechanism Machine Theory*, vol. 43, no. 3, pp. 253–270, 2008.
- [24] O. Ogorodnikova, "Human robot interaction: The safety challenge," Ph.D. dissertation, Dept. Mechatron., Opt. Eng. Inf., Budapest Univ. Technology and Economics, Budapest, Hungary, 2010.
- [25] B. Dhillon and A. Fashandi, "Safety and reliability assessment techniques in robotics," *Robotica*, vol. 15, no. 6, pp. 701–708, 1997.
- [26] J. Guiochet, D. Martin-Guillerez, and D. Powell, "Experience with model-based user-centered risk assessment for service robots," in *Proc. 2010 IEEE 12th Int. Symp. High-Assurance Systems Engineering*, Washington, DC, pp. 104–113.
- [27] (2010). Safety of machinery—General principles for design—Risk assessment and risk reduction. International Standard Organization-12100 [Online]. Available: www.iso.org
- [28] D. Smith and K. Simpson, *Safety Critical Systems Handbook: A Straightforward Guide to Functional Safety, IEC 61508 (2010 Edition) and Related Standards, Including Process IEC 61511 and Machinery IEC 62061 and ISO 13849*. Amsterdam, The Netherlands: Elsevier Science, 2010.
- [29] S. Lee and Y. Yamada, "Strategy on safety function implementation: Case study involving risk assessment and functional safety analysis for a power assist system," *Adv. Robot.*, vol. 24, no. 13, pp. 1791–1811, 2010.

- [30] S. Haddadin, S. Haddadin, A. Khoury, T. Rokahr, S. Parusel, R. Burgkart, A. Bicchi, and A. Albu-Schäffer, "A truly safely moving robot has to know what injury it may cause," in *Proc. IEEE/RSJ Int. Conf. Intelligent Robots Systems*, 2012, pp. 5406–5413.
- [31] (2006). Robots for industrial environments—Safety requirements. International Standard Organization-10218-1 [Online]. Available: www.iso.org
- [32] (2012). Safety requirements: Non-medical personal care robot. International Standard Organization-13482. [Online]. Available: www.iso.org
- [33] S. Haddadin, A. Albu-Schäffer, and G. Hirzinger, "Requirements for safe robots: Measurements, analysis and new insights," *Int. J. Robot. Res.*, vol. 28, nos. 11–12, pp. 1507–1527, 2009.
- [34] J.-J. Park, H.-S. Kim, and J.-B. Song, "Safe robot arm with safe joint mechanism using nonlinear spring system for collision safety," in *Proc. IEEE Int. Conf. Robotics Automation*, May 2009, pp. 3371–3376.
- [35] S. Haddadin, A. Albu-Schäffer, F. Haddadin, J. Rossmann, and G. Hirzinger, "Study on soft-tissue injury in robotics," *IEEE Robot. Automat. Mag.*, vol. 18, no. 4, pp. 20–34, 2011.
- [36] J. Versace, "A review of severity index," in *Proc. Stapp Car Crash Conf.*, 1971, pp. 149–170.
- [37] E. Gurdjian, J. Webster, and H. Lissner, "Observations on the mechanism of brain concussion, contusion, and laceration," *Surg. Gynecol. Obstet.*, vol. 101, pp. 680–690, Dec. 1955.
- [38] D. Gao and C. Wampler, "Head injury criterion," *IEEE Robot. Automat. Mag.*, vol. 16, no. 4, pp. 71–74, Dec. 2009.
- [39] A. Bicchi and G. Tonietti, "Fast and soft arm tactics: Dealing with the safety-performance trade-off in robot arms design and control," *IEEE Robot. Automat. Mag.*, vol. 11, no. 2, pp. 22–33, 2004.
- [40] S. Haddadin, A. Albu-Schäffer, and G. Hirzinger, "Safety analysis for a human-friendly manipulator," *Int. J. Social Robot.*, vol. 2, no. 3, pp. 235–252, 2010.
- [41] M. Zinn, O. Khatib, B. Roth, and J. K. Salisbury, "Playing it safe [human-friendly robots]," *IEEE Robot. Automat. Mag.*, vol. 11, no. 2, pp. 12–21, June 2004.
- [42] D. Shin, I. Sardellitti, and O. Khatib, "A hybrid actuation approach for human-friendly robot design," in *Proc. IEEE Int. Conf. Robotics Automation*, May 2008, pp. 1747–1752.
- [43] D. Shin, I. Sardellitti, Y.-L. Park, O. Khatib, and M. Cutkosky, "Design and control of a bio-inspired human-friendly robot," *Int. J. Robot. Res.*, vol. 29, no. 5, pp. 571–584, 2010.
- [44] O. Ogorodnikova, "How safe the human-robot coexistence is? Theoretical presentation," *Acta Polytech. Hungarica*, vol. 6, no. 4, pp. 51–74, 2009.
- [45] K. Ikuta, H. Ishii, and M. Nokata, "Safety evaluation method of design and control for human-care robots," *Int. J. Robot. Res.*, vol. 22, no. 5, pp. 281–297, 2003.
- [46] J. Heinzmann and A. Zelinsky, "Quantitative safety guarantees for physical human-robot interaction," *Int. J. Robot. Res.*, vol. 22, nos. 7–8, pp. 479–504, 2003.
- [47] J.-J. Park and J.-B. Song, "Collision analysis and evaluation of collision safety for service robots working in human environments," in *Proc. Int. Conf. Advanced Robotics*, June 2009, pp. 1–6.
- [48] M. V. Damme, P. Beyl, B. Vanderborght, R. V. Ham, I. Vanderniepen, A. Matthys, P. Cherelle, and D. Lefevere, "The role of compliance in robot safety," in *Proc. 7th IARP Workshop Technical Challenges Dependable Robots Human Environments*, 2010, pp. 65–71.
- [49] J. A. Newman, N. Shewchenko, and E. Welbourne, "A proposed new biomechanical head injury assessment function—The maximum power index," in *Proc. 44th Stapp Car Crash Conf.*, 2000, pp. 215–247.
- [50] F. DiLorenzo, *Power and Bodily Injury*. Warrendale, PA: Soc. Automotive Eng., 1976.
- [51] M. Rahimi, "Systems safety for robots: An energy barrier analysis," *J. Occupational Accidents*, vol. 8, no. 12, pp. 127–138, 1986.
- [52] J. L. Wood, "Dynamic response of human cranial bone," *J. Biomech.*, vol. 4, no. 1, pp. 1–12, 1971.
- [53] S. Margulies and K. Thibault, "Infant skull and suture properties: Measurements and implications for mechanisms of pediatric brain injury," *J. Biomech. Eng.*, vol. 122, pp. 364–371, Aug. 2000.
- [54] N. Yoganandan, F. Pintar, D. Maiman, J. Cusick, A. S. Jr, and P. Walsh, "Human head-neck biomechanics under axial tension," *Med. Eng. Phy.*, vol. 18, no. 4, pp. 289–294, 1996.
- [55] K. Saita, Y. Yamada, N. Tsuchida, K. Imai, H. Ikeda, and N. Sugimoto, "A failure-to-safety 'kyozon' system with simple contact detection and stop capabilities for safe human-autonomous robot coexistence," in *Proc. IEEE Int. Conf. Robotics Automation*, May 1995, vol. 3, pp. 3089–3096.
- [56] B. Povse, D. Koritnik, R. Kamnik, T. Bajd, and M. Munih, "Industrial robot and human operator collision," in *Proc. IEEE Int. Conf. Systems Man Cybernetics*, 2010, pp. 2663–2668.
- [57] M. Wassink and S. Stramigioli, "Towards a novel safety norm for domestic robotics," in *Proc. IEEE/RSJ Int. Conf. Intelligent Robots Systems*, 2007, pp. 3354–3359.
- [58] J. Park, S. Haddadin, J. Song, and A. Albu-Schäffer, "Designing optimally safe robot surface properties for minimizing the stress characteristics of human-robot collisions," in *Proc. 2011 IEEE Int. Conf. Robotics Automation*, May 2011, pp. 5413–5420.
- [59] S. Haddadin, S. Haddadin, A. Khoury, T. Rokahr, S. Parusel, R. Burgkart, A. Bicchi, and A. Albu-Schäffer, "On making robots understand safety: Embedding injury knowledge into control," *Int. J. Robot. Res.*, vol. 31, no. 13, pp. 1578–1602, 2012.
- [60] P. Sandin, *Robot Mechanisms and Mechanical Devices Illustrated* (TAB Robotics Series). New York: McGraw-Hill, 2003.
- [61] W. T. Townsend and J. K. Salisbury, "Mechanical design for whole-arm manipulation," in *Robots and Biological Systems: Towards a New Bionics?* (NATO ASI Series), P. Dario, G. Sandini, and P. Aebischer, Eds. Berlin, Germany: Springer, 1993, vol. 102, pp. 153–164.
- [62] G. Hirzinger, A. Albu-Schäffer, M. Hahne, I. Schaefer, and N. Sporer, "On a new generation of torque controlled light-weight robots," in *Proc. IEEE Int. Conf. Robotics Automation*, 2001, vol. 4, pp. 3356–3363.
- [63] A. De Luca, "Feedforward/feedback laws for the control of flexible robots," in *Proc. 2000 IEEE Int. Conf. Robotics Automation*, vol. 1, pp. 233–240.
- [64] S. Haddadin, K. Krieger, N. Mansfeld, and A. Albu-Schäffer, "On impact decoupling properties of elastic robots and time optimal velocity maximization on joint level," in *Proc. IEEE/RSJ Int. Conf. Intelligent Robots Systems*, 2012, pp. 5089–5096.
- [65] J. K. Salisbury, "Active stiffness control of a manipulator in cartesian coordinates," in *Proc. IEEE Conf. Decision Control Including Symp. Adaptive Processes*, Dec. 1980, vol. 19, pp. 95–100.
- [66] B. M. Jau, "Human-like compliance for dexterous robot hands," in *Proc. IFTOMM, 9th World Congr. Theory Machines Mechanisms*, Aug. 1995.
- [67] A. Albu-Schäffer, O. Eiberger, M. Grebenstein, S. Haddadin, C. Ott, T. Wimbock, S. Wolf, and G. Hirzinger, "Soft robotics," *IEEE Robot. Automat. Mag.*, vol. 15, no. 3, pp. 20–30, Sept. 2008.
- [68] R. Schiavi, A. Bicchi, and F. Flacco, "Integration of active and passive compliance control for safe human-robot coexistence," in *Proc. IEEE Int. Conf. Robot. Automation*, May 2009, pp. 259–264.
- [69] W. Wang, R. N. Loh, and E. Y. Gu, "Passive compliance versus active compliance in robot-based automated assembly systems," *Ind. Robot: Int. J.*, vol. 25, no. 1, pp. 48–57, 1998.
- [70] M. M. Williamson, G. A. Pratt, and F. R. Morgenthaler, "Series elastic actuators," in *Proc. IEEE/RJS Int. Conf. Intelligent Robots Systems*, 1995, pp. 399–406.
- [71] G. Tonietti, R. Schiavi, and A. Bicchi, "Design and control of a variable stiffness actuator for safe and fast physical human/robot interaction," in *Proc. IEEE Int. Conf. Robotics Automation*, 2005, pp. 526–531.
- [72] S. Wolf and G. Hirzinger, "A new variable stiffness design: Matching requirements of the next robot generation," in *Proc. IEEE Int. Conf. Robotics Automation*, May 2008, pp. 1741–1746.

- [73] A. Jafari, N. Tsagarakis, B. Vanderborght, and D. G. Caldwell, "A novel actuator with adjustable stiffness (AwAS)," in *Proc. IEEE/RSJ Int. Conf. Intelligent Robots Systems*, 2010, pp. 4201–4206.
- [74] L. Visser, R. Carloni, R. Unal, and S. Stramigioli, "Modeling and design of energy efficient variable stiffness actuators," in *Proc. IEEE Int. Conf. Robotics Automation*, May 2010, pp. 3273–3278.
- [75] C. English and D. Russell, "Implementation of variable joint stiffness through antagonistic actuation using rolamite springs," *Mech. Mach. Theory*, vol. 34, no. 1, pp. 27–40, 1999.
- [76] S. Haddadin, A. Albu-Schaffer, O. Eiberger, and G. Hirzinger, "New insights concerning intrinsic joint elasticity for safety," in *Proc. IEEE/RSJ Int. Conf. Intelligent Robots Systems*, Oct. 2010, pp. 2181–2187.
- [77] A. Albu-Schäffer, S. Haddadin, C. Ott, A. Stemmer, T. Wimbock, and G. Hirzinger, "The DLR lightweight robot: Design and control concepts for robots in human environments," *Ind. Robot: Int. J.*, vol. 34, no. 5, pp. 376–385, 2007.
- [78] A. Albu-Schäffer, C. Ott, and G. Hirzinger, "A unified passivity-based control framework for position, torque and impedance control of flexible joint robots," *Int. J. Robot. Res.*, vol. 26, no. 1, pp. 23–39, 2007.
- [79] M. Grebenstein, A. Albu-Schaffer, T. Bahls, M. Chalon, O. Eiberger, W. Friedl, R. Gruber, S. Haddadin, U. Hagn, R. Haslinger, H. Hoppner, S. Jorg, M. Nickl, A. Nothelfer, F. Petit, J. Reill, N. Seitz, T. Wimbock, S. Wolf, T. Wusthoff, and G. Hirzinger, "The DLR hand arm system," in *Proc. IEEE Int. Conf. Robotics Automation*, 2011, pp. 3175–3182.
- [80] M. Zinn, O. Khatib, and B. Roth, "A new actuation approach for human friendly robot design," in *Proc. IEEE Int. Conf. Robotics Automation*, Apr. 2004, vol. 1, pp. 249–254.
- [81] N. Ulrich and V. Kumar, "Passive mechanical gravity compensation for robot manipulators," in *Proc. IEEE Int. Conf. Robotics Automation*, Apr. 1991, vol. 2, pp. 1536–1541.
- [82] H.-O. Lim and K. Tanie, "Human safety mechanisms of human-friendly robots: Passive viscoelastic trunk and passively movable base," *Int. J. Robot. Res.*, vol. 19, no. 4, pp. 307–335, 2000.
- [83] T. Ishida and A. Takanishi, "A robot actuator development with high backdrivability," in *Proc. IEEE Conf. Robotics, Automation Mechatronics*, June 2006, pp. 1–6.
- [84] N. Lauzier and C. Gosselin, "3-DOF cartesian force limiting device based on the delta architecture for safe physical human-robot interaction," in *Proc. IEEE Int. Conf. Robotics Automation*, May 2010, pp. 3420–3425.
- [85] J. Craig, "Introduction to robotics: Mechanics and control," in *Series Addison-Wesley Series in Electrical and Computer Engineering: Control Engineering*. Englewood Cliffs, NJ: Pearson/Prentice Hall, 2005.
- [86] G. Zeng and A. Hemami, "An overview of robot force control," *Robotica*, vol. 15, no. 5, pp. 473–482, 1997.
- [87] G. Ferretti, G. Magnani, and P. Rocco, "Toward the implementation of hybrid position/force control in industrial robots," *IEEE Trans. Robot. Automat.*, vol. 13, no. 6, pp. 838–845, Dec. 1997.
- [88] J. de Schutter and H. van Brussel, "Compliant robot motion: II. A control approach based on external control loops," *Int. J. Robot. Res.*, vol. 7, pp. 18–33, July 1988.
- [89] T. Yoshikawa, "Dynamic hybrid position/force control of robot manipulators—Description of hand constraints and calculation of joint driving force," *IEEE J. Robot. Automat.*, vol. 3, no. 5, pp. 386–392, Oct. 1987.
- [90] S. Stramigioli, *Modeling and IPC Control of Interactive Mechanical Systems: A Coordinate-Free Approach* (Series Lecture Notes in Control and Information Sciences). New York: Springer-Verlag, 2001.
- [91] N. Hogan, "Impedance control—An approach to manipulation. I—Theory. II—Implementation. III—Applications," *ASME Trans. J. Dyn. Syst. Meas. Control B*, vol. 107, pp. 1–24, Mar. 1985.
- [92] S. Chan, B. Yao, W. Gao, and M. Cheng, "Robust impedance control of robot manipulators," *Int. J. Robot. Automat.*, vol. 6, no. 4, pp. 220–227, 1991.
- [93] A. Hace, K. Jezernik, and S. Uran, "Robust impedance control," in *Proc. IEEE Conf. Control Applications*, 1998, pp. 583–587.
- [94] R. Kelly, R. Carelli, M. Amestegui, and R. Ortega, "On adaptive impedance control of robot manipulators," in *Proc. IEEE Int. Conf. Robotics Automation*, 1989, pp. 572–577.
- [95] R. Luo, H. Huang, C. Yi, and Y. Perng, "Adaptive impedance control for safe robot manipulator," in *Proc. 9th World Congr. Intelligent Control and Automation*, 2011, pp. 1146–1151.
- [96] J. Buchli, F. Stulp, E. Theodorou, and S. Schaal, "Learning variable impedance control," *Int. J. Robot. Res.*, vol. 30, no. 7, pp. 820–833, 2011.
- [97] Z.-H. Jiang, "Impedance control of flexible robot manipulators," in *Robot Manipulators*, M. Ceccarelli, Ed. Rijeka, Croatia: In-Tech, 2008, pp. 211–224.
- [98] L. Biagiotti, H. Liu, G. Hirzinger, and C. Melchiorri, "Cartesian impedance control for dexterous manipulation," in *Proc. IEEE/RSJ Int. Conf. Intelligent Robots Systems*, 2003, vol. 4, pp. 3270–3275.
- [99] Z. Chen, N. Lii, M. Jin, S. Fan, and H. Liu, "Cartesian impedance control on five-finger dexterous robot hand DLR-HIT II with flexible joint," in *Intelligent Robotics and Applications* (Series Lecture Notes in Computer Science), vol. 6424, H. Liu, H. Ding, Z. Xiong, and X. Zhu, Eds. Berlin Heidelberg, Germany: Springer-Verlag, 2010, pp. 1–12.
- [100] R. Ortega, A. van der Schaft, B. Maschke, and G. Escobar, "Interconnection and damping assignment passivity-based control of port-controlled Hamiltonian systems," *Automatica*, vol. 38, no. 4, pp. 585–596, 2002.
- [101] C. Secchi, S. Stramigioli, and C. Fantuzzi, *Control of Interactive Robotic Interfaces: A Port-Hamiltonian Approach* (Series Springer Tracts in Advanced Robotics). New York: Springer-Verlag, 2007.
- [102] T. Wimboeck, C. Ott, and G. Hirzinger, "Passivity-based object-level impedance control for a multifingered hand," in *Proc. IEEE/RSJ Int. Conf. Intelligent Robots Systems*, 2006, pp. 4621–4627.
- [103] A. Zanchettin, B. Lacevic, and P. Rocco, "A novel passivity-based control law for safe human-robot coexistence," in *Proc. IEEE/RSJ Int. Conf. Intelligent Robots Systems*, 2012, pp. 2276–2281.
- [104] M. Laffranchi, N. Tsagarakis, and D. Caldwell, "Safe human robot interaction via energy regulation control," in *Proc. IEEE/RSJ Int. Conf. Intelligent Robots Systems*, Oct. 2009, pp. 35–41.
- [105] A. D. Luca, A. Albu-Schaffer, S. Haddadin, and G. Hirzinger, "Collision detection and safe reaction with the DLR-III lightweight manipulator arm," in *Proc. IEEE/RSJ Int. Conf. Intelligent Robots Systems*, Oct. 2006, pp. 1623–1630.
- [106] S. Haddadin, A. Albu-Schaffer, M. Frommberger, J. Rossmann, and G. Hirzinger, "The 'DLR crash report': Towards a standard crash-testing protocol for robot safety—Part I: Results," in *Proc. IEEE Int. Conf. Robotics Automation*, 2009, pp. 272–279.
- [107] S. Haddadin, A. Albu-Schaffer, M. Frommberger, J. Rossmann, and G. Hirzinger, "The 'DLR crash report': Towards a standard crash-testing protocol for robot safety—Part II: Discussions," in *Proc. IEEE Int. Conf. Robotics Automation*, 2009, pp. 280–287.

Tadele Shiferaw Tadele, Robotics and Mechatronics, Faculty of Electrical Engineering, Mathematics, and Computer Science, University of Twente, The Netherlands. E-mail: t.s.tadele@utwente.nl; metitad@gmail.com.

Theo J.A. de Vries, Robotics and Mechatronics, Faculty of Electrical Engineering, Mathematics, and Computer Science, University of Twente, The Netherlands. E-mail: t.j.a.devries@utwente.nl.

Stefano Stramigioli, Robotics and Mechatronics, Faculty of Electrical Engineering, Mathematics, and Computer Science, University of Twente, The Netherlands. E-mail: s.stramigioli@utwente.nl.

Rethinking the Machines in Which We Live

A Multidisciplinary Course in Architectural Robotics



By Apoorva D. Kapadia, Ian D. Walker, Keith Evan Green, Joe C. Manganelli, Henrique Houayek, Adam M. James, Venkata Kanuri, Tarek Mokhtar, Ivan Siles, and Paul Yanik

Attempting to bridge the educational gap between robotics and other disciplines is always challenging, but it is likely to provide interesting results. This point is exemplified in a graduate-level class, architectural robotics, enrolling students from electrical, computer, and mechanical engineering as well as human factors psychology and architecture [1]. Architectural

robotics is formally defined in [2] as “intelligent and adaptable built environments (featuring embedded robotic components) that sense, plan, and act.” In [2], which sets out a vision for architectural robotics, Gross and Green assert that “perhaps the greatest challenge for architectural robotics is defining the community” and ask, “who is cultivating this line of research?” We believe robotics professionals should play a major role in defining and leading this emerging field. The class discussed in this article is aimed at defining the scope of the field and its community from a robotics perspective.

Digital Object Identifier 10.1109/MRA.2013.2287456
Date of publication: 24 June 2014

The class is cross-listed in the Electrical and Computer Engineering and Architecture Departments at Clemson University and engages multidisciplinary teams of students in open-ended hardware-based projects focusing on robotic systems working in, or augmenting, the built environment. While the classical education in these disciplines highlights the design as a key element, what design means and how students are exposed to it differ significantly between each population.

The motivation of the class is to promote collaborative research between the two title fields; this is a promising area but has so far been elusive in

Robotics still awaits that singularity that will make robot use widespread and ubiquitous in people's everyday existence.

tion, domestic environments, and education [3, Ch. 52–55], robots are still largely restricted to industrial, remote, and hazardous environments [3, Ch. 42 and 47]. Robotics still awaits that singularity that will, as predicted in innumerable science fiction stories, make robot use widespread and ubiquitous in people's everyday existence.

One engineered product familiar to all and often overlooked by technologists is the built environment inhabited by humans at wide-ranging scales, from that of furniture to that of the metropolis. In shaping the built environment, architects collaborate with engineering disciplines outside of robotics (e.g., structural and civil engineers) to bring the added value of form making (aesthetics), framing of human activity (programming), and technical performance/expression (tectonics). The tectonic aspect of the built environment has long been advanced by architects and consulting engineers and has intensified in recent years with the advent of increasingly advanced technologies and methods, particularly as a result of the information technology revolution. Curiously, despite this advancement, there has been almost no incursion of robotics or its elements into architecture or built environments. Architecture as a field has a long and rich history of innovation [4], and its economic impact vastly overshadows that of robotics. Widespread adoption of robotic technologies within architecture would likely have a major positive impact on robotics.

Robotics Interfacing with Architecture

Two highly desirable activities arise naturally from the above-mentioned discussion: 1) identification of ways in which robotics, in its current state, can transition usefully into architecture and 2) identification and removal of the key barriers currently preventing such transitions.

We believe the key barriers to progress in 2) are interdisciplinary communication and, more importantly, the lack of corresponding education at the graduate level. The architectural robotics course is thus aimed, at the high level, to be at the intersection of architecture and engineering and, at the detailed level, to develop common concepts necessary for creating new robotic environments.

Visions and early investigations on robotics interfacing with architecture have begun to emerge. Mitchell [5] postulated that in the near future, “our buildings will become... robots for living in.” Subsequent efforts have concentrated on either adding sensory/computational elements to existing architecture (smart buildings) [6], [7] or introducing self-contained robots into existing spaces [3, Ch. 55]. The second approach appears to be the obvious way to introduce robotics into architecture. However, it is argued here that a more interesting (and practical) approach involves a tighter coupling of the fields, applying robotics techniques and theory to move the mass that forms the core shape of the environment.

The explicit goals of this graduate-level course at Clemson University are to explore the boundary between robotics and architecture and promote creativity at their intersection while addressing the challenge of widely differing expectations between the engineers, architects, and psychologists. All of the course activities are designed to be open ended, with the key objects being the creative process and design methodology rather than any specific end product. This has led to valuable insight into the nature of inherent disciplinary biases and the surprises that can result when the creative strengths of the two fields are suitably catalyzed.

This course is not the first effort aimed at combining engineering and other disciplines in graduate classes [8]. However, it is unique in that it focuses on the robotic elements as an integral part of environmental design (e.g., in plumbing, air conditioning, etc.) as opposed to being introduced into a previously built space. The first offering of the class in the spring 2009 semester was found to be the richest in terms of new pedagogical information and is thus the focus

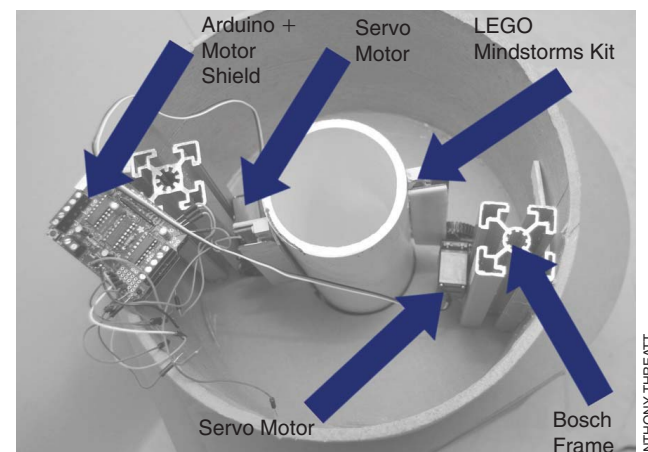


Figure 1. An example of architectural robotics: a wirelessly controlled rack and pinion system used to adjust the height of a table surface. (Photo courtesy of Anthony Threatt.)

ANTHONY THREATT

of this article. The extensive feedback and suggestions (mostly oral) provided by the students factored greatly into the design and structure of the class in subsequent semesters.

Course Structure, Hardware Technologies, and Components

The underlying philosophy for the class is to allow students from each discipline to experience the creative efforts and methodology of the other discipline(s) firsthand while simultaneously using their own disciplinary expertise. We believe that joint exploration of a project using hardware (at a reduced scale given the nature and cost of most architectural applications) is the most effective approach. Since this philosophy entails an intensive collaboration of architects and engineers, a commonly usable hardware basis for the class projects was required.

An inexpensive and readily available platform, Arduino [9], had previously been used by both architects and engineers [10]; hence, its selection was a natural choice. A varied suite of sensors, actuators, and construction material was made available, including stepper and servomotors, light-emitting diodes (LEDs), infrared and optical sensors, and limit switches, as well as LEGO products, Bosch framing components, card paper, etc., some of which are shown in Figure 1. The purchase of more specialized components was sanctioned depending on the requirements of the project and their potential for long-term use in the class.

Visualization software and rapid prototyping tools were also extensively used. The architects made virtual 3-D models using Rhino and AutoCAD and physical models using CNC laser cutters and milling machines. This process expedited critical analyses, allowing for quicker identification and mitigation of various challenges posed during the design and development stages. The students did not have external support in the form of departmental engineers or technicians, although there was no ban on seeking help. However, most of the students had experience with machining tools, and they were encouraged to assist one another.

The size of the class was kept small due to the limited availability of laboratory space, machining equipment, and components, and thus no project management tools were required. However, such tools could be used if the scope, time frame, and complexity of the projects were altered. The class was designed to be an active learning experience, partly due to the hands-on approach required from the students toward project design and delivery as well as an experiment in the studio technique used extensively in architecture, similar to [11].

The primary method of assessment was a set of three multiweek projects. Students were paired together in two-person engineer–architect teams (also engineer–psychologist teams in subsequent iterations); the combination was changed for each project to maximize the diversity of interaction and expose each student to varying thought processes. This was essential given the varying student experience levels; registrants ranged from first-year graduate students (one engineering and

one architecture student) to Ph.D. candidates (one architecture student). The students were assigned project partners and given the project theme, requirements, and execution time frame (one to two weeks were set aside for project conceptualization). The students were expected to brainstorm and come up with project ideas, which would be presented to the class. Upon satisfactory presentation of the aim, feasibility, and scope, the project would be given the go-ahead, with weekly progress reports and milestone demonstrations leading up to the final presentation. At the end of each project, the students had to upload project details, scenarios, images, videos, and source code to a dedicated class work group.

Articles and papers were assigned to be discussed in each class, typically alternating between architecture and robotics as subjects. The readings started with tutorials on definitions, research, and practices of architectural robotics ([12], [13], and [5, Ch. 4]) before delving into the more traditional aspects of both fields [14], leading to contemporary paradigms [15], and finally coming full circle to thoughts of the future and the integration of systems in an increasingly digital age [articles from *IEEE Spectrum Special on the Singularity* [16] (the authors can be contacted for a full list of articles)]. To further the collaborative environment, the students were asked to lead discussions on each article in the presence of the instructors. In addition to these discussions, the instructors taught introductory-level material in their respective areas, including multimedia presentations and videos, to give students a better idea of both fields. The students were graded based on discussion participation, project design, integration, and demonstration and

At the end of each project, the students had to upload project details, scenarios, images, videos, and source code to a dedicated class work group.

work group.

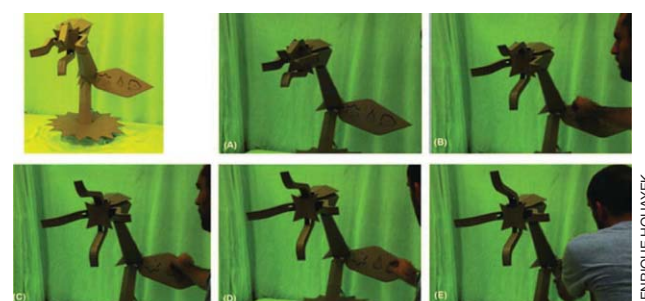
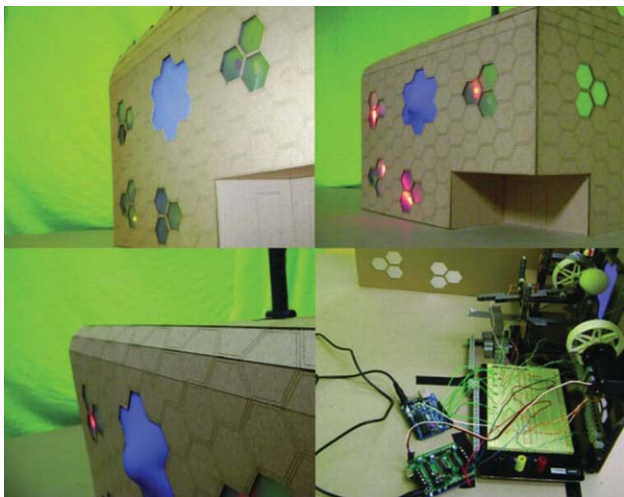


Figure 2. Project 1—Interactive Flower: this project attempted to cultivate children's creativity by providing a hands-on interactive experience about the natural diurnal cycle of a flower while also helping them associate geometric shapes. Initially, in a closed-petal configuration, the flower opens up fractionally as an ingredient (geometric block) is correctly placed. The flower blooms fully when all three pieces are correctly placed and closes fractionally with each piece's removal, for immediate reuse. (Photo courtesy of Henrique Houayek.)



PAUL YANIK

Figure 3. Project 2—Shelter in a Storm: this project aimed to design building skins that could morph from conventional shapes to more aerodynamic ones to dissipate high wind forces such as hurricane winds. A wind-speed sensor would detect the presence of sustained wind gusts above a designated safe threshold, activating the morphing mechanism. The conventionally shaped building would then self-adjust components of its external surface to project a convex face toward the oncoming wind. The curved surfaces would dissipate the winds and thereby reduce the force on the underlying structure as with domed buildings and safeguarding the structure.

closeness of projects to the proposed concept, although project deliverables were weighted heaviest.

Project Experiences and Summaries

Each project had an overarching theme with goals to integrate the thought processes of both disciplines to find a balanced solution (details of the individual projects can be found in [1]). The aim of the first project from both the students' and instructors' perspectives was to familiarize everyone with Arduino and with one another. This was the shortest and least demanding project in terms of deliverables, but it was challenging due to the possibility of a culture clash in approaches.



TAREK MOKHTAR

Figure 4. Project 2—The Directing Leaf: the leaf was designed to work with existing urban infrastructure in the event of tornadoes around or within city limits. In the event of a tornado sighting, the leaf would light up and point the population toward shelters and safer areas. A radio link to a receiver and speaker system would play area-specific warning messages to complement the visual aids. Upon relaxation of the situation, the leaves would return to their resting state and the speaker system would update the population. This system was designed to blend into the environment, though not inconspicuously, and was also capable of lighting up street blocks during festive seasons.

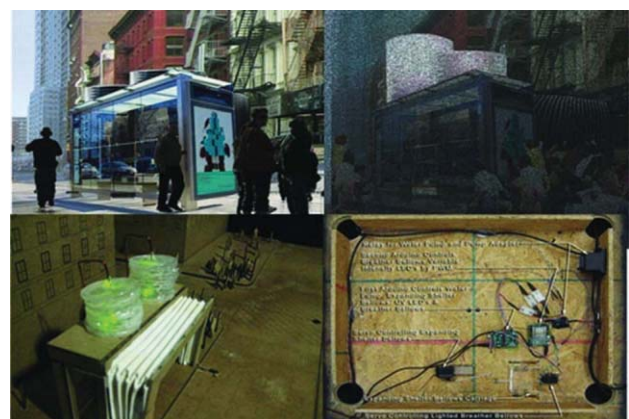


TAREK MOKHTAR

Figure 5. Project 2—The Directing Leaf: schematic diagram of the leaf on trees on a city block.

An initial difficulty was due to the inherent differences in the meaning of the word *design* as understood by architects and engineers. Architects generally consider design to be a qualitative phenomenological experience appealing to the aesthetic sensibilities, while, to engineers, the word is a representation of a quantitative process for a specified performance-related goal focusing on functionality; the human factors psychologists' definition lies somewhere between these two. The instructors hoped that after the initial shock caused by students' contrasting expectations had subsided, the architects and engineers would work out an acceptable compromise, minimally sacrificing performance, or aesthetic quality.

Project 1 required a system design incorporating off-the-shelf toys to engage children, with no constraints on age group (LEGO blocks were used in the exemplary project in Figure 2), to force dialog between teammates. This allowed the students to develop relatively simple systems while exploring the capabilities of Arduino. This project was designed to create a relaxed environment to spark the creativity and collaboration of both fields. From the students'



JOE MANGANELLI

Figure 6. Project 2—The Particulate Control and Air Purifier (pCAP): added onto existing city infrastructure, pCAP was designed as an urban response mechanism to minimize the dispersion of airborne particulates and gases while providing shelter and purified air to those trapped within the noxious atmosphere. Augmented bus shelters would function as glowing beacons in the dusty haze, where purified air would be available. The pCAP used modified fire suppression sprinkler heads mounted on building parapets and actuated by gas and vibration sensors to produce atmospheric mist to trap the particulates.

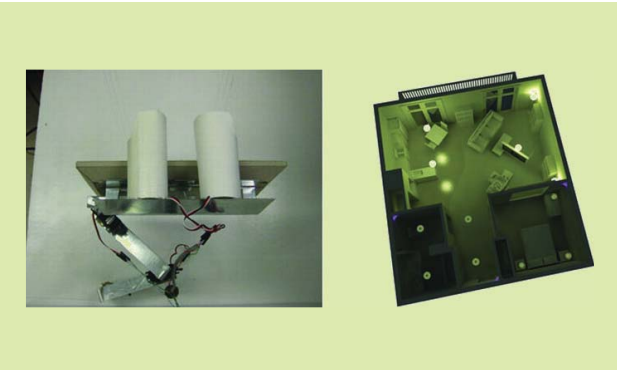


Figure 7. Project 3—Redundant Robot Manipulator and Environment for ReLiS: ReLiS sought to automate heavy use and critical systems in living units based on the needs of occupants. It consists of a television mounted on a manipulator, which tracks the position of the occupant around the unit, while also providing position-based intelligent lighting based on the zonal location of the occupant.

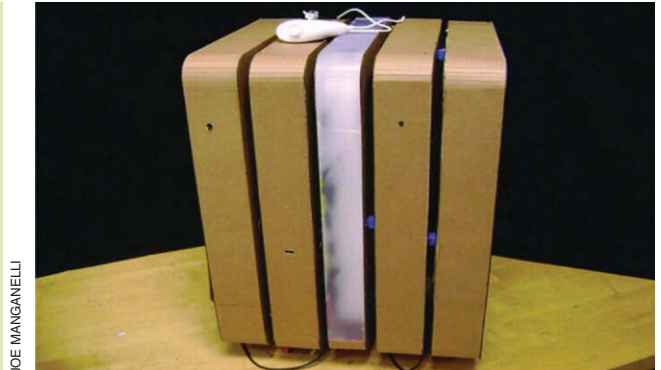


Figure 9. Project 3—The mKare Side Table: the mKare is an interactive mobile unit built to aid the physically challenged in their daily lives. It was fitted with omnidirectional wheels, powered by servo motors, and controlled by a Wii remote to ensure movement in all directions. The sides provide sturdy flaps that rise up and extend themselves whenever desired, providing more workspace for daily activities while also keeping the overall size of the table compact.



Figure 8. Project 3—The Emotionally Together Armature (ET): ET consists of an overhead two-degree-of-freedom robot crane capable of motion along the length and width axes of a single room. A hanging armature picks up and deposits objects while using infrared sensors to avoid obstacles. ET was proposed with an option to minimize aspects of loneliness by analyzing the occupant's voice for emotional affect and then providing an automated response.

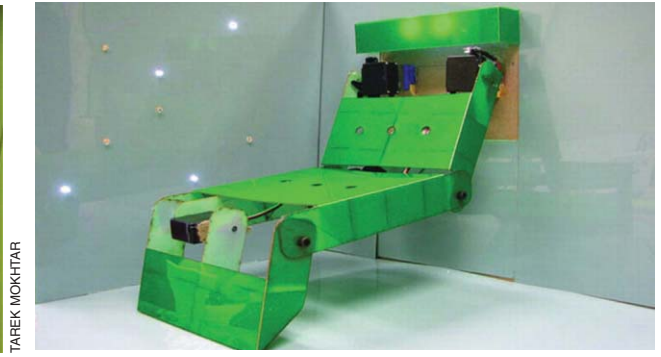


Figure 10. Project 3—Interactive Inflatable Furniture (IIF): addressing the difficulty for senior citizens in performing mundane activities such as getting out of bed or off of a chair, IIF aimed to increase the quality of life of both healthy elderly individuals as well as those with impaired mobility. Thus, the IIF was constructed of balloons overlaying a rigid three-link robot manipulator forming a chair that changes shape based on the preference of the user.

responses, it was found that this project represented a greater learning curve for architects than for engineers due to the limited exposure of architects to the concept of programming and sensor/actuator interfacing. While these projects demonstrated the ways in which robotics might actively support the physical environment, they still remained robots within environments. The intellectual growth was significant for the architects but not for the engineers.

The goal of Project 2 was to expand the range of possibilities, requiring the exploration of how robotics could augment existing architecture or provide a paradigm shift in architectural design. This project was meant to allow the architects to showcase their skills, specifically for urban disaster detection/management with no constraints on scope, scale, or components. These projects were more environmental than robotic, and therefore, the learning curve was greater for the engineers, as their systems were required to operate within the architectural envelope. The architects played leading roles, both in environmental analysis and, using knowledge gained from Project 1, selection of sensors and actuators for the scale

models of the environments. The students reported that, in Project 2, there was a greater appreciation of one another's ideas, significantly less friction regarding approach, and less time needed for brainstorming compared to Project 1, which allowed for more time to develop and refine concepts.

The results (from the instructors' perspectives) were innovative and thought provoking. In contrast to the Project 1 efforts, the Project 2 visions (shown in Figures 3–6) literally expanded the environmental space at the cost of practical feasibility. With the exception of the directing leaf (Figures 4 and 5), it is difficult to imagine the technologies presented being viably and commercially scaled to the size of

Widespread adoption of robotic technologies within architecture would likely have a major positive impact on robotics.

the environments studied. Nevertheless, at this stage, the instructors noted that the architects were fully engaged and the engineers were perceiving the available architectural palette.

The next step was to challenge both disciplines simultaneously to create a fully synergistic system, a truly architectural robotics product. In contrast to Projects 1 and 2, Project 3 incorporated constraints, with feasibility as a consideration but

The field of architectural robotics promises to support and enhance human needs and desires.

person's transition into aged care [18] to try to tackle a big global social problem.

This project was allotted the maximum amount of time (five weeks, as opposed to the two weeks given for Project 1 and four weeks for Project 2) to allow the groups to create complex environments, refine the mechanisms, and truly integrate their systems. It also resulted in the closest collaborations in the class, as noted by the students. The engineers freely suggested architectural innovations, while the architects were comfortable and confident in recommending sensing and actuation mechanisms, as evidenced by the students' oral conceptual presentations. Simultaneously, the students and instructors noted less time being taken for analyses as the semester progressed, with insightful comments from both sides on other students' subject matter.

The instructors found that, at a high level, the line between the two individual disciplines became increasingly blurred and the students ceased to be engineers or architects and simply became members of the group. The architects gained insight into robot modeling—kinematics and dynamics, sensor fusion, and algorithmic considerations—while the engineers developed a greater appreciation for the incorporation of aesthetics and form into a system along with the composition of space.

All Project 3 designs, in one way or another, were about changing the shape of the human environment. These projects either involved applications/adaptations of robotics manipulator concepts or the mobile robot paradigm. Every

project required user sensing and localization within the home setting. While the robotic technologies were not groundbreaking in and of themselves, it could be argued that the applications certainly were and that they could just as easily be applied to more conventional home or work settings. It is important to note that these environments were created from the ground up, with the robotic components already embedded in them (Figures 7, 8, and 10) as opposed to being added to an existing architectural structure like in Projects 1 and 2 (providing ideas for 2) in Remark 1).

The outcomes of the collaborative process produced concepts of high potential. This is noteworthy due to the open-ended nature of these research problems, hinting that although high-tech devices and computers are now ubiquitous, robotics technology has not yet realized its potential in the home environment as it has in almost every other aspect of our lives [19].

Assessment and Evaluation

The evaluation of the success and impact of the class was made at several levels, most of which were qualitative or oral. From the instructors' perspectives, the class (and its successors) surpassed expectations in its primary goal of producing a group of graduate students who were well qualified to conduct research in architectural robotics. Of the eight students in this first class, four have completed Ph.D. theses in the area (three architects and one engineer) and one student is working on a technology closely associated with the architectural robotics paradigm. A similar ratio of students in subsequent classes has followed into research in architectural robotics, as highlighted in Table 1. In the fall 2010 and 2011 offerings of the class, the issue of having fewer nonengineers than engineers was mitigated by the presence of architecture students who had previously taken the class. These students served as teaching assistants, stepping in to work actively on some projects while simultaneously consulting on others. This interest and expertise has seeded and catalyzed the highly successful research program of the two class instructors over the past several years, including a multiyear grant awarded by the U.S. National Science Foundation to conduct fundamental research into robot environments for aging in place; the initial foundational ideas, research, and student involvement for this were laid during the initial class offering.

Throughout the course, some key fundamental research insights emerged. For example, in the third group of projects, the innovations in the robot mechanisms proposed

were minor. However, the way the projects were deployed in the environment was novel, especially the interaction and communication with the people in it. The nontraditional use of lighting was particularly noted. This highlighted the point that architectural robotics is fundamentally about people.

Often, traditional architecture designs are beautiful yet sterile envelopes and the architect exits the process before or when people

Table 1. Students in architectural robotics offerings.

Class Offerings	Engineers	Architects	Other Disciplines	Theses
Spring 2009	4	4	—	5
Fall 2009	3	2	1	2
Fall 2010	5	3	—	1
Fall 2011	6	1	1	2
Fall 2012	3	5	—	N/A

enter (and often wish to modify) the built environment. One important lesson from the class for the architects was that built environments ought to have a temporal existence based around the people who inhabit them. For the engineers, a key lesson was that robotics should be more than (and different from) the precise but insensitive instruments seen in industry. With people at the core of the design, the emphasis was placed on adaptability and compliance rather than precision and repeatability. Overall, the collective efforts of the class stressed the notion that simply bringing a complete robot, such as a humanoid, into an existing environment, the classical goal for roboticists, may not necessarily be the best solution. Instead, the notion of unpacking the humanoid and embedding parts of it appropriately into the environment, a key research concept that was expanded on in the research of the instructors [20], emerged during the course of this class.

While there was no obvious glass ceiling to shatter, the knowledge and understanding gained through this course are necessary for the advancement of both disciplines (architecture and robotics). Robotic technology is slowly developing toward ubiquitous domestic use, although the social and psychological implications for a robotic domestic space are not yet fully understood. In addition, the architecture and building industries are often slow adopters of cutting-edge technologies. While not a direct mandate, a part of the class directive is to hasten the fusion of architecture and robotics and simultaneously advance both fields.

By all accounts, the students found the experience of the class to be positive, especially considering that this was the first offering at Clemson University and not a requirement toward their degrees. They found the opportunity to collaborate with another department great and unique. In the students' own words, "the outcome of tighter integration as a result of the brainstorming sessions was generally achieved over the course of the class." It was noted that, in the final project, all of the students self-organized to further refine their ideas once the initial paradigms were developed. The students found that spending a significant amount of time outside the class working on the projects allowed them to learn from one another on the job and gave them a greater appreciation of one another's contributions and ideas. The students noted the usefulness of the idea evaluations before building each project, claiming that the "interim reviews to talk about the projects pushed the ideas about as far as we could take them." These reviews initially also served as arbitrations when the team members did not fully agree on the project design or needed to reduce the complexity. Almost no arbitration was required for the final project, while the first and second projects required some intervention to ensure that the scope and scale of the projects were achieved.

The students independently expressed surprise at the closeness with which they worked. Starting with the second project, they compiled unified lists of components and materials to be purchased. The work group created for the class was also noted to be helpful. While the instructors had access

to the work group, it was primarily used by the students as a resource for sharing basic code, choices of components, materials, and refining of scenarios or ideas.

It was also noted that confidence in the course improved over time, and a suggestion (as yet unimplemented) that the instructors consider the potential of making this a two-part, year-long course, as opposed to the current single semester offering, was tabled. The positive experience affected enrollment (the class has since been highly oversubscribed), although, in addition to space and equipment constraints, the instructors believe that the dynamics of the class works best in a reasonably small group of less than ten students. This is not to say that a similar class cannot be successful if it is larger elsewhere with other instructors.

One weakness identified (and still an issue in the fifth holding of the class) is a lack of a suitable introductory text for robotics. Existing texts are aimed at either the general public or engineering graduate students. We have not yet found an introduction to robotics suitable for a technically educated professional without an engineering background. Practical problems also resulted from the scale and hobby quality of the electronics used. Sensors and actuators were imprecise, poorly characterized, or underpowered, requiring ad hoc and time-consuming work-arounds to achieve the desired results. Partly due to this and the tight schedule, from the engineering perspective, the algorithms used were generally simple and open loop. Time was invested in postprocess documentation to highlight such difficulties to streamline the efforts of future students. In subsequent class offerings, this problem has been significantly reduced by having a graduate of the class serve as a teaching assistant. The student responses were also noteworthy in this regard, given that they all claimed to have put far more work into this course than their other courses. Some students even claimed to have worked longer hours for this course than any other course thus far, but, at the same time, they wanted more time to spend on the projects. This desire was only stated at the end of the course as the students began to reflect on their experiences. The students and instructors noted the lack of benchmarks for time frames in this regard, but this situation was rectified in future offerings.

In a short period, 15 weeks, students with very different backgrounds learned to work in unison with a common understanding.

Take Aways

In a short period, 15 weeks, students with very different backgrounds learned to work in unison with a common understanding. This resulted in new insight into the topic of architectural robotics and how to proceed when conducting research in the area. As the assignments evolved, what initially manifested itself as a problem was actually one of the greatest

benefits of interdisciplinary collaborations: the inherent mismatch of the capabilities and purviews of the respective team members. Initially, teams struggled with the desire to develop a project idea without a full awareness of how each partner could use his or her skills to create a successful system. Notably, stressing on collaboration brought forth innovative results not attainable by either partner working alone. Some of the resulting projects cannot be defined as either architecture or engineering, but rather a productive, compelling hybrid of both—an architectural robotic system.

The field of architectural robotics promises to support and enhance human needs and desires. The gradual embedding of robotics throughout the built environment will, in the coming decades, have a broad social impact as these technologies sustain and, in some cases, augment everyday work, school, and leisure activities. This course served as an early effort for rising robotics engineers and architects to learn from one another in the process of dealing with a hybrid of their traditional concerns. It can be postulated that the buildings of tomorrow will be actively responsive to various external forces, including weather, security, and human needs. The expansion of one field into the other is inevitable and offers the potential for engineers and architects working together to advance human needs and desires and safeguard the environment.

Acknowledgments

This work was supported in part by an NSF Grant IIS-0534423. This article was presented in part at the IEEE International Conference on Robotics and Automation, Anchorage, Alaska, May 2010 [1].

References

- [1] A. Kapadia, I. D. Walker, K. E. Green, J. Manganelli, H. Houayek, A. M. James, V. Kanuri, T. Mokhtar, I. Siles, and P. Yanik, "Architectural robotics: An interdisciplinary course rethinking the machines we live in," in *Proc. IEEE Int. Conf. Robotics Automation*, Anchorage, AK, 2010, pp. 48–53.
- [2] M. Gross and K. Green, "Architectural robotics, inevitably," *ACM Interact. Mag.*, vol. 19, no. 1, pp. 28–33, 2012.
- [3] B. Siciliano and O. Khatib, Eds., *Springer Handbook of Robotics*. Berlin Heidelberg, Germany: Springer-Verlag, 2008.
- [4] P. Vitruvius, *The Ten Books on Architecture*. Mineola, NY: Dover Publications, 25 B.C.
- [5] W. Mitchell, *E-Topia*. Cambridge, MA: MIT Press, 2000.
- [6] B. Johanson, A. Fox, and T. Winograd, "Inventing wellness systems for aging in place," *IEEE Pervasive Comput.*, vol. 2, no. 2, pp. 67–74, 2002.
- [7] N. Streitz, J. Geissler, and T. Holmer, "Roomware for cooperative buildings: Integrated design of architectural spaces and information spaces," in *Proc. Cooperative Buildings—Integrating Information, Organization Architecture*, Darmstadt, Germany, 1998, pp. 4–21.
- [8] M. Gross and E. Do, "Environments for creativity: A lab for making things," in *Proc. SIGCHI conf. Creativity Cognition*, Washington, D.C., 2007, pp. 27–36.
- [9] D. Mellis, M. Banzi, D. Cuartielles, and T. Igoe, "Arduino: An open electronic prototyping platform," in *Proc. Alt CHI*, San Jose, CA, 2007, pp. 1–11.
- [10] J. Braumann and S. Brell-Cokcan, "Digital and physical computing for industrial robots in architecture," in *Proc. Computer Aided Architectural Design Research Asia*, Hong Kong, China, 2012, pp. 317–326.
- [11] S. Kuhn, "Learning from the architecture studio: Implications for project-based pedagogy," *Int. J. Eng. Educ.*, vol. 17, nos. 4–5, Apr. 2001.
- [12] N. Negroponte, *Soft Architecture Machines*. Cambridge, MA: MIT Press, 1975.
- [13] K. Oosterhuis, *Towards an E-Motive Architecture*. Basel, Switzerland: Birkhauser Press, 2003.
- [14] L. Nocks, Ed., *The Robot: The Life Story of a Technology*. Baltimore, MD: Johns Hopkins Press, 2008.
- [15] C. Diana, "How I learned to stop worrying and love the hackers," *Interactions*, vol. 11, no. 2, pp. 44–48, Mar. 2008.
- [16] *IEEE Spectr. Special on the Singularity*, vol. 6, no. 45, June 2008.
- [17] E. Mynatt, I. Essa, and W. Rogers, "Increasing the opportunities for aging in place," in *Proc. Conf. Universal Usability*, Arlington, VA, 2000, pp. 65–71.
- [18] E. Dishman, "Inventing wellness systems for aging in place," *IEEE Computer*, vol. 37, no. 5, pp. 34–41, May 2004.
- [19] B. Gates, "A robot in every home," *Sci. Amer.*, vol. 296, no. 1, pp. 58–65, Jan. 2007.
- [20] I. Walker and K. E. Green, "Architectural robotics: Unpacking the humanoid," in *Proc. Archibots Workshop, 11th Int. Conf. Ubiquitous Computing, Supplemental Proc.*, Orlando, FL, 2009, pp. 28–29.

Apoorva D. Kapadia, Department of Electrical and Computer Engineering, Clemson University, Clemson, South Carolina. E-mail: akapadi@clemson.edu.

Ian D. Walker, Department of Electrical and Computer Engineering, Clemson University, Clemson, South Carolina. E-mail: iwalker@clemson.edu.

Keith Evan Green, Department of Architecture, Clemson University, Clemson, South Carolina. E-mail: kegreen@clemson.edu.

Joe C. Manganelli, Department of Architecture, Clemson University, Clemson, South Carolina. E-mail: jmangan@clemson.edu.

Henrique Houayek, Department of Architecture, Clemson University, Clemson, South Carolina. E-mail: hde@clemson.edu.

Adam M. James, Department of Architecture, Clemson University, Clemson, South Carolina. E-mail: amjames@clemson.edu.

Venkata Kanuri, Department of Electrical and Computer Engineering, Clemson University, Clemson, South Carolina. E-mail: vkanuri@clemson.edu.

Tarek Mokhtar, Department of Architecture, Clemson University, Clemson, South Carolina. E-mail: tmokhta@clemson.edu.

Ivan Siles, Department of Mechanical Engineering, Clemson University, Clemson, South Carolina. E-mail: isiles@clemson.edu.

Paul Yanik, Department of Electrical and Computer Engineering, Clemson University, Clemson, South Carolina. E-mail: pyanik@clemson.edu.



ICAR 2015
27-31 JULY
İSTANBUL
Turkey

**THE 17TH INTERNATIONAL CONFERENCE
 ON ADVANCED ROBOTICS**

www.icar2015.org



ODTÜ
METU



Organizing Committee

Aydan M. Erkmen, Afşar Saranlı
 (General Co-chairs)
 Middle East Technical Univ., Turkey

E. İlhan Konukseven
 (General Vice Chair)
 Middle East Technical Univ., Turkey

Uluc Saranlı, Sinan Kalkan
 (Program Co-chairs)
 Middle East Technical Univ., Turkey

Sinan Kalkan, Erol Şahin
 (Publicity and Publications Co-chairs)
 Middle East Technical Univ., Turkey

Yiğit Yazıcıoğlu, Erhan Öztop
 (Tutorial and Workshop Co-chairs)
 Middle East Technical Univ., Turkey
 Özyegin Univ., Turkey

A. Buğra Koku, Amit Kumar Pandey
 (Financial and Sponsorship Co-chairs)
 Middle East Technical Univ., Turkey
 Aldebaran Robotics, France

Serhat Erkçük, Veysel Gazi, Erhan Öztop,
 (Local Organization Chairs)
 Kadir Has University, Kemerburgaz
 University, Özyegin University, Turkey

**İsmet Erkmen, Oussama Khatib,
 Paolo Fiorini**
 (Advisory Board)
 Middle East Technical Univ., Turkey
 Stanford University, USA
 Verona University, Italy

For Conference Technical Inquiries:
 Assoc. Prof. Dr. Afşar Saranlı
 METU Dept. of Elect. and Elec. Eng.
 Phone : +90 312 210 4529
 Fax : +90 312 210 2304
 E-Mail : afsars@metu.edu.tr
<http://www.icar2015.org>

CALL FOR PAPERS

The 17th International Conference on Advanced Robotics, ICAR 2015 is organized by Middle East Technical University in collaboration with Kadir Has University. The conference will take place in Kadir Has University campus in Istanbul, Turkey, on July 27-31, 2015.

ICAR 2015 will be technically co-sponsored by the IEEE Robotics and Automation Society. The technical program of ICAR 2015 will consist of plenary talks, workshops and oral presentations. Submitted papers should describe original work in the form of theoretical modelling, design, experimental validation, or case studies from all areas of robotics, focusing on emerging paradigms and application areas including but not limited to:

Robotics Vision

Cognitive Robotics

Robotics Architectures

Mobile Robots

Humanoid Robots

Self-Localization and Navigation

Spatial Cognition

Human-Robot Interaction

Multi-Robot Systems

Search and Rescue Robots

Learning and Adaptation

Cooperation and Competition

Dynamics and Control

Adversarial Planning

Robot Operating Systems

Simulation and Visualization

Robot Swarms

Biologically-Inspired Robots

Embedded and Mobile Hardware

Robotic Entertainment

Robot Competitions

Unmanned Aerial Robots

Underwater Robotic Systems

Educational Robotics

Rehabilitation Robotics

Immersive Robotics

Important Dates:

Paper submission

February 1, 2015

Workshop and tutorial proposals

February 1, 2015

Notification of acceptance

April 15, 2015

Camera-ready papers

May 15, 2015

ICAR 2015 Conference

July 27-31, 2015

Paper Submission:

Original technical paper contributions are solicited for presentation at ICAR 2015. Accepted papers will be published in IEEE Xplore conference proceedings. Submissions should be 6-8 pages following the IEEE Xplore format available at:
http://www.ieee.org/conferences_events/conferences/publishing/templates.html

Papers will be submitted online via EasyChair:

<https://www.easychair.org/conferences/?conf=icar2015>

**For general inquiries, please contact
 Organizers/PCO: Bakhus Tourism Industry
 and Trading Inc. (Head Office)**

Mrs. Nagihan TANRISEVEN
 Cinnah Cad.72/15, 06690, Çankaya, Ankara,
 Turkey

Tel : +90 312 466 1500
 Fax : +90 312 466 1525
 Email : congress@icar2015.org
nagihan@icar2015.org



Conference Venue :

Kadir Has University
 Conference Center
 Address: Kadir Has Caddesi
 Cibali / İSTANBUL 34083
 Phone ::90 (212) 533 65 32
<http://www.khas.edu.tr/en/>

 EDUCATION

RAS Technical Education Program Leads the New Tech Revolution

By Paolo Fiorini

In the media and in various technical discussions, robotics is described as the new technological revolution that will impact everybody's life in a way comparable with the introduction of computers and cellular phones. As experts in this area, we may or may

not agree on the exact time of this revolution, but we certainly agree that the moment in which robots will become pervasive devices is getting closer.

Similarly, a second point is that robotic technologies will create jobs, and we need to empower students with the necessary competences. Thus, the IEEE Robotics and Automation Society (RAS) has given increased attention to education, to competitions, and to all those activi-

ties that generate enthusiasm and attention and, hopefully, attract students to robotics. To emphasize this interest, the summer and winter schools addressing doctoral training have been renamed the Technical Education Program (TEP), to indicate RAS's broader interest in education and training in robotics.

The RAS TEP program is organized to fund three schools per year, one in the amount of US\$40,000 and the other two at US\$20,000 each. The topics are proposed by the school organizers, and the largest support is assigned on a rotating basis among the three geographical areas of RAS: the Americas (Area 1); Europe, Africa, and Middle East (Area 2); and Asia, Australia, and Pacific Rim (Area 3). The yearly deadline is approximately one month before the IEEE International Conference on Robotics and Automation (ICRA) to allow the proposal review and the selection of the RAS-TEP awards during ICRA. At the end of each school, the organizers send a report to the RAS Education Committee describing the school results in quantitative terms, and the Education Committee is charged with assessing the quality and

impact of the school to better organize future programs.

We received 15 submissions for 2015. Each proposal was evaluated on three main measures: technical quality, organization structure, and financial aspects. The evaluation was carried out by a panel of representatives from the Member Activities Board and the Technical Activities Board in two steps.

The RAS Education Committee is pleased to announce the 2015 supported TEPs:

- the Summer School on Agricultural Robotics in Sydney, Australia, in January 2015
- the Second International Summer School on Social Human–Robot Interaction in Mariehamn, Finland, 24–28 August 2015
- the Summer School on Experimental Methodology, Performance Evaluation, and Benchmarking in Robotics in Benicassim, Spain, 14–18 September.

For more information and details on the educational opportunities available through RAS, please visit www.ieee-ras.org.

At the end of each school, the organizers send a report to the RAS Education Committee describing the school results in quantitative terms.

students with the necessary competences. Thus, the IEEE Robotics and Automation Society (RAS) has given increased attention to education, to competitions, and to all those activi-

Digital Object Identifier 10.1109/MRA.2014.2334933
Date of publication: 10 September 2014



CALL FOR PAPERS

Special Issue on *Replicable and Measurable Robotics Research*

There are a number of issues in robotics, related to performance measurement, methods for the objective comparison of different algorithms and systems, the possibility itself to replicate published results.

We are now at a point where it is possible to give concrete directions for experiment planning, execution, and reporting, allowing objective performance comparisons and potentially affecting the content of obtained results, not only their 'production process'.

The key point to allow replication and comparison of results is having adequate data support: all the data necessary to repeat a given experiment.

This will be the very first well-structured example of a publication in robotics, which will list a series of replicable and objectively measurable results.

Contributed papers reporting about experiments, benchmarking methods, challenges and competitions are solicited. They need to include results on real robots and be described in such a way to allow their replication. In particular challenges and competitions might be needed to compare intelligent or system level behaviors and capabilities. We seek papers on challenges and competitions describing real world events with real robots and designed as robotics 'replicable experiments'. Any application area of Robotics and Automation can be considered, such as: Aerial Robotics, Rehabilitation and Assistive Robotics, Medical Robotics, Industrial robotics, Prosthetics and Exoskeletons, Wearable Robotics, Marine Robotics, and more

Timeline:

Call for papers	June 2014
Deadline for paper submission	10 November 2014
First review	6 February 2015
Final review	20 May 2015
Publication	September 2015

Guest Editors:

Fabio Bonsignorio, Institute of Biorobotics, Scuola Superiore S. Anna, Pisa, Italy and CEO and founder of Heron Robots. (Corresponding guest editor)

John Hallam, Maersk Institute, University of Southern Denmark, Odense, Denmark.

Angel P. del Pobil Robotic Intelligence Laboratory, Jaume I University, Castellon, Spain.

Complete details at

<http://www.ieee-ras.org/publications/ram/ram-special-issues>



SOCIETY NEWS

ICRA 2014 Award Winners

During the IEEE International Conference on Robotics and Automation (ICRA) on 4 June in Hong Kong, the IEEE Robotics and Automation Society (RAS) recognized the 2014 award winners, pictured in Figures 1–7, for their outstanding accomplishments and service to RAS and the robotics and automation community.

RAS George Saridis Leadership Award in Robotics and Automation

Paolo Dario

The BioRobotics Institute, Italy

For pioneering and consolidating robotics as pervasive technology, with interdisciplinary and visionary ideas, extending RAS leadership through inclusiveness toward other communities.

Oussama Khatib

Stanford University, California, United States

In recognition of his vision and leadership in introducing and nurturing important innovations in conferences in robotics and automation.

IEEE RAS Distinguished Service Award

Anthony A. (Tony) Maciejewski

Colorado State University, Colorado, United States



Figure 1. From left: Oussama Khatib, RAS President Raja Chatila, and Paolo Dario.



Figure 3. From left: Kyu Jin Cho, Raja Chatila, and Davide Scaramuzza.



Figure 2. From left: Raja Chatila and Tony Maciejewski.



Figure 4. From left: Torsten Kroeger and Raja Chatila.

For contributions to RAS technical activities and continuing service as vice president for financial activities.

Rosalyn Graham Snyder

Raleigh, North Carolina, United States

For her never-ending commitment in the support of all RAS activities in 25 years of service, from the start of the Society to the fastest-growing Society of the IEEE.

RAS Early Career Award (Academic)

Kyu Jin Cho

Seoul National University, Seoul, Korea

For fundamental contributions to soft robotics and biologically inspired robot design.

Davide Scaramuzza

University of Zurich, Switzerland

For his major contributions to robot vision and visually guided micro aerial vehicles.

RAS Early Career Award (Industry/Government)

Torsten Kroeger

Stanford University, United States, and Reflexxes GmbH, Germany



Figure 5. From left: Roland Siegwart and Raja Chatila.

For his scientific contributions to online trajectory generation and sensor-based motion control of robot systems widely used in industry and academia.

IEEE Inaba Technical Award for Innovation Leading to Production

Roland Siegwart

Eth Zurich, Switzerland

For outstanding contributions in fostering innovation and entrepreneurship, for the development of novel robotic technologies and the transition of this technology to industry.

IEEE Robotics and Automation Award for Product Innovation

Daimler AG, Mercedes-Benz Cars

In recognition of robot farming based on soft robotics technologies—a milestone toward highly flexible robot manufacturing.

RAS Chapter of the Year Award

Peru Section Chapter

Chair: Antonio Moran.

Changes to the Technical Activities Board

During the RAS Administrative Committee (AdCom) meeting held on 6 June in Hong Kong, there were a number of changes and additions concerning the Technical Activities Board (TAB). TAB focuses on the research content of the Society, tracking technical developments and encouraging innovation in applications, theory, models, metrics, experiments, architec-



Figure 6. From left: Michael Zürn, senior manager at Daimler AG, Mercedes-Benz Cars, and Raja Chatila.

tures, products, initiatives, and other technical areas.

Fumihiro Arai (Figure 8) of Nagoya University in Japan was approved as the new vice president for technical activities. He has been a member of the RAS AdCom for five years and is cochair of the RAS Technical Committee (TC) on Micro-/Nanorobotics, which received the Most Active TC Award in 2009. Arai replaces Satoshi Tadokoro, as Tadokoro was recently named president-elect.

The AdCom also approved three new TCs: the TC on Human Movement and Understanding, the TC on Robot Mechanisms and Design, and the TC on Robotic Hand, Grasping, and Manipulation.

The TC on Human Movement Understanding

Cochairs

- Emel Demircan—Stanford University, California, United States, and University of Tokyo, Japan
- Dana Kulić—University of Waterloo, Canada
- Denny Oetomo—University of Melbourne, Australia
- Mitsuhiro Hayashibe—INRIA, France.

Scope

Robotics research has drawn much inspiration from humans as a system: in the design of the anthropomorphic aspects of manipulators, sensors, and actuators; approaches for coordinating full-body motions; and the higher-level strategies for realizing complex tasks and interacting with the external environment and other humans. Today, robotics as a field has matured to the



Figure 7. From left: Antonio Moran and Raja Chatila.

point where methodologies developed and used in robotics may be leveraged to address research questions in many other fields, ranging from neuroscience to computer animation. Together with the tools from biomechanics, robotics

The Mechanisms and Design TC seeks to bring together researchers with an interest in innovative mechanical hardware in robotic systems.



Figure 8. Fumihiro Arai.



Figure 9. The participants from the International Workshop on Hybrid Fusion of Robot-Human Biofunctions Toward Cyborg.

The TC on Robot Mechanisms and Design

Cochairs

- Aaron Dollar—Yale University, Connecticut, United States
- Kyujin Cho—Seoul National University, Korea
- Claudio Semini—Italian Institute of Technology, Italy
- Matei Ciocarlie—Google, United States.

Scope

The Mechanisms and Design Technical Committee seeks to bring together researchers with an interest in innovative mechanical hardware in robotic systems. Relevant topics include

- compliant and variable-stiffness mechanisms
- the design of hardware for open-source dissemination
- the design of robot systems incorporating novel mechanisms
- materials and fabrication technologies as they relate to novel design and mechanism paradigms
- mechanism synthesis
- novel actuator technologies
- novel transmission technologies
- parallel mechanisms
- parameter selection and sizing of actuators
- underactuated mechanisms.

The TC on Robotic Hand, Grasping, and Manipulation

Cochairs

- Hyouk Ryeol Choi—Sungkyunkwan University, Korea

- Marco Gabaccini—University of Pisa, Italy
- Rod Grupen—University of Massachusetts Amherst, United States
- Yu Sun—University of South Florida, United States.

Priority Areas for the TC

- Established areas
 - multifinger robotic hand design
 - hand sensor and actuator design
 - force and tactile sensing
 - grasping force control
 - multimodal sensing
 - sensor-based control
 - grasping planning
 - grasp contact modeling
 - grasp quality measure
 - dexterous manipulation
 - human grasping and manipulation modeling and learning.
- Emerging areas
 - underactuated hand design
 - underactuated grasping
 - caging
 - whole-body grasping
 - grasp synergies
 - grasping with uncertainties
 - task-oriented grasping
 - in-hand manipulation
 - learning and cognitive development of grasping and manipulation.

Newly Formed Beijing Chapter Welcomes RAS Distinguished Lecturers

On 30 May 2014, Prof. Toshio Fukuda and Prof. Qiang Huang hosted a full-day workshop, the International Workshop on Hybrid Fusion of Robot-Human Biofunctions Toward Cyborg, at Beijing Institute of Technology (BIT),

China (Figure 9). The workshop was coorganized by IEEE Beijing Section Robotics and Automation Society Chapter; the Innovation Center of the 111 Project Mobile Platform Design and Manufacture (BIT), the Ministry of Education/State Administration of Foreign Experts Affairs; and the Laboratory of Biomimetic Robots and Systems (BIT), Ministry of Education.

The purpose of the workshop was to bring together scholars from around the world, including academic researchers and doctors, to discuss a research frontier and clinical works on the robot–human hybrid fusion system. The agenda began with an overview by Prof. Fukuda on the concept of workshop theme. The first speaker, Arianna Menciassi from the Scuola Superiore Sant’ Anna, presented innovative work on advanced materials and systems that could enable the development of biohybrid actuators, based on living contractile muscle cells, and biohybrid sensors, based on stimuli-sensitive cells. Prof. Kazuhiro Sakai, from the University of Human Arts and Sciences, gave a presentation on the current status in prosthetics. He introduced the idea that both user’s demand and financial issue were important to determine appropriately prosthetic design and component selection. Prof. Yasuhisa Hasegawa, from Nagoya University, presented progressive work on cooperative control of an exoskeletal assistive system to help paraplegics walk. Finally, Prof. Jinglong Wu, from the Institute of Complex Medical Engineering Incorporation, introduced research on human brain mapping of visual and tactile functions and early detection for neuron disorders.

The workshop not only gave robotics researchers’ an opportunity to share their experiences and their visions on biohybrid systems but also invited some doctors to introduce their needs and ideas in regenerative medicine and rehabilitation, guiding us toward appropriate and effective research directions for the future.

Travel support for some of the speakers was made possible through the

IEEE RAS Distinguished Lecturer program, which gives up to US\$3,000 for an approved speaker to present at a Chapter or TC event. For more information, details can be found at ieee-ras.org in the “RAS Resources” section, under “About RAS.”

IEEE Fellows

The IEEE grade of Fellow is a distinction reserved for select IEEE Members whose extraordinary accomplishments in any of the IEEE fields of interest are deemed fitting of this prestigious grade elevation. The following IEEE RAS members were elevated in 2014.

2014 RAS Fellows Evaluated by the IEEE Robotics and Automation Society

- Martin Buss—Technische Universität Muenchen, Germany
for contributions to haptic telepresence systems and autonomous robots
- James Colgate—Northwestern University, United States
for contributions to the field of haptics
- Liyi Dai—U.S. Army Research Office, United States
for leadership and contributions to discrete event systems and singular systems
- Daniel Lee—University of Pennsylvania, United States
for contributions to machine learning algorithms for perception and motor control
- John Leonard—Massachusetts Institute of Technology, United States
for contributions to navigation and mapping for mobile robots and autonomous underwater vehicles
- Stefan Schaal—University of Southern California, United States
for contributions to robot learning and modular motion planning
- Metin Sitti—Carnegie Mellon University, United States
for contributions to micro and nanoscale robotic systems
- Hong Zhang—University of Alberta, Canada
for contributions to collective robotics and intelligent sensing in oil sand mining.

New Fellow Online System

The task of nominating a Senior Member for Fellow grade got easier with the new Fellow Online System. Multiple upgrades were incorporated, but three main enhancements will please nominators. After a nominator logs into the system, the first requirement will be to input the nominee’s Member number. Entering this information will immediately let the nominator know whether the nominee meets the requirements of being an active IEEE Senior or Life Senior Member and whether the nominee has been a Member in good standing for five years or more. If a nominee is ineligible, the system will prevent the nominator from filling out the entire form to avoid any unnecessarily wasted time.

Another new feature requires inputting the Member numbers of the references. The nomination must include at least five but no more than eight references from IEEE Fellows. Entering a reference’s Member number will immediately inform the nominator whether or not the reference is eligible.

The best feature is allowing nominators the capability to make changes to main text, to update e-mail addresses, to add and delete reference and endorsement names, and to delete nominations they prepared out of the system up to the 1 March deadline. Providing nominators this kind of flexibility will give them the opportunity to prepare a better nomination.

After the deadline has been reached, the system will authenticate all the data and verify that each nomination package is complete. As soon as this process is finished, a confirmation will be sent to the nominators letting them know whether the nomination will be considered.

The system is now open and ready to accept nominations for the class of 2016. Starting the process early will alleviate last-minute issues. You can visit the Fellow Web site at www.ieee.org/fellows, then click “Online Nomination Form” to begin.

—Rosann Marosy

2014 RAS Fellows Evaluated by Other IEEE Societies

- Rene Vidal—Johns Hopkins University, United States
Evaluated by the IEEE Computer Society *for contributions to subspace clustering and motion segmentation in computer vision*
- Robert Kozma—University of Memphis, United States
Evaluated by the IEEE Computational Intelligence Society *for contributions to fuzzy control system design and analysis*
- Ali Jadbabaie—University of Pennsylvania, United States
Evaluated by the IEEE Control Systems Society *for contributions to the*

contributions to pattern-based computation based on large-scale networks and random graphs

- Kazuo Tanaka—University of Electro-Communications, Japan
Evaluated by the IEEE Computational Intelligence Society *for contributions to fuzzy control system design and analysis*
- Ali Jadbabaie—University of Pennsylvania, United States
Evaluated by the IEEE Control Systems Society *for contributions to the*



Figure 10. From left: Jakob Berghofer (Organizing Committee and Product Management Service Robotics, KUKA); Dr. Alin Albu-Schäffer (member of the jury and head of the Institute of Robotics and Mechatronics, DLR); Flavio Fontana, Elias Mueggler, and Matthias Faessler (Robotics and Perception Group); Dr. Bernd Liepert (president of the jury and chief technology officer, KUKA); and Dr. Rainer Bischoff (Organizing Committee and head of technology development, KUKA).

theory of multiagent coordination and control

- Hermano Krebs—Massachusetts Institute of Technology, United States
Evaluated by the IEEE Engineering in Medicine and Biology Society for contributions to rehabilitation robotics and the understanding of neurorehabilitation.

Members in the News

Many RAS members were involved as participants and sponsors of the first

The TAB focuses on the research content of the Society, tracking technical developments and encouraging innovation.

ias Faessler, and Flavio Fontana (Figure 10).

An international panel of judges selected the Swiss team from more than 30 contestants as it impressed the panel with its application, “Cooperative Air-Ground Robotics: Removing Obstacles in the Way—Search and Rescue Missions.”

The application involves the cooperation of a quadcopter with a KUKA youBot moving along the ground. The quadcopter, equipped with a camera, autonomously flies around a defined area, generates a map, and provides the acquired data to the youBot. This enables the ground-based youBot to reach its destination quickly to provide assistance, for example, in a disaster zone.

KUKA set up the Innovation Award to optimize the preparation of technology transfer from science to industry.

RAS member Dr. Carrick Detweiler, codirector of the NIMBUS Lab at the University of Nebraska–Lincoln (UNL), and his students recently participated in a three-day interdisciplinary residency exploring the intersection



Figure 11. UNL dance students Vivian Kim (left) and Marisol Herling (right) rehearse choreography with tethered robots operated by Adam Taylor, a student from the department of computer science and engineering.

of technology, science, design, and movement (see Figures 11 and 12).

In conjunction with 2014 National Robotics Week in the United States, the Lied Center for Performing Arts and students at the University of Nebraska–Lincoln UNL College of Architecture, Department of Computer Sciences and Engineering, and the Glenn Korff School of Music Dance Program joined forces with dancers from STREB, an internationally renowned dance company known for their gravity-defying choreography and performances at the 2012 London Olympics.

Since January, the students had been collaborating to create an innovative exhibition combining architectural designs created by UNL students, choreography developed by UNL dancers featuring found objects and props, and aerial robots from the UNL’s NIMBUS Laboratory.

Dr. Detweiler said, “Interacting with dancers has helped to push the boundaries of our robots and the students. In the current system, the robots were pre-programmed, and we relied on the dancers to react to the timing of the robots. In the future, we envision incorporating aspects of our research to allow the robots to adapt to the dancers.”

Dr. Detweiler and students at the NIMBUS Lab are currently focused on advancing the systems and software



Figure 12. Dr. Carrick Detweiler demonstrates the capabilities of the UNL Nimbus Lab’s aerial robots for Elizabeth Streb, founder of the STREB Extreme Action Company.

for aerial robots to enable close and safe interactions with the environment. As part of a National Robotics Initiative project, they are developing an aerial water sampler that can obtain water samples from hard to access locations to aid water scientists. They are also developing aerial robots that can wirelessly charge sensors and closely monitor crops. To ensure safe operation while interacting with the environment, they are working on automated techniques to analyze the software and system as it is running to detect faults and minimize risk. They are also developing algorithms that adapt the level of autonomy to take advantage of the skills of domain expert operators.





ICRA 2015

**IEEE International Conference
on Robotics and Automation**

Seattle, Washington (USA)
26-30 May

Honorary Chair

Ruzena Bajcsy (University of California, Berkeley)

General Chair

Lynne Parker (University of Tennessee)

Program Chair

Nancy M. Amato (Texas A&M University)

Program Co-Chairs

Danica Kragic (Royal Institute of Technology, KTH)

Hong Qiao (Chinese Academy of Sciences)

Jing Xiao (University of North Carolina, Charlotte)

CEB Editor-in-Chief

Allison Okamura (Stanford University)

Finance Chair

Yi Guo (Stevens Institute of Technology)

Workshops and Tutorials Chair

Monica Anderson (University of Alabama)

Workshops and Tutorials Co-Chairs

Spring Berman (Arizona State University)

Alicia Casals (Technical University of Catalonia)

Yukie Nagai (Osaka University)

Interactive Sessions Chair

Ani Hsieh (Drexel University)

Interactive Sessions Co-Chair

Ming Lin (University of North Carolina, Chapel Hill)

Awards Chair

Lydia Kavraki (Rice University)

Awards Co-Chairs

Jessica Hodgins (Carnegie Mellon University)

Daniela Rus (Massachusetts Institute of Technology)

Carme Torras (CSIC-UPC)

Publication Chair

Dawn Tilbury (University of Michigan)

Publicity Chair

Nora Ayanian (University of Southern California)

Publicity Co-Chairs

Raffaella Carloni (University of Twente)

Mihoko Otake (Chiba University)

Exhibitions Chair

Robin Murphy (Texas A&M University)

Exhibitions Co-Chair

Cecilia Laschi (Scuola Superiore Sant'Anna)

Sponsorships Co-Chairs

Manuela Veloso (Carnegie Mellon University)

Maja Mataric (University of Southern California)

Industry Forum Chair

Aude Billard (Ecole Polytechnique Federale de Lausanne)

Industry Forum Co-Chairs

Dana Kulic (University of Waterloo)

Angelika Peer (TU Munich)

Yuru Zhang (Beihang University)

Developing Countries Outreach Chair

Bernardine Dias (Carnegie Mellon University)

Developing Countries Outreach Co-Chairs

Chinwe Ekenna (Texas A&M University)

Ayorkor Korsah (Carnegie Mellon University)

Career Fair Chair

Hadas Kress-Gazit (Cornell University)

Career Fair Co-Chairs

Maren Bennewitz (University of Freiburg)

Jana Kosecka (George Mason University)

PhD Forum Chair

Ayanna Howard (Georgia Institute of Technology)

PhD Forum Co-Chairs

Jamie Paik (EPFL)

Xiaorui Zhu (Harbin Institute of Technology)

Competitions

Sonia Chernova (Worcester Polytechnic Institute)

Travel Awards Chair

Maria Gini (University of Minnesota)

Student Activities Chair

Lydia Tapia (University of New Mexico)

Student Activities Co-Chair

Hanna Kurniawati (University of Queensland)

K-12 Outreach Chair

Radhika Nagpal (Harvard University)

Web Chair

Shawna Thomas (Texas A&M University)

Local Arrangements Chair

Kristy Morganson (University of Washington)

Local Arrangements Co-Chair

Maya Cakmak (University of Washington)

ICRA is the IEEE Robotics and Automation Society's flagship conference and is a premier international forum for robotics researchers to present their work. The 2015 conference will be held May 26-30, 2015 at the Washington State Convention Center in Seattle, WA, USA.

The conference will include plenary and mini-plenary sessions, contributed paper sessions, workshops and tutorials, an industrial forum, exhibits, and robot challenges as well as some events that are new to ICRA, such as a PhD forum, a career fair, and a developing countries forum.

Contributed Papers

Papers reporting on novel research in robotics and automation are invited. All papers will be reviewed using a single-blind review process: authors declare their names and affiliations in the manuscript for the reviewers to see, but reviewers do not know each other's identities, nor do the authors receive information about who has reviewed their manuscript.

Prospective authors should submit PDF versions of their paper. Six pages in standard ICRA format are allowed for each paper, including figures. A maximum of two additional pages can be purchased. Authors are invited to submit a video to complement their submission. Detailed instructions for submission are available on the conference website.

Paper Presentation

Papers will be presented in two modes, interactive and oral. Sessions will include both interactive and oral papers, with interactive papers having brief spotlight oral presentations preceding the interactive portion of the session, which will be held in the session room.

Tutorials and Workshops

Proposals for half-day or full-day workshops and tutorials are invited. Workshops and tutorials will be held on May 26 and 30, before and after the main contributed sessions. Workshops provide an informal forum for participants in an active research area. Tutorials target more established research areas and provide insights to the state of the art, presented by recognized researchers in the field. Detailed instructions for submission are provided on the conference website.

Career Fair and PhD Forum

For the first time, ICRA 2015 will include a Career Fair and a PhD Forum. The Career Fair will provide an opportunity for conference sponsors to have booths and interact with prospective employees. The PhD Forum will provide an opportunity for a group of Ph.D. students to discuss and explore their research interests and career objectives with a panel of established researchers in robotics and automation to help them network with both junior and senior researchers. Information regarding participation in these events will be on the conference website.

Exhibits

The Washington State Convention Center has plentiful and excellent space for exhibits. It is adjacent to the plenary sessions and conference registration, and will be the location for the opening reception and for refreshments during the breaks during the conference. Information for prospective exhibitors will be available on the web site.

Important Dates

1 October 2014: Paper Submission deadline

30 January 2015: Paper acceptance notification

27 February 2015: Final contribution deadline

URL: <http://www.icra2015.org>

WOMEN IN ENGINEERING

Lead Beyond: The WIE International Leadership Conference

By Laura Margheri

Silicon Valley is known worldwide as a major center of technology innovation, strong academia-industry collaboration, creativity, leader growth, and new economic and entrepreneurship models. Therefore, it is not surprising that San Francisco was chosen as the location for the first

The IEEE WIE is a channel to inspire, engage, and advance women in engineering.

- IEEE Women in Engineering (WIE) International Leadership Conference, a new conference held in May 2014 and organized by the IEEE WIE Committee.

More than 350 women engineers, managers, technologists, scientists, and entrepreneurs met to share new ideas, gain inspiration, foster discussion, and encourage collaboration, all with the common vision of advancing career opportunities for women in engineering.

“Lead Beyond. Developing Inspirational Women Who Change the World” was the title and the main theme of the event. The speakers at the conference were women who have made their mark in the community. Their experience and advice were presented with passion and high technical quality during plenary talks or in parallel tracks on the following themes:

Digital Object Identifier 10.1109/MRA.2014.2334151
Date of publication: 10 September 2014



The 2014 WIE Meeting. (Photo by Kate McDevitt.)

- empowerment—skills to help women advance in their careers
- engagement—hands-on skills development workshops
- inspiration—presentations/skills to inspire women to achieve their goals
- enjoyment—work/life balance, reducing stress, and enjoying life.

There is not just one single rule to becoming a leader, and it is not exclusive to one's technical and scientific skills. There are many other aspects related to the personality traits and some tricks that can make the difference in developing a strategy for innovation. Three key attributes were emphasized above all: passion, moving out of your comfort zone, and encouraging collaboration and leveraging “hive mind.”

Passion

You have to be full of passion for your work in any case. Moreover, leaders should be particularly able to communicate their own passion,

both to their teams and to the public, and should encourage the passion of others. It is important to inspire the team constantly, nurture a passionate environment, and appeal to internal motivators. In addition, a leader should teach the team to communicate passion as well because it can be used as a key to enter the market. People may forget the words you say, but they will never forget how you make them feel.

Move Out of Your Comfort Zone

Taking risks is indispensable for leading innovation. Being creative and thinking differently are necessary to anticipate market and customer needs and, together with flexible methods and models, allow for a prompt response to change. Change is, in fact, everywhere, so leaders should be able to adjust; they have to be humble and accept the changes by considering that failure is a part of the road toward success.

Encourage Collaboration and Leverage “Hive Mind”

Teamwork is fundamental for a leader. Being a leader is not just about you; it is about the people around you that you lead, and it is about giving them power—positive power. As a leader, it is necessary to work as a sponsor of team members to be more than a

mentor to give them opportunities to grow and realize their projects.

There is no formula for becoming a leader. You have to embrace what is unique and different about you. These qualities can foster diversity and innovation.

The IEEE WIE, with its events and activities, is a great channel to inspire,

engage, and advance women in engineering, to share experiences of success and career growth in the industrial and academic fields to convey important lessons from women to other women and men.



TC SPOTLIGHT (continued from p. 25)

© AIST-CNRS-JRL



Figure 3. Optimal whole-body reaching motions with multiple contacts for the humanoid robot HRP-2.

Outreach Activities Outside the RAS

Several activities aim to bridge the gap between the mathematical optimization and the robotics communities via activities at major mathematical optimization and scientific computing conferences.

A minisymposium on model-based optimization in robotics will be organized at the High Performance Scientific Computing Conference in Hanoi, Vietnam, in March 2015, which has a strong focus on optimization.

Two keynote presentations at major mathematical optimization conferences (the French–German–Polish Conference on Optimization and the European Conference on Computational Optimization) advertising robotics applications and the TC have been delivered.

Members of the TC can receive regular information via the TC's Web site and a newly established newsletter and can engage in scientific discussions. If you wish to join the TC, please send an e-mail to Katja Mombaur (kmombaur@uni-hd.de) or join via our Web page at www.tc-opt.uni-hd.de.



moving?

You don't want to miss any issue of this magazine!

change your address

BY E-MAIL: address-change@ieee.org

BY PHONE: +1 800 678 IEEE (4333) in the U.S.A.
or +1 732 981 0060 outside the U.S.A.

ONLINE: www.ieee.org, click on quick links, change contact info

BY FAX: +1 732 562 5445

Be sure to have your member number available.

 CALENDAR**2014****14–18 September**

IROS 2014: IEEE/RSJ International Conference on Intelligent Robots and Systems. Chicago, Illinois, USA. www.iros2014.org

26–30 September

RRSS 2014: IEEE-RAS Response Robotics Summer School and Workshop. Perth, Australia. www.wiki.ssrrsummerschool.org/doku.php?id=2014:home

22–25 October

ICCAS 2014: 14th International Conference on Control, Automation and Systems. Gyeonggi-do, Korea. www.2014.iccas.org/

27–30 October

SSRR 2014: IEEE International Symposium on Safety, Security, and Rescue Robotics. Hokkaido, Japan. www.ssrr-conference.org/2014

9–12 November

MHS 2014: International Symposium on Micro-NanoMechatronics and Human Science. Nagoya, Japan. www.mein.nagoya-u.ac.jp/mhs/

18–20 November

Humanoids 2014: IEEE-RAS 14th International Conference on Humanoid Robots. Madrid, Spain. www.humanoids2014.com

Digital Object Identifier 10.1109/MRA.2014.2347572
Date of publication: 10 September 2014

5–10 December

ROBIO 2014: IEEE International Conference on Robotics and Biomimetics. Hanoi, Vietnam. www.robio2014.org

10–12 December

ICARCV 2014: International Conference on Control, Automation, Robotics, and Vision. Marina Bay Sands, Singapore. www.icarcv.org/2014/

13–14 December

SII 2014: IEEE/SICE International Symposium on System Integration. Tokyo, Japan. www.si-sice.org/SII2014/

22–24 December

ICIAFs 2014: International Conference on Information and Automation for Sustainability. Sri Lanka. www.iciafs.org

2015**January**

Summer School on Agricultural Robotics. Sydney, Australia.

2–5 March

HRI 2015: 10th ACM/IEEE International Conference on Human-Robot Interaction. Portland, Washington, USA. www.humanrobotinteraction.org/2015/

11–12 May

TePRA 2015: IEEE International Conference on Technologies for Practical Robot Applications. Woburn, Massachusetts, USA. www.ieeerobot-tepra.org

11–13 May

INCOM 2015: 15th IFAC Symposium on Information Control Problems in Manufacturing. Ottawa, Canada. www.incom2015.org/

25–30 May

ICRA 2015: IEEE International Conference on Robotics and Automation. Seattle, Washington, USA. www.icra2015.org

21–24 June

WHC 2015: IEEE World Haptics Conference. Chicago, Illinois, USA.

27–31 July

ICAR 2015: International Conference on Advanced Robotics. Istanbul, Turkey.

24–28 August

Second International Summer School on Social Human-Robot Interaction. Mariehamn, Finland.

14–18 September

Summer School on Experimental Methodology, Performance Evaluation and Benchmarking in Robotics. Benicassim, Castellon, Spain.

28 September–2 October

IROS 2015: IEEE/RSJ International Conference on Intelligent Robots and Systems. Hamburg, Germany.

3–5 November

Humanoids 2015: IEEE-RAS International Conference on Humanoid Robots. Seoul, Korea. 

2014 RAS ADCOM ELECTION

THE IEEE ROBOTICS AND AUTOMATION SOCIETY ELECTION VOTING WILL BEGIN SOON FOR RAS MEMBERS TO ELECT SIX NEW MEMBERS TO THE SOCIETY'S ADMINISTRATIVE COMMITTEE, TO SERVE THREE-YEAR TERMS BEGINNING 1 JANUARY 2015.

IN THE MONTH OF SEPTEMBER, VOTING MEMBERS (GRADUATE STUDENTS AND HIGHER GRADE MEMBERS) WILL RECEIVE THE ADCOM ELECTION INFORMATION PACKAGES DELIVERED VIA E-MAIL OR POSTAL MAIL IF REQUESTED OR E-MAIL IS NOT AVAILABLE. THE PACKAGE INCLUDES A SLATE OF THE CANDIDATES, THEIR BIOGRAPHIES AND POSITION STATEMENTS. CANDIDATE INFORMATION IS ALSO POSTED ON WWW.IEEE-RAS.ORG.

THE CANDIDATES FOR THE SIX POSITIONS ARE:

Geographical Area 1

Lydia Kavraki, Rice University, USA

Peter Luh, University of Connecticut, USA

Robin Murphy, Texas A&M University, USA

Tim Salcudean, University of British Columbia, Canada

Richard Vaughan, Simon Fraser University, Canada

Geographical Area 2

Wolfram Burgard, University of Freiburg, Germany

Danica Kragic, Royal Institute of Technology (KTH), Sweden

Carme Torras, Institut de Robòtica i Informàtica Industrial (CSIC-UPC) Barcelona, Spain

Geographical Area 3

Yasushi Nakauchi, University of Tsukuba, Japan

Zhi Dong Wang, Chiba Institute of Technology, Japan

I-Ming Chen, Nanyang Technological University (NTU), Singapore



 **ERRATA**

Due to a production error, Figure 1 in “Group Mapping” by Sajad Saeedi, Liam Paull, Michael Trentini, Mae Seto, and Howard Li [1] on page 63 in the June 2014 issue of *IEEE Robotics and Automation Magazine* was incorrectly portrayed. See Figure 1 here for the correct representation of that figure. We apologize for any confusion this may have caused.

Reference

- [1] S. Saeedi, L. Paull, M. Trentini, M. Seto, and H. Li, “Group mapping,” *IEEE Robot. Automat. Mag.*, vol. 21, no. 2, pp. 60–72, June 2014.

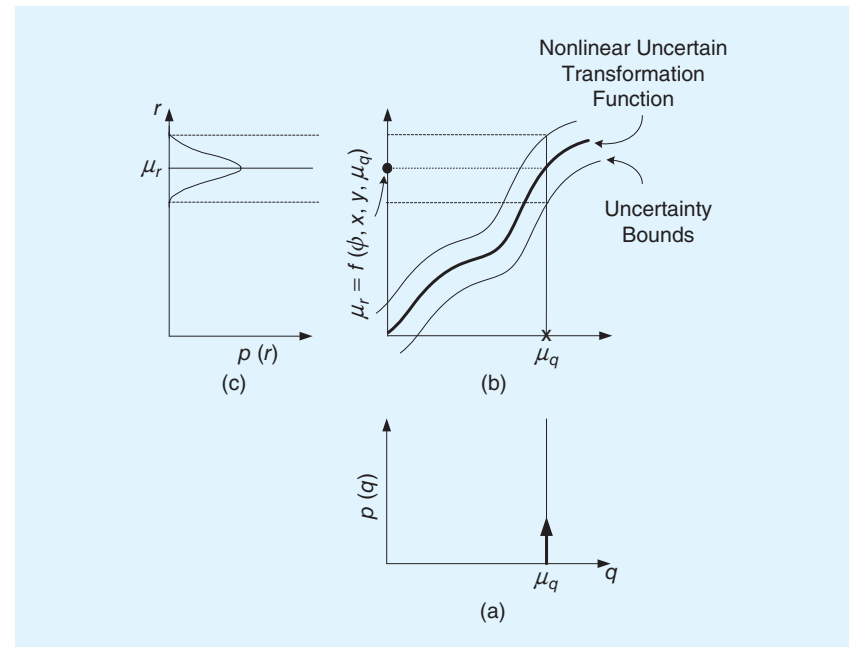
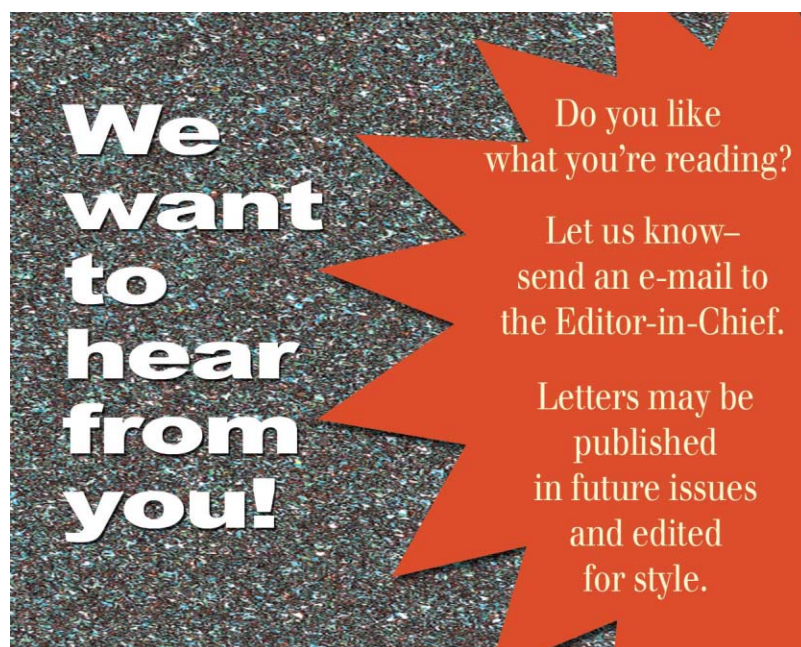


Figure 1. (a) A point q with the distribution of $p(q)$ is transformed by an uncertain transformation function. (b) The uncertainty of the transformation function is shown by setting boundaries around the nominal function. (c) After linearization, the transformed point, r , will have a Gaussian distribution, $p(r)$.

Digital Object Identifier 10.1109/MRA.2014.2346093
Date of publication: 10 September 2014



TURNING POINT (continued from p. 168)

FP: It's a difficult problem, and I do know there's some ongoing discussion within our Society on ways to alleviate the review burden. Some of these ideas are also tied to finding ways for members of our community to receive the credit they deserve for their conference publications, at least relative to other disciplines. I think we'll be hearing more about these ideas in the near future.

EG: Since you mention conference publications, one of the things I've struggled with is how much to add to a conference paper for it to be able to evolve into a transactions paper.

FP: We have guidelines in our information for authors, but you can see that, ultimately, the threshold is a subjective one. I've known authors who deliberately hold back showing everything in their conference paper so that

they have enough new material to justify submitting to *T-RO*. In most cases, however, it's not a huge dilemma for our authors. Also, our editors and associate editors are experienced and will indicate clearly what needs to be done for successful evolution, assuming, of course, that the result meets our criterion for research significance.

EG: As you said earlier, the publications landscape in robotics is changing rapidly. Where is *T-RO* positioned?

FP: Robotics publications are proliferating to the point where we might soon have a bubble on our hands. At *T-RO*, we're faced with the huge task of filtering and curating this ever-growing body of research. Naturally, we want to publish the best papers from the entire ecosystem of robotics, which, as you know, is continually evolving. New

problems and research emerge, and old problems keep coming back. Just look at the resurgence of hands and grasping, for example.

EG: Let me ask one final question that I hope will lead to some practical advice for our readers. If I have what I think is a rather nice result, how should I decide whether to submit to *T-RO* or a more specialized journal?

FP: That's a tough question. If you ask some of our more experienced senior researchers to name the publications that they're most proud of, I think most would list a number fewer than ten. If, at the end of your career, you think this paper could be on that list, then absolutely—I want you to submit your paper to *T-RO*.



LEARNING HAS NO
BOUNDARIES

YOU KNOW YOUR STUDENTS NEED IEEE INFORMATION.
NOW THEY CAN HAVE IT. AND YOU CAN AFFORD IT.

IEEE RECOGNIZES THE SPECIAL NEEDS OF SMALLER COLLEGES, and wants students to have access to the information that will put them on the path to career success. Now, smaller colleges can subscribe to the same IEEE collections that large universities receive, but at a lower price, based on your full-time enrollment and degree programs.

Find out more—visit www.ieee.org/learning

IEEE

AD INDEX

The Advertisers Index contained in this issue is compiled as a service to our readers and advertisers: the publisher is not liable for errors or omissions although every effort is made to ensure its accuracy. Be sure to let our advertisers know you found them through *IEEE Robotics & Automation Magazine*.

Advertiser	Page	URL	Phone
Adept MobileRobots	Cover 2	www.mobilerobots.com	+1 603 881 7960
ATI Industrial Automation	12	www.ati-ia.com/rft	+1 919 772 0115
Barrett Technology, Inc.	Cover 4	www.barrett.com	+1 617 252 9000
Butterfly Haptics, LLC	16	http://butterflyhaptics.com	
Cyberbotics Ltd.	5	www.cyberbotics.com	
Force Dimension	Cover 3	www.forcedimension.com	+41 22 362 6570
ICAR 2015	151	www.icar2015.org	+90 312 466 1500
IEEE Marketing Dept.	13	www.ieee.org/tryieeexplore	
KUKA Laboratories	3	www.kuka-labs.com/en/service_robots	+49 1805 968 268
KVH Industries	7	www.kvh.com/1750IMU	+1 401 847 3327
Maxon Precision Motors	15	www.maxonmotorusa.com	
Newark Element14	9	www.newark.com	+1 800 463 9275
Robotnik Automation	21	www.robotnik.eu	
ServoCity	11, 17	www.ServoCity.com	+1 620 221 0123
youBot Store GmbH	19	www.youbot-store.com	

Digital Object Identifier 10.1109/MRA.2013.2290958

AD SALES OFFICES

James A. Vick
Sr. Director, Advertising Business
Phone: +1 212 419 7767
Fax: +1 212 419 7589
jv.ieemedia@ieee.org

Marion Delaney
Advertising Sales Director
Phone: +1 415 863 4717
Fax: +1 415 863 4717
md.ieemedia@ieee.org

Susan Schneiderman
Business Development Manager
Phone: +1 732 562 3946
Fax: +1 732 981 1855
ss.ieemedia@ieee.org

Product Advertising
MidAtlantic
Lisa Rinaldo
Phone: +1 732 772 0160
Fax: +1 732 772 0164
lr.ieemedia@ieee.org
NY, NJ, PA, DE, MD, DC, KY, WV

New England/South Central
Eastern Canada
Jody Estabrook
Phone: +1 774 283 4528
Fax: +1 774 283 4527
je.ieemedia@ieee.org
CT, ME, VT, NH, MA, RI, AR, LA, OK, TX
Canada: Quebec, Nova Scotia, Newfoundland, Prince Edward Island, New Brunswick

Southeast
Thomas Flynn
Phone: +1 770 645 2944
Fax: +1 770 993 4423
tf.ieemedia@ieee.org
VA, NC, SC, GA, FL, AL, MS, TN

Midwest/Central Canada
Dave Jones
Phone: +1 708 442 5633
Fax: +1 708 442 7620
dj.ieemedia@ieee.org
OH, IL, IA, KS, MN, MO, NE, ND, SD, WI
Canada: Manitoba, Saskatchewan, Alberta

Midwest/Ontario, Canada
Will Hamilton
Phone: +1 269 381 2156
Fax: +1 269 381 2556
wh.ieemedia@ieee.org
IN, MI. Canada: Ontario

West Coast/Mountain States
Western Canada
Marshall Rubin
Phone: +1 818 888 2407
Fax: +1 818 888 4907
mr.ieemedia@ieee.org
AZ, CO, HI, NM, NV, UT, AK, ID, MT, WY, OR, WA, CA.
Canada: British Columbia

Europe/Africa/Middle East/Asia/Far East/Pacific Rim
Louise Smith
Phone: +44 1875 825 700
Fax: +44 1875 825 701
les.ieemedia@ieee.org
Europe, Africa, Middle East, Asia, Far East, Pacific Rim, Australia, New Zealand

Recruitment Advertising
Midatlantic
Lisa Rinaldo
Phone: +1 732 772 0160
Fax: +1 732 772 0164
lr.ieemedia@ieee.org
NY, NJ, CT, PA, DE, MD, DC, KY, WV

New England/Eastern Canada
Liza Reich
Phone: +1 212 419 7578
Fax: +1 212 419 7589
e.reich@ieee.org
ME, VT, NH, MA, RI
Canada: Quebec, Nova Scotia, NewfoundlandPrince Edward Island, New Brunswick

Southeast
Cathy Flynn
Phone: +1 770 645 2944
Fax: +1 770 993 4423
cf.ieemedia@ieee.org
VA, NC, SC, GA, FL, AL, MS, TN

Midwest/South Central
Central Canada
Darcy Giovingo
Phone: +1 224 616 3034
Fax: +1 847 729 4269
dg.ieemedia@ieee.org
AR, IL, IN, IA, KS, LA, MI, MN, MO, NE, ND, SD, OH, OK, TX, WI
Canada: Ontario, Manitoba, Saskatchewan, Alberta

West Coast/Southwest/Mountain States/Asia
Tim Matteson
Phone: +1 310 836 4064
Fax: +1 310 836 4067
tm.ieemedia@ieee.org
AZ, CO, HI, NV, NM, UT, CA, AK, ID, MT, WY, OR, WA, WA. Canada: British Columbia

Europe/Africa/Middle East
Louise Smith
Phone: +44 1875 825 700
Fax: +44 1875 825 701
les.ieemedia@ieee.org
Europe, Africa, Middle East



JUNE 22–25, 2015
NORTHWESTERN UNIVERSITY
EVANSTON, ILLINOIS USA

The 6th Joint Eurohaptics
 Conference and
 IEEE Haptics Symposium

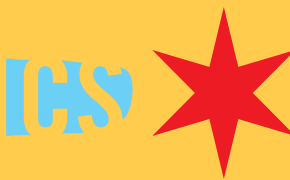
PARTICIPATION

We solicit original contributions related to any topics in the field of haptics. Contributions may include:

- * **Regular papers (6 pages).** Accepted papers will be published in the electronic proceedings and on IEEE Xplore. All authors will be expected to give podium presentations. The top 10% of submissions will be referred to the IEEE Transactions on Haptics for expedited review of an evolved, journal-length version.
- * **Work-in-Progress papers (4 pages).** These papers should highlight late-breaking research results, and will be evaluated on the basis of novelty rather than completeness. Accepted papers will be presented in poster format at the conference and will be published in the electronic proceedings only. Authors will retain copyright.
- * **Demonstrations.** Demonstrations are a critical component of any haptics conference. Due to limited space, a brief proposal must be submitted for each demonstration, and up to 50 will be selected.
- * **Half-day and Full-day Workshops and Tutorials.** The first day of the conference will be dedicated to workshops and tutorials, offering participants an opportunity to dive deeper into selected areas.

Further details will be made available at

WWW.HAPTICS2015.ORG



IMPORTANT DATES

- Technical Paper Submission**
January 23, 2015
- Workshop & Tutorial Proposal Submission**
February 6, 2015
- Paper Acceptance Notification**
March 20, 2015
- Camera-Ready Paper Submission**
April 10, 2015
- Work-in-Progress Paper Submission**
Demonstration Submission
April 14, 2015
- Work-in-Progress Acceptance Notification**
Demonstration Acceptance Notification
April 28, 2015
- Early Registration**
May 6, 2015

ORGANIZATIONS

- Sponsors**
 IEEE Robotics & Automation Society

- Technical Co-sponsors**
 IEEE Technical Committee on Haptics
 Eurohaptics Society

TOPICS

- * Haptic Interface Design & Control
- * Tactile Display
- * Haptic Sensors and Actuators
- * Human-Computer Interaction Involving Haptics
- * Multi-Modal Systems Involving Haptics
- * Teleoperation and Virtual Environments
- * Haptic Rendering and Modeling
- * Shared Haptic Control and Collaboration
- * Human Haptic Perception
- * Neuroscience of Touch
- * Human-Robot Haptic Interaction
- * Haptics in Industrial and Commercial Applications
- * Embedded/Situated/Ubiquitous Haptics
- * Other Innovative Applications of Haptics



Publishing in *IEEE Transactions on Robotics*

In this issue, Eugenio Guglielmelli (EG), editor-in-chief (EiC) of *IEEE Robotics and Automation Magazine*, interviews Frank Park (FP), EiC of *IEEE Transactions on Robotics* (*T-RO*) about publishing papers.

EG: Could you begin by identifying what you think are the most exciting areas of robotics research today from a publications perspective?

FP: If you're asking whether there's some list of hot and cold topics that we secretly maintain at *T-RO*, I can unequivocally tell you the answer is no. Now, I could tell you my personal preferences, but that would be beside the point. Unlike some other journals where the EiC can filter papers based on personal tastes, at *T-RO*, it's our community—the authors, reviewers (who are quite often authors themselves), and our 40 editorial board members—who collectively decide what types of papers we publish.

EG: So are you saying that there is some collective process for deciding what areas are hot and cold?

FP: No, I didn't mean to imply that. Each paper is judged on its own merit. I think maybe what you're asking is whether there's some conscious deliberation during the review process on whether a paper addresses a timely and interesting topic.

At some level, I'm sure the reviewers and editors do consider that. The more

important criterion, however, is research significance. This is different from originality and novelty, which is something I think reviewers sometimes overemphasize. A result can be novel or original while having little research significance. Perhaps that's the reason why no one bothered to do it that way. At the same time, a paper can report an advance of significant research value on a decades-old problem.

EG: I'll be more direct this time. Most authors understand the general principles behind writing a good scientific paper and getting it published. What are some additional considerations for getting a paper published in *T-RO*?

FP: I wish I had a formula or algorithm that broke it down cleanly, but I don't. The closest thing to one that I've seen is an article by the former EiC, Seth Hutchinson, published in the December 2010 issue of this magazine. It's cleverly titled "Surviving the Review Process" rather than something more attention grabbing like "How to Get Your Paper Published." It's a very lucid description of our review process and makes clear, for example, that decisions are not the outcome of a majority vote by the reviewers. Obviously, all reviews are not equally valid, and our editors try to sort out any contradictory comments by the reviewers, pointing out which need to be addressed and which can be ignored. Our associate editors, editors, and I are always checking each other's reasoning and arguments behind decisions. I like to think that we get it right most of the time.

EG: Is this then an admission that sometimes you get it wrong?

FP: I'm sure authors who've had their papers rejected by *T-RO*—you can put me firmly on that list—will say "absolutely." I'll concede that it's infrequent, but it does happen. However, it's more often the case of a less-than-deserving paper getting in rather than a strong paper being rejected. Sometimes a borderline paper is revised and resubmitted, and the reviewers may then only superficially check whether their criticisms have been addressed. I attribute these lapses to reviewer fatigue, and it's a growing problem.

We have three flagship conferences—the IEEE International Conference on Robotics and Automation, IEEE/RSJ International Conference on Intelligent Robots and Systems, and IEEE International Conference on Automation Science and Engineering—not to mention numerous other workshops, symposia, and other journals that ask for reviews, and we have reached a point where finding willing and qualified reviewers is becoming increasingly difficult. By the way, I don't mean to imply that some of our published papers are bad. Today there are many forums in robotics for publishing one's work, and *T-RO* naturally seeks to publish work of the highest impact. I like to think we get it right most of the time, but it is a subjective threshold.

EG: I agree completely that we're getting saturated with review requests these days. What can be done?

(continued on p. 165)

force dimension

To display the digital world to your hands | to invent new ways to interact with computers and machines | we manufacture and market the finest precision master haptic devices for leading-edge applications in research, medical and industry.

With its unique 7 active degrees-of-freedom, the **sigma.7** is at the heart of the **Force Dimension master console** designed for seated operators. The two end-effectors cover the user's natural range of motion and offer a very high level of forces and torques, making it the most accomplished and versatile master console available today. The combination of full gravity compensation and driftless calibration contributes to greater user comfort and accuracy. Conceived and manufactured in Switzerland, the **Force Dimension master console** with dual **sigma.7** is customizable and designed for demanding applications where performance and reliability are critical.

Force Dimension
Switzerland

www.forcedimension.com
info@forcedimension.com





Barrett Technology®



Perception Palm

Sensor Suite for BH8-282

Unobstructed vision, range finding, and laser-grid emitter.

The closer the Hand is to the object, the better the performance, right up until the grasp is fully secured.



Patent #7,168,748

design :: Barrett Communications :: www.barrettcommunications.com

Barrett Technology®

Barrett Technology has a large global customer base of leading research organizations utilizing the proven technology of the WAM and BarrettHand for applications in vision, AI, mobile systems, medical, haptics, advanced manipulation, and automation. **Visit us at www.barrett.com.**